Analysis of Cadmium Zinc Telluride Detector Performance and Characteristics for Applications in Gamma-Ray Imaging Spectrometers

by

Yvan A. Boucher

A dissertation submitted in partial fulfillment
of the requirements for the degree of
Doctor of Philosophy
(Nuclear Engineering and Radiological Sciences)
in The University of Michigan
2013

Doctoral Committee:

Professor Zhong He, Chair
Adjunct Associate Professor John A. Nees
Professor Sara A. Pozzi
Professor David K. Wehe

To the He-Men

TABLE OF CONTENTS

LIST OF FIGURES

Figure

LIST OF TABLES

Table

CHAPTER I

Introduction and Background

1.1 Gamma Rays and How to Detect Them

Gamma rays are electromagnetic radiation of high frequency and high energy [1]. They are produced as a result of a nuclear reaction, which can be anything from the fission of a large nucleus to the decay of an unstable nucleus. The energy at which a gamma ray is emitted from a nucleus is determined by the energy difference between the initial and final states of the nucleus, with sometimes more than one gamma ray being emitted to account for the total energy released in the form of gamma radiation. Therefore, the gamma-ray energy released following a reaction is predictable. However, the opposite is also true. If distinct gamma rays are measured, a nuclear reaction to produce those gamma rays can be determined. This opens the door for many applications for the measurement of gamma radiation.

Depending on the precise situation, a measurement of gamma radiation can tell different things. In a passive environment, a measurement of gamma rays indicates that a radioactive source is present. By intelligently studying the energies of the gamma rays measured, the identity of the source(s) present can be determined. This is important for the control and protection of special nuclear material than can be used in making nuclear weapons, for the identification of harmful radiation near workers in a facility, or many other suitable applications. In an active environment, where an

external nuclear radiation source is used to induce a nuclear reaction in a material of interest, a measurement of gamma rays can be used to determine the exact material that is being actively interrogated.

Gamma rays are ionizing radiation that can interact with material through three predominant interactions. They can undergo photoelectric absorption, Compton scattering or pair production. Photoelectric apsorption occurs when an incident gamma-ray interacts with an atom, is fully absorbed, and a photoelectron from one of the shells of the absorber atom is released with an energy equal to the energy of the incident gamma ray minus the binding energy of that electron [2]. Rearrangement of the electrons in the electron shell fills the vacancy left by the photoelectron and the binding energy is released in the form of a characteristic x-ray or auger electron, both of which are typically reabsorbed in the near-by detector material [2]. Compton scattering occurs between an incident gamma ray and an electron. The products of the reaction are a recoil electron and a scattered gamma ray, with the energy of each depending on the scattering angle. Pair production occurs when an incident gamma ray interacts with the electric field of a nucleus to form an electron-positron pair. The rest mass of the electron-positron pair, 1.02 MeV, is required in the incident gamma ray for pair production to occur, and any excessive energy is carried off by the electron-positron pair [2]. The electron and positron typically travel a very short distance before depositing all of their energy in the detector material. The positron will then annihilate with an electron, releasing two 511 keV photons. If both of these photons are reabsorbed in the detector material, then a full measurement of the incident gamma-ray energy is made. Otherwise, if one or both of these photons escape the detector material, it will contribute to the single or double-escape peaks below the incident gamma-ray energy.

All of these interactions result in energy being transferred from the gamma ray to an electron or electron-positron pair in the detector material. The electron energy

is what is then measured by the detector. Through understanding the specific application for which gamma rays are being measured as well as how they interact in material helps determine what type of detector material should be used. The next section will explore varying types of gamma ray detectors and which ones are best for different applications.

1.2 Gamma Ray Detectors

1.2.1 Scintillators and Semiconductors

There are two prevailings means to measure the energy of the electrons produced from the interaction of gamma rays with material. The first is to transduce the kinetic energy of the electron to detectable light—a process called scintillation. The light is then converted back into electrons through either a photomultiplier tube or a photodiode. Proportionality between the kinetic energy of the original electron and the number of electrons created in the photomultiplier tube or photodiode is maintained throughout the process. The second technique is to have the secondary electron excite many electrons from the valence band to the conduction band of a semiconductor to create electron-hole pairs. A number of electron-hole pairs proportional to the gamma-ray energy are created, and a bias is applied to the semiconductor to cause these pairs to drift through the material and induce a charge on collecting electrodes. Both of these techniques are able to create energy spectra of the gamma rays incident on the material.

The quality of the energy spectrum, however, is quite different for the two techniques. Due to the inefficient process for conversion of the incident gamma ray to a charge signal in scintillation detectors, the energy required to create a single information carrier is on the order of 100 eV or greater [2]. This significantly reduces the number of carriers produced following the interaction of a single gamma ray and

leads to degraded energy resolution due to the statistical fluctuations. Alternatively, semiconductors will have a number of information carriers determined by the band gap energy and the fano factor. Typical band gap energies are on the order of several eV, leading to at least an order of magnitude more information carriers than for scintillation detectors. This allows semiconductor detectors to have a much lower theoretical limit of energy resolution. If energy resolution were the only metric for choosing a gamma-ray detector, semiconductor detectors would be almost always the best option, however there are other factors.

Efficiency for measuring gamma rays is also important. The efficiency is determined by several factors, including the size of the detectors and the likelihood for a gamma ray to interact with the material. Scintillation detectors can be grown to larger dimensions, increasing their efficiency. Gamma rays have a higher probability to interact with materials with a higher atomic number, leading to preferentially choosing materials for either scintillation or semiconductor detectors that are further down the periodic table. Materials with high atomic number are available for both scintillator and semiconductor detectors.

Other factors that impact the decision of what detector to use for a specific application include cost, simplicity and stability. Scintillators tend to be cheaper and simpler. However the worse energy resolution prohibits their use in applications requiring excellent energy resolution. They are much better suited for applications that require a higher efficiency for detection of gamma rays, but with less stringent requirements on energy resolutions. Such an application would be for primary inspection with portal monitors, where a higher probability of detecting a radioactive source is needed, but there are not concerns about creating a detailed characterization of that source. A secondary inspection would then be used to fully characterize the source, and would require a detector with better spectroscopic capabilities. The opposite application that is much more suited for a semiconductor detector is the characteri-

zation of special nuclear material. High energy resolution is required to characterize the isotopics of the material.

1.2.2 Semiconductor Materials

The most well-established semiconductor gamma-ray detectors are silicon or germanium. Due to its low atomic number, silicon detectors tend to be best for very low energy gamma rays or x rays. High purity germanium (HPGe) detectors have a slightly higher atomic number (32) and can be grown to relatively large sizes (750 cm^3) [2]. The small band gap energy of 0.7 eV and only 3 eV per electron-hole pair generated allows for excellent energy resolution due to the improved statistics of more information carriers for the same amount of gamma-ray energy deposited compared to other detectors. However, the small band gap energy prohibits the use of germanium detectors at room-temperature because of the large thermally-induced leakage current [2]. Germanium detectors are cooled to temperatures of around 77 K by coupling the detector to a dewar of liquid nitrogen or a mechanical cooler. The cooling requirement makes HPGe detectors an acceptable choice for a detector for laboratory measurements that require excellent energy resolution, but less suitable for field measurements where a more robust detector is a better option. Such a detector would be a room-temperature semiconductor detector that has a high atomic number and be available in large volumes. Suitable wide-band gap semiconductors are CdZnTe, HgI_2, and TlBr.

Cadmium Zinc Telluride (CdZnTe) emerged as a room-temperature semiconductor detector in the early 1990's [3]. Early results showed a promising energy resolution of $\sim$3% at 662 keV, but the volume was restricted to 5×5×5 mm^3 due to issues with material growth [4]. More advanced readout electronics were developed to help improve the performance of these crystals—as will be discussed in the next section. In order to match the efficiency of HPGe detectors at higher energies, larger volume

detectors were required. The first $20\times20\times15$ mm^3 detector that achieved sub-1% energy resolution at 662 keV was grown by eV Products in 2006 [5]. Nonetheless, there were still crystal growth issues to overcome as CdZnTe crystals tend to have a wide range of defects [6–9]. Recent progress to reduce the number of defects in the growth of large volume CdZnTe has been made at Redlen Technologies, Inc. using the traveling heater method [10–12]. Over the years, the improvement of the crystal quality can be tracked through a comparison of the recorded values of the mobility-lifetime product. Values on the order of $10^{-3}cm^2/V$ were recorded in the late 1990's [13]. Recent measurements show values on the order of $10^{-2}cm^2/V$, indicating that higher quality material is now available [14]. The recent progress in improved crystal quality makes CdZnTe a leading candidate for room-temperature semiconductor detector applications.

Mercuric iodide (HgI_2) became an exciting option for room-temperature semiconductors starting in the early 1970's and continuing into the 1980's [15–17]. HgI_2 has a higher effective atomic number than germanium as well as a higher density [2]. Unfortunately, poor charge mobility, material non-uniformity and crystal polarization limited the affective use of HgI_2 in planar detector geometries [18, 19]. Better performance has been achieved using a pixellated anode configuration [20–22], yet growth of HgI_2 continues to be plagued by defects and regions of poor charge collection [23].

Thallium bromide (TlBr) has gained recent interest as another possible room-temperature semiconductor detector. With a high atomic number and density, TlBr would be an efficient gamma-ray detector and detectors have been fabricated with performances below 1% FWHM at 662 keV [24]. However, TlBr is an immature detector material compared to CdZnTe. The best performance for TlBr has been achieved on 5 mm thick detectors. Detectors as large as 18 mm thick have been grown, but their performance is worse compared to the thinner detectors [25]. TlBr also suffers from a polarization phenomena that requires the detectors to be cooled

to $-20°C$ [26, 27].

1.3 Cadmium Zinc Telluride

Along with improvements to the crystal quality of CdZnTe over the last two decades, there have been improvements to the read-out electronics that have allowed the technology to mature significantly. The order of magnitude difference between the mobility-lifetime product of the holes and electrons in CdZnTe created the need for the development of single-polarity charge sensing techniques for reading out the signals from a CdZnTe crystal.

The first single-polarity charge sensing devices used a coplanar grid anode electrode pattern [4]. This technique uses two electrodes with a voltage difference between them to allow the electrons to be collected by only one of the electrodes. Solving for the weighting potential difference between the two anode electrodes under this configuration shows that a relationship can be found that makes the measurement independent of the depth of interaction under the assumption that the trapping of electrons is negligible [28]. Since the trapping of electrons is known to not be negligible, a gain correction is able to be applied to account for the 4-10% of electrons that were trapped and improve the performance of coplanar grid CdZnTe detectors [28,29]. The complanar grid technique is however limited by the inability to correct for spatial nonuniformities in the CdZnTe, and even with recent material grown by the traveling heater method can only achieve near 2% FWHM at 662 keV [30].

Another technique to employ single-polarity charge senging is to use a pixellated anode design. The first pixellated CdZnTe detectors were made in 1994 for thin detectors [31]. The small pixel effect can then be used along with depth sensing techniques to create a 3-D position-sensitive detector [32–34]. Using an 11×11 anode electrode pattern and 40 depth bins, a single detector can be separated into 4,840 voxels. Correcting for the gain in each voxel independently allows the spatial variation

in the uniformity of the crystal to be corrected to improve the overall performance [35–37]. With the recent improvements to the crystal growth methods, large-volume detectors ($20\times20\times15$ mm^3) produce energy spectra below 1% FWHM at 662 keV [5]. Future improvements to the crystal quality and read-out electronics may allow CdZnTe detectors to rival the spectroscopy achievable with HPGe detectors.

The 3-D position-sensing capability also allows for the development of gamma-ray imaging techniques. Using the 3-D position of each interaction of a Compton scattering event followed by a photoelectric absorption allows a 4π image to be created of the incident direction of the gamma ray on the CdZnTe detector [38–42]. More sophisticated techniques based on Compton imaging have been developed for source tracking and 3-D imaging [43, 44]. Since Compton scattering in CdZnTe is not probable at lower energies (below 300 keV), a coded aperture technique has been developed to be able to localize lower energy sources [45].

Improved read-out electronics allowed for arrays of 3-D position-sensitive CdZnTe detectors to be formed. The feasibility of operating detectors in coincidence in an array was shown in 2007 [46]. However, there were not enough high-quality CdZnTe crystals available to populate an 18-detector array at the time. With the improvements made by Redlen Technologies, Inc. over the past few years, enough detectors are now available to make several 18-detector array systems of 3-D position-sensitive CdZnTe detectors. The following chapters will describe in detail the work completed to build, calibrate, characterize and improve these gamma-ray imaging spectrometers.

CHAPTER II

CdZnTe Array Systems

The most challenging part of operating a single 3-D position-sensitive device is handling the signals from all of the anode electrodes simultaneously. The CdZnTe detectors are pixellated with an 11×11 pattern, which means that there are 121 separate channels that need to be read out at the same time and processed as a single event. This requires an application specific integrated circuit (ASIC) and additional hardware to process the events. First, a description of the CdZnTe detectors will be provided, which will be followed by a description of the hardware required for data acquisition. Having laid the foundation for the CdZnTe array system, the chapter will conclude with a thorough explanation of how the 18-detector CdZnTe gamma-ray imaging spectrometer was built and calibrated.

2.1 CdZnTe Detector Specifications

Each CdZnTe detector is 20×20×15 mm^3. The anode electrode uses an 11×11 pixel pattern, with a steering grid in the gap between the pixels. The steering grid is 100 μm wide and there is a 200 μm gap between the grid and the pixel. The pixel pitch is 1.72 mm. The guard ring around the outside of the edge pixels is 500 μm. A layout of the anode electrode pattern is shown in Fig. 2.1. The steering grid is used to prevent the charge formed over the gaps between pixels from failing to

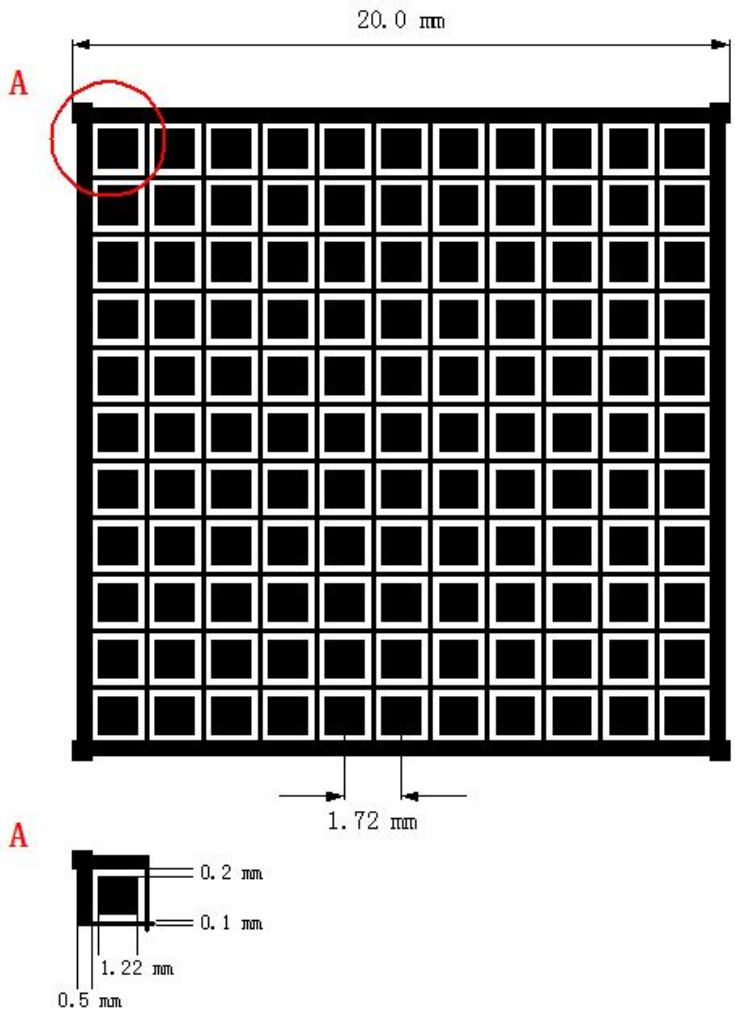

Figure 2.1: Diagram of the anode electrode pattern for one of the 20×20×15 mm^3 CdZnTe detectors.

be collected by a pixel by forcing all of the electric field lines to end on the anode electrodes. To accomplish this, the grid is biased to a lower negative voltage that is determined uniquely for each detector since each detector tends to have a different grid-to-pixel resistance. A lower resistance leads to a higher leakage current to produce the same voltage and create the same steering effect. A higher leakage current may lead to increased electronic noise and cause a degradation in spectroscopic performance. Therefore, the optimal grid bias is uniquely found for each detector prior to calibration.

Each detector is provided a cathode bias of -3000V. The cathode is required to be stable, meaning that there are not large, non-gamma-ray pulses present when monitoring the cathode signal on an oscilloscope. These pulses will continuously trigger the system and prevent useful measurements from being collected. Cathode breakdown can have several possible causes, including a low detector bulk or surface resistance, damage to the cathode surface, or high humidity leading to condensation on the cathode surface. To attempt to eliminate humidity as a cause of cathode breakdown, it is best to isolate the detectors as much as possible and have them sealed from the atmosphere as much as possible. It is also best to keep them at room temperature, cooling them below room temperature will tend to cause condensation and lead to cathode breakdown.

The CdZnTe detectors also tend to have worse performance as temperature increases, with eventually no longer functioning if the temperature of the system reaches temperatures as high as $40°C$. At this temperature, the grid-to-pixel resistance breaks down, and the anode pixels are overcome with electronic noise. Therefore it is best to keep the detectors at or within a few degrees of room temperature.

2.2 System Hardware

The current CdZnTe array systems utilize an analog ASIC made by Gamma Medica-Ideas. The GMI VAS_UM2.3/TAT4 ASIC has 129 total channels, which can be broken up into three different types [47].

The first type consists of the 123 normal channels to process the negative charge signals from the anode electodes—two of the channels are unused for the detectors with the 11×11 anode electrode pattern. Each channel has both a charge amplitude sensing and electron drift sensing circuit integrated into a single chip. The block diagram for a single channel is shown in Fig. 2.2 [47]. By combining the two circuits into a single chip, the entire ASIC is able to be shrunk down and mounted to a

front-end board with a similar dimensional footprint as the 2×2 cm^2 area CdZnTe detectors. A picture of a GMI VAS_UM2.3/TAT4 ASIC is shown in Fig. 2.3. The second type consists of the 5 special channels designed to read out the positive charge signals from the cathode and anode steering grid channels. The three spare channels that are designed for positive charge signals are useful as it is far more likely to damage a pre-amplifier on the cathode channel that is connected to a -3000V source, than it is to damage an anode channel that is effectively grounded. The final channel is a test channel used for monitoring the output waveform of the shaper for diagnostic purposes [47].

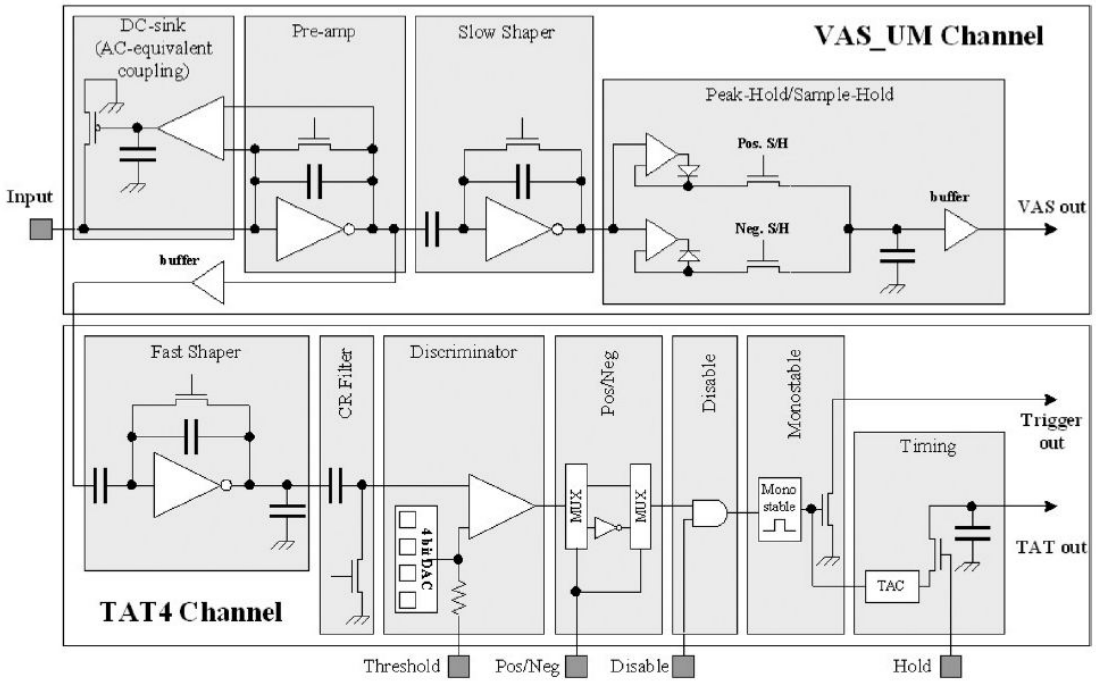

Figure 2.2: The block diagram of a single channel on the GMI VAS_UM2.3/TAT4 ASIC.

Each channel uses a $1\mu s$ shaping time and has a dynamic range from approximately 30 keV to 3 MeV. The lower level of the dynamic range is controlled by a threshold value for the charge collected by a single electrode. If the charge observed on a single channel crosses this threshold, then the system is triggered. A separate

Figure 2.3: Picture of the GMI VAS_UM2.3/TAT4 ASIC.

threshold is set for the anode channels and the cathode channel. Typically, a single lower level threshold is set for all anode channels in a single detector such that no channels are triggered constantly by electronic noise. The cathode threshold is also set such that the detector is not continuously triggered by electronic nosie. The hold time is also adjustable and is normally set to $4\mu s$, which is long enough for all charge created in the detector to drift to the anode electrodes. After the hold time is reached, all channels that have been triggered will be read out and their information will be passed to the FPGA on the system's motherboard.

Each ASIC dissipates approximately 0.45 W, and therefore generates a fair amount of heat. As temperature changes, the performance varies. For the optimal operation of the equipment, it is best to regulate the temperature of the ASICs so that consistent operation is achieved.

The motherboard (MOCA) is shown in Fig. 2.4. The MOCA board has 9 connectors for ASIC modules arranged in a 3×3 array. The FPGA on the MOCA board is used to control the ASICs, perform the data acquisition, and transfer the signals to the computer [47]. The analog-to-digital converters used to convert the analog signals from the ASIC to digital signals for the FGPA are located on the MOCA board. The MOCA board also houses the bias network for the ASICs and the power regulators used to provide the ASIC and MOCA components with the correct power values.

The current array systems use a digital read-out board, which connects to a digital I/O card in the computer as the interface between the MOCA board and the data acquisition software. Future systems will replace this extra hardware by replacing

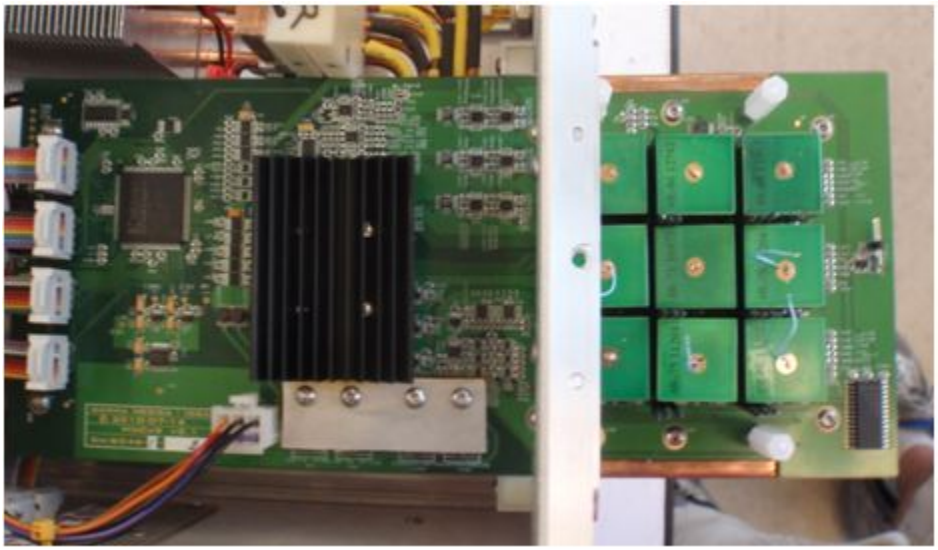

Figure 2.4: Picture of the MOCA board fully populated with 9 20×20×15 mm^3 CdZnTe detectors. The FPGA is located at the left side of the picture, and the wires at the far left of the picture are connected to the digital readout board to transfer the acquired data to the computer for data processing.

the current FPGA on the MOCA board with an FPGA capable of connecting to a computer via USB or Ethernet.

2.3 System Calibration

The first step in getting a CdZnTe array system working is to assemble the hardware components. Then the system can be biased and calibrated. The steps taken to get the first two 18-detector CdZnTe gamma-ray imaging spectrometers fully operational are outlined in the following sections.

2.3.1 Assembly and Biasing

The hardware components described above are incorporated into a system design created by James Berry, a mechanical and electrical engineer. The first system was built in July, 2010. Several pictures of this system during the assembly stages can be

seen in Fig. 2.5, 2.6, 2.7, 2.8. The second system was built in June, 2011. Several pictures of this system can be seen in Fig. 2.9, 2.10, 2.11.

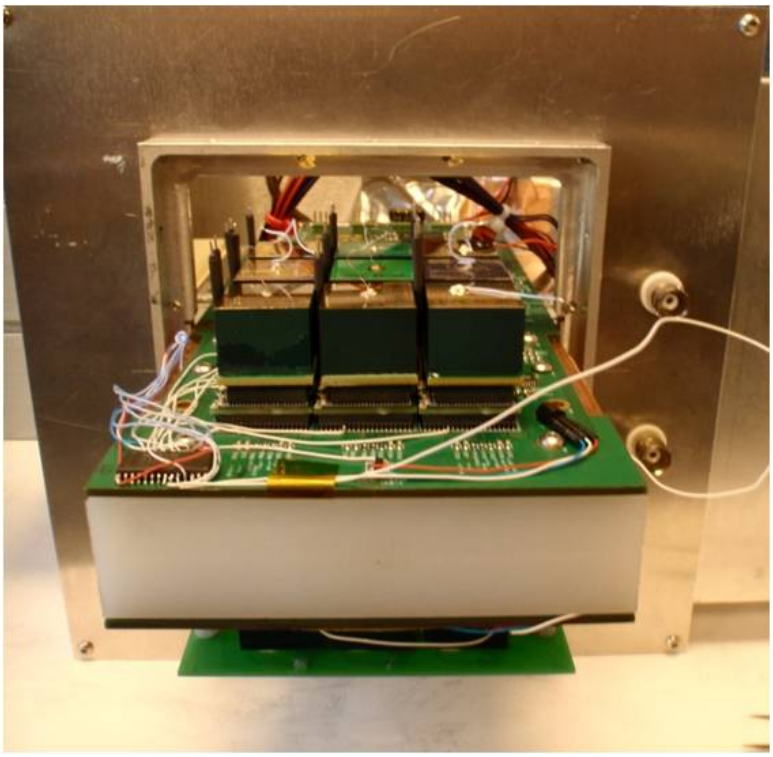

Figure 2.5: Picture of the assembled detector head of the first 18-detector CdZnTe array system.

Figure 2.6: Picture of one of the populated MOCA boards placed in the first CdZnTe array system.

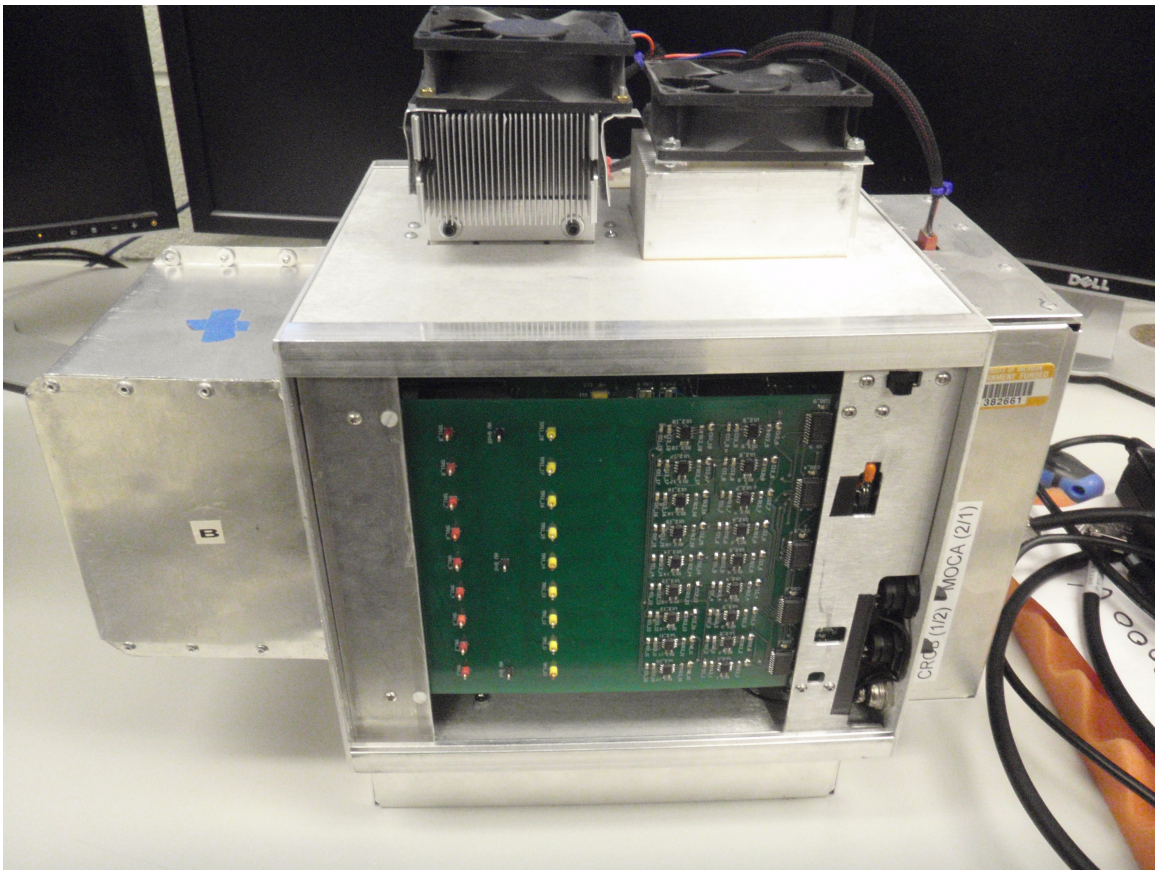

Figure 2.7: Picture of the assembled first CdZnTe array system with a side panel removed showing the high voltage generation board. The detector head can be seen at the left side enclosed in an aluminum housing.

The main components included in each system are the two MOCA boards, which are placed back to back with a separation of 55 mm and 41 mm for the first and second systems, respectively. Nine $20\times20\times15$ mm^3 CdZnTe detectors are mounted to 9 ASICs and attached to each of the MOCA boards in a 3×3 array. Between the two MOCA boards is located a heat pipe assembly which is connected to two peltier devices. These draw the heat produced by the ASICs away from the detector head and are dissapated through heat exchangers at the top of the system. The front of each MOCA board extrudes from the front of box and is encased in a separate enclosure for thermal and humidity isolation from the rest of the system. This is called the detector head. The high voltage required for the cathode and grid voltages of each

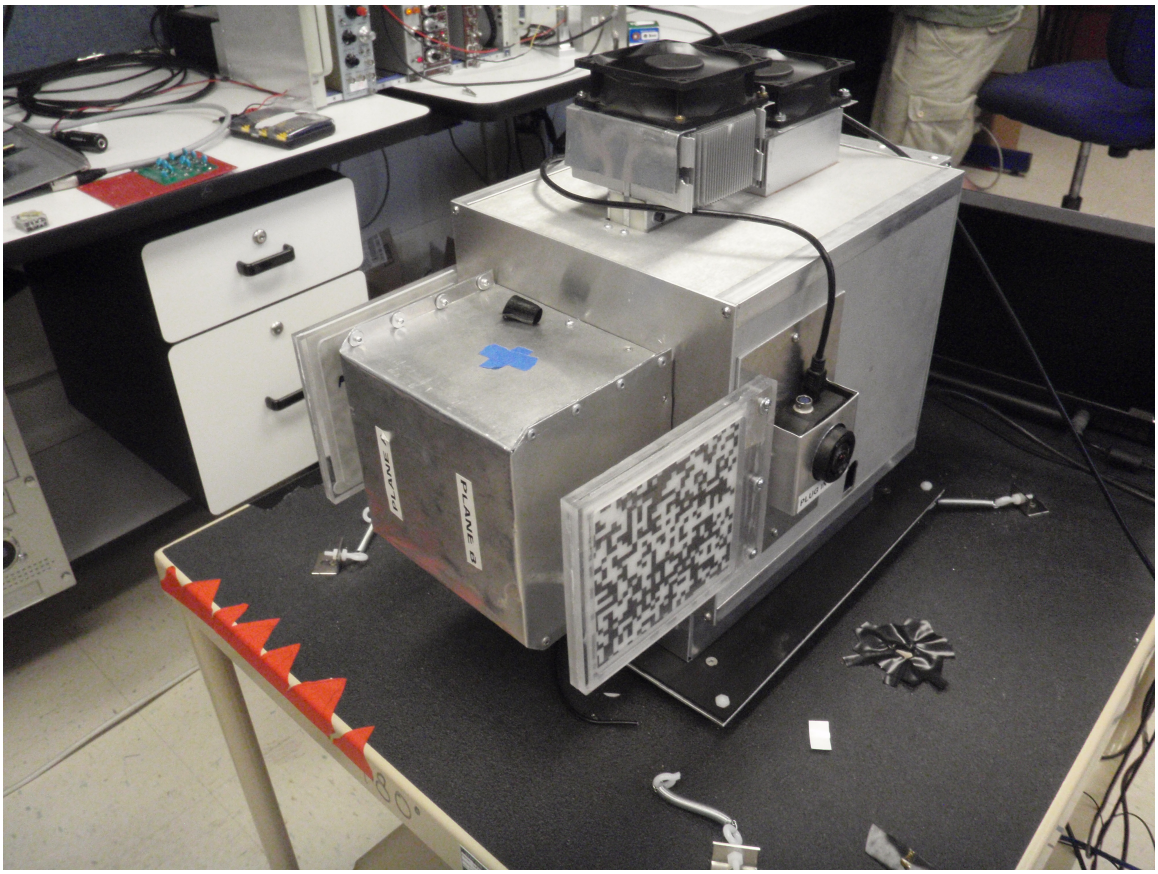

Figure 2.8: Picture of the first fully assembled CdZnTe array system complete with coded aperture masks and optical cameras.

detector are generated on high voltage boards located in the larger box behind the detector head. Two bulkhead boards are used for the transferring of these voltages from the main system to the detector head. A high voltage distribution board then routes these voltages to the correct channels of each detector.

An individual cathode bias and grid bias is generated for each detector. This allows for each detector to have a different optimal grid bias. The individual cathode biases were for the flexibility of being able to bias down a single detector if it is behaving abnormally and creating problems in other detectors. This flexibility has not shown to be useful and future systems would be advised to have a single high voltage generation shared by all detectors in the system for simplicity. Individual grid biases would still be required since each detector has a unique optimal grid biases.

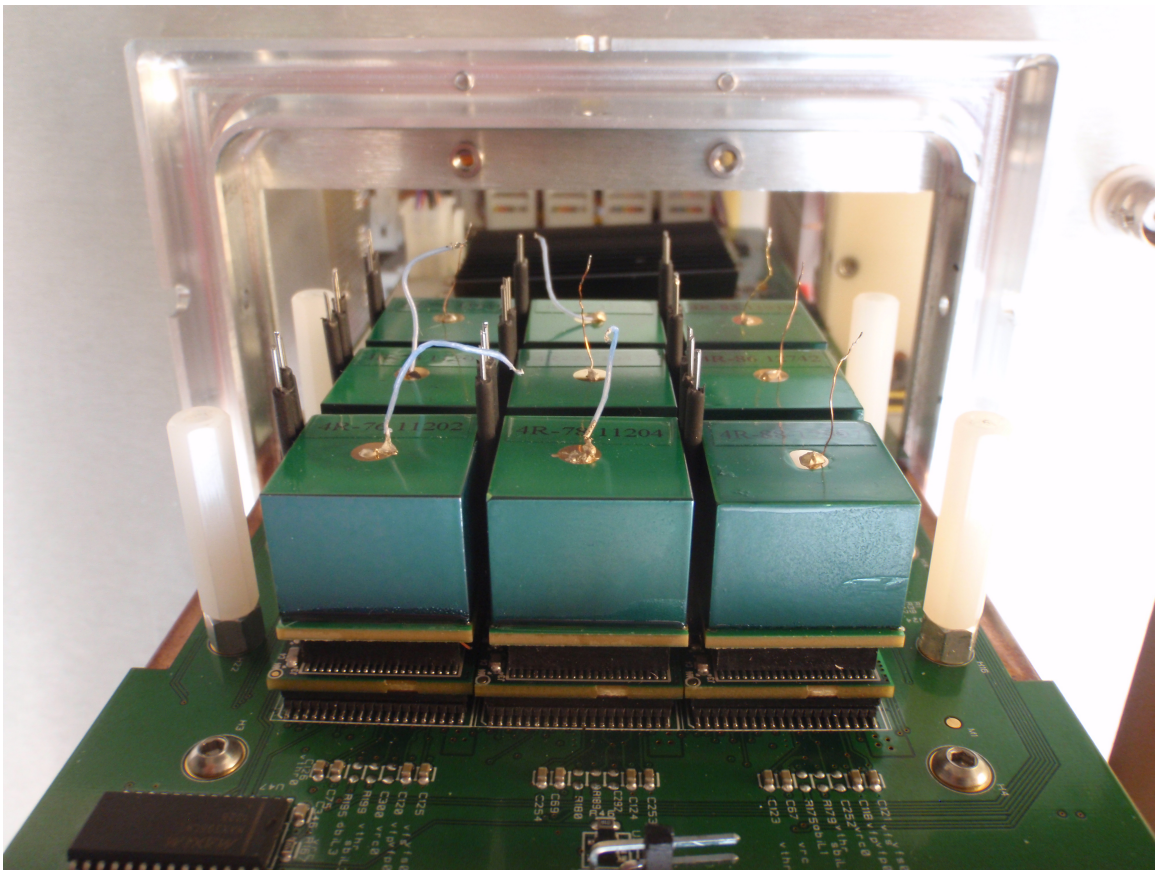

Figure 2.9: Picture of the detector head of the second CdZnTe array system.

Once the system is assembled, the system is first checked to make sure there is not noise triggering in the detectors. Without any bias, the detectors should not trigger. If this is confirmed, the next step is to slowly step the cathode bias up to -3000V. It was determined that the detectors can handle biasing up rapidly, however the ASICs can be damaged by ramping up the bias too quickly. A step of -10V every three seconds was determined to be the fastest safe procedure for the ASICs. Each of the 18 detectors is biased simultaneously. After reaching full cathode bias, the detectors are once again checked to make sure that there is no noise triggering and that each cathode is stable without breakdown.

If all detectors pass these tests, then the grids are biased up. An approximation of the optimal grid bias is taken from the original testing of each detector upon receipt from the manufacturer, yet further measurements are taken to guarantee that the

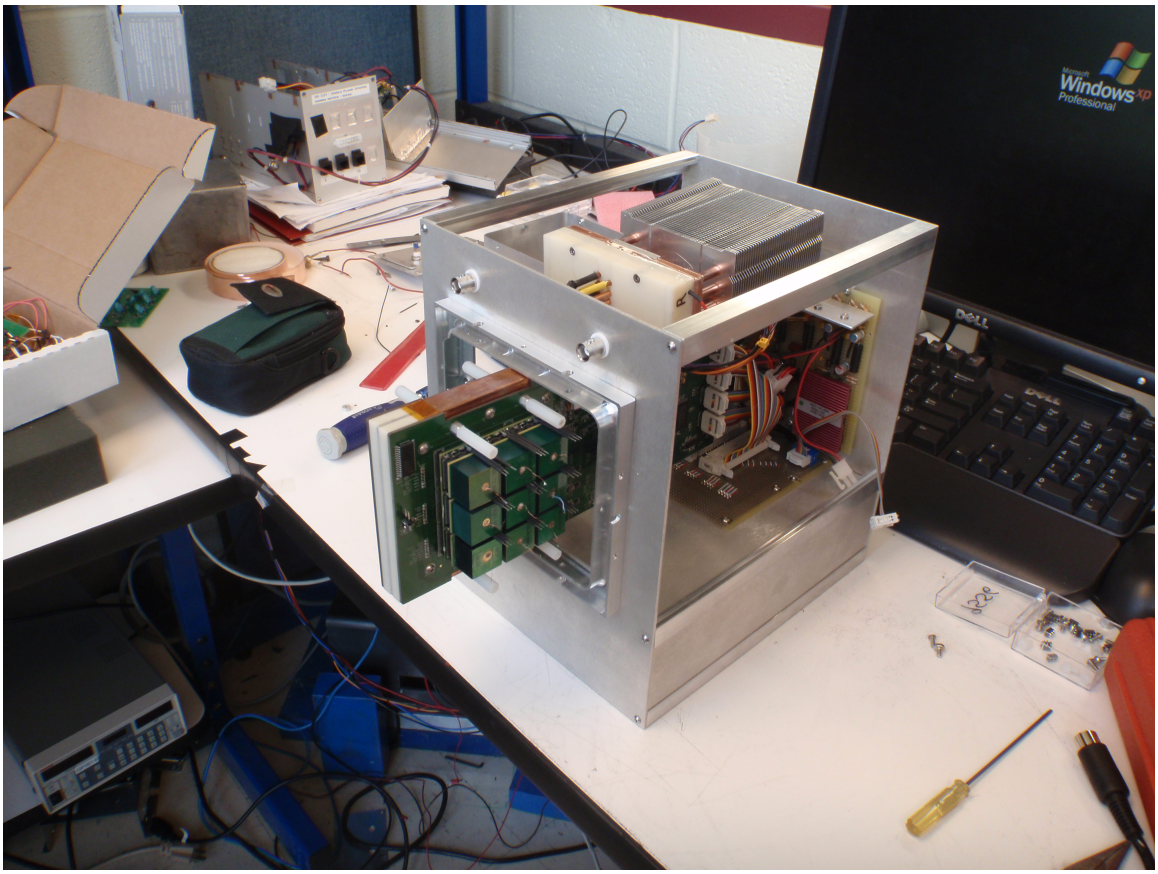

Figure 2.10: Picture of the second CdZnTe array system during assembly. The heat pipes extend from underneath the shown MOCA board to the top of the system (right side of picture) where the peltier devices and heat sinks dissipate the heat generated by the ASICs.

optimal setting is found for each detector. This is accomplished by taking repeated short measurements with a ^{137}Cs at several grid biases to determine the voltage at which the optimal steering is achieved. By comparing the energy spectra for events that triggered neighboring pixels, which are normally single interaction events occurring over the grid, the optimal grid bias can be selected. An example of the collected spectra for one of the detectors of the first array system is shown in 2.12. The optimal grid bias can be seen to be -90V due to having the narrowest peak and best peak-to-valley ratio. Therefore, this grid bias tends to steer most of the electrons to the collecting anodes and not degrade the energy resolution with additional electronic

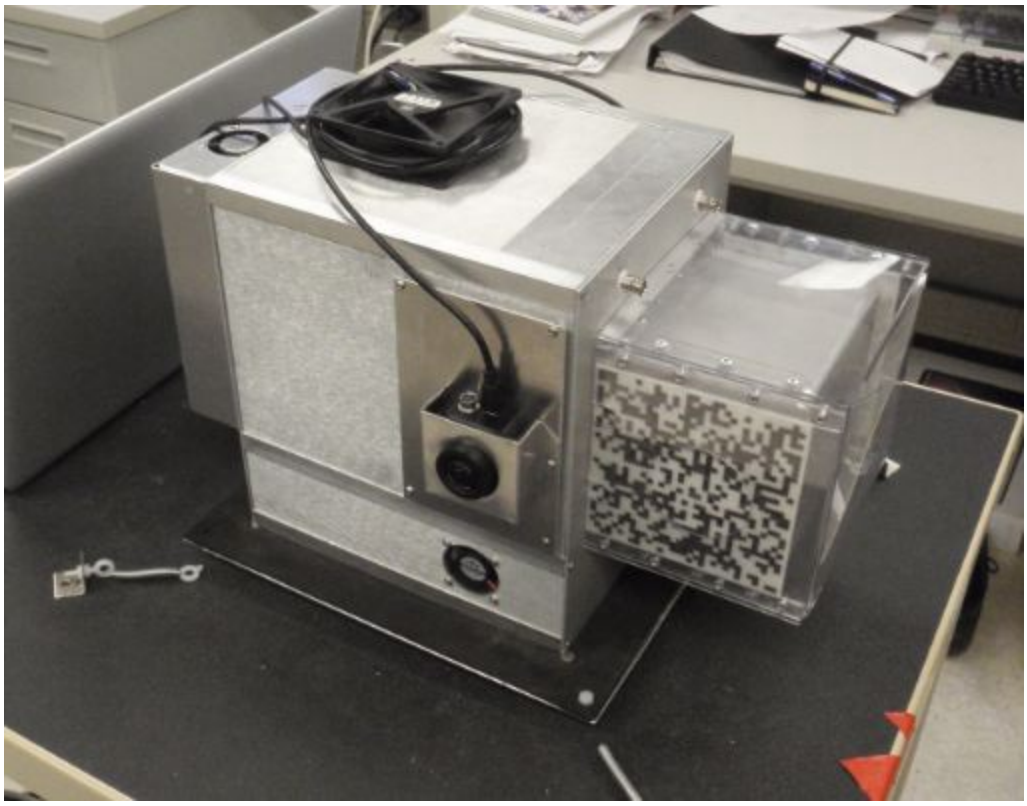

Figure 2.11: Picture of the second fully assembled CdZnTe array system complete with coded aperture masks and optical cameras.

noise.

With the system now at full bias for all of the detector cathodes and grids, the system is ready to be calibrated.

2.3.2 Calibration

The largest part of the calibration of the CdZnTe array system is the gain correction based on events from a ^{137}Cs source. The ^{137}Cs source is first positioned in front of one of the planes in such a position that each detector receives roughly the same fluence. Enough counts are collected in each of the 9 detectors of the first plane to perform a full calibration of each detector, and then the procedure is repeated for the 9 detectors of the second plane.

In a single detector, there is a weak correlation between anode signal amplitude

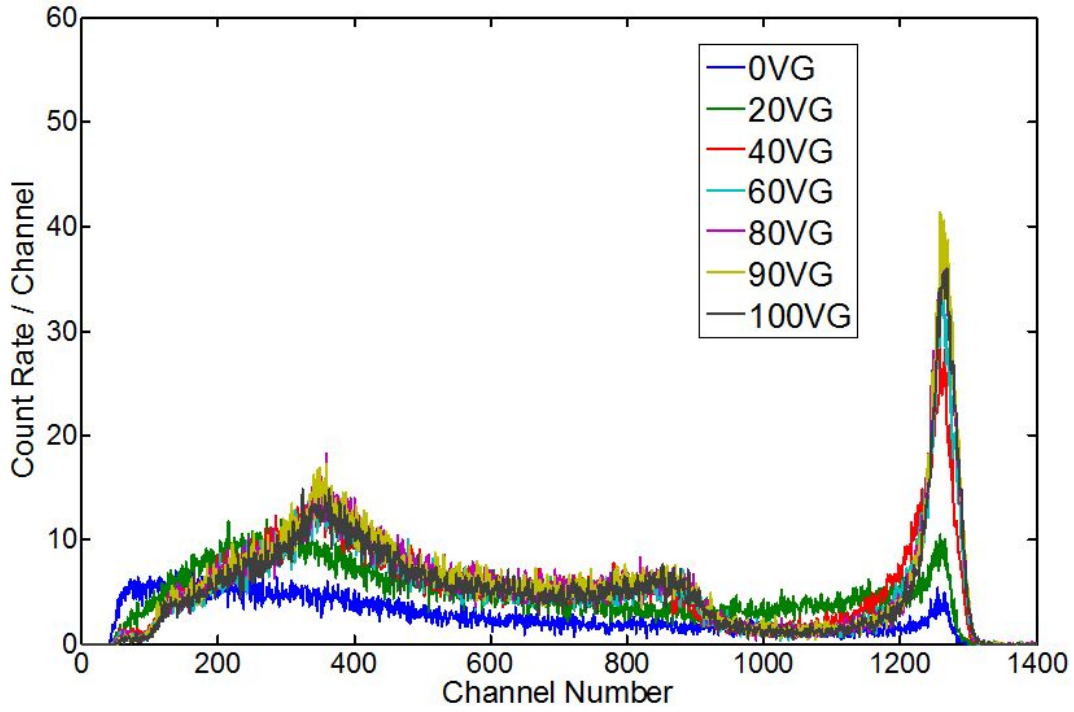

Figure 2.12: Graph of the energy spectra collected for two-pixel side-neighboring events in detector 4R-30 at multiple grid biases.

and depth due to the small pixel effect, while the cathode signal amplitude varies linearly with the depth of interaction. Therefore, the cathode-to-anode signal ratio can be used to determine the depth of interaction for every single-pixel event in the detector. The depths are separated into 40 depth bins for each of the 121 anode pixels in a detector. Therefore, each single-pixel event is added to the raw amplitude signal spectrum collected for one of the 4840 detector voxels. A gain correction for the effects of electron trapping is then found for each voxel to align the photopeaks produced from the ^{137}Cs source to the correct energy (in keV).

Taking a step backward, before the depth of interaction can be determined for each event, a slight adjustment needs to be made for each event to correct for the peak hold drop [48]. Fig. 2.13 shows the effect that the peak hold drop has on the amplitude determination from the GMI ASIC. It can be seen that the signal deficit is different as a function of the energy deposited in a single channel, therefore requiring

a signal amplitude dependent correction. This correction is unique to each ASIC but within each ASIC, each channel behaves similarly. Thus, a sample channel in each detector in the system was tested to determine the signal amplitude dependent correction for the peak hold drop.

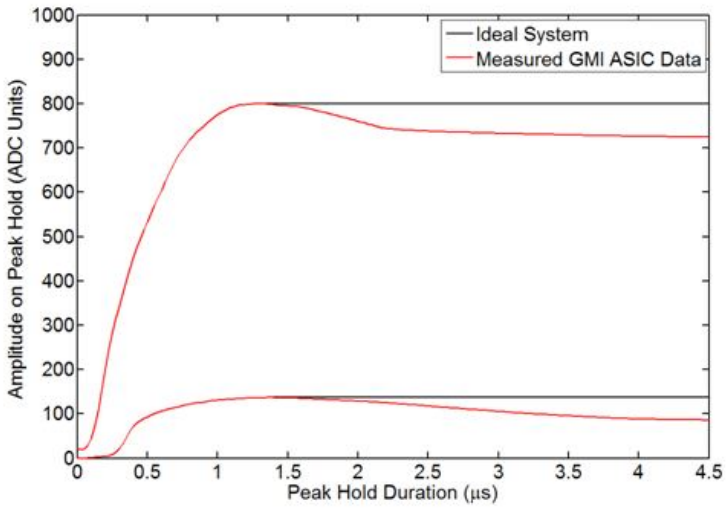

Figure 2.13: Graph showing the peak hold drop issue in the GMI ASIC.

In addition to the position-sensitive gain correction, the depth obtained from the cathode-to-anode signal ratio is also correlated to the drift time to provide a second measure of the depth of interaction. This allows the depth of interaction to be known for multiple pixel events. The cathode-to-anode signal ratio cannot be used for these events since the cathode signal is shared between the multiple interactions. Cathode and anode time-amplitude-walk corrections and a weighting-potential-cross-talk correction are also found for each detector.

A full non-linearity calibration is also completed to account for the ASIC non-linearity. Gamma-ray sources with emission lines spanning the full dynamic range of the ASIC were used. The sources and lines used in the non-linearity correction are shown in Table 2.1. A fifth-order polynomially fit is determined for each pixel.

Table 2.1: Sources used to complete the ASIC non-linearity correction for the CdZnTe array systems.

Source	Energy (keV)
^{241}Am	59.5
^{133}Ba	81.0
	276.4
	302.9
	356.0
	383.9
^{57}Co	122.1
^{60}Co	1173.2
	1332.5
^{137}Cs	661.7
^{22}Na	511.0
	1274.5
^{24}Na	1368.6
	1732.0
	2754.0

2.3.3 Calibration Results

Following the completion of the calibration of each system, a thorough analysis was conducted to understand and characterize the performance of the system. Results were compiled for the overall performance of the full 18-detector system, as well as the individual performance of each detector.

The first 18-detector CdZnTe array system built in July, 2010 had an overall energy resolution of 1.44% FWHM at 662 keV for all events combined. The best spectroscopic performance is for single-pixel events, which showed an energy resolution of 1.08% FWHM at 662 keV. The spectrum for all events combined for the fist system is shown in Fig. 2.14.

The energy resolution for each detector as a function of the number of pixels triggered is one indicator of the consistency of performance from one detector to the next. The results, shown in Fig. 2.15, indicate that there is variation from detector to detector on overall performance. Several of the detectors can achieve below 1%

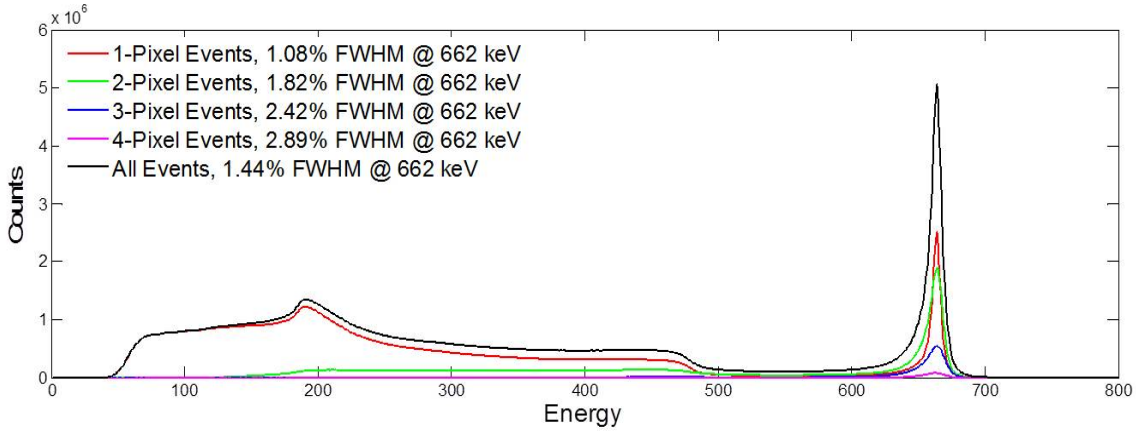

Figure 2.14: The energy spectrum for all events combined in the first 18-detector CdZnTe array system.

FWHM at 662 keV for single-pixel events. Several of the detectors have a much steeper degradation when moving to higher numbers of triggered pixels which is an indicator of a poor steering effect due to a poorly operating steering grid.

The spectroscopic performance of the first CdZnTe array system can also be judged by looking at the pixel-by-pixel response throughout all of the detectors. The energy resolution pixel map for all 18 detectors is shown in Fig. 2.16 and 2.17. The results show that there is significant variation from pixel to pixel on most of the detectors. Only 4 of the detectors, two on each plane, show excellent and uniform energy resolution throughout the detector. A histogram of the energy resolution in each pixel of the 18-detector system (Fig. 2.18) shows that 50.3% of the pixels achieve below 1% FWHM at 662 keV, but with a prominent tail of pixels with quite poor energy resolution. The count rate uniformity of each detector, shown in Fig. 2.19, also indicates the poor quality of most of the detectors.

The second 18-detector CdZnTe array system was built in June, 2011 and had an overall energy resolution of 1.21% FWHM at 662 keV for all events combined. For single-pixel events the system achieved an energy resolution of 0.96% at 662 keV. The spectrum for all events combined for the second system is shown in Fig. 2.20.

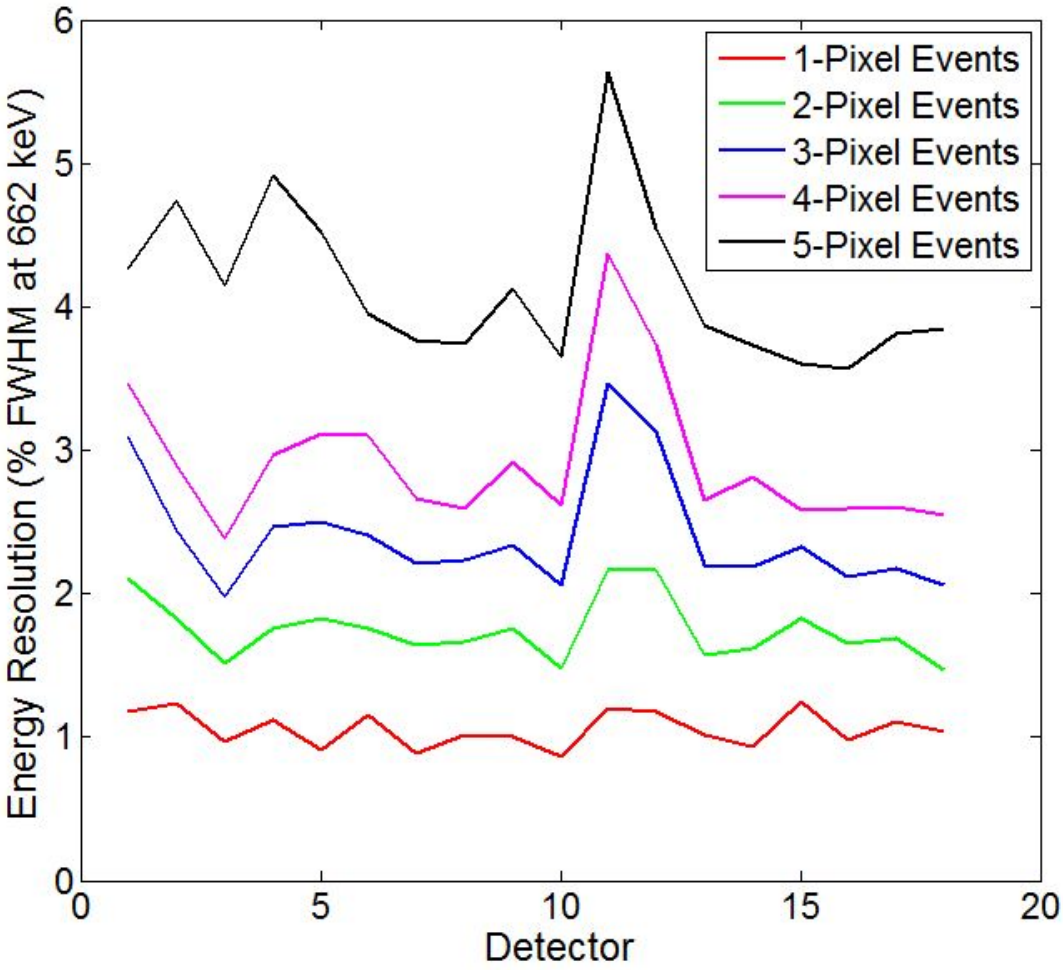

Figure 2.15: Graph of the energy resolution for each detector in the first CdZnTe array system as a function of the number of triggered pixels.

The improved performance of the second system compared to the first system is better shown by energy resolution for each detector as a function of the number of pixels triggered. As shown in Fig. 2.21, the recorded energy resolution in % FWHM at 662 keV is below 1% for a majority of the detectors in the second system. The energy resolution also does not drop off as quickly for higher numbers of triggered pixels. Several factors contributed to the better performance of the second system, including improved hardware design leading to lower electronic noise introduced by the internal cathode and grid bias supplies and better temperature control of the system. However, the number one contributor is improved detector quality, which can

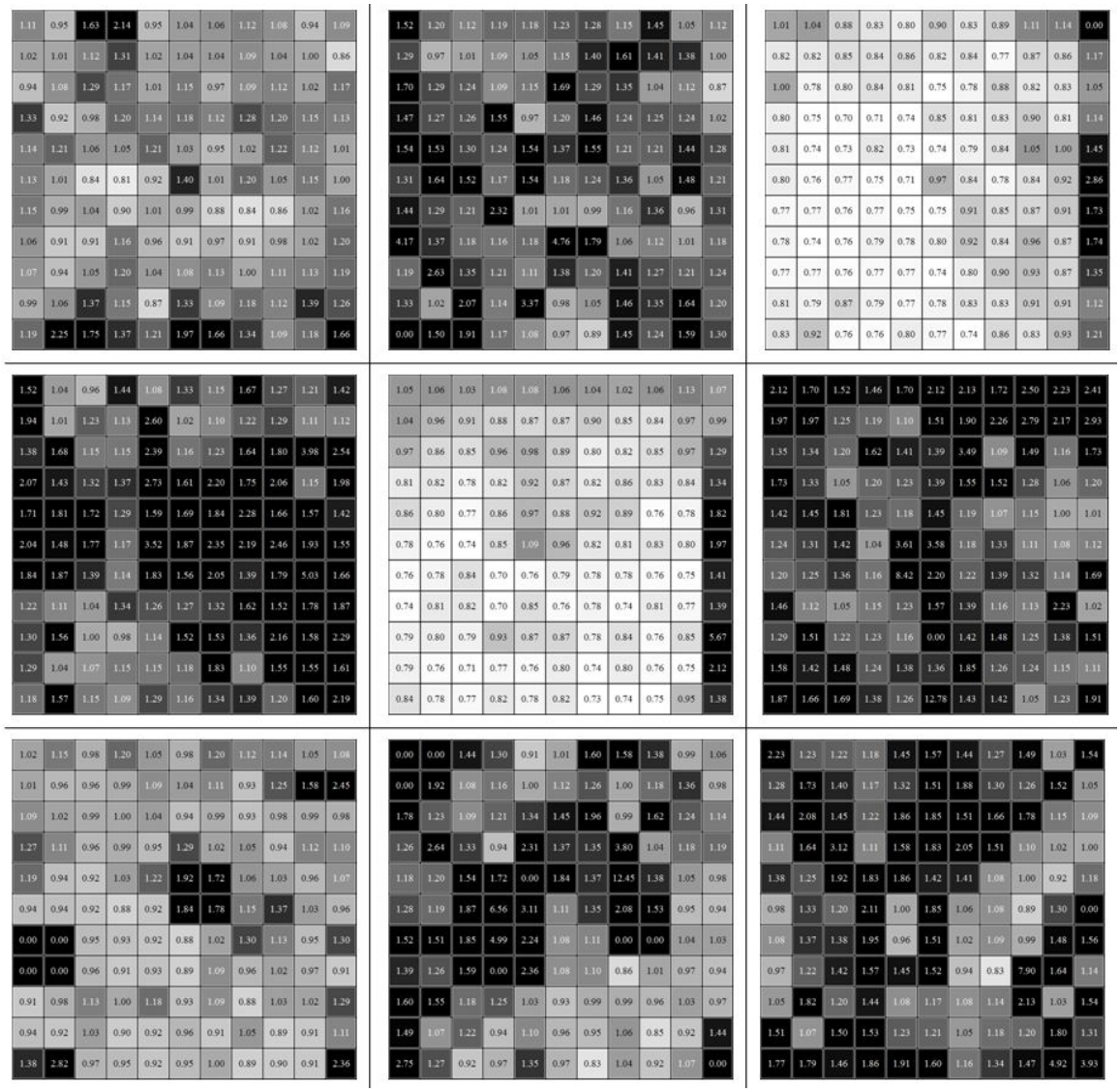

Figure 2.16: The detector-by-detector energy resolution pixel maps for all 9 detectors of the first plane of the first CdZnTe array system. The energy resolution is in units of % FWHM at 662 keV.

be attributed to both higher quality crystals and improved fabrication techniques.

The higher crystal quality of the second CdZnTe array system is more clear through analysis of the pixel-by-pixel performance of each of the detectors. The energy resolution pixel map for all 18 detectors is shown in Fig. 2.22 and 2.23. Each detector shows little variation in the pixel-by-pixel energy resolution values, with one exception. Therefore, the second system has both better and less varying energy res-

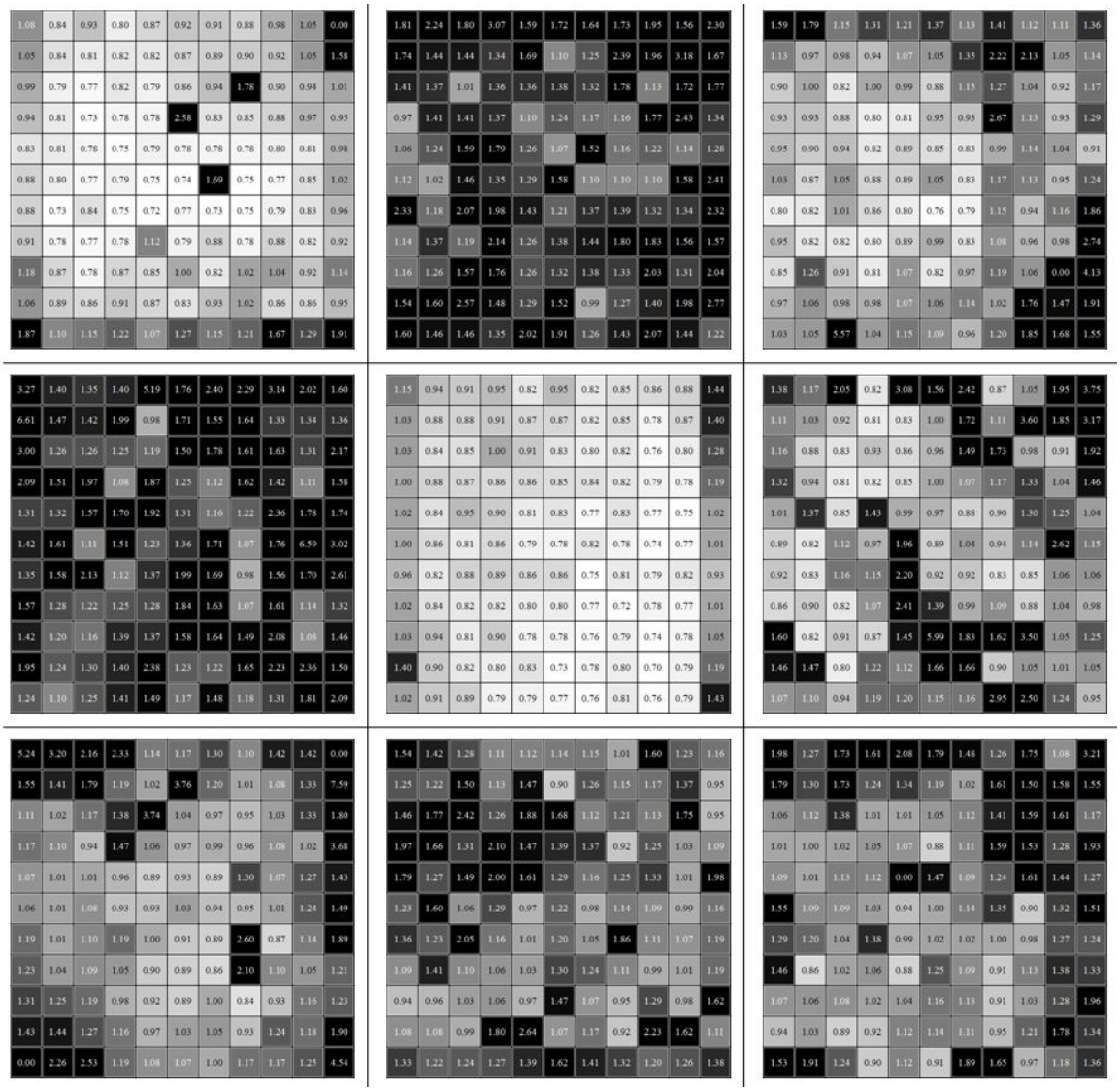

Figure 2.17: The detector-by-detector energy resolution pixel maps for all 9 detectors of the second plane of the first CdZnTe array system. The energy resolution is in units of % FWHM at 662 keV.

olution. As expected, the histogram of the energy resolution value for every pixel in the second CdZnTe array system shifts dramatically towards lower value. Shown in Fig. 2.24, 87.3% of the pixels achieving below 1% FWHM at 662 keV. The improved performance of the second system carries over to the count rate uniformity, shown in Fig. 2.25. The second system shows good uniformity in every detector with many of them, including one entire plane, exhibiting excellent count rate uniformity. The

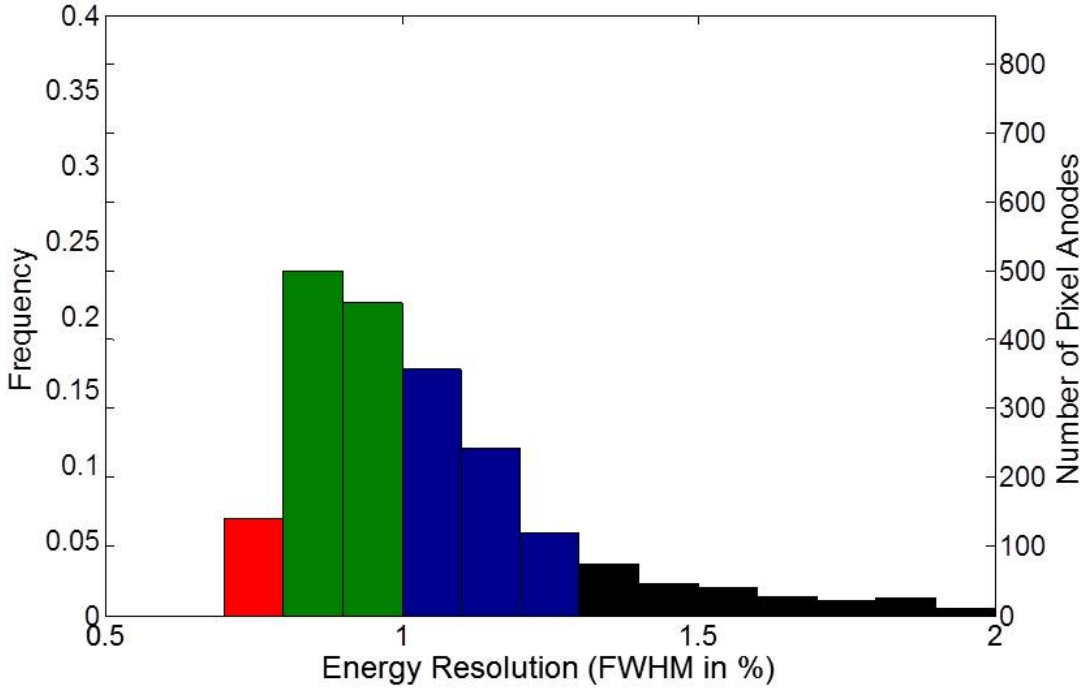

Figure 2.18: Histrogram of the energy resolution recorded in each pixel of the first CdZnTe array system.

worst detectors in the second CdZnTe array system would be consider one of the best detectors in the first system.

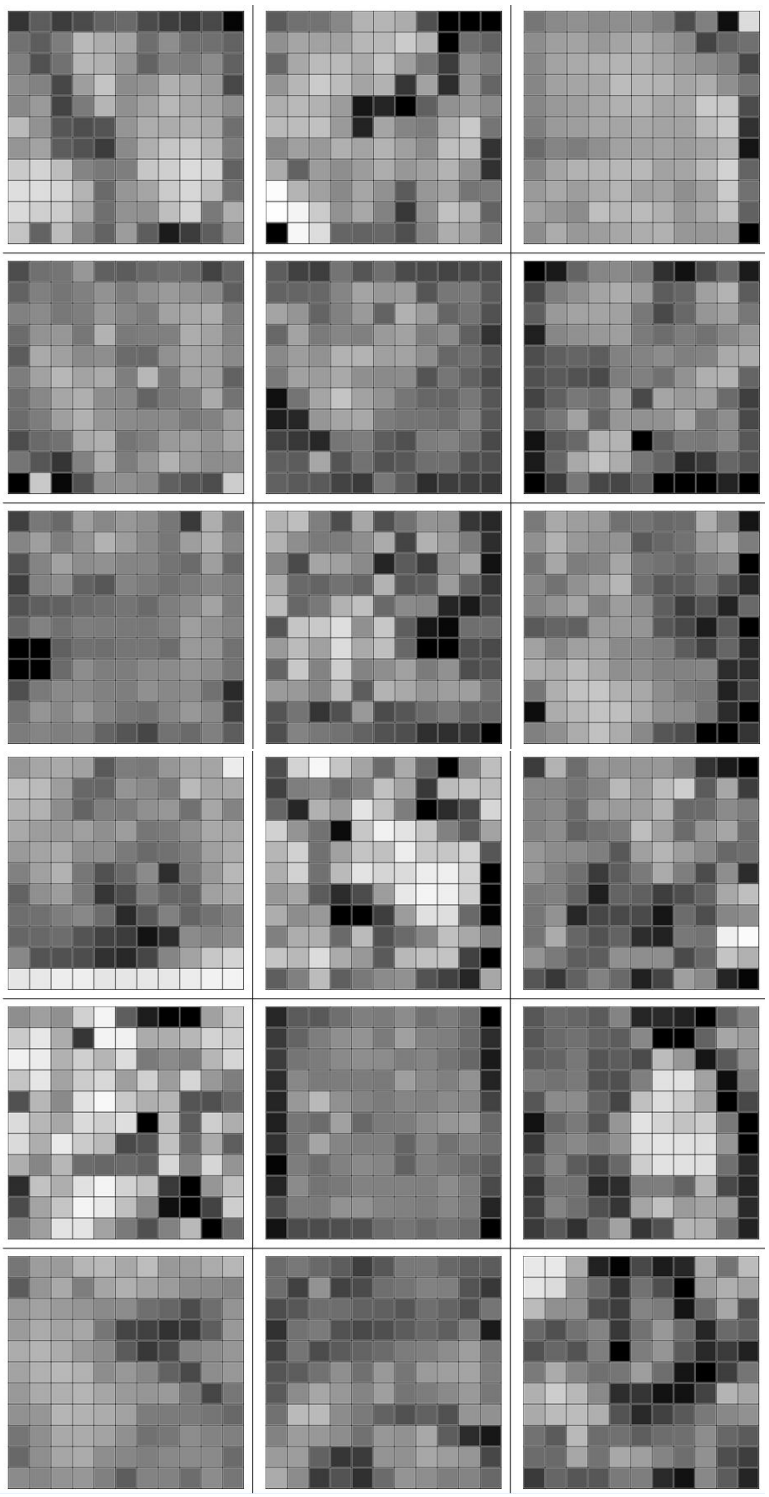

Figure 2.19: The detector-by-detector count rate uniformity pixel maps for all 18 detectors of the first CdZnTe array system. The color of the pixel indicates the number of counts recorded in the pixel; the same scale is used for each detector in the system.

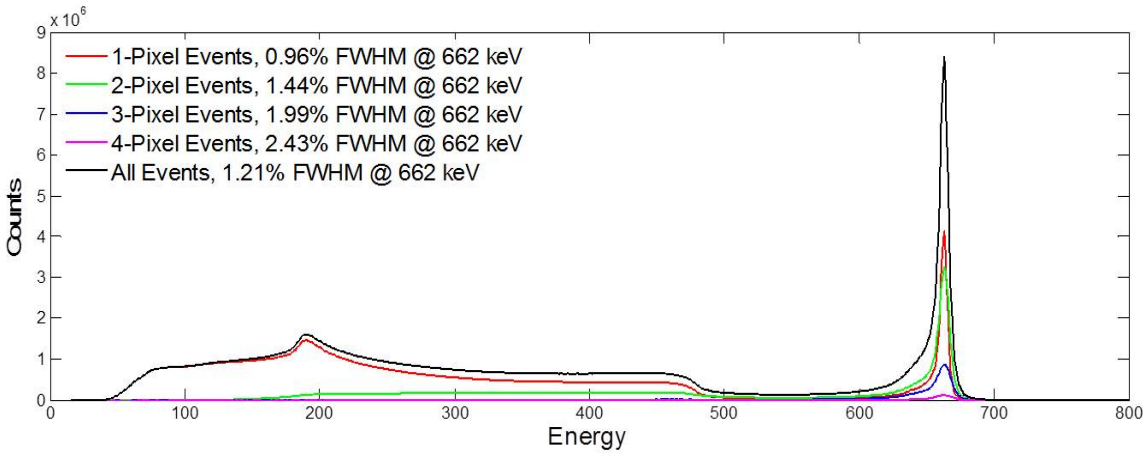

Figure 2.20: The energy spectrum for all events combined in the second 18-detector CdZnTe array system.

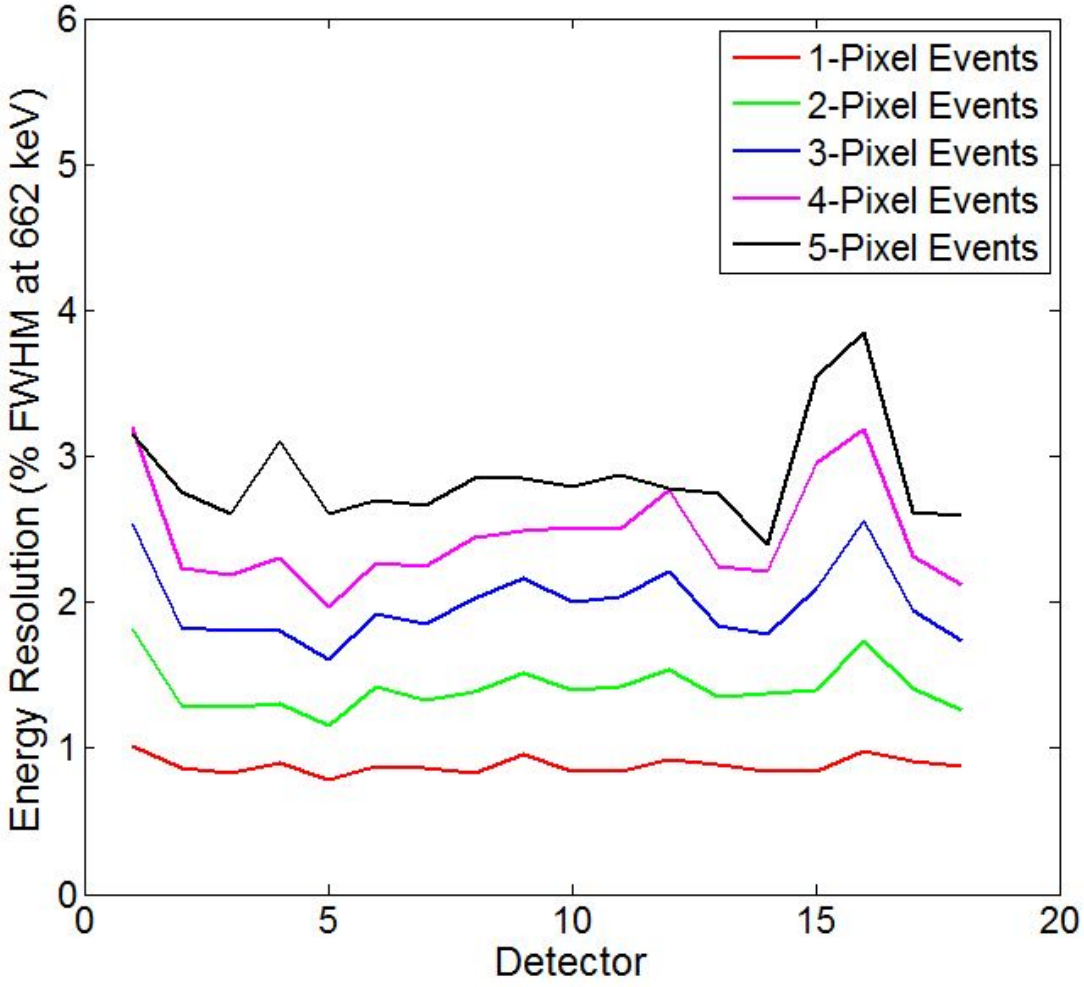

Figure 2.21: Graph of the energy resolution for each detector in the second CdZnTe array system as a function of the number of triggered pixels.

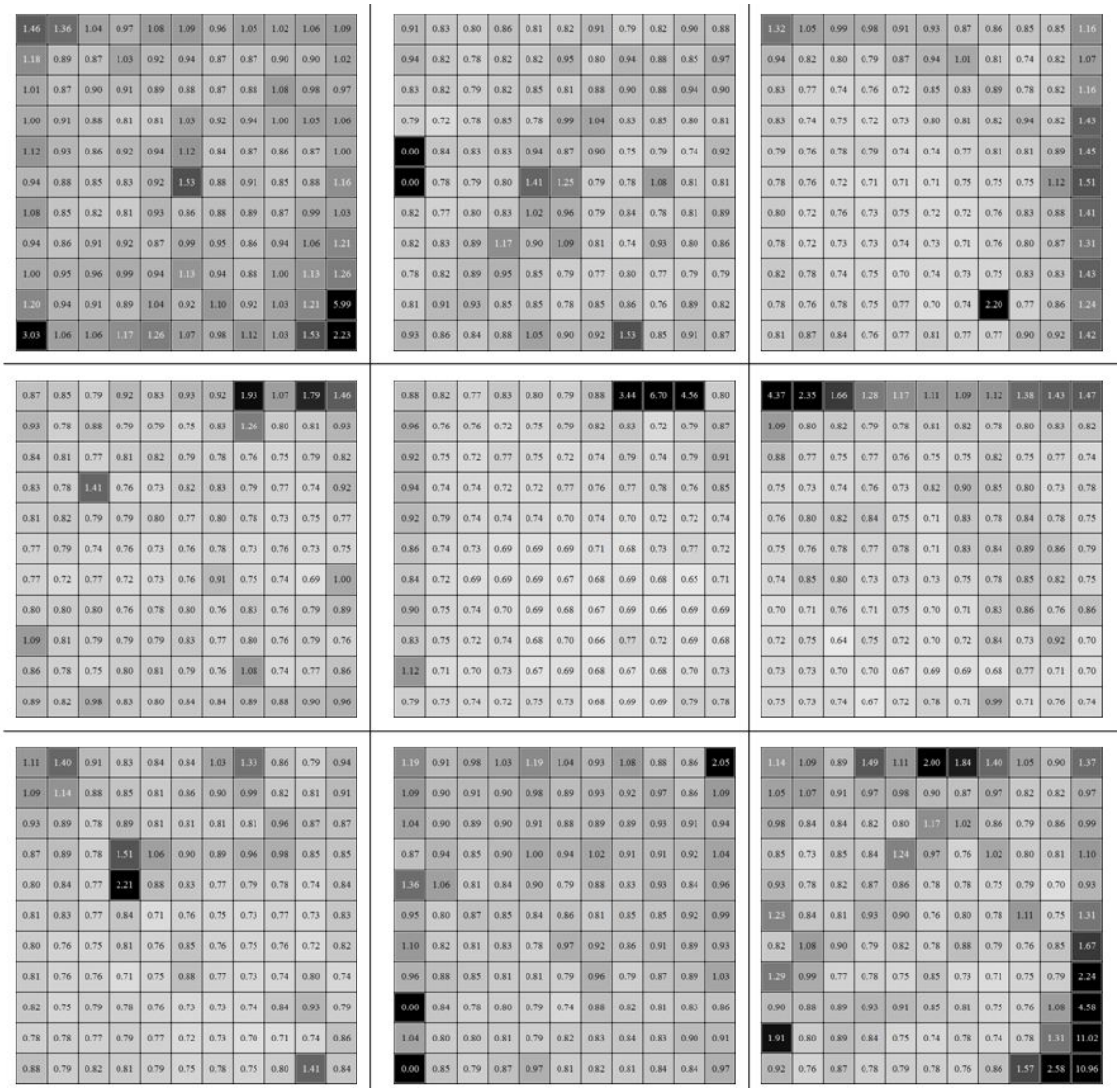

Figure 2.22: The detector-by-detector energy resolution pixel maps for all 9 detectors of the first plane of the second CdZnTe array system. The energy resolution is in units of % FWHM at 662 keV.

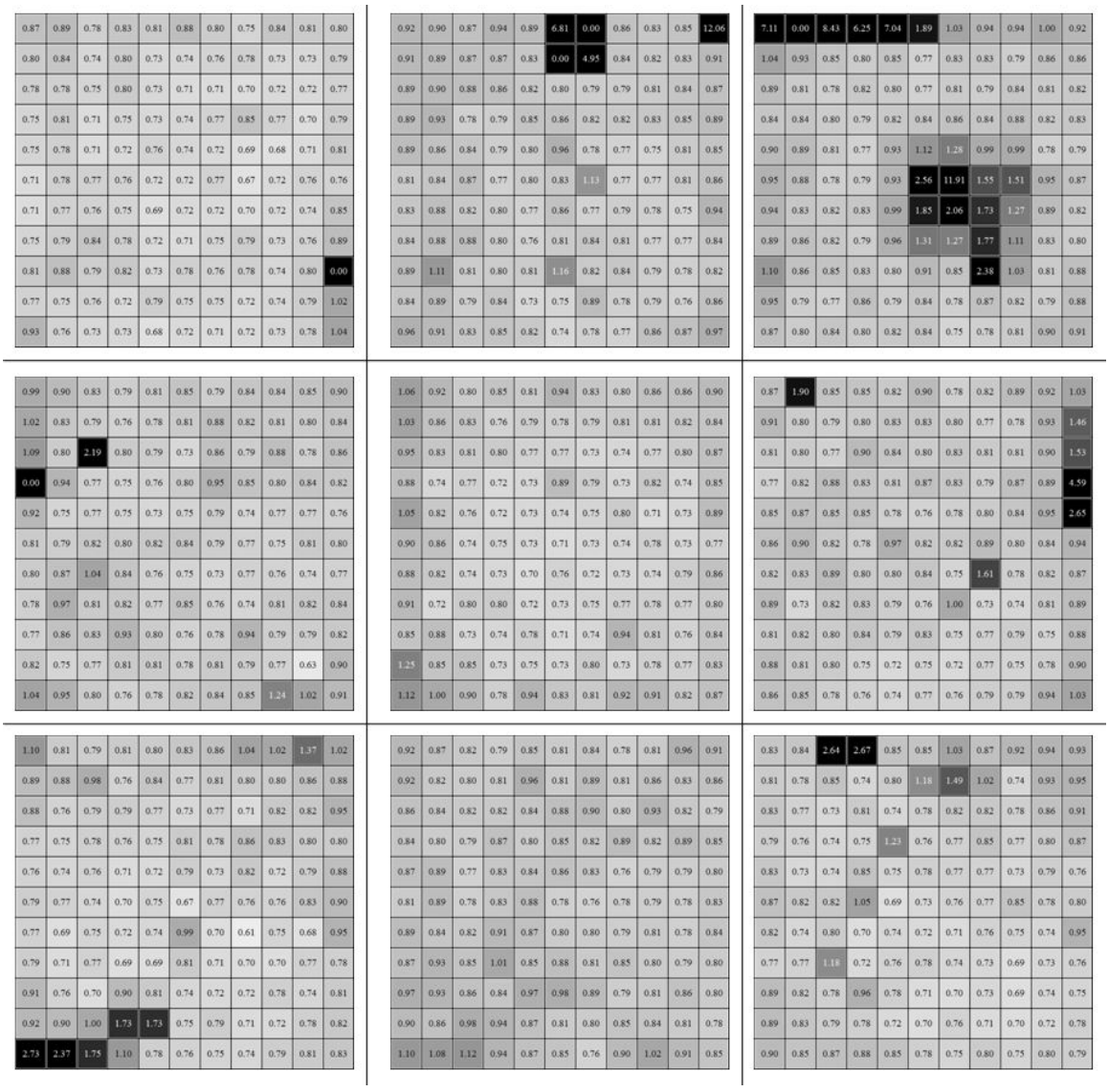

Figure 2.23: The detector-by-detector energy resolution pixel maps for all 9 detectors of the second plane of the second CdZnTe array system. The energy resolution is in units of % FWHM at 662 keV.

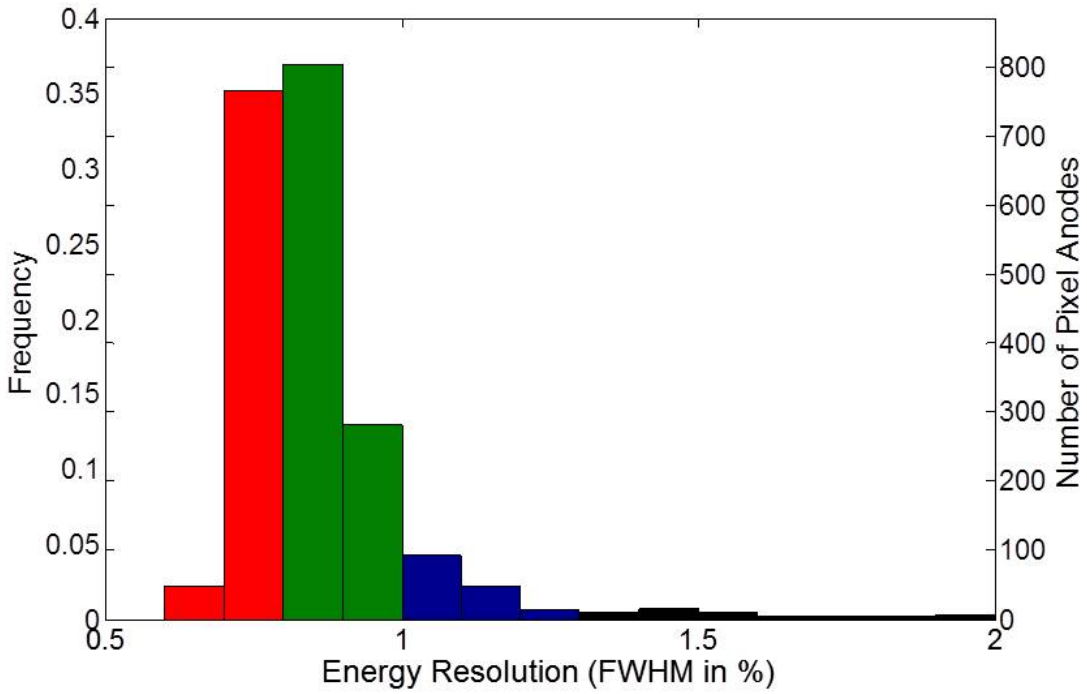

Figure 2.24: Histrogram of the energy resolution recorded in each pixel of the second CdZnTe array system.

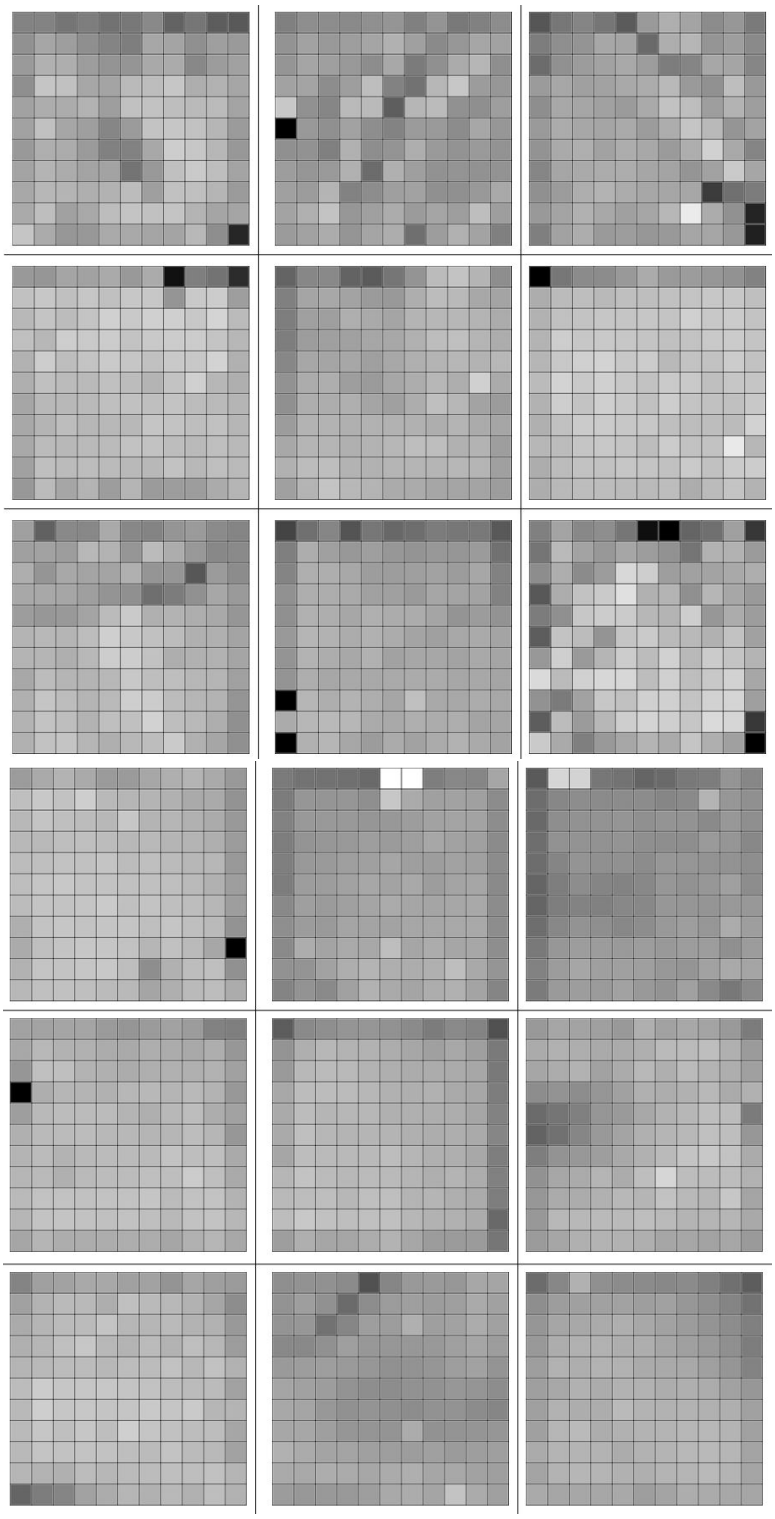

Figure 2.25: The detector-by-detector count rate uniformity pixel maps for all 18 detectors of the second CdZnTe array system. The color of the pixel indicates the number of counts recorded in the pixel; the same scale is used for each detector in the system.

CHAPTER III

CdZnTe Detector Characterization

As can be seen from the vastly improved performance of the second 18-detector CdZnTe array system compared to the first system, much progress was made over the course of the 9 months between construction of the two systems. In this time, some of the flaws of the first system were fixed, including a reduction in electronic noise produced by the systems internal power supplies and an added ability to manually control system temperature—the first system allowed for no control over the temperature of the system as the peltier device voltages and fan speeds were fixed. However, while these changes may have helped improve the spectroscopic performance slightly, they cannot account for the magnitude of the improvement. The improved detector quality is the primary reason for the observed spectroscopic improvement of the second CdZnTe array system. The following sections will compare results from the detectors received from Redlen Technologies, Inc. to study influences on spectroscopic and imaging performance from other detector characteristics.

3.1 Performance and Characteristics

3.1.1 Detector Testing Procedures

Redlen Technologies, Inc. manufactured 177 pixellated $20\times20\times15$ mm^3 CdZnTe detectors. Of these detectors, 143 of them passed specifications with the remaining

being returned due to failure. The specifications set on these detectors are that all of the detectors operate stably at -3000V cathode bias, have a working grid with a leakage current below 2.5 nA/V and electronic noise below 12 ADC channels (∼6 keV), are absent of more than 1 non-functioning pixel, have a raw energy resolution below 5% FWHM at 662 keV for single-pixel events in all pixels combined, and have no dead layers near the cathode surface. A cathode dead layer is found if more than 5 pixels do not detect ^{241}Am when irradiated from the cathode side.

The general characteristics of 145 of these detectors were thoroughly analyzed. Each detector's data was analyzed using identical event reconstruction algorithms. The 32 detectors excluded from this analysis did not have data available for reprocessing, and were removed to avoid conflicting results due to the presence of a different reconstruction algorithm.

Identical procedures were used to complete the room-temperature study of each detector. The procedures were designed to fully quantify each detector's spectroscopic and imaging performance as well as to determine possible causes for performance degradation. The issues leading to performance degradation were given to the manufactueres to help them improve their growth and fabrication procedures in order to improve the future CdZnTe detector quality.

The first step is to assemble the test box, shown in Fig. 3.1, that the detector and ASIC are tested within. After all connections to the computer, high voltage cathode supply and high voltage grid supply are properly made, the detector is biased to confirm that there are no improperly connected anode pixels. A bad anode pixel would be due to a short between the anode pixel and the grid, which would cause the pixel to become excessively noisy and require disabling. Next, the system is slowly biased up to -3000V on the cathode, and the optimal grid bias (OGB) is determined by finding the grid bias with the best peak-to-valley ratio for 2-pixel side-neighboring events. An energy threshold of approximately 30 keV is set. The main performance

characterization study using ^{137}Cs is then performed at -3000V cathode bias and OGB to fully determine the detectors spectroscopic performance. The last measurement to determine spectroscopic performance is a study of the low energy efficiency of each crystal using ^{241}Am to determine the number of pixels that have a dead layer near the cathode preventing the detection of the low energy gamma rays produced by ^{241}Am.

Figure 3.1: The setup of the test box for the CdZnTe detectors. Pictured is one of the 20×20×15 mm^3 detectors mounted on a carrier board, which is plugged into an ASIC, which is then plugged into the motherboard. The motherboard is connected to a computer for data acquisition. Located above the detector is the high voltage distribution board, which is used to distribute the cathode and grid biases to the detector from external high voltage supplies.

An energy calibration identical to the one described in Sec. 2.3.2 is completed with the omission of two steps. The peak hold drop is not corrected because the effects on overall spectroscopic performance are second order compared to the effects of the detector quality, the effects are not detector related, and the time required to perform such an analysis on every detector is not meritted. The non-linearity correction is omitted for the same reasons.

During the calibration, several parameters of interest are recorded for detailed analysis. The raw energy resolution is obtained prior to applying the gain correction to each detector voxel. The average noise in the system is obtained by measuring the average baseline fluctuations in each pixel during events that interacted in other pixels. A novel method for measuring the electron mobility-lifetime product was used to study the charge transport characteristics. Following the 3D-position dependent correction to the amplitude signals, an energy spectrum for all events in the detector is created to determine the overall energy resolution at 662 keV. An example spectrum is shown in Fig. 3.2. Since the correction is performed on a pixel-by-pixel basis, a corrected spectrum and energy resolution can be determined for each pixel; an example of the pixel-by-pixel corrected energy resolution is also shown in Fig. 3.2.

Following the calibration measurement, each detector's imaging performance is characterized using two measurements. First, a ^{137}Cs point source is placed approximately 25 cm from the cathode surface of the detector, and a 20-minute measurement is taken. The source is then moved to be 25 cm from the side surface of the detector, and a second 20-minute measurement is taken. The original calibration based on ^{137}Cs is then used to reconstruct the energy and 3-D position of each interaction. Using only 2-pixel photopeak events in a simple back projection reconstruction, the angular resolution of the point spread function for each source direction is estimated. Only the angular resolution of the polar angle is measured through cathode surface imaging, while the side surface imaging measures both the polar and azimuthal angular resolutions, as shown in Fig. 3.3. The 25-cm source distance is chosen in order to minimize the near-field effects of the source while still maintaining a reasonable count rate and source-to-background ratio. The point spread functions of the cathode-surface direction and the side-surface direction differ greatly because of characteristics associated with the uniformity of the crystal and depth sensing ability, hence the need for the two measurements. Examples of an image generated from both the cathode and side

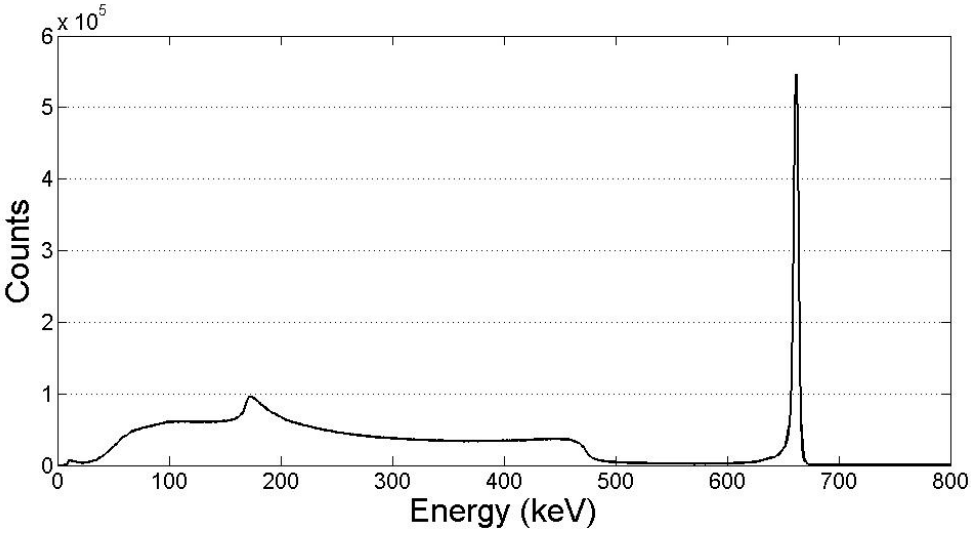

0.80	0.78	0.84	0.72	0.71	0.75	0.74	0.72	0.74	0.74	0.78
0.81	0.74	0.75	0.69	0.76	0.71	0.75	0.71	0.71	0.75	0.75
0.80	0.73	0.76	0.79	0.68	0.69	0.73	0.69	0.68	0.77	0.74
0.72	0.71	0.72	0.75	0.67	0.75	0.72	0.73	0.75	0.72	0.76
0.76	0.71	0.77	0.72	0.73	0.69	0.70	0.70	0.70	0.74	0.70
0.74	0.69	0.69	0.70	0.67	0.70	0.73	0.71	0.74	0.71	0.74
0.71	0.73	0.70	0.65	0.68	0.71	0.71	0.73	0.76	0.72	0.72
0.76	0.68	0.72	0.66	0.69	0.75	0.71	0.72	0.71	0.69	0.72
0.77	0.73	0.70	0.73	0.65	0.69	0.72	0.70	0.67	0.67	0.70
0.74	0.71	0.68	0.69	0.69	0.71	0.68	0.66	0.69	0.67	0.69
0.80	0.73	0.71	0.69	0.72	0.70	0.67	0.72	0.71	0.73	0.82

Figure 3.2: (top) Example 3D-corrected single-pixel events spectrum with a 1 keV bin width for one of the Redlen CdZnTe detectors. The corrected energy resolution was found to be 0.72% FWHM at 662 keV. The detector achieves 1.23%, 2.02% and 3.28% FWHM for 2, 3, and 4-pixel events, respectively. (bottom) The pixel-by-pixel corrected energy resolutions for each of the 121 pixels in units of % FWHM at 662 keV. This is the same detector as the above example energy spectrum.

surfaces of a CdZnTe detector used for this quantification are shown in Fig. 3.4.

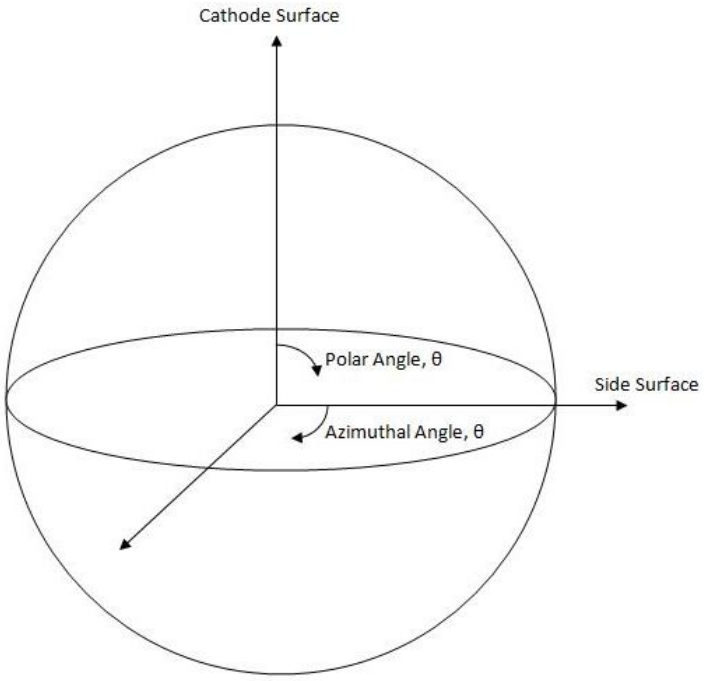

Figure 3.3: The layout of the coordinate system in relation to the surfaces of the detector to show that the measurements of a source on the cathode surface will only be a measurement of the polar angle, whereas the measurements of a source on the side surface are a measurement of both the azimuthal and polar angles.

3.1.2 General Characteristics

The calibration results from the 145 20×20×15 cm^3 CdZnTe detectors analyzed show excellent performance. This is the most extensive study to date on large-volume CdZnTe detectors. A large number of 1-cm^3 CdZnTe detectors were grown by Redlen for use as coplanar-grid detectors and showed performance comparable to the best commercially available coplanar-grid detectors [30]. Redlen also produced 80 15×15×10 mm^3 CdZnTe pixellated detectors for the GammaTracker project which showed the potential for growing large volume crystals that can achieve near 1% FWHM at 662 keV [49].

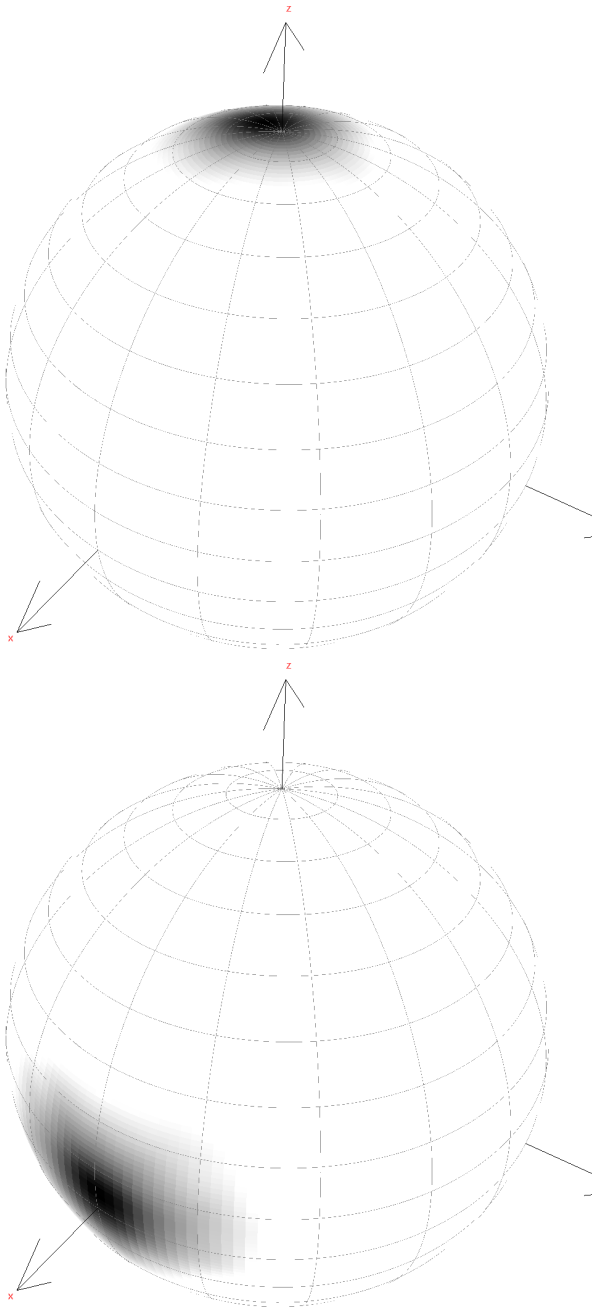

Figure 3.4: Example image produced for a ^{137}Cs placed 25 cm from the cathode surface (above) and 25 cm from the side surface (below) of a CdZnTe detector. From the cathode surface image, a polar angular resolution of 24.4 degrees was determined. From the side surface image, an azimuthal angular resolution of 29.9 degrees and a polar angular resolution of 36.1 degrees were determined.

The performance of the CdZnTe detectors can be evaluated across several parameters. The foremost parameter of interest is the energy resolution measured at 662 keV for single-pixel events following the 3-D energy reconstruction. The data from all detectors are shown in Fig. 3.5; a majority of the detectors achieved sub-1% energy resolution. Another parameter of interest is the average noise of each detector during operation. This is measured by calculating the average fluctuation in the baseline in pixels that did not trigger. A histogram of the average noise in each detector is shown in Fig. 3.6. A detector with noise of 8 ADC units corresponds to variations of approximately 4 keV for 662 keV events, which have a pulse height of approximately 1300 ADC channels. The histogram indicates that most detectors have relatively low noise and that there is not significant variation in the measured noise of each detector. The noise typically varies with the leakage current measured between the anode pixels and the steering grid, therefore the consistency between detectors displays that the detectors have a consistent leakage current. The OGB is another parameter that can be tracked across all of the detectors tested. Fig. 3.7 shows that the detectors typically have an OGB in the range of -40 V to -200 V. The variation between detectors is due to a variation in the grid-to-pixel resistance. Detectors with a high resistance tend to have a lower OGB, whereas a lower resistance requires a higher OGB to achieve the same steering effect. The grid bias has little effect on the electric field through the detector other than to make the field lines end on the anode electrodes instead of on the gap.

One of the objectives of this work was to improve the understanding of the relationship between different detector parameters and the 3-D-corrected energy resolution for single-interaction photopeak events. It is shown in Fig. 3.8 that there is no correlation between the OGB and the energy resolution. This is expected because the OGB is primarily dependent on the resistance between the anode pixels and the steering grid, whereas the energy resolution will be dependent on the bulk crystal

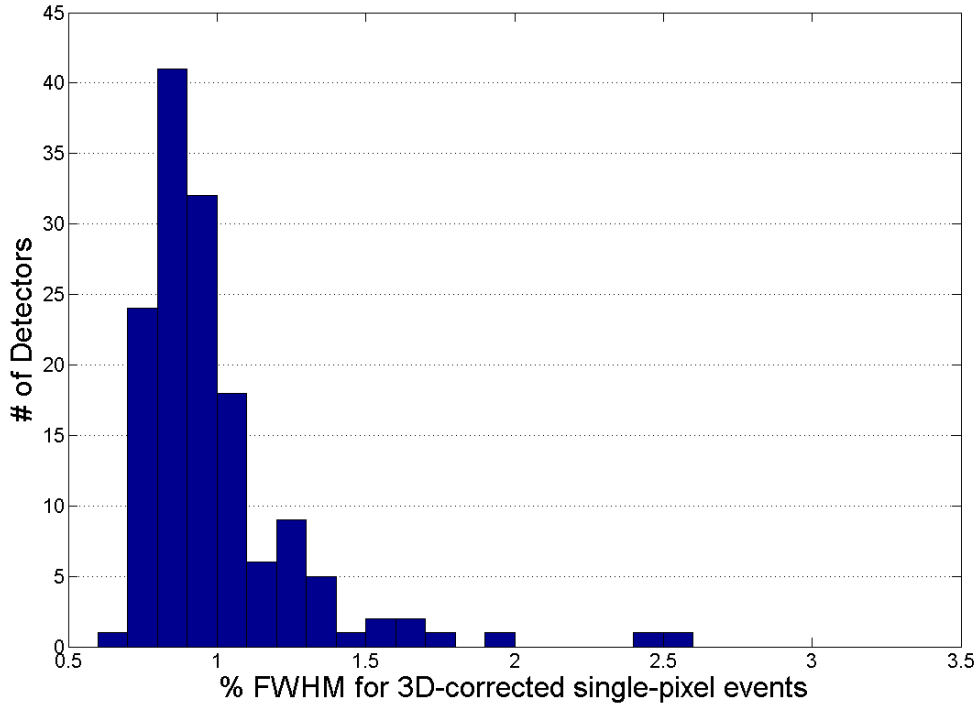

Figure 3.5: Energy Resolution results for all detectors tested using a 0.1% FWHM bin width.

properties. The average noise of a detector is shown to be weakly correlated to the corrected energy resolution in Fig. 3.9. Noisy detectors are more likely to have a degraded energy resolution correlated to the higher baseline fluctuations; however detectors with lower noise may or may not show excellent performance as the other factors leading to poor detector performance are a more dominant factor.

One of the most interesting relationships to study is the relationship between the raw and corrected energy resolutions. The "raw" energy resolution is generated before the depth correction is applied to the events in the CdZnTe detector. A simple gain correction is applied to the events in each pixel to eliminate effects from gain deficit. Any pixel can suffer from gain deficit if it has a lower signal amplitude beyond statistical fluctuation than the average of other pixels in the detector. A pixel is classified as having gain deficit if its signal is decreased by more than 100

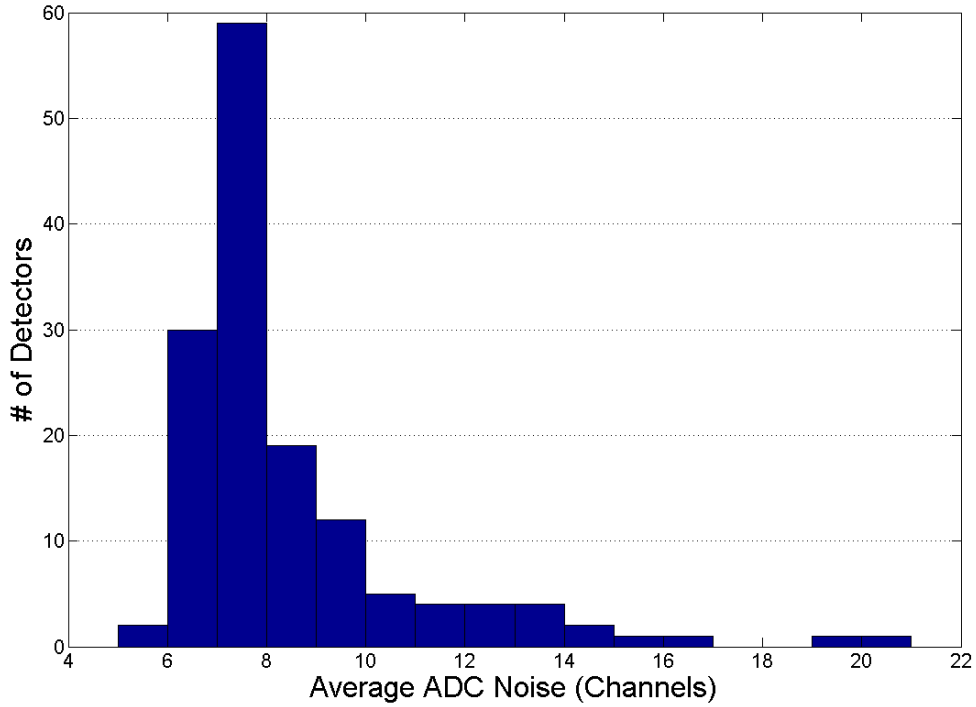

Figure 3.6: Noise performance of all detectors tested using a bin width of 1 channel.

ADC channels for a full-energy ^{137}Cs single-pixel event—an event that typically has a signal amplitude of approximately 1300 ADC units. This effect is most likely caused by poor fabrication of the anode electrode surface leading to a flawed connection to the CdZnTe crystal. A comparison between the raw and corrected energy resolutions for single-pixel events in the 145 CdZnTe detectors is shown in Fig. 3.10.

Fig. 3.10 shows a clear correlation between the raw and corrected energy resolutions; however, this result is misleading. A plot of the ratio between the corrected and raw energy resolutions in Fig. 3.11 shows that for detectors with a low raw energy resolution, there is little improvement for the corrected energy resolution, whereas detectors with a higher raw energy resolution have greater improvement in their corrected energy resolutions. This displays that poor raw energy resolution is due to a depth dependence of the gain due to electron trapping and charge transportation in the detectors and can be accounted for through the depth correction. The charge

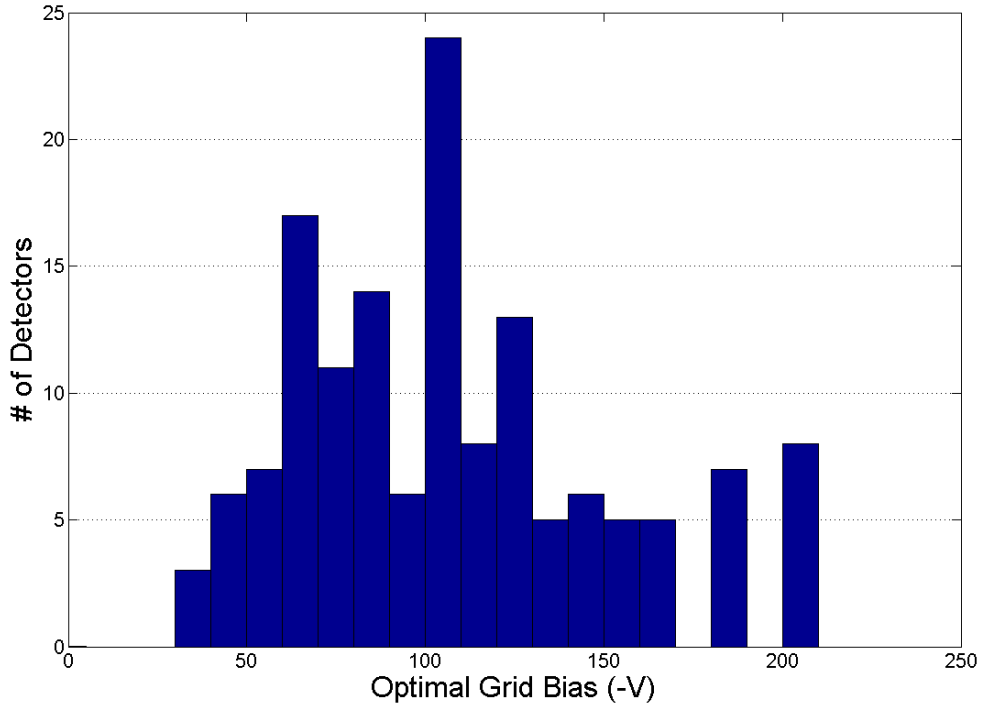

Figure 3.7: Optimal grid bias (OGB) for all of the detectors tested using a 10V bin width.

transport properties in the detector will be further discussed in Sec. 3.1.3. Effectively, the raw energy resolution puts a ceiling on what the corrected energy resolution can be for a detector since the 3-D correction never degrades the spectroscopic performance. This ceiling is the cause for the apparent correlation seen in Fig. 3.10.

A strong correlation between the single-pixel event corrected energy resolution and the two-pixel event corrected energy resolution was determined using Fig. 3.12. It shows that the a dominant predictor of the multiple-pixel energy resolution in a detector is the single-pixel performance; no other parameters were found with as strong of a correlation. This follows the expectation that the multiple-pixel energy resolution tracks with the quadrature summation of the uncertainty in the two interaction's energies, with a slight degradation due to weighting-potential cross-talk and other factors that will be discussed in Sec. 5.3.3.

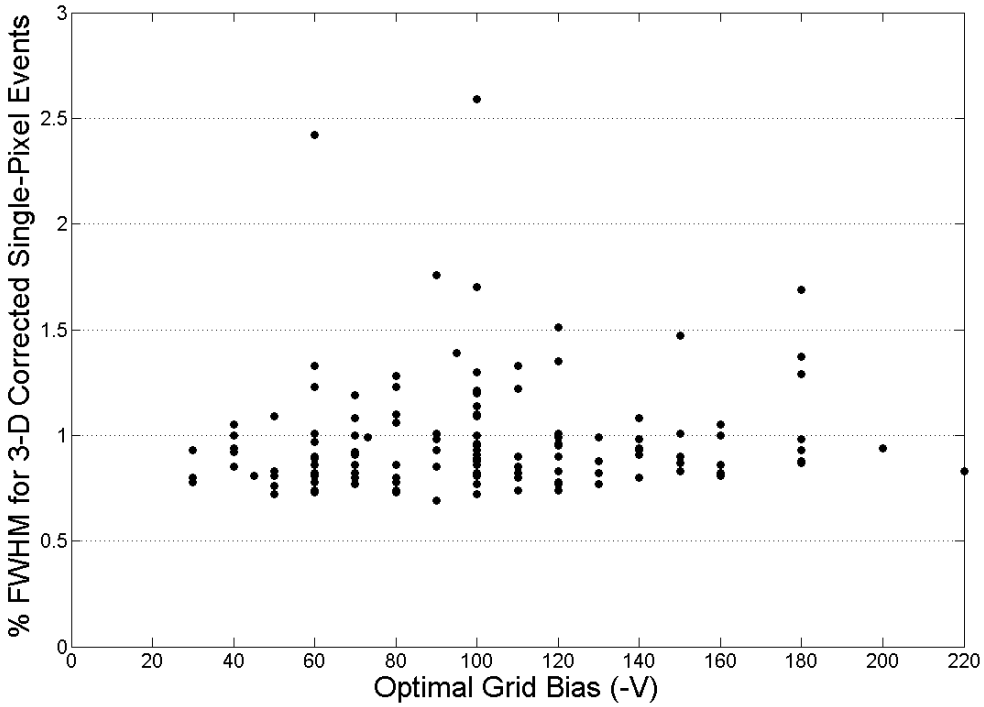

Figure 3.8: Relationship between the OGB and the energy resolution.

Several other detector issues presented themselves during the testing of the 177 detectors. Related to detector fabrication, 32 of the 145 detectors analyzed had at least one pixel that showed the phenomenon called gain deficit. This deficit was uniform and consistent for all events over the pixels showing this trait, which allowed the 3-D position correction to correct for the issue simultaneously with the correction for the electron trapping over the pixel. However, the gain deficit tended to produce detectors with larger than expected raw energy resolutions, as the different gains on each pixel, when summed together for all pixels, created wider energy spectra. Also related to detector fabrication is the presence of a thin dead layer near the cathode surface of the detector. While this thin layer will tend to have little effect on the detector performance at higher energies, low energy gamma rays, such as those from ^{241}Am, are more likely to interact in this dead layer for a source located on the cathode side of the detector. Therefore, each detector was also tested to determine

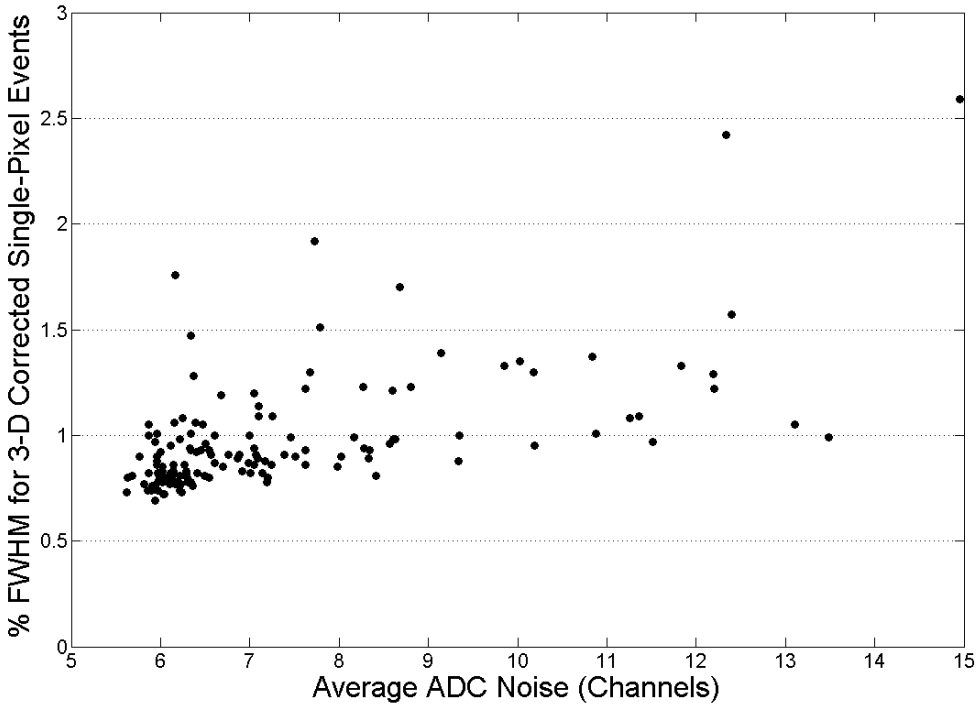

Figure 3.9: Relationship between the average noise and the energy resolution showing a correlation coefficient of 0.36.

the number of pixels that failed to detect the 60 keV gamma rays produced by ^{241}Am. A histogram of the results presented in Fig. 3.13 shows that a majority of detectors do not suffer from this problem, but that some detectors may have severely degraded performance. The dead layer is believed to be introduced during the fabrication of the cathode surface.

The testing of the 145 detectors occurred over the course of 30 months, allowing for tracking of the performance of the detectors over time. Fig. 3.14 shows that the corrected energy resolution tended to improve over time. Studying the low-energy performance of detectors over time—shown in Fig. 3.15—demonstrates that the cathode fabrication by Redlen Technologies Inc. has also improved.

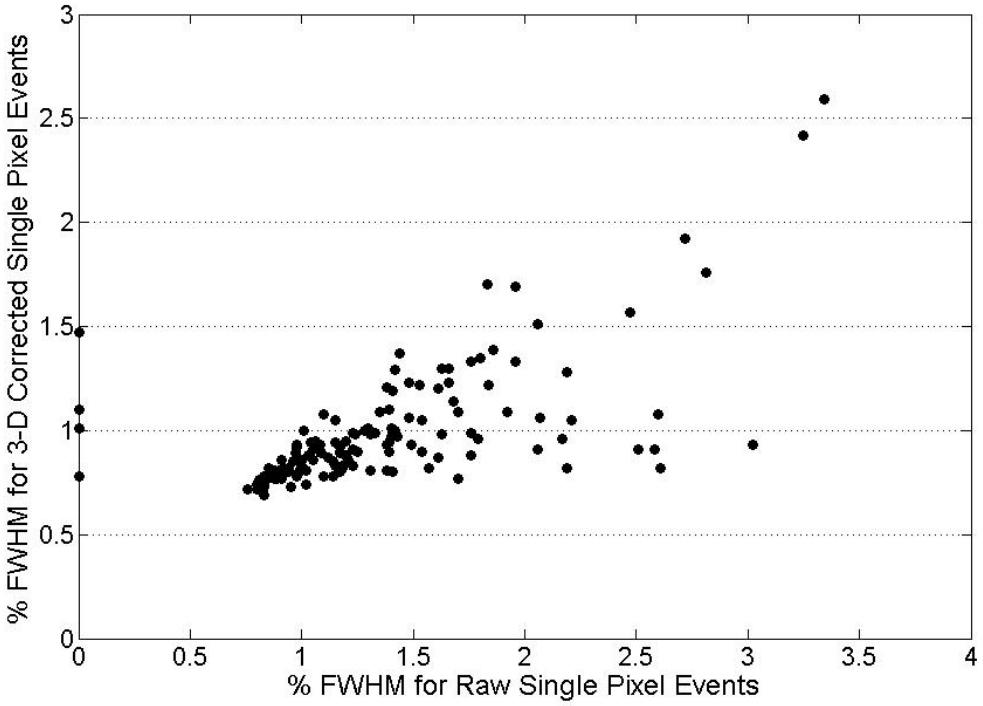

Figure 3.10: Relationship between the raw and corrected energy resolution.

3.1.3 Charge Transport Properties

Thorough understanding of the characteristics of charge carrier transport in a semiconductor detector is important for determining the material quality and the overall detector spectroscopic performance. Two typical quantities to characterize the charge transport are the electron mobility (μ_e) and the mean free drift time (τ_e). The derived quantity $\mu_e\tau_e$ is a common metric for studying semiconductor properties.

Typical methods for measuring $\mu_e\tau_e$ are conducted using α-particle spectroscopy and are based on the Hecht relation [50]. However, methods based on the Hecht relation tend to be biased towards lower value of $\mu_e\tau_e$ due to ballistic deficit and surface trapping [13]. Therefore, a direct measurement technique based on single polarity charge sensing can be used to improve the determination of $\mu_e\tau_e$ [13].

The technique described in Ref. [13] uses measurements of charge collection at different voltages to determine the value of $\mu_e\tau_e$. This technique has been altered to

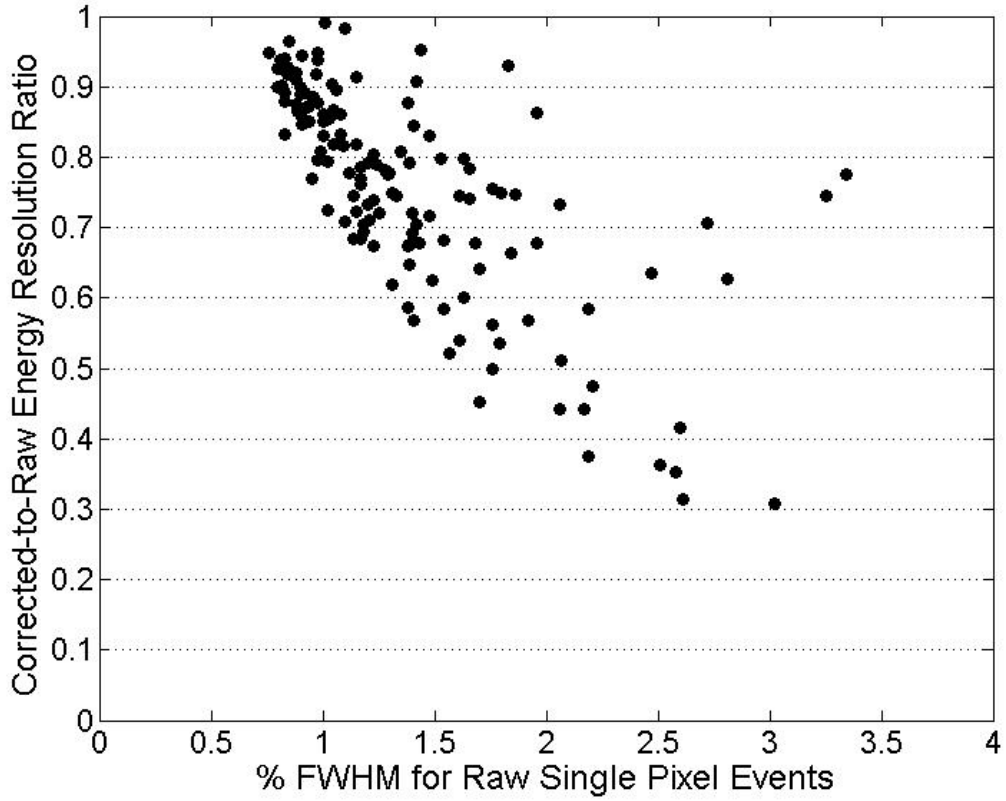

Figure 3.11: Relationship between the raw energy resolution and the corrected-to-raw energy resolution ratio showing that the depth correction has a larger impact on the detectors with poor raw spectroscopic performance.

utilize the standard calibration data acquired for the 20×20×15 mm^3 CdZnTe detectors, allowing for comparisons to be made between the spectroscopic performance and their charge transport properties for the 145 detectors analyzed from Redlen Technologies, Inc.

3.1.3.1 Methodology

During the standard calibration of a detector, raw single-pixel energy spectra are collected as a function of the three dimensional interaction location. An example of the spectra for a single pixel exhibiting the amplitude suppression due to electron trapping is shown in Fig. 3.16. Taking advantage of the relatively constant anode

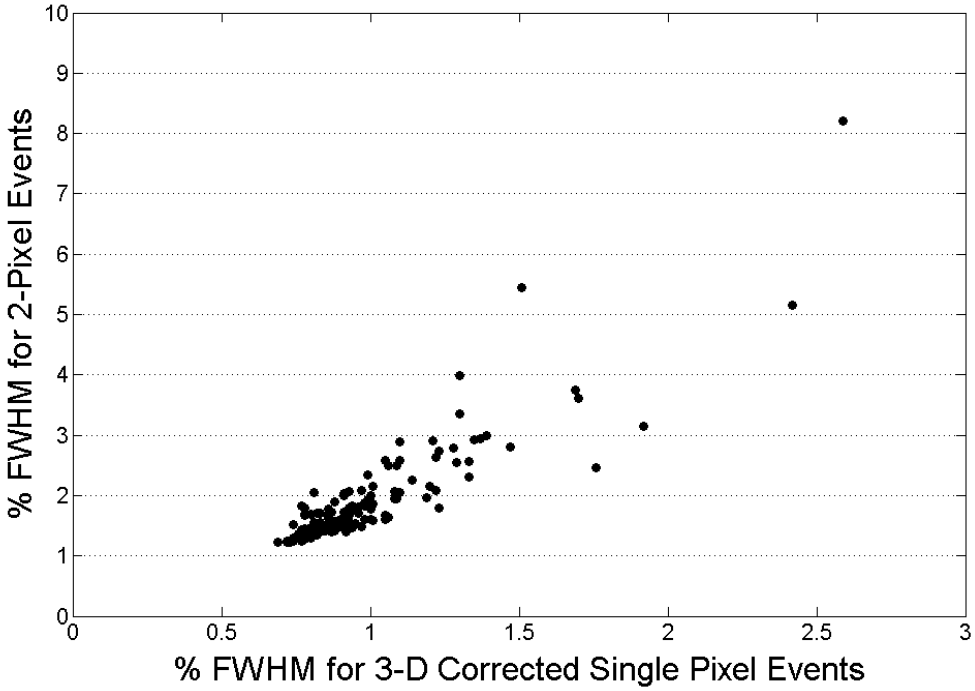

Figure 3.12: Relationship between the single-pixel and two-pixel corrected energy resolutions showing a correlation coefficient of 0.79.

signal amplitude due to the small pixel effect and the depth-sensitive cathode signal amplitude, the cathode-to-anode signal ratio is used to determine the depth of interaction [34]. For each voxel, a raw photopeak energy centroid and raw timing peak centroid—which is an independent measure of the depth of interaction—are found.

The mean free drift time, the mobility, and their product can now be calculated from the information obtained from each voxel. From Equation 3.1 for the signal amplitude deficit resulting from electron trapping losses, the electron mean free drift time, τ_e, can be derived as shown in Equation 3.2.

$$N = N_0 \times e^{-t/\tau_e} \tag{3.1}$$

$$\tau_e = \frac{(t_2 - t_1)}{ln(N_2/N_1)} \tag{3.2}$$

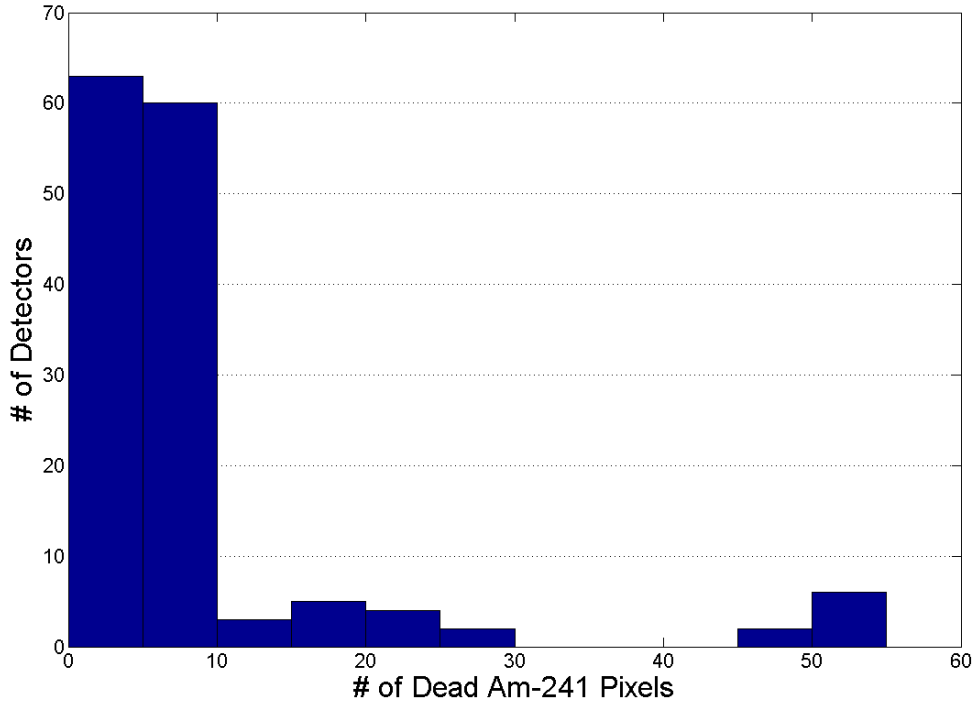

Figure 3.13: The performance of the CdZnTe detectors at low energies, as determined by the number of pixels failing to measure the 60 keV photopeak from ^{241}Am. A bin width of 5 dead Am-241 pixels was used.

where τ_e is the electron mean free drift time, t is the drift time, and N is the raw photopeak energy centroid.

The drift time between two vertical positions within a pixel in the detector can be determined from the drift time versus depth relationship for that pixel. An example relationship for a single pixel is shown in Fig. 3.17, which shows that the depth of interaction can be uniquely mapped to drift time. The non-linearity of the depth of interaction to drift time mapping can be primarily attributed to a non-uniform electric field near the anode and cathode surfaces. To limit the effect of electric field non-uniformity, the center region of the detector which has the best linearity is used to determine τ_e—depths ranging from 7.5mm to 13.125mm. Therefore, the relationship between the photopeak energy centroid and depth can be used to determine τ_e through

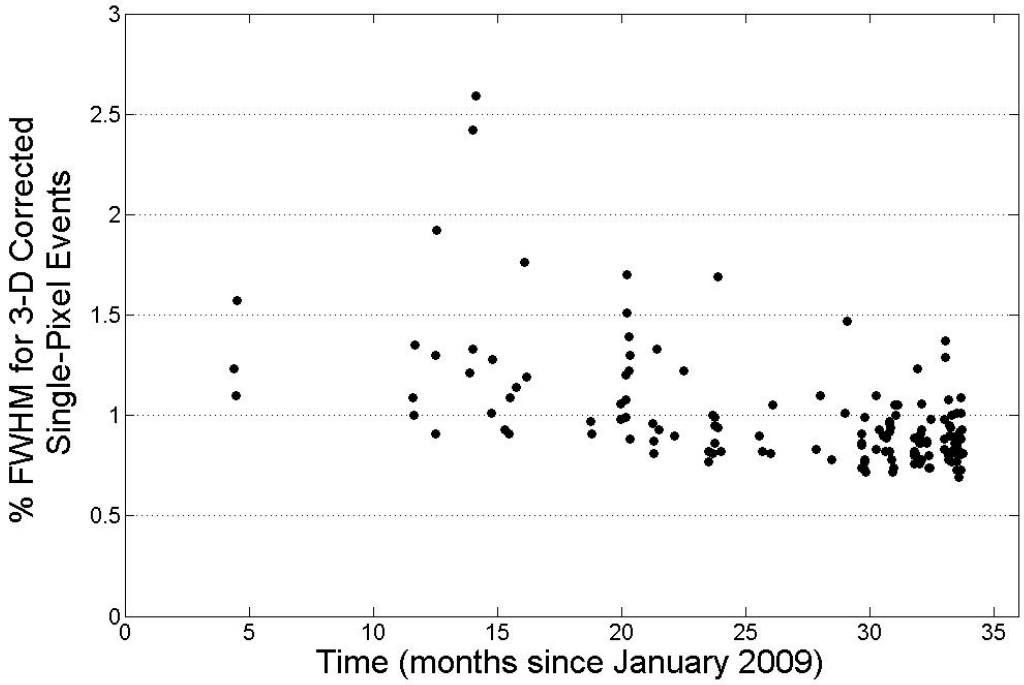

Figure 3.14: Energy resolution performance of the CdZnTe detectors over time.

mapping each depth to its unique drift time. The relationship between photopeak centroid and depth is shown for a single pixel in Fig. 3.18.

The electron mobility, μ_e, is calculated from solving Equation 3.3. Any non-uniformity in the electric field is accounted for by integrating the velocity, v, and electric field, E, over the depth, z, as shown in Equation 3.4. The final result, Equation 3.5, gives μ_e as a function of the velocity and the magnitude of the voltage, V, in that region of the detector. The non-linearity in the drift time versus depth relationship shown in Fig. 3.17 is accounted for by integrating over the depth.

$$v = \mu_e E \tag{3.3}$$

$$\int_{z=7.5mm}^{13.125mm} v \cdot dz = \mu_e \int_{z=7.5mm}^{13.25mm} E \cdot dz = \mu_e \cdot V \cdot x \tag{3.4}$$

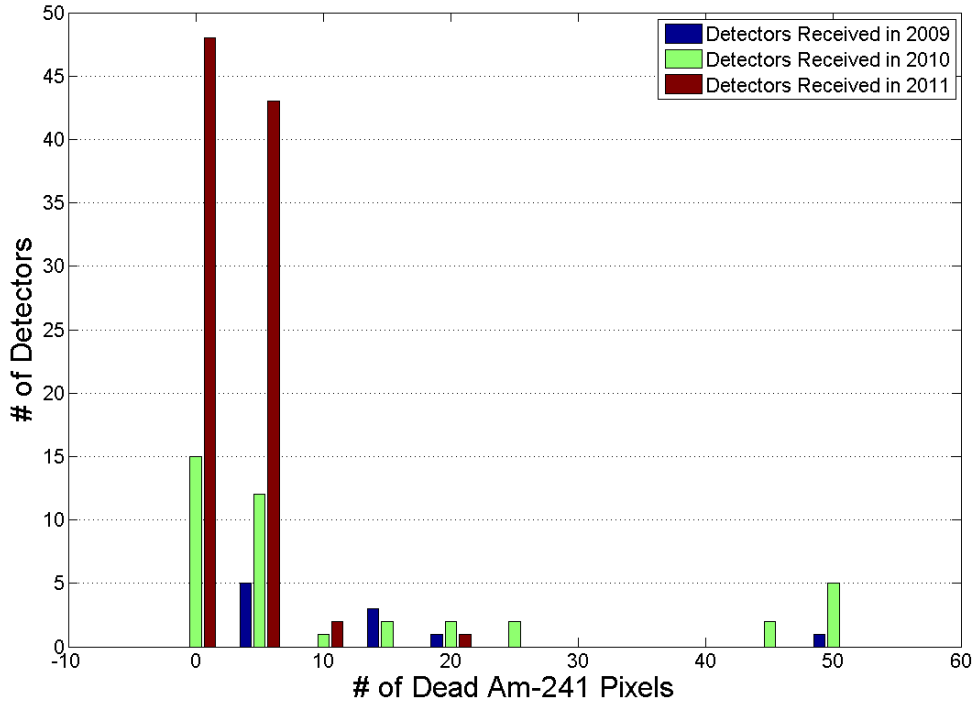

Figure 3.15: Improvement in cathode fabrication of CdZnTe detectors over time as shown by the improvement in the low energy performance. A bin width of 5 dead Am-241 pixels was used.

$$\mu_e = \frac{1}{V \cdot x} \int v \cdot dz = \frac{1}{V \cdot x} \sum_{i=7.5mm}^{13.125mm} \frac{z_{i+1} - z_i}{t_{i+1} - t_i} dz \tag{3.5}$$

where μ_e is the electron mobility, dz is the width of the depth bins (0.375mm), and x is a scaling factor to account for the limits of integration. The scaling factor x is equal to the depth range divided by the total thickness, or $\frac{5.625mm}{15mm} = 0.375$.

The electron mobility and mean free drift time can then be multiplied to find $\mu_e\tau_e$, as shown in Equation 3.6.

$$\mu_e\tau_e = \frac{(t_2 - t_1)}{V \times ln(N_2/N_1)} \sum_{i=20}^{34} \frac{z_{i+1} - z_i}{t_{i+1} - t_i} dz \tag{3.6}$$

As shown in Fig. 3.18, the relationship between the depth of interaction and

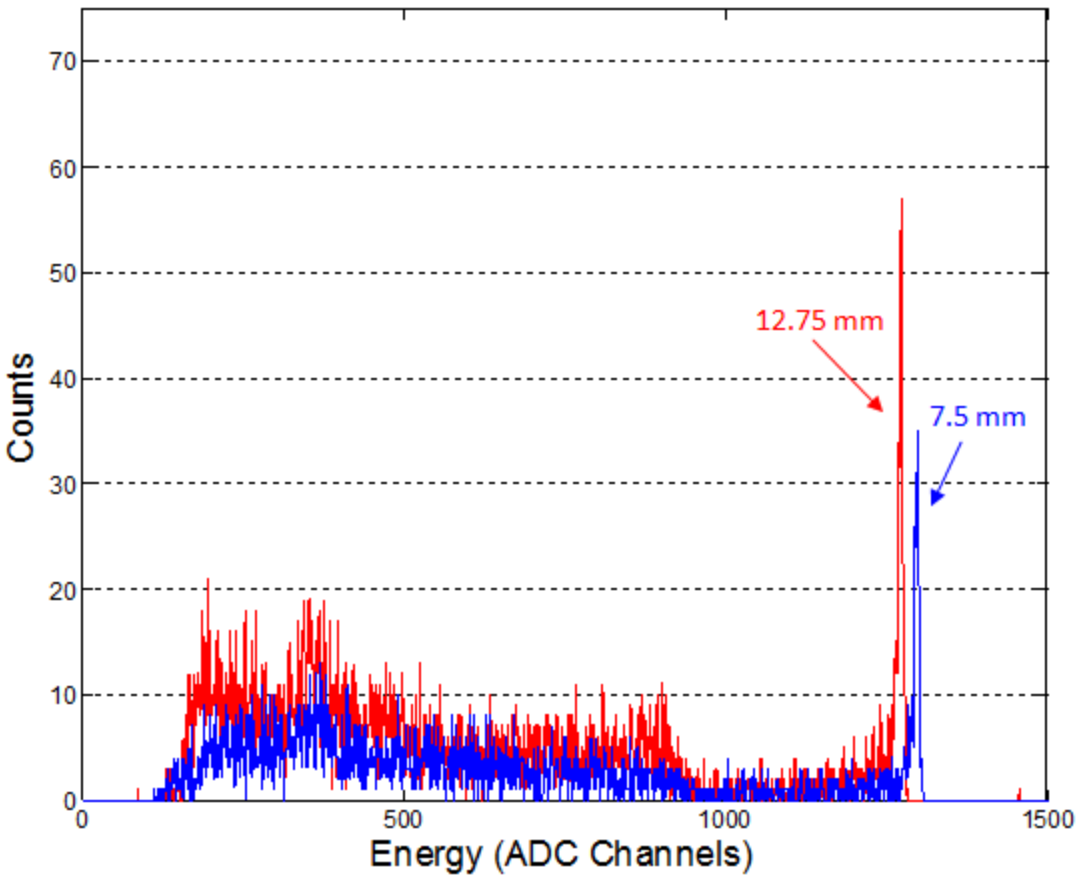

Figure 3.16: Energy spectra showing the signal loss due to electron trapping between two different interaction depths (7.5 & 12.75 mm relative to the anode) within a single pixel of a 15mm-thick CdZnTe detector.

the photopeak centroid is approximately linear in the center region of the detector. Therefore, depths of interaction ranging from 7.5mm to 13.125mm were used to determine values for τ_e and $\mu_e\tau_e$ using York's solution to a linear least squares fit with known error in both parameters [51]. A weighting potential correction was performed based on the weighting potential values shown in Fig. 3.19. The induced charge on an anode pixel is proportional to the difference in weighting potential between the gamma-ray interaction location and the anode surface; therefore, without a correction, pulse heights for interactions near the anode will be underestimated compared to interactions near the cathode.

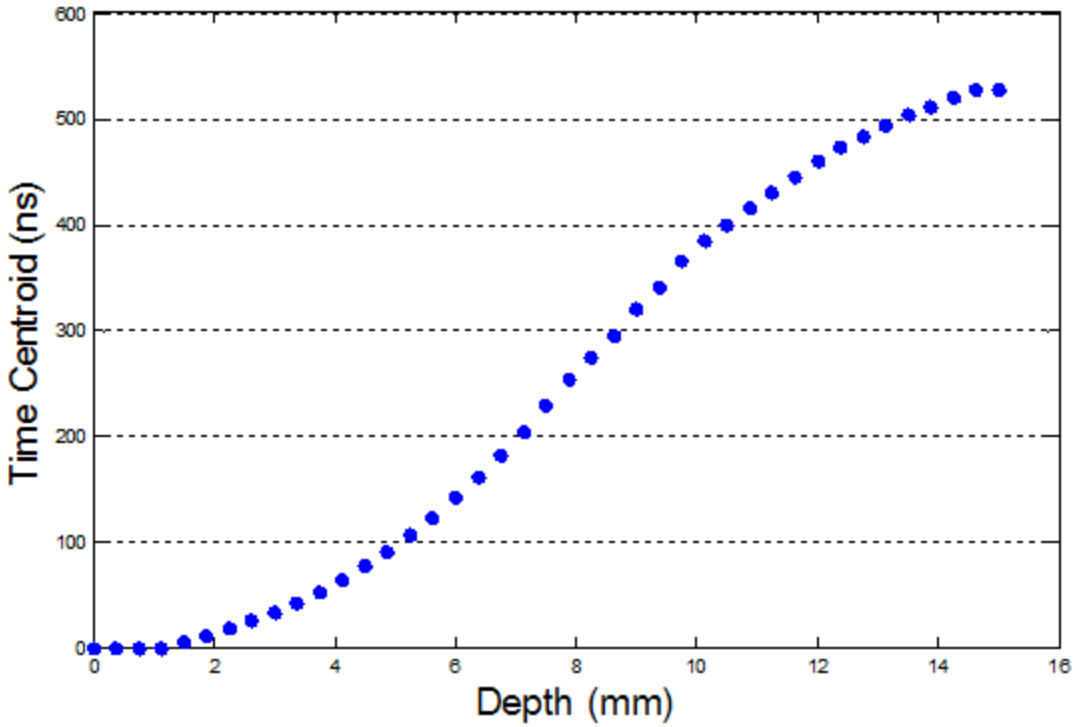

Figure 3.17: Relationship for the drift time versus the depth of interaction that is used to uniquely map drift time to depth. The depth of interaction is determined using the cathode-to-anode signal ratio.

This provides μ_e, τ_e and $\mu_e\tau_e$ for each of the 121 pixels in the detector. It should be noted that these calculated values are averaged over all interaction depths within each pixel. The pixel-by-pixel values can then be averaged to determine the value for all three parameters for an entire detector. The uncertainty in $\mu_e\tau_e$ is also determined for each pixel based on the measured depth uncertainty within the device and the statistical uncertainty of determining the photopeak centroid at each depth [52]. The depth uncertainty is less than 1mm, but a 1mm depth uncertainty was used as a conservative estimate [48]. Propagation of error was used to determine the overall uncertainty in $\mu_e\tau_e$.

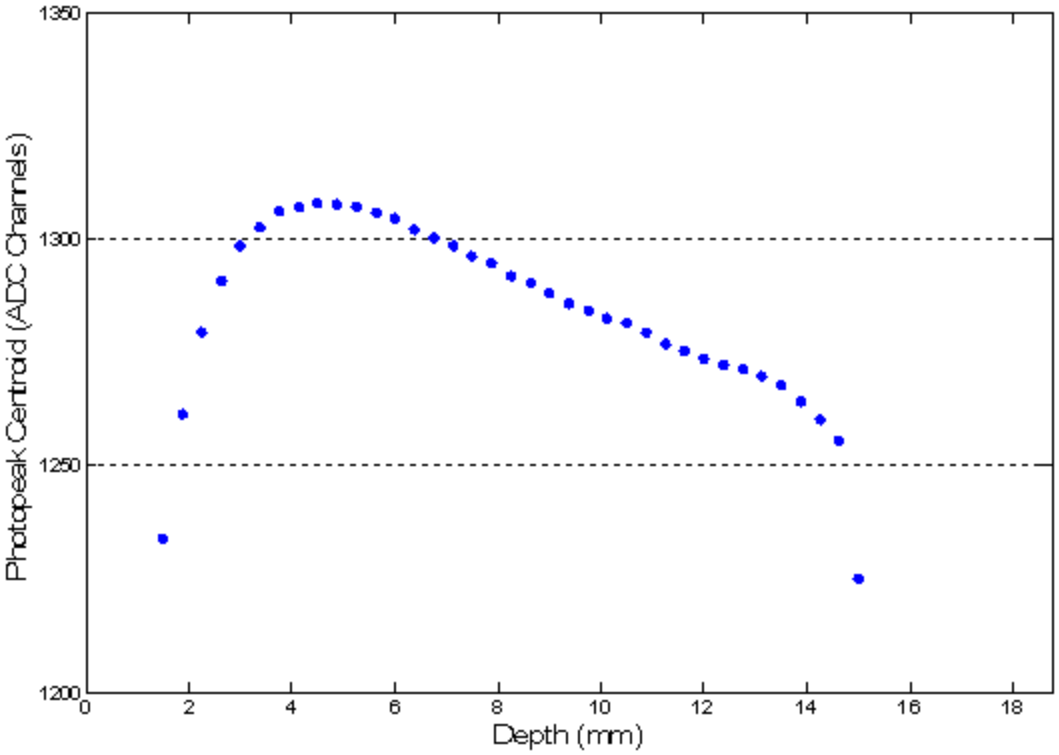

Figure 3.18: Relationship between photopeak centroid and depth of interaction that is used to determine τ_e and $\mu_e\tau_e$.

3.1.3.2 Results

Measured values for μ_e, τ_e and $\mu_e\tau_e$ for two 2×2×1.5 cm^3 CdZnTe detectors made by Redlen Technologies, Inc. were determined using the methodology explained above. These have been compared against the method described in Ref. [13] in Table 3.1. Comparable results for 1 cm^3 CdZnTe detectors grown by Redlen Technologies, Inc. have been found using a technique based on the Hecht relation [30]. Other research groups using the Hecht relation to measure the electron mobility-lifetime product have also found comparable results [53].

The uncertainty in $\mu_e\tau_e$ for Detector #1 and Detector #2 were measured to be 0.03 $\times 10^{-2}\ cm^2/V$ and 0.01 $\times 10^{-2}\ cm^2/V$, respectively. The comparability between the values from each method verifies the accuracy of this new method. This new method has the advantage of determining both μ_e and τ_e. Measured values of $\mu_e\tau_e$ range

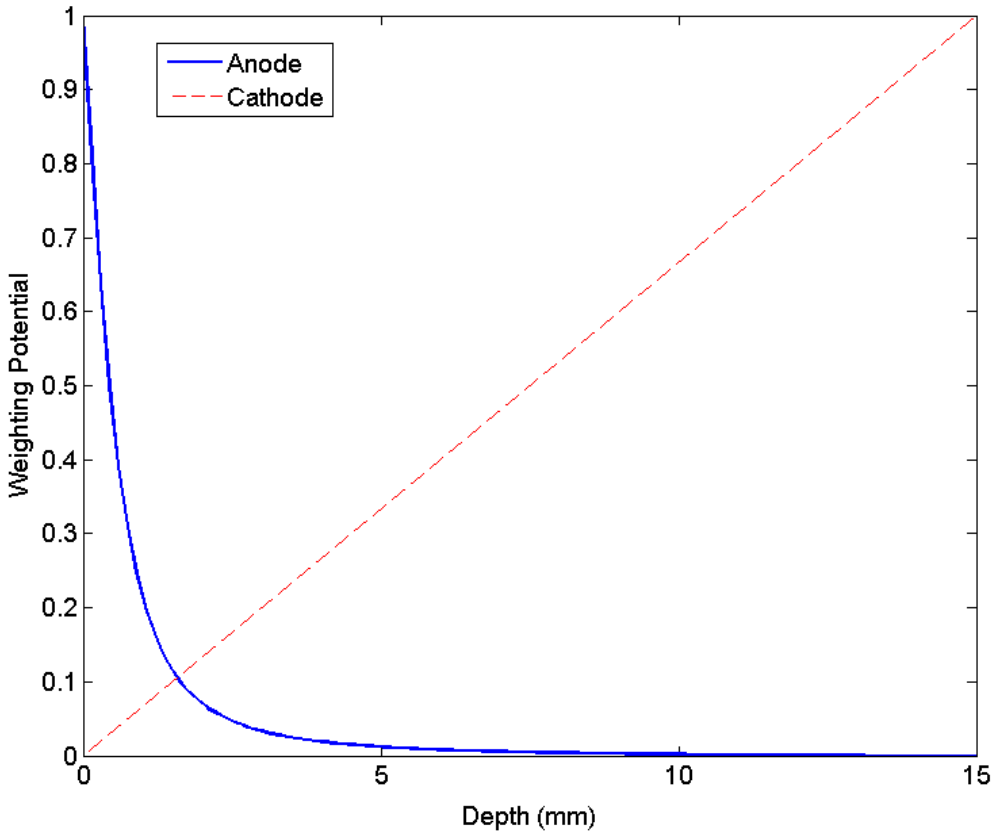

Figure 3.19: Weighting potential values for an anode pixel and the planar cathode. The linearity of the cathode weighting potential allows for the use of the cathode-to-anode signal ratio to determine the depth of interaction.

from 0.5×10^{-2} to 5.3×10^{-2} cm^2/V. Measured values of τ_e range from 10 to 90 μs. Measured values of μ_e range from 0.014×10^{-2} to 0.11×10^{-2} $cm^2/V\mu s$. The variation in μ_e is slightly larger than expected and can be attributed to the non-linearity in the electric field; however, it does not appear that these variations cause a larger than expected variation in $\mu_e\tau_e$.

This method was used to analyze trends relating the relative electron trapping within a detector to its performance. In Fig. 3.20, it can be seen that there is a correlation between the electron trapping and the raw energy resolution of a device. This is expected as the raw photopeak will fall in a different amplitude bin for a

Table 3.1: Comparison of values for $\mu_e\tau_e$.

	$\mu_e\tau_e$ ($\times 10^{-2}\ cm^2/V$)	μ_e ($\times 10^{-2}\ cm^2/V\mu s$)	τ_e (μs)	$\mu_e\tau_e$† ($\times 10^{-2}\ cm^2/V$)
Detector #1	1.27 ± 0.17	0.045 ± 0.005	29.0 ± 0.8	1.41 ± 0.84
Detector #2	1.01 ± 0.09	0.055 ± 0.005	18.5 ± 0.2	1.06 ± 0.30

† using method described in Ref. [13]

full energy event near the cathode compared to an event in the middle of the active volume, which is also different from an event near the anode. These differences cause a spread in the overall spectrum dependent on the severity of the electron trapping. However, the 3-D energy reconstruction can correct for the degradation as there is a much smaller correlation between the amount of electron trapping and the corrected energy resolution in Fig. 3.21. This is achievable since the correction is performed for each voxel in the detector, which corrects the electron trapping as a function of depth. This means that the overall spectroscopic performance of a CdZnTe detector is roughly independent of the amount of electron trapping present in the detector. A limitation put on this finding is that detectors with severe trapping problems—below $1 \times 10^{-2}\ cm^2/V$—show a correlated poor energy resolution. However, this is a small fraction of the crystals that have been delivered by Redlen Technologies, Inc.

The weak correlation between $\mu_e\tau_e$ and the energy resolution after the 3D position reconstruction can be further exemplified by studying the pixel-by-pixel values of $\mu_e\tau_e$ and energy resolution, as seen in Fig. 3.22 and 3.23. It may appear that some regions of the detector show correlation between the two parameters, however, other pixels showing good energy resolution correspond to pixels that have lower values of $\mu_e\tau_e$.

The overall trend is that poor energy resolution can be found in pixels that show a larger variation in the trapping compared with the surrounding pixels. To better understand this perceived relationship, the measured uncertainty in $\mu_e\tau_e$ is compared against both raw and corrected energy resolution for single-pixel events at 662 keV; the results are presented in Fig. 3.24 and 3.25, respectively. There is a better correlation

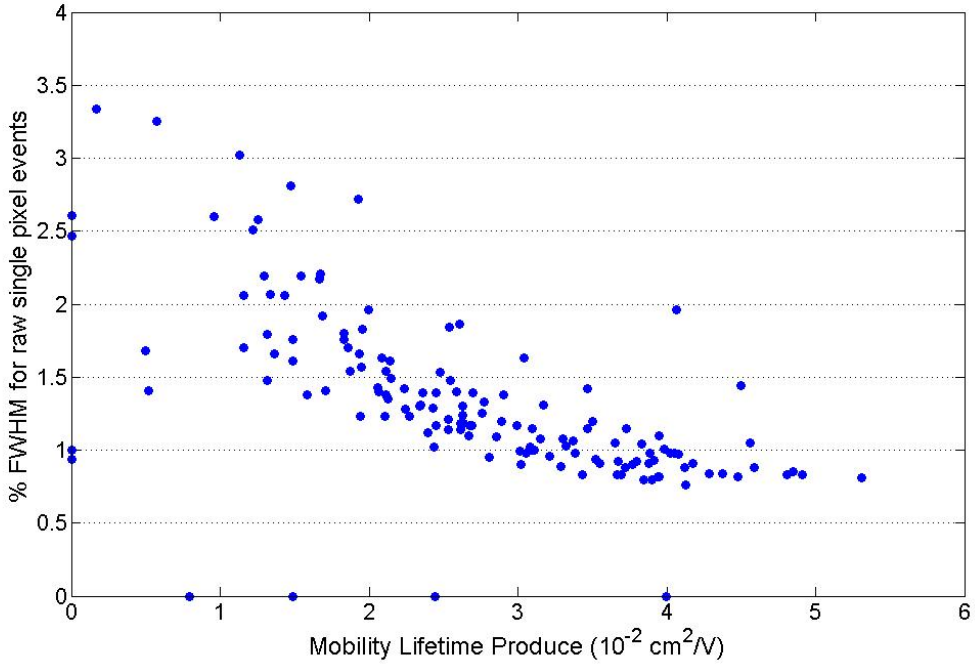

Figure 3.20: $\mu_e\tau_e$ versus raw FHWM of full-energy peak for single pixel events. A linear fit has a correlation coefficient of -0.40.

between corrected energy resolution and $\mu_e\tau_e$ uncertainty than between raw energy resolution and $\mu_e\tau_e$ uncertainty. These results are expected. The uncertainty in the measured value of $\mu_e\tau_e$ is determined by several factors. The uncertainty in the depth of interaction and the statistical uncertainty in the photopeak centroid at each depth contribute to the uncertainty for $\mu_e\tau_e$ in each pixel. Larger fluctuations in this uncertainty will correspond to inconsistent trapping, causing an abnormal spread to the amplitude distribution at each depth within the pixel. This increases the uncertainty in the photopeak centroid, which causes an increased uncertainty in the value of $\mu_e\tau_e$ for the pixel. A second factor that can increase the overall uncertainty in $\mu_e\tau_e$ is the pixel-by-pixel fluctuation in the electron trapping. Larger than expected variations between pixels would cause an increased uncertainty in the averaged value of $\mu_e\tau_e$. These variation would not be expected to impact the raw energy resolution as this is dominated by the first order effect of the overall electron trapping within

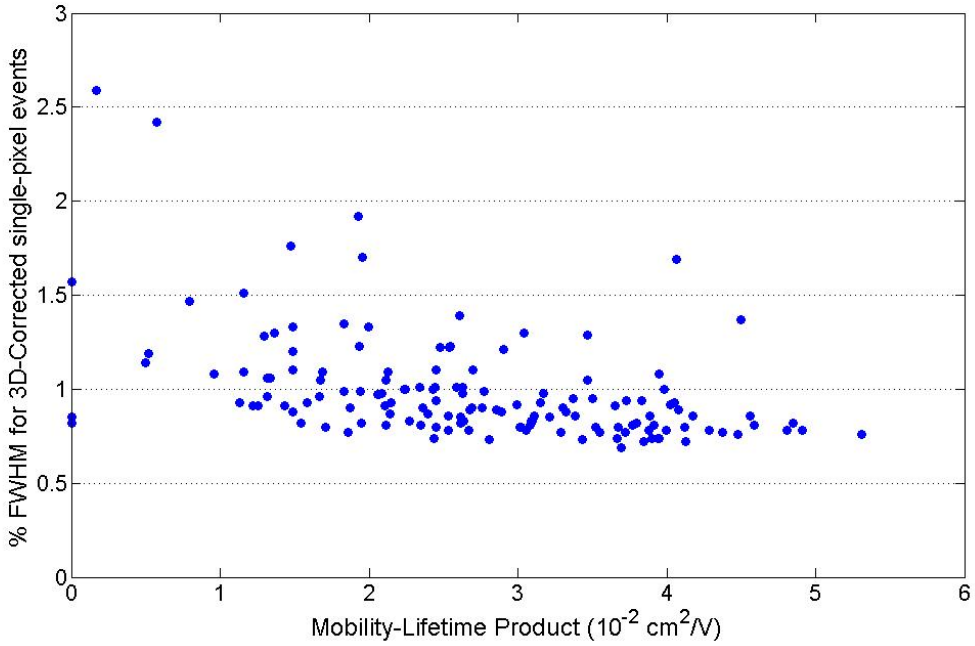

Figure 3.21: $\mu_e\tau_e$ versus corrected FHWM of full-energy peak for single pixel events. A linear fit has a correlation coefficient of -0.19.

the device. The corrected energy resolution fluctuates with these variations since two different events over the same pixel at the same depth would result in different signal amplitudes induced on the anode electrode. Having occurred in the same voxel of the detector, each event would have the same correction parameters, resulting in different corrected energies. After many events with inconsistent electron trapping, a wider spread in the corrected energy spectrum would be created.

3.1.4 Imaging Characterization

The imaging performance of the pixelated CdZnTe detectors is weakly correlated with the corrected energy resolution, as shown in Fig. 3.26. The angular resolution is primarily dependent on the position uncertainty of the events used to create the images. The position uncertainty affects the energy resolution if events are reconstructed to a different voxel than the true interaction position, resulting in the application of

5.01	4.01	3.31	3.56	3.83	3.52	3.54	2.99	3.17	3.72	5.23
4.50	3.23	3.19	3.19	2.99	2.65	2.99	2.88	2.96	3.68	2.28
3.49	3.00	2.92	2.61	2.50	2.42	2.39	2.64	2.84	3.26	3.94
3.38	2.85	2.73	2.62	2.55	2.65	2.46	2.78	3.16	2.94	3.65
3.10	2.77	2.40	2.62	2.76	2.61	2.88	2.65	2.54	2.61	3.13
2.85	2.52	2.63	2.58	2.71	2.50	2.50	2.58	2.30	2.40	3.01
2.81	2.54	2.53	2.46	2.61	2.61	2.54	2.50	2.34	2.33	2.78
3.00	2.64	2.54	2.46	2.49	2.75	2.62	2.56	2.47	2.38	2.61
2.71	2.43	2.32	2.29	2.43	2.66	2.42	2.58	2.55	2.57	2.64
2.32	2.13	2.26	2.13	2.41	2.49	2.67	2.56	2.51	2.66	3.02
2.22	2.25	2.36	2.58	2.65	2.90	2.73	2.87	2.88	3.29	3.16

Figure 3.22: $\mu_e\tau_e$ for each of the 121 pixels in an example CdZnTe detector. $\mu_e\tau_e$ has units of 10^{-2} cm^2/V.

improper calibration parameters. Therefore, the weak correlation between the angular resolution and the corrected energy resolution results from the dependence of both on the accuracy of the 3-D position determination of each event. Fig. 3.26 also shows that the angular resolution is consistently better for cathode surface imaging relative to side surface imaging. The overall degradation of the side surface imaging is due to the larger role of the depth uncertainty as the interactions incident from the side surface tend to scatter across fewer depths—during forward scattering—than interactions from the cathode surface. The polar angular resolution is degraded compared to the azimuthal angular resolution because of the dependence on the depth

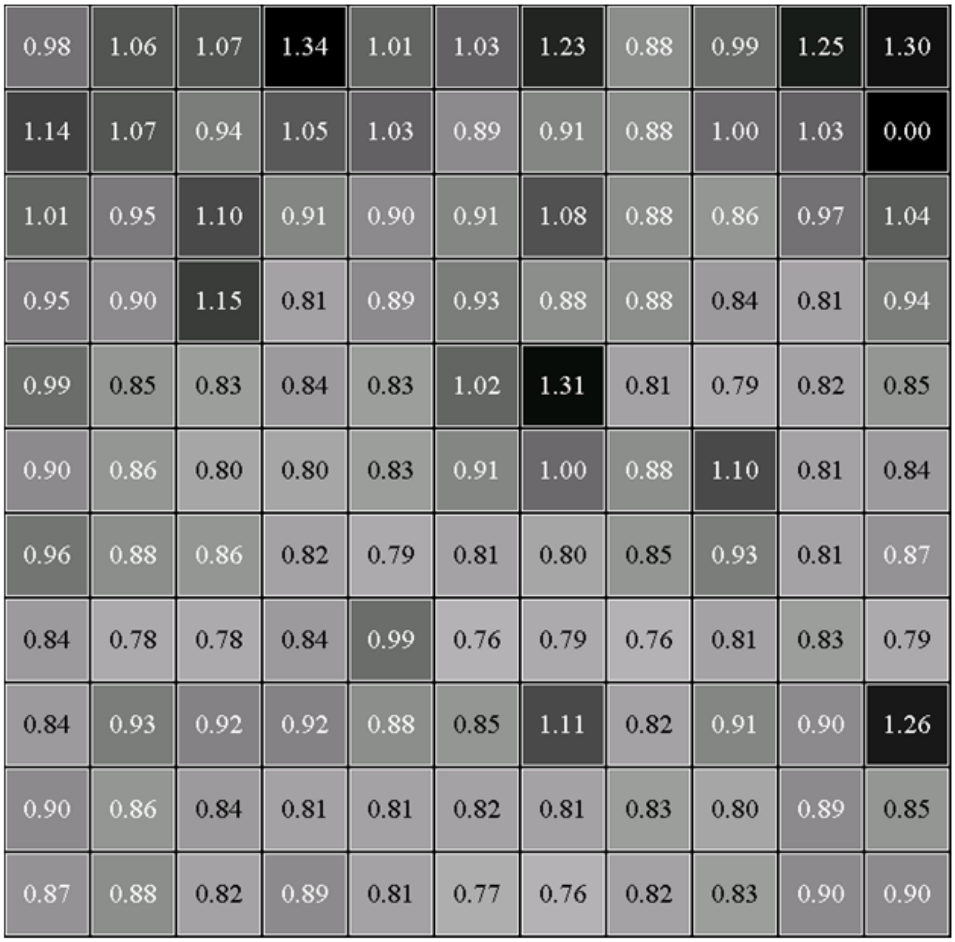

Figure 3.23: The 3D corrected energy resolution for single pixel events (in % FWHM at 662 keV) for each of the 121 pixels in an example CdZnTe detector.

uncertainty of the calculation of the polar angle [54]. A more predictive parameter that can be used to pre-determine higher quality imaging detectors is the FWHM of the calculated-to-measured cathode ratio (CMCR), as shown in Fig. 3.27. The CMCR is determined using two-pixel events, for which only a single cathode signal is measured. The energy-weighted depths determined from the electron drift time of each interaction are used to back calculate what each interaction's cathode signal would have been for a single-interaction event. These signals are summed to calculate the expected total cathode signal, which is compared to the measured cathode signal. If these numbers do not agree it indicates that the reconstruction of the depth from

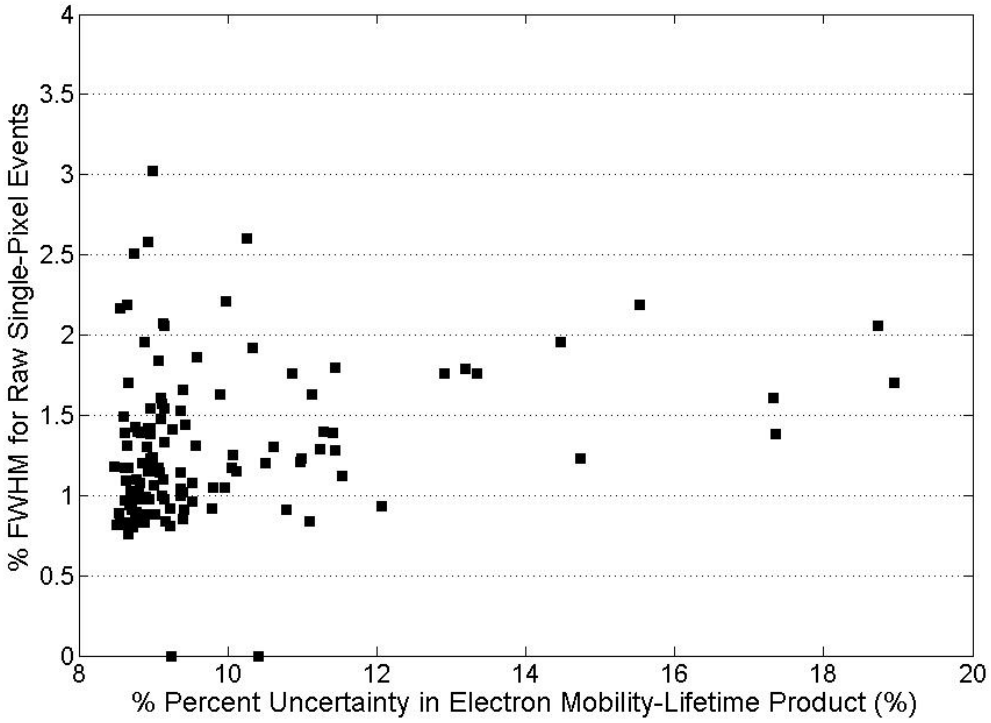

Figure 3.24: Percent uncertainty in $\mu_e\tau_e$ versus raw FHWM for single-pixel events. A linear fit has a correlation coefficient of 0.04.

the drift time is not accurate. The narrower the spread in this ratio, the better the multiple interaction depth resolution for the detector, which will lead to better image quality. Therefore, as seen in Fig. 3.27, the detectors with a better depth correction tend to show better imaging performance.

3.2 Operational Stability

An additional metric to characterize the overall performance of the 20×20×15 mm^3 CdZnTe detectors is to test their long-term operational stability. Stability in 1.5cm-thick CdZnTe detectors has been shown in space physics experiments [55]. For large-volume CdZnTe detectors to be suitable for various applications, it is necessary that they are capable of stable operation over long periods of time without significant degradation. The two 18-detector CdZnTe array systems were tested over the

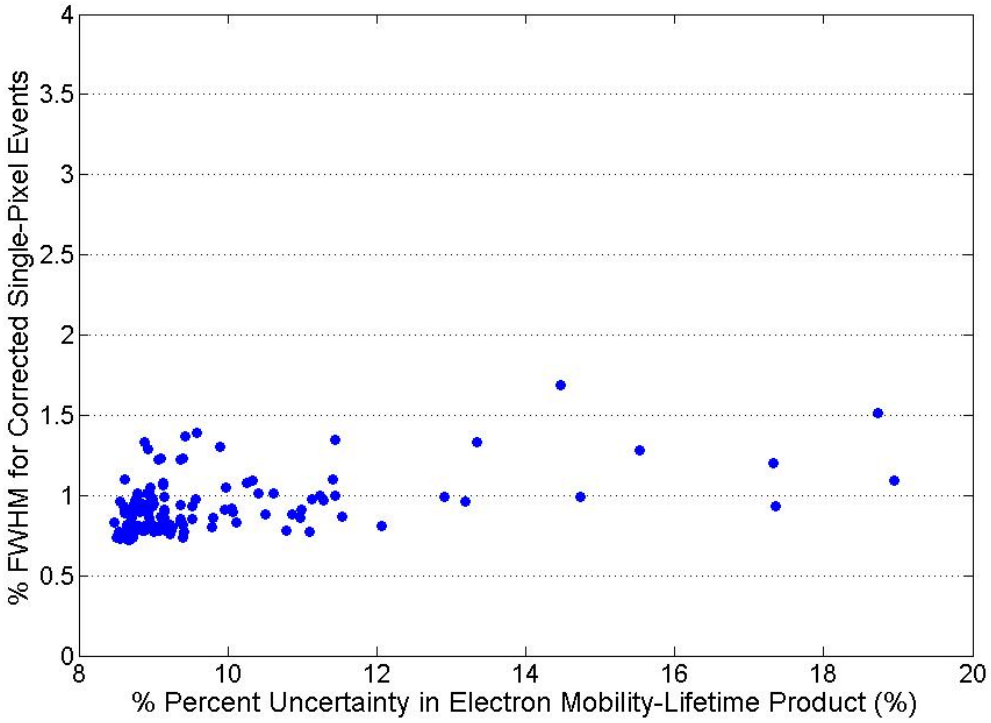

Figure 3.25: Percent uncertainty in $\mu_e\tau_e$ versus corrected FHWM for single-pixel events. A linear fit has a correlation coefficient of 0.20.

course of 11-20 months, which has allowed for extensive study into the properties and characteristics of CdZnTe detectors during extended operation.

Testing of the long-term stability of the first array system started in September, 2010, and continued for 18 months. During that time, it was almost continuously biased without any replacement of its detectors. The system was only biased down for transport to and from the laboratory at the University of Michigan for outside experiments. The duration of the system being off was typically no longer than 24-36 hours. The system has been recalibrated twice—in January 2011 and January 2012. Measurements were unable to be made more frequently as the system was being used for other research applications. The system was used for measurements of weak radiation sources, limiting the total dose deposited in the system over its current lifespan.

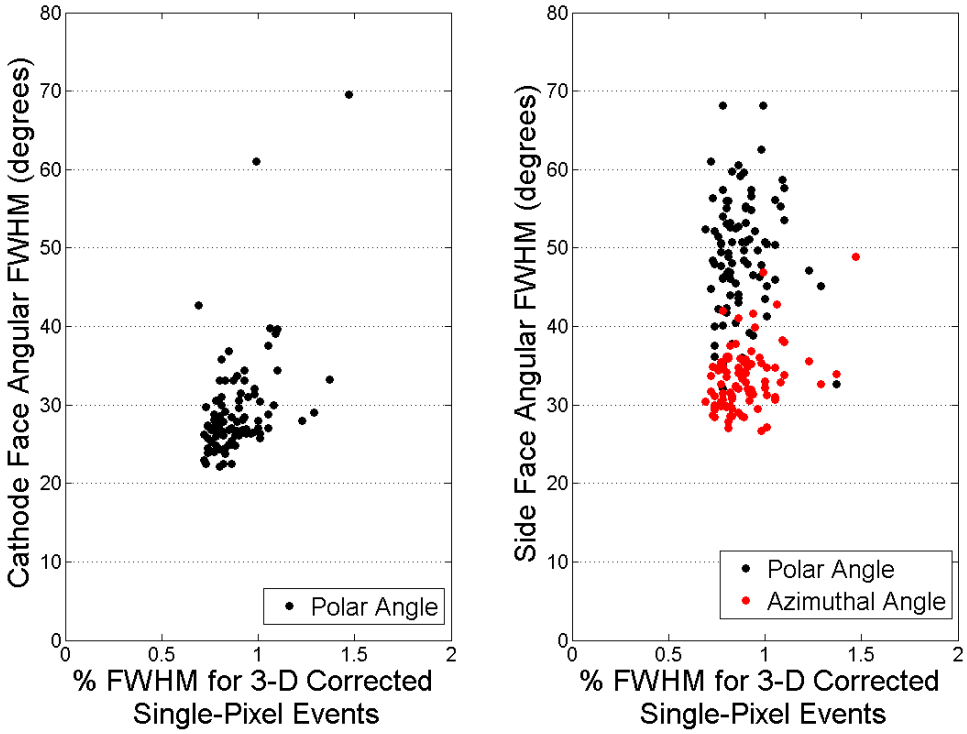

Figure 3.26: Relation between the 3D-corrected energy resolution and the imaging performance. The energy resolution has a 0.26 correlation coefficient compared with the cathode face angular FWHM, a 0.15 correlation coefficient compared with the side face angular FWHM, and a 0.06 correlation coefficient compared with the side face polar FWHM.

The second CdZnTe array system was built in June 2011 and has been used for similar research applications as the first system. It has also been almost continuously biased throughout its lifespan, with only being biased down for transportation to measurements outside of the laboratory for a maximum time of 24-36 hours. The two systems have experienced similar testing intensity over their lifespans. The system was also recalibrated in January 2012.

The first method for analyzing the stability of the CdZnTe detectors used in the first and second CdZnTe array systems is to compare the results of separate calibrations of each system. The results for the corrected energy resolution of the 18 detectors in both systems are shown in Fig. 3.28. The energy resolution of the

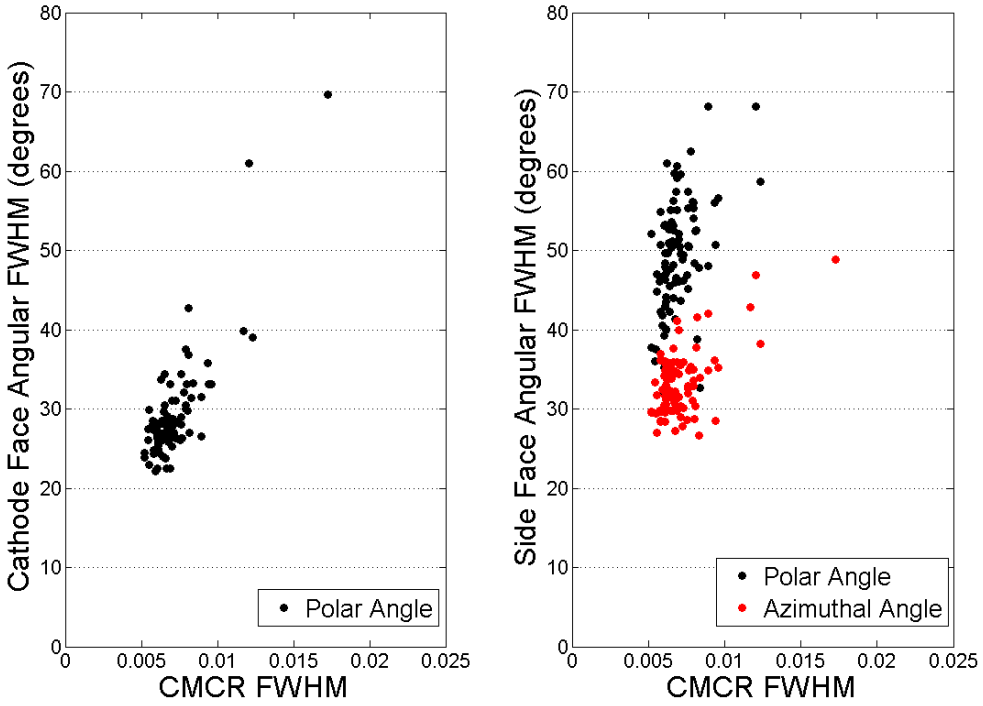

Figure 3.27: Relationship between the calculated-to-measured cathode ratio (CMCR) and the imaging performance. The CMCR has a 0.70 correlation coefficient compared with the cathode face angular FWHM, a 0.37 correlation coefficient compared with the side face angular FWHM, and a 0.43 correlation coefficient compared with the side face polar FWHM.

detectors in the first system is shown to vary between calibrations, whereas the second system shows much more consistent results for all of its detectors between the two calibrations. The initial assembly and testing of the first system was rushed and little was known of the dependence of the first system on factors such as temperature, which can contribute to the variation between the first and second calibrations. Due to these outside factors affecting the comparability of the results from the September 2010 calibration, the remaining analysis will focus on the later results which held these factors more consistent. The results for the calibrations of the first system in January 2011 and January 2012 show more consistency in the energy resolution for each detector; however the results for January 2012 show an average degradation of

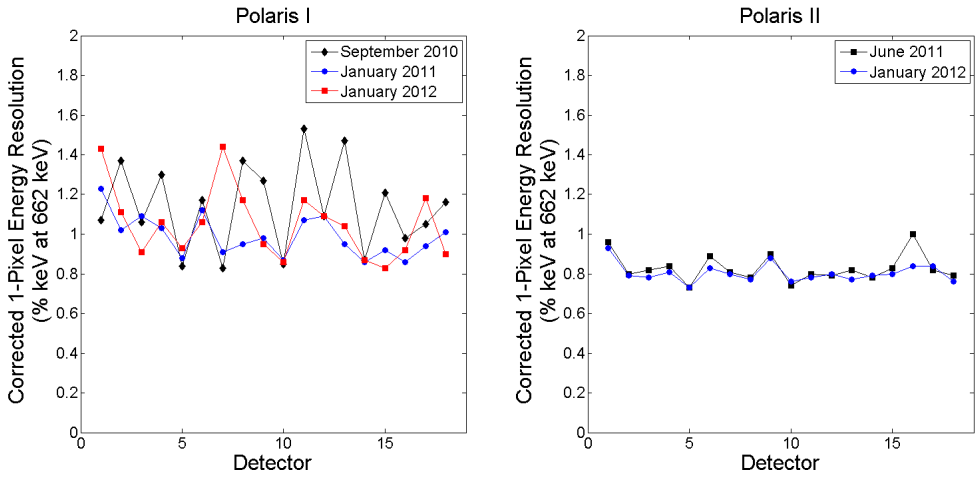

Figure 3.28: Comparison of the corrected single-pixel energy resolution for the first (left) and second (right) CdZnTe array systems.

0.063% FWHM from the previous calibration. This will be further analyzed using results from each of the detectors from system testing throughout the year between the calibrations. As stated before, the second system shows much more consistent energy resolution values for each detector in the calibrations from June 2011 and January 2012. An average improvement of 0.019% FWHM was observed for the second Polaris system. The results from testing throughout the lifespan of the system confirm improved stability of these detectors.

Each detector's electron mobility (μ_e), mean free electron drift time (τ_e), and electron mobility-lifetime product ($\mu_e\tau_e$) are compared between the calibrations of each CdZnTe array system in Fig. 3.29 and 3.30, respectively. The comparability of the results for the charge transport properties between the separate calibrations of each detector in both systems shows the stability of the bulk crystal over time.

In addition to the multiple calibrations performed at different stages of each system's lifespan, measurements were made every few months to monitor their spectroscopic performance. All measurements use the same bias settings as were used during calibration of the system and the temperature is held constant between 22 and 25 $^{\circ}C$. The constant temperature removes the impact of the ASIC on the results as

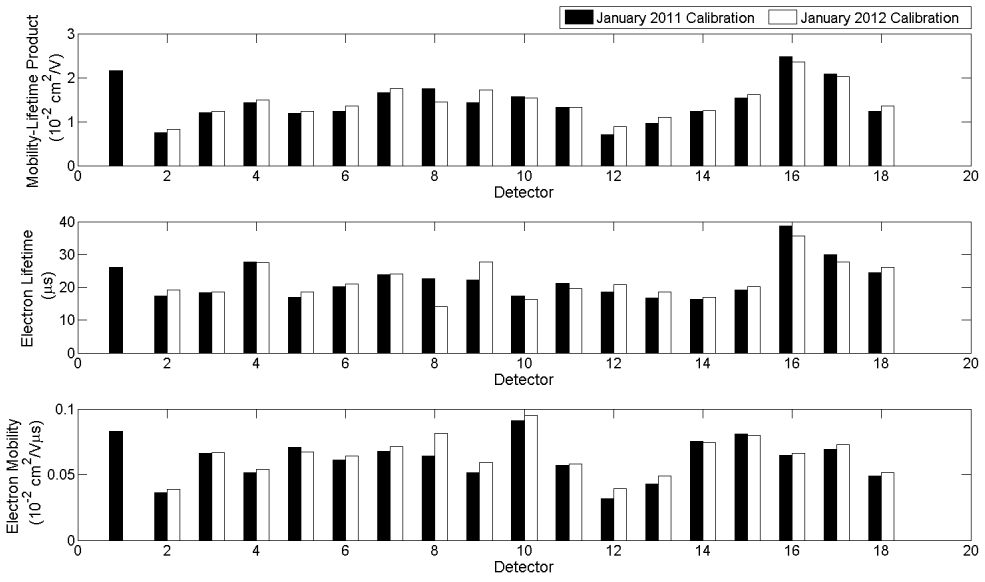

Figure 3.29: Comparison of the charge transport parameters for the January 2011 and January 2012 calibrations of the first CdZnTe array system.

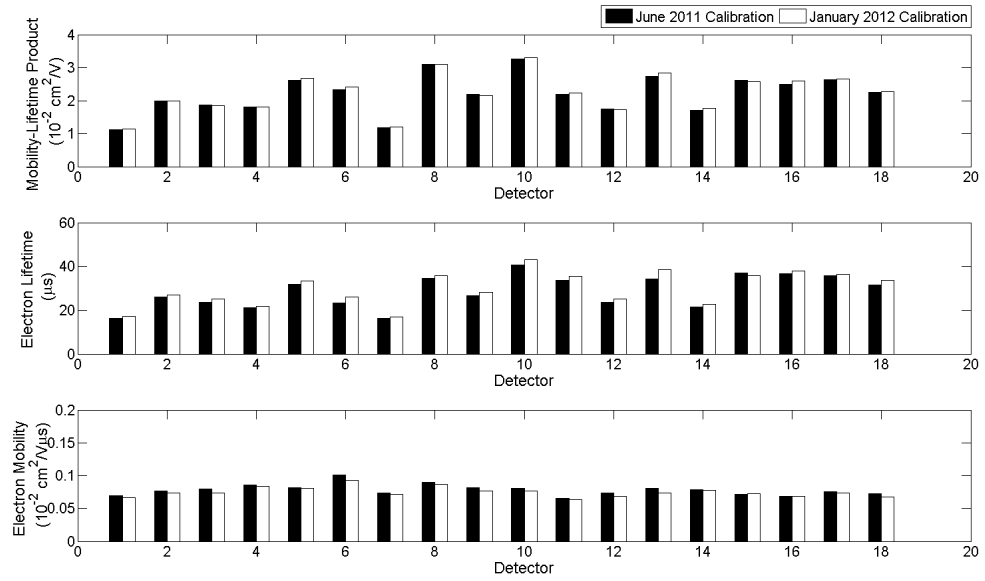

Figure 3.30: Comparison of the charge transport parameters for the June 2011 and January 2012 calibrations of the second CdZnTe array system.

temperature variation is known to affect the ASIC gain. The ASIC is known to be stable over time as the results presented in Sec. 3.1 used several ASICs over many

months without any degradation. The measurements consisted of acquiring sufficient data in each of the 18 detectors using a ^{137}Cs source to track the performance of the detectors over time. Since not enough data was collected in each detector to perform a calibration, the corrected energy resolution is tracked using the previously completed calibration. Only single-pixel events were studied to focus on the stability of the detectors and avoid the complications of the multiple-pixel event reconstructions. The average detector noise and the raw energy resolution are also tracked for these measurements. All comparisons are made by averaging results from all 121 pixels since the fluctuations observed between pixels within a single detector are small.

For the first system, this was completed using measurements in January, April, June, September, and December in 2011 and January 2012. Results showing the corrected energy resolution of each of the 18 detectors using the January 2011 calibration are shown in Fig. 3.31. A slight degradation over time is identified on each of the detectors. The measurement acquired in January 2012 is also corrected using the January 2012 calibration to show that a recalibration of the system helps improve the performance; however the initial performance of the system from the previous calibration could not be restored. Similar analysis using the second array system; data collected in June, August, and December in 2011 and January 2012 were corrected with the June 2011 calibration in Fig. 3.32. The CdZnTe detectors in the second system prove to be more stable than the detectors in the first system, and the analysis shows that the recalibration does not improve the performance. It was expected that the recalibration did not improve the performance as the stability of the detectors in the system lead to the conclusion that a recalibration was not necessary.

To better understand why the detectors in the first system show a degradation while the detectors of the second system show better stability, the raw energy resolution and detector noise were compared for each of the measurements. As shown in Fig. 3.33 for the first system, the degradation in the corrected energy resolution

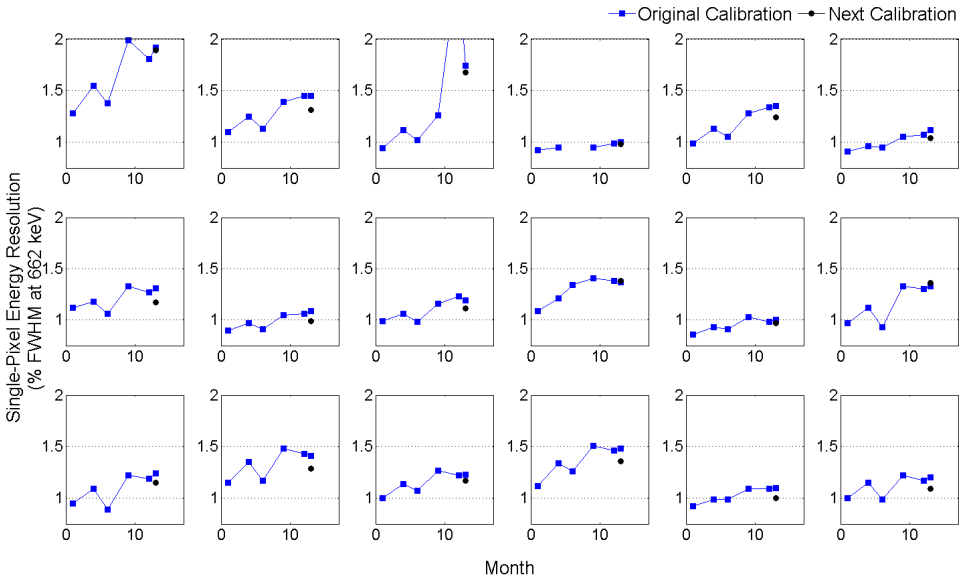

Figure 3.31: Results tracking the corrected energy resolution of each of the 18 detectors in the first system between the January 2011 and January 2012 calibrations. The last measurement is corrected using both the January 2011 and January 2012 calibrations to show whether or not a new calibration improved the performance of each detector.

tracks fairly consistently with a degradation in the detector noise but with no apparent relation to the raw energy resolution. Similar analysis in Fig. 3.34 for the second system shows good stability in all three parameters. The raw energy resolution is dependent on the crystal quality, therefore changes in the material quality over time would manifest itself through a correlation between the raw and corrected energy resolutions, which was not seen in the data. This was previously confirmed by the consistent charge transport properties for each calibration. Instead the correlation between the noise and the corrected energy resolution implies that detectors that will be less stable over time will tend to show an increase in their noise.

A leading cause of high detector noise is the resistance (or lack thereof) between the pixels and the steering grid. A measurement of the leakage current between the anode pixels and the steering grid will quantify the performance of the steering grid. An increase in this leakage current over time would lead to a degradation in the

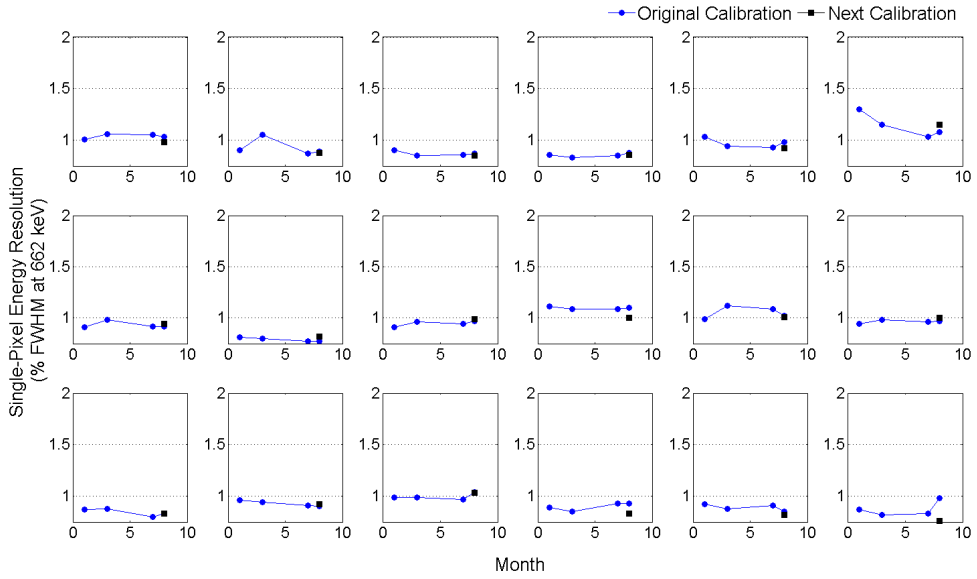

Figure 3.32: Results tracking the corrected energy resolution of each of the 18 detectors in the second system between the June 2011 and January 2012 calibrations. The last measurement is corrected using both the June 2011 and January 2012 calibrations to show whether or not a new calibration improved the performance of each detector.

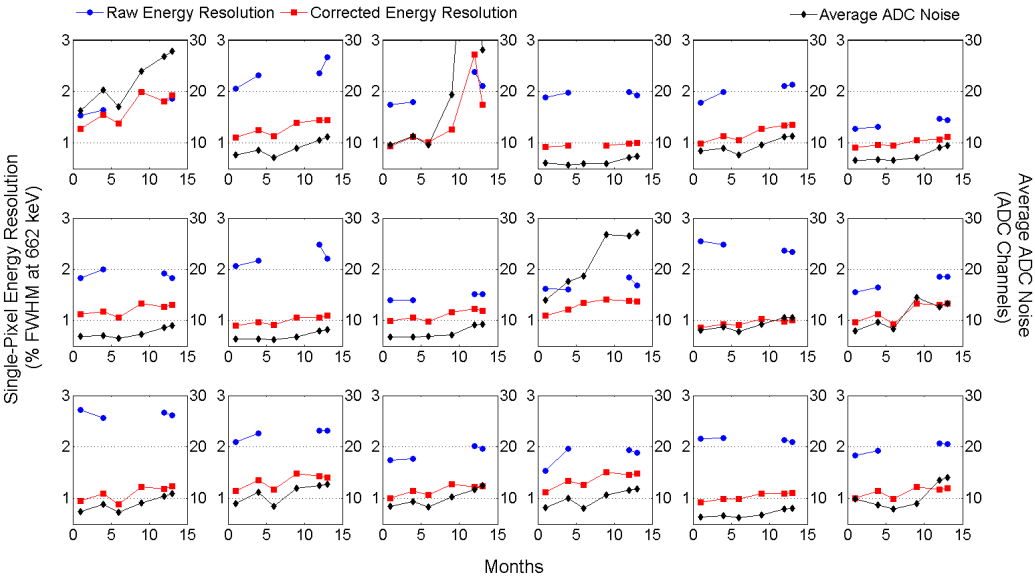

Figure 3.33: Results tracking the raw and corrected energy resolutions as well as the average detector noise for each of the detectors in the first system during the period between the January 2011 and January 2012 calibrations.

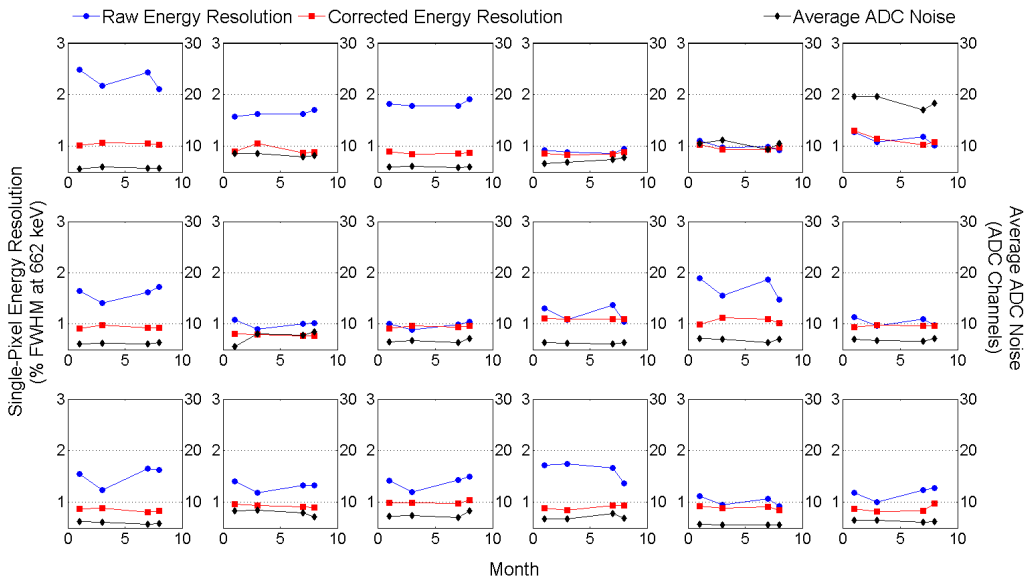

Figure 3.34: Results tracking the raw and corrected energy resolutions as well as the average detector noise for each of the detectors in the second system during the period between the June 2011 and January 2012 calibrations.

performance of the detector—which is accompanied by an increase in the detector noise. The increase in leakage current is most likely caused by surface related issues, not likely due to a change in bulk material properties. Due to the use of an internal power supply for the grid voltages of each of the detectors in the Polaris system, a measurement of the grid-to-pixel leakage current cannot be acquired. Instead, to characterize the surface related issues, the fraction of flawed pixels in each detector was recorded. A flawed pixel is any pixel that shows either a signal gain deficit or no signal altogether. A pixel is classified as having gain deficit if its signal is decreased by more than 100 ADC channels for a full-energy ^{137}Cs single-pixel event—an event that typically has a signal amplitude of approximately 1300 ADC units. As seen from Fig. 3.35 and Fig. 3.36 for the first and second Polaris systems, respectively, the first Polaris system has more flawed pixels, and many more pixels with a severe deficit that is greater than 400 ADC channels. The number of flawed pixels did not change in either system over time. The more surface related problems in the first system

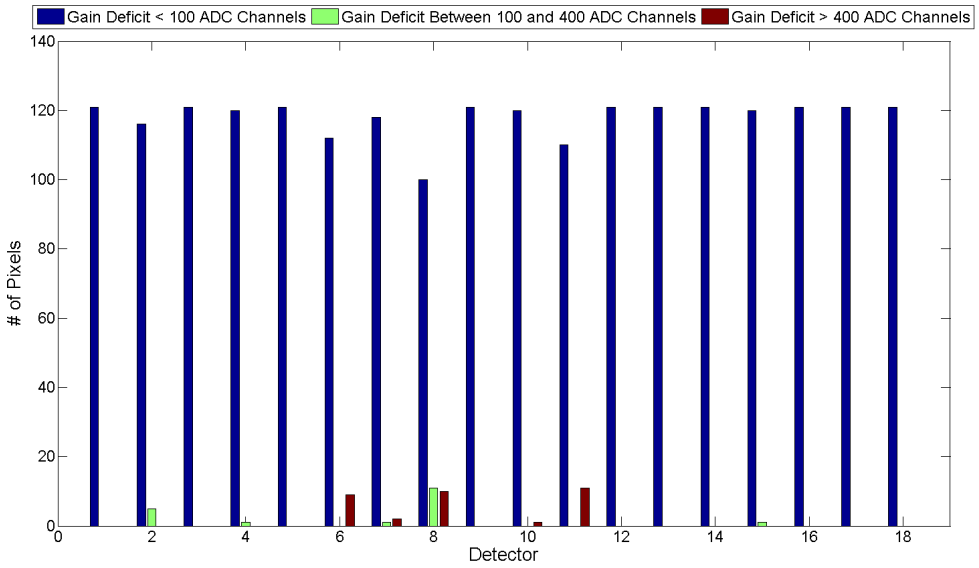

Figure 3.35: The fraction of flawed pixels in each of the detectors in the first CdZnTe array system.

could be related to poorer surface resistance between anode pixels and the steering grid which has lead to increased detector noise and a slightly degraded 3-D-corrected energy resolution. The stability of the second Polaris system could be attributed to fewer surface related issues in the later detectors from Redlen Technologies, Inc.

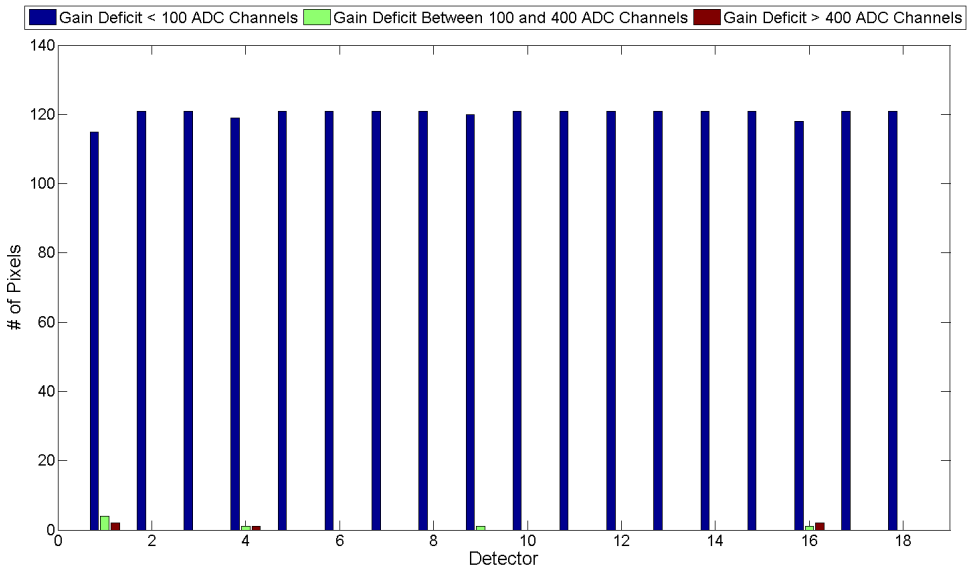

Figure 3.36: The fraction of flawed pixels in each of the detectors in the second CdZnTe array system.

CHAPTER IV

Array System Characterization for High Energy Applications

The dynamic range of the GMI VAS_UM2.3/TAT4 is limited to 3 MeV on each channel. This does not prevent the application of the 18-detector CdZnTe array system to measurements of gamma rays above 3 MeV. As long as the total energy is split across enough anode electrodes, events can be processed that do not have any saturated ASIC anode channels. The experimental considerations and results are discussed below. Additionally, to better understand the performance of the system at higher energiers, events across all energies were compared to characterize the breakdown of events into different categories.

4.1 Experimental Considerations

Special considerations need to be made for proper operation of the system for high energy events. As noted previously, the dynamic range of each ASIC channel is nominally 3 MeV. This is the same for both the cathode and anode channels.

For each cathode channel, a test pulse was input to find the highest amplitude for cathode signals prior to saturation. This amplitude is then used as a software threshold for events with a saturated cathode signal. For each anode pixel, the non-

linearity correction extends up to the 2754 keV peak from ^{24}Na. Beyond that point, the non-linearity fitting is not known to remain accurate and a software threshold is set to reject events which had a single anode signal greater than 2800 keV.

There are several possibilities by which the system can register a full energy event from a gamma ray above 3 MeV. The simplest way is for the gamma ray to scatter between multiple detectors, depositing under the threshold energy in each detector. However it is possible to collect full energy events in a single detector. Since the cathode records an induced charge proportional to the depth of interaction, the energy-weighted average depth of interaction for all of the events needs to be close enough to the anode to prevent the cathode signal from reaching saturation. A 6 MeV gamma ray would require an average depth of interaction between the midpoint of the detector and the anode surface to have a cathode signal below 3 MeV. Therefore, it would be expected that single detector events at high energies have a larger fraction of events towards the anode surface. For events to stay below the anode threshold, the charge needs to be spread over several anode pixels. Several Compton scattering intercations followed by a lower energy photoelectric absorption would achieve this. Even if a single interaction deposits over 3 MeV, there is no guarantee that a single pixel will collect all of the charge. Large energies generate larger electron clouds, which will be more likely to result in charge sharing between neighboring pixels. This allows a single electron cloud of greater than 3 MeV to be collected by multiple pixels, each receiving less than 3 MeV and preventing the event from crossing any channels high energy threshold. These are only several possibilities that lead to events not being rejected for crossing one of the high energy thresholds, and even more are available when pair production is considered, as the 511 keV annihilation photons help to spread the collection of energy throughout the system.

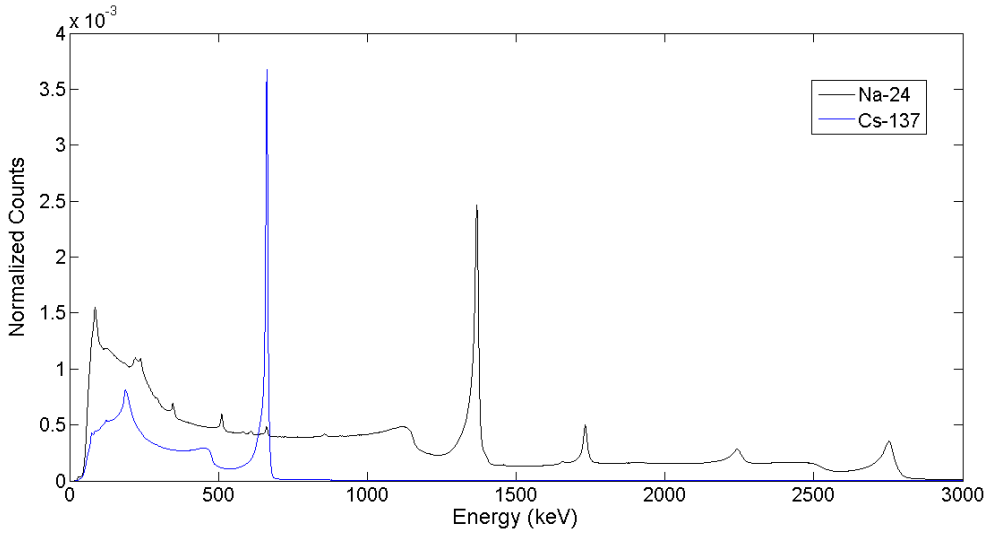

Figure 4.1: Spectra collected from the second 18-detector CdZnTe array system using ^{24}Na and ^{137}Cs sources.

4.2 Results

Before looking at results from sources of gamma rays above 3 MeV, Fig. 4.1 shows spectra collected from ^{24}Na and ^{137}Cs using the 2^{nd} CdZnTe array system. Data was collected over a lengthy period of time to achieve good statistics for the non-linearty calibration. The good statistics of the 2754 keV and 661.7 keV photopeaks allow for good comparisons between the events above 3 MeV and those below 3 MeV. As shown in Sec. 2.3.3, the system achieves 1.21% FWHM at 661.7 keV. The performance at 2754 keV is measured to be 2.45% FWHM.

To explore the performance of the system above 3 MeV, neutron activation of ^{16}O was used to generate gamma rays at 6.1 MeV. A 14.5 MeV neutron generator was used to activate the ^{16}O in water. The water was then flowed through a hose to an enclosure located next to the system, but on the other side of a large neutron shield from the neutron generator. A picture of the setup is seen in Fig. 4.2. The ^{16}O undergoes an (n,p) reaction to form ^{16}N, which decays with a 7.13 s half-life back to ^{16}O. During 69% of these decays a 6129 keV gamma ray is emitted; a 7115 keV

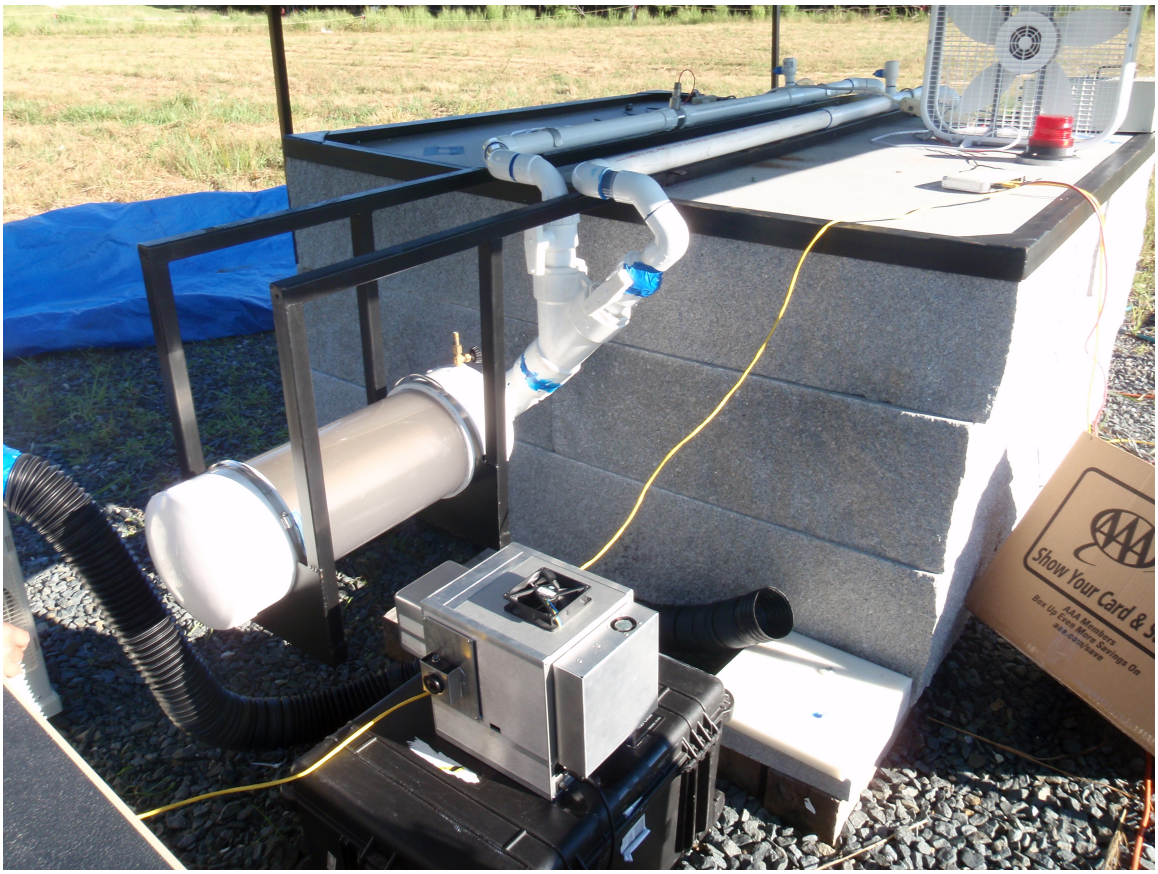

Figure 4.2: Picture of the setup of the ^{16}O activation measurement for the study of system performance above 3 MeV.

gamma ray is emitted with 5% of the decays; various other gamma rays are emitted during less than 1% of the decays. The separation between the neutron generator and the detector system cuts back on the background caused by neutrons in the CdZnTe system and from 2.2 MeV prompt gamma rays from the reaction of a neutron with hydrogen in the water. The activity of the source was degraded due to the short half-life of the activation product; however, the primary goal was to have a clean, low background source, not a high activity source. Ann Parsons and Suzanne Nowicki from NASA Goddard are to thank for providing the facility for neutron activation.

The spectrum resulting from the measurement using the setup shown in Fig. 4.2 and the calibration described in Sec. 2.3.2 with the special considerations described is shown in Fig. 4.3. Focusing on the high energy portion of this spectrum, as shown

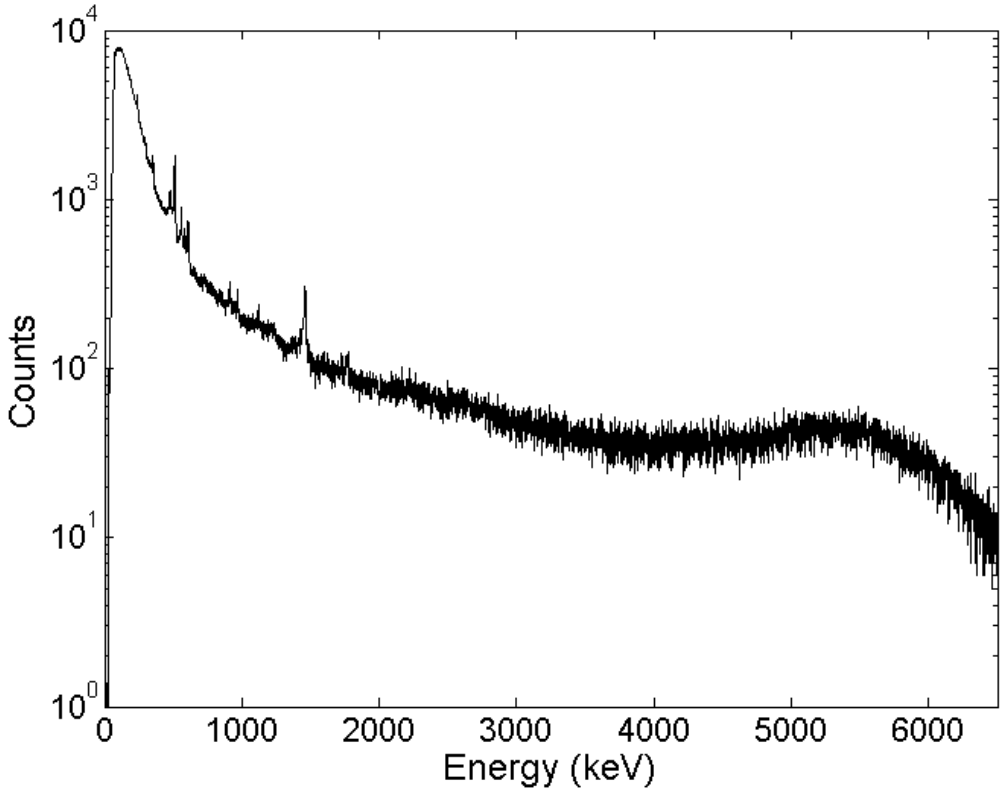

Figure 4.3: Graph of the spectrum collected from the measurement of neutron activated ^{16}O using the CdZnTe array system.

in Fig. 4.4, shows that a broad hump is seen between 5 and 6 MeV. The photopeak at 6.129 MeV is missing, along with the single and double escape peaks from the escape of the 511 keV annihilation gamma ray resuling from pair production. Those peaks should occur at 5.107 and 5.618 MeV, respectively. It appears that the energy reconstruction was failing to account for all factors, leading to the blurring of events from the three expected features into a single, broad hump. The dominant factor is the inclusion of transient signals, which will be discussed in Sec. 4.2.1.

The fraction of events that are rejected due to saturation of either an anode or cathode channel of one of the 18 ASICs are recorded to determine how effectively the energy is collected by multiple electrodes. Of all events, only 3.4% have at least one saturated anode channel, only 1.2% have a saturated cathode channel, and 0.4% have

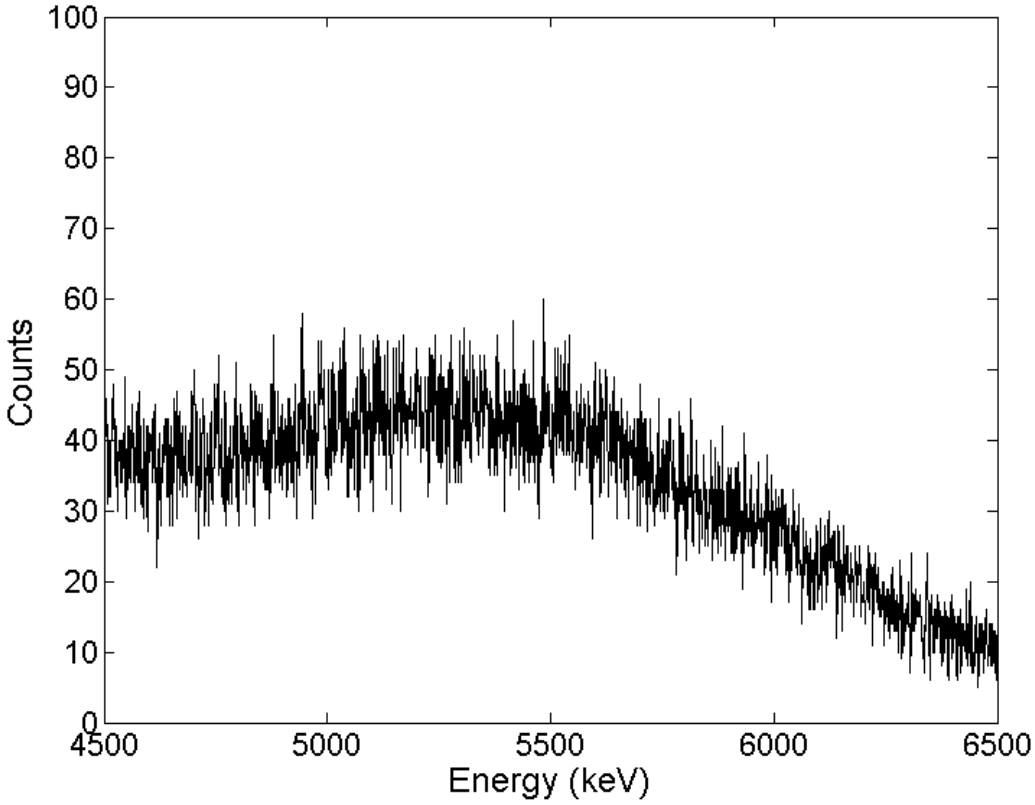

Figure 4.4: Graph of the high-energy portion of the spectrum collected from the measurement of neutron activated ^{16}O using the CdZnTe array system.

both a saturated anode and cathode channel. However, at higher energies, a larger fraction of events need to be rejected due to saturated channels. At 6.1 MeV, 45.1% of events have a saturated anode channel, 20.0% have a saturated cathode channel, and 8.6% have both a saturated anode and cathode channel. Overall, 56.5% of events have to be rejected due to either a saturated anode or cathode channel.

4.2.1 Transient Signal Rejection

While the electrons are drifting through the bulk of the detector, they are inducing charge on all of the anode pixels simultaneously. When the charge then approaches the collecting anode pixel, the signals induced on the neighboring pixels flip sign to account for the charge not being collected on that pixel. This effect is shown in Fig.

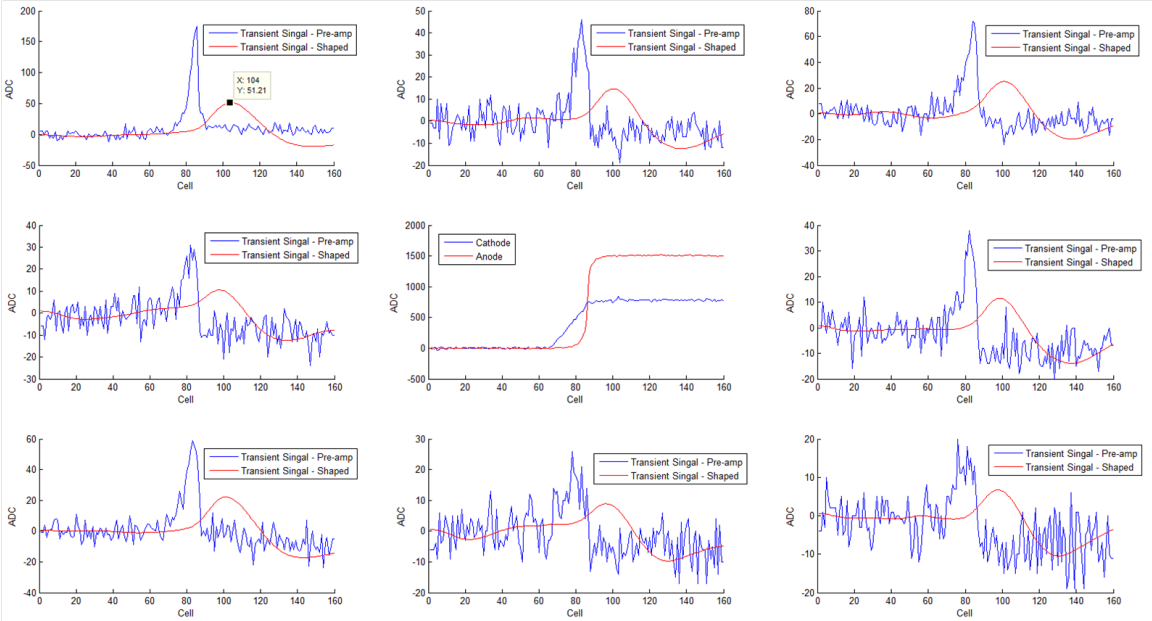

Figure 4.5: Graphs of the induced charge on the collecting anode (center) and the 8 neighboring pixels.

4.5 where the charge was collected in the center pixel, and transient signals are shown for the surrounding 8 pixels [56]. When the ASIC is reading out, any channel that has a signal that crosses the lower energy threshold holds the maximum amplitude to determine the energy collected on that electrode. The transient signals have an ampliduted that is proportional to the energy deposited. For lower-energy events these transient signals are too small to cross the threshold. At higher energies, some events will have transients large enough to trigger the peak hold circuitry, such as the event in the upper left corner of Fig. 4.5. However, this pixel did not actually collect any charge, and therefore will falsely shift the events recorded energy above the actual deposited energy. This effect becomes far more prevelant at higher energies since each interaction will tend to have larger electron clouds, which will induce larger transient signals on neighboring pixels that do not collect any charge.

In the absence of waveforms shown in Fig. 4.5, the ratio between the energies of neighboring pixels can be used to determine if transient signals are present. All neigh-

boring pixel events cannot be neglected since many real events can either have Compton scatters that occur on neighboring pixels or have the interaction occur over the grid, resulting in the electron cloud splitting and being collected by side-neighboring pixels. However these two situations tend to have smaller energy ratios—larger energy to smaller energy—than the ratios observed for transient signals. The inclusion of these signals in each event leads to the degraded performance shown in Fig. 4.3.

To determine the best energy ratio for the rejection of transient signals, several different values were tested. The best value is sufficiently small to catch the highest fraction of transient signal events, but not so large that too many actual charge collection events are thrown out. The spectra for energy ratio values of 5, 10, 15 and 20 are shown in Fig. 4.6. The spectra for the energy ratio of 20 shows broadening of the single escape, double escape and photopeak on the high energy side compared against energy ratios of 10 or 15, indicating that the ratio is too large to catch a sufficient fraction of the transient signals. On the other side, the performance for an energy ratio of 5 shows a broadening of each feature on the lower side, which is indicative of too small of an energy ratio. Performance at energy ratios of 10 and 15 is very similar.

To determine the best energy ratio, lower energy events can be used. If too small an energy ratio is used, the low-energy tail of the 661.7 keV photopeak from ^{137}Cs will become extended. Fig. 4.7 shows this trend. The slightly elongated tail for the photopeak of ^{137}Cs photopeak makes lower energy ratios less ideal. Therefore, an energy ratio of 15 is chosen as the best option since it generates the best performance for transient rejection at high energies with the least degradation of performance at lower energies where it is more likely to reject a real energy deposition than a transient signal.

The full spectrum following the rejection of transient signals for the ^{16}O activation measurement is shown in Fig. 4.8. Improved performance with a clear single escape,

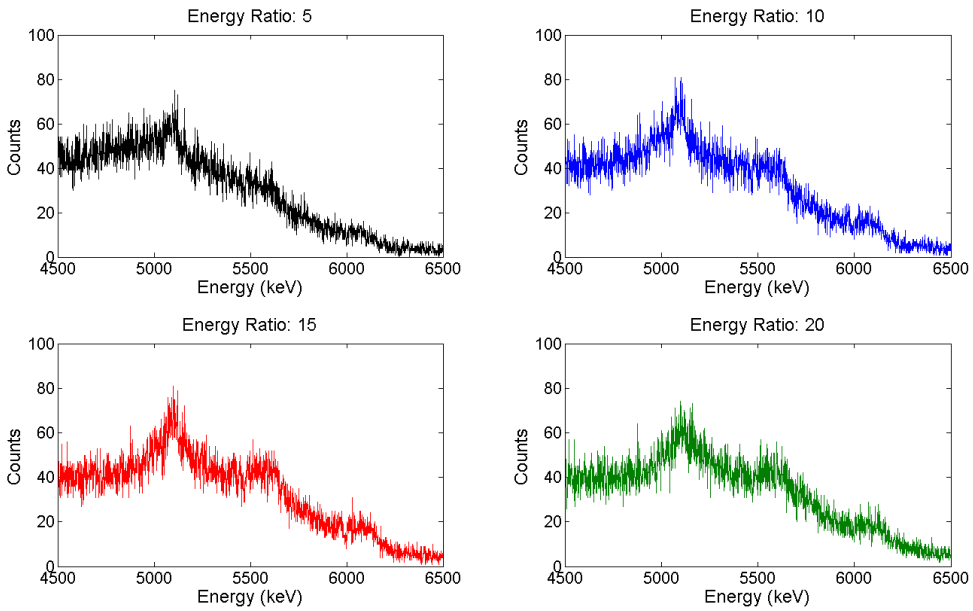

Figure 4.6: Spectra from the measurement of neutron activated ^{16}O using different values for the energy ratio between the neighboring pixels.

double escape and photopeak is displayed. 74% of the full-energy events had at least one signal rejected. This shows that a 18-detector CdZnTe array system with a ASIC that has a dynamic range up to 3 MeV can still be used for measurements above 3 MeV since the charge collection is spread across multiple channels.

4.2.2 Event Breakdown

As exemplified from the respective spectra for ^{137}Cs, ^{24}Na and ^{16}O activation, the spectroscopic performance of the CdZnTe array system degrades at higher energies. Typical systems have lower energy resolutions at higher energies due to improved statistics of charge generation and the smaller impact of electronic noise. Above 3 MeV—and particularly present at 6 MeV—the effects of the transient signals are the leading cause performance degradation. Without the waveform for each pixel, not all transient signals can be rejected, and in the process of trying to reject a majority of them, real energy depositions are also thrown out. However, this is not

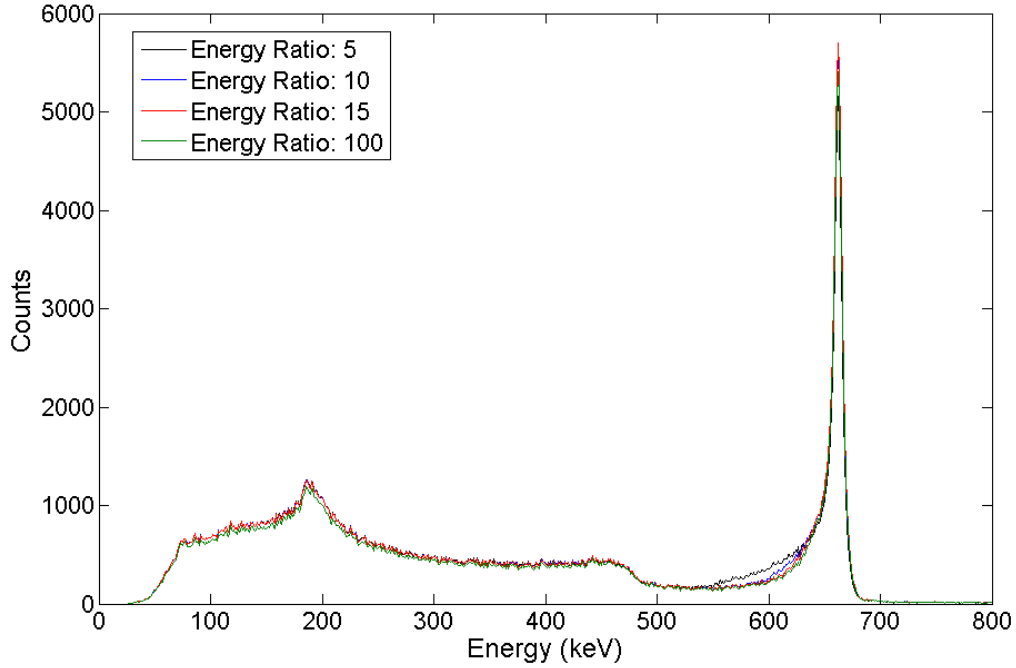

Figure 4.7: Spectra from a ^{137}Cs source showing the effects of the rejection of events based on the energy ratio.

the only contributing factor to the spectroscopic degradation. To better understand the reasons for the degraded spectroscopic performance, events will be broken down into categories that can shed light onto the relevant issues.

The number of pixels involved in the charge collection is closely related to the energy resolution as the quadrature summation of the noise becomes worse with a larger number of pixels involved. As shown in Fig. 4.9, higher energy events tend to have a larger number of pixels triggered. They also have a broader distribution of the number of pixels triggered. However this can only account for a small part of the degradation as the system nominally has about 5 keV electronic noise. This will increase to just over 11 keV of electronic noise for a 5-pixel event, which does not account for the magnitude of degradation present at 2754 keV.

The number of triggered pixels is a misleading parameter in terms of understanding the events occuring in the system from a single incident gamma ray at high

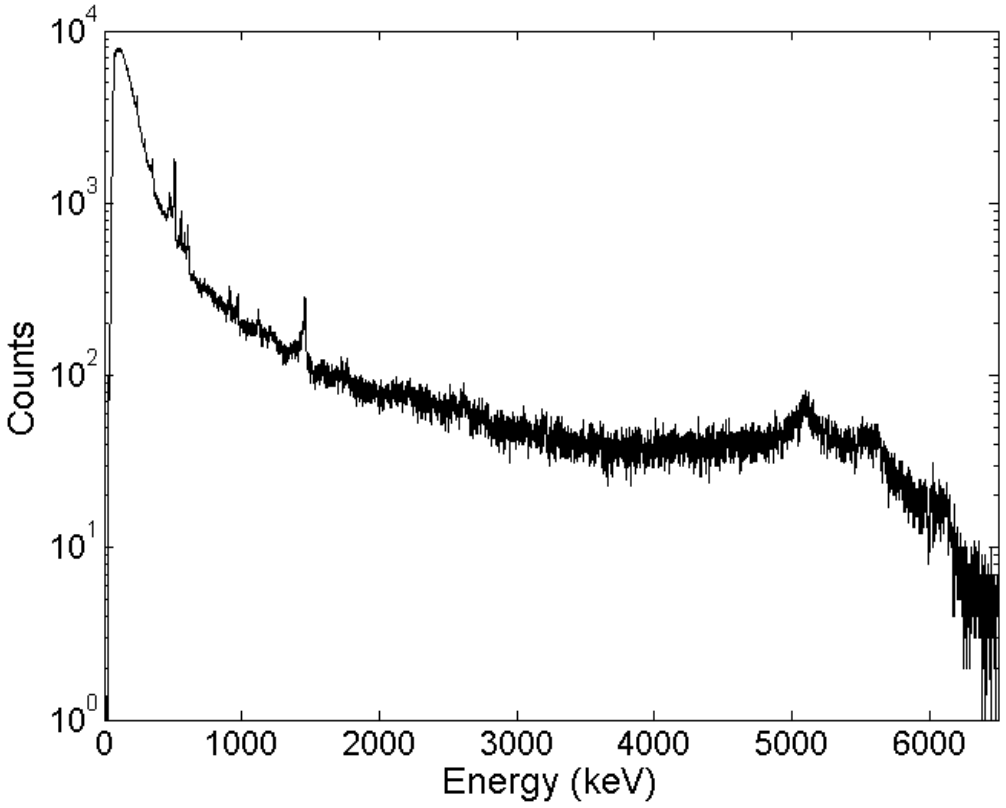

Figure 4.8: Spectra of the measurement of neutron activated ^{16}O using an energy ratio of 15 for transient signal rejection.

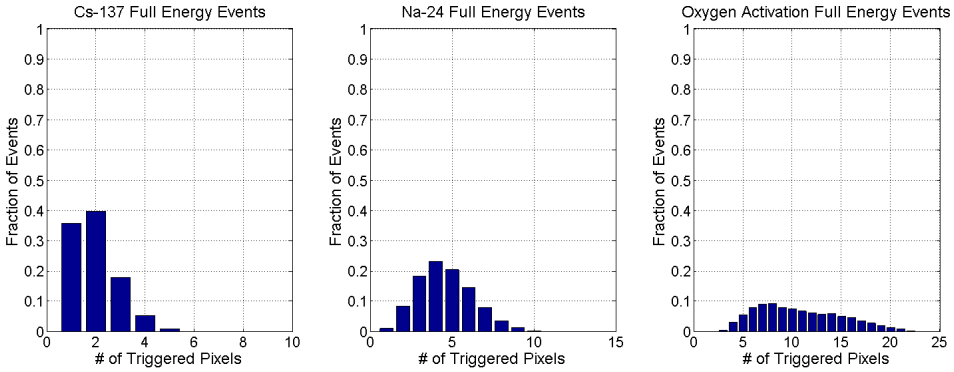

Figure 4.9: Breakdown of the number of triggered pixels for full-energy events from ^{137}Cs, ^{24}Na and ^{16}O activation.

energies. The large electron clouds result in charge sharing and transient signals, which make the number of triggered pixels significantly larger than the number of interactions. Assuming that all neighboring triggered pixels are either charge sharing

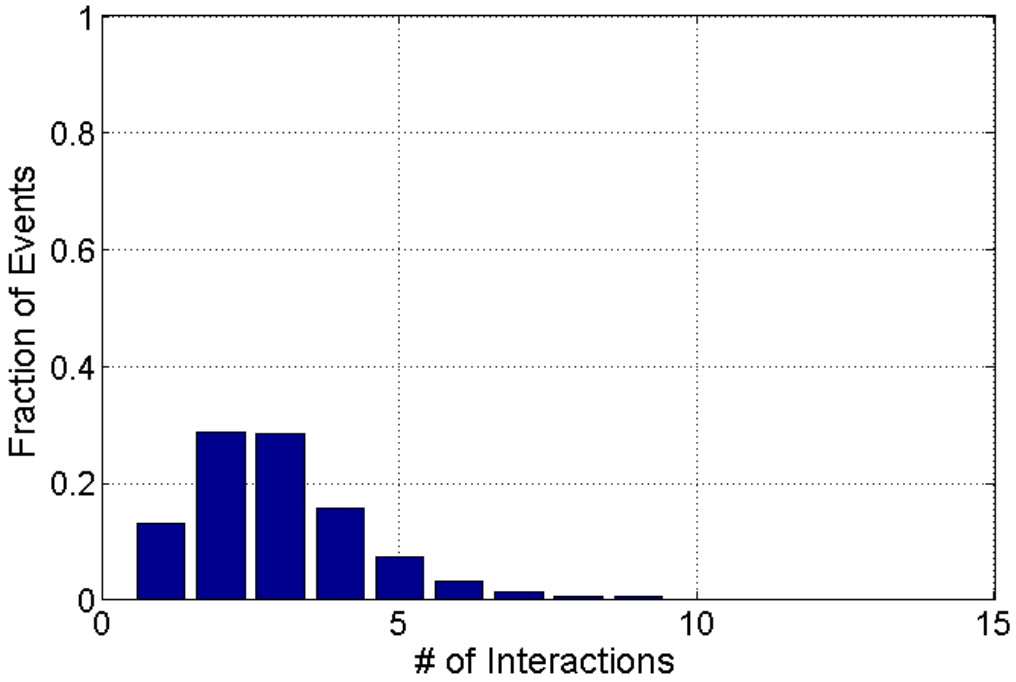

Figure 4.10: Breakdown of the number of interactions for full-energy events from ^{16}O activation.

or a transient signal, then the number of interactions can be deduced. The resulting distribution for full-energy events from the ^{16}O activation measurement is shown in Fig. 4.10. This is a flawed assumption since it is possible for multiple Compton scatters to occur over neighboring pixels. A large fraction of these full-energy depositions are also due to pair production, and the annihilation photons can interact over neighboring pixels as well. Nonetheless, in the absence of the waveforms which have been shown to provide event classification capabilities, this is a simple way to show that distribution of number of triggered pixels at 6 MeV is misleading. The number of interactions will not have a direct effect on the energy resolution, as that is tied to the summation of the noise from all of the triggered pixels, but it is an important consideration for imaging applications.

At higher energies, it is more probable to have an event interact with more than one detector. The interactions can also take place in detectors in each plane of the

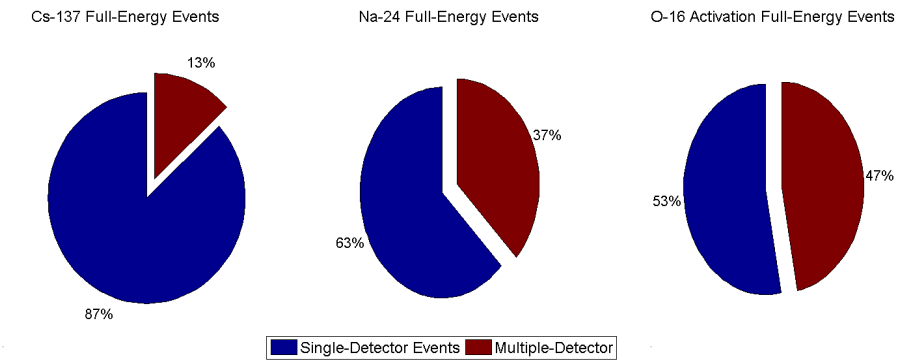

Figure 4.11: Breakdown of the fraction of interdetector events for full-energy events from ^{137}Cs, ^{24}Na and ^{16}O activation.

system. The fraction of interdetector and interplane events at different energies are shown in Fig. 4.11 and 4.12, respectively. As expected, the percentage of interdetector events significantly increases from 662 keV to 2.75 MeV and 6.13 MeV. The same is true for the interplane events with the exception that an increase in interplane event percentage does not take place between 2.75 and 6.13 MeV. This is attributed to the increased probability of pair production compared with Compton scattering, as the probability of a 511 keV gamma ray being incident on and reaching the second plane is smaller than the probability that a higher energy scattered gamma ray will reach the second plane.

A greater number of interdetector events will cause a slight degradation due to the misalignment of the energies recorded between different detectors. From the calibration results at 661.7 keV, the overall performance for single-pixel events in all detectors combined was 0.96 % FWHM. However, the performance of each detector individually was significantly better than the results for all detectors combined, as shown in Fig. 4.13. This misalignment is introduced by the energy non-linearity correction to improve the system's performance across all energies. This correction improves performance, but has limitations to the amount of improvement achievable. The energy non-linearity correction is studied in greater deal in Chapter V through

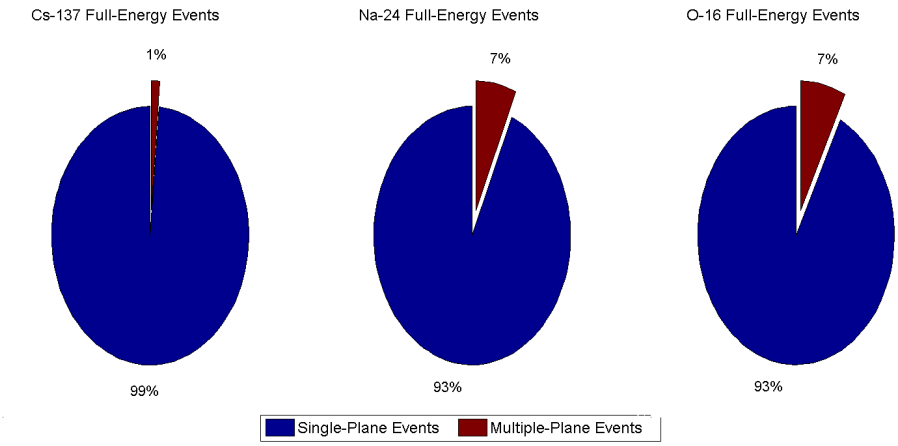

Figure 4.12: Breakdown of the fraction of interplane events for full-energy events from ^{137}Cs, ^{24}Na and ^{16}O activation.

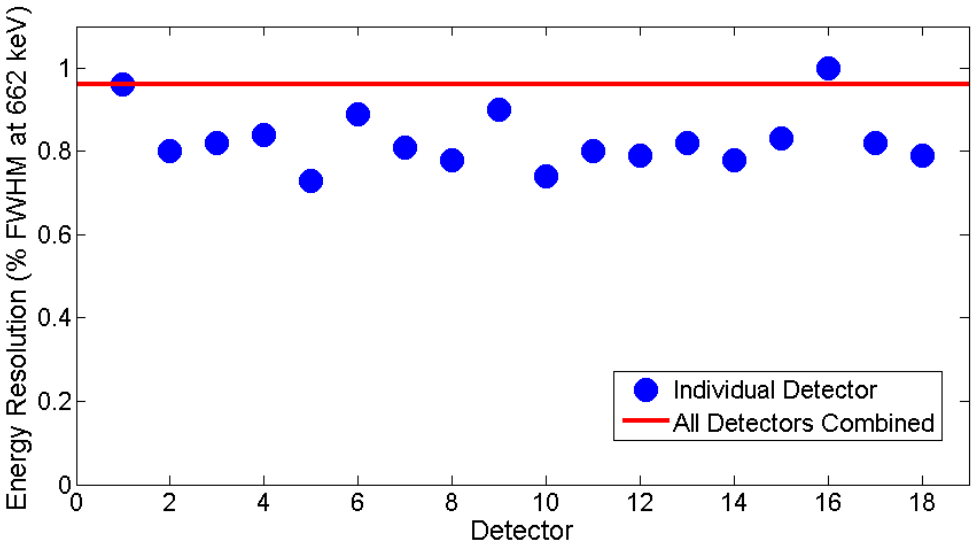

Figure 4.13: Comparison between the energy resolution at 662 keV of each detector in the 18-detector CdZnTe array system and for all detectors combined.

coincidence measurements between a single CdZnTe detector and an HPGe detector.

4.3 High Energy Measurement Conclusions

Overall, the 18-detector CdZnTe array system was shown to be able to operate at energies up to 6.13 MeV. The spectroscopic performance of the system above 3 MeV

was degraded due partly to an increased number of pixels collecting the energy but mostly due to the presence of transient signals which cannot be uniformly rejected without also rejecting some portion of real energy depositions. An energy ratio of 15 for neighboring pixel energy depositions was found to be optimal for achieving decent spectroscopic performance across all energies.

CHAPTER V

Coincidence Experiment

Two parameters of CdZnTe detectors that are of particular interest to understanding the spectroscopic performance are the energy resolution and the energy offset. Identification and characterization of radioactive sources requires knowing the energy deposited and the energy resolution determines the ability to distinguish between sources close in energy. These parameters are studied as a function of the energy deposited through coincidence measurements between a CdZnTe detector and a HPGe detector.

The exceptional energy resolution and linearity of the HPGe detector provides a known energy. Combined with the known energy of the source, the expected energy for each interaction in the CdZnTe is determined. Comparison against the measured energy in the CdZnTe detector gives a quantification of the energy resolution and energy offset as a function of the energy deposited. Ideally, this quantification would be completed as a function of position in the device to study CdZnTe detector efficiency; however, the data acquisition did not allow for the magnitude of data required for that analysis to be taken in a timely fashion.

The coincidence measurements were inspired by coincidence experiments to study NaI detectors conducted by John Valentine in the 1990's [57]. Coincidence experiments to study CdZnTe pulse heigh linearity have been conducted at Kansas State

University for Frisch collar detectors [58]. Another experiment studied the linearity and energy resolution of a 5mm-thick CdZnTe detector with an 4×4 anode pixel array [59]. The experiment and results presented in the following sections differs from these previous experiments for several key reasons. The 20×20×15 mm^3 CdZnTe detectors will change the characteristics of the measurement, particularly when analyzing events interacting in multiple pixels. More importantly, the energy resolution and linearity of a detector are extremely dependent on the read-out electronics. Therefore, the analysis conducted below would be different even if conducted using the same crystal but with a different ASIC type.

5.1 Experimental Setup

To get reliable results for the energy resolution and linearity of CdZnTe, a single, high-quality detector was chosen. This detector, labeled 4R-107, was placed in a test box just as described in Section 3.1.1. The same calibration procedures as described in Section 2.3.2, with the modification that there is only a single detector in the system. The non-linearity calibration did not use a ^{24}Na source. The coincidence measurements are based on ^{137}Cs, and therefore do not require non-linearity to extend up to 2754 keV. The calibration spetrum for the detector, shown in Fig. 5.1, shows the excellent spectroscopic performance. This excellent performance, combined with the excellent unifromity that is exemplified by the resolution pixel map in Fig. 5.2, were the basis for the selection of this detector for the coincidence experiments.

An electrically-cooled, coaxial HPGe detector from ORTEC was used as the second detector. The detector was connected to a GaGe card for the data acquisition. The GaGe card performs digital acquisition of the waveforms from the HPGe detector. A sample rate of 10 MS/s was used and events with 512 samples recorded both before and after the system trigger. A dynamic range of ±200 mV was set. Trapezoidal shaping with a 12.5 μs shaping time and an 800 ns flattop was performed for amplitude

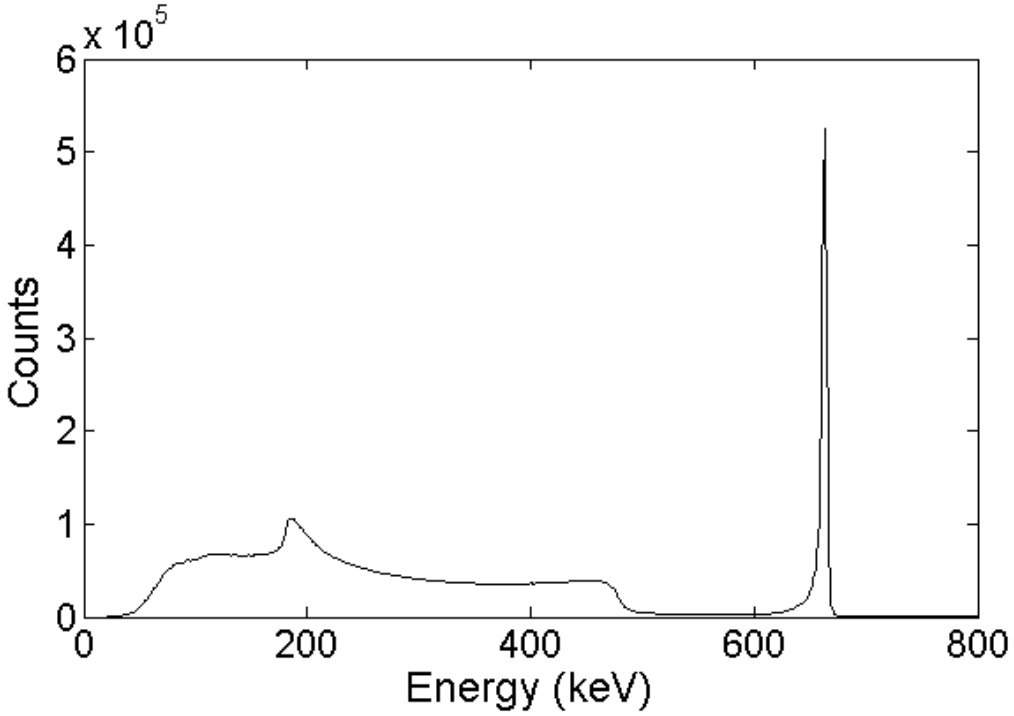

Figure 5.1: Spectrum of single-pixel events from the calibration of CdZnTe detector 4R-107 for the coincidence experiments. The detector achieved 0.76% FWHM at 662 keV for single-pixel events.

determination. With these settings, a maximum count rate of approximately 150 counts per second is achievable via the GaGe card. A ^{137}Cs spectrum from the HPGe detector showing an energy resolution of 0.30% FWHM at 662 keV is displayed in Fig. 5.3. A non-linearity energy correction was obtained through a single measurement using the following sources: ^{133}Ba, ^{57}Co, ^{137}Cs, and ^{22}Na. The resulting spectrum is shown in Fig. 5.4. Midway through the coincidence experiments, the GaGe card was replaced with a second GaGe card due to the experimental requirements of other researchers. A similar calibration was performed on this second card. The lineary energy calibration equation is shown for in Equation 5.1.

$$E = (A \times S) - O \tag{5.1}$$

where E is the energy recorded in the HPGe detector in keV, S is the signal amplitude,

1.05	0.99	0.81	1.03	1.23	1.04	0.86	0.76	0.75	0.76	0.77
0.93	0.92	0.85	0.81	0.79	0.76	0.76	0.76	0.73	0.76	0.73
0.93	0.86	0.80	0.82	0.80	0.75	0.75	0.72	0.70	0.77	0.74
0.83	0.80	0.81	0.73	0.79	0.74	0.77	0.73	0.74	0.71	0.79
0.82	0.74	0.79	0.72	0.72	0.73	0.72	0.71	0.74	0.70	0.75
0.76	0.73	0.70	0.73	0.69	0.74	0.76	0.73	0.76	0.72	0.70
0.77	0.88	0.80	0.72	0.68	0.71	0.85	0.70	0.78	0.76	0.73
0.78	0.67	0.81	0.77	0.70	0.69	0.75	0.69	0.68	0.68	0.79
0.80	0.75	0.71	0.76	0.68	0.66	0.72	0.71	0.71	0.73	0.74
0.82	0.72	0.74	0.73	0.71	0.69	0.69	0.76	0.76	0.70	0.74
0.92	0.74	0.73	0.73	0.76	0.74	0.78	0.74	0.68	0.71	0.74

Figure 5.2: Energy resolution pixel map for CdZnTe detector 4R-107. The units are % FWHM at 662 keV for single-pixel events.

A is the gain factor of the HPGe detector and equal to 0.0256 keV/ADC unit, and O is the energy offset of the GaGe card. The first GaGe card had an offset of 10.302 keV; the second GaGe card had an offset of 0.2455 keV.

The coincidence setup between the CdZnTe detetor and HPGe detector is shown in the diagram in Fig. 5.5. A 662 keV gamma ray from a ^{137}Cs source will scatter in the CdZnTe detector, then deposit its remaining energy in the HPGe detector. As shown in the block diagram in Fig. 5.6, a trigger signal is sent to the HPGe detector from the CdZnTe detector. No signal is sent back to the CdZnTe detector from the HPGe detector. The trigger sent from the CdZnTe detector is in the form of 16-bit binary event number, which begins at 1 for the first event in the CdZnTe detector. All events from the CdZnTe detector, even those not resulting in a coincident interaction in the HPGe system, are recorded and saved for post-processing. In the HPGe detector,

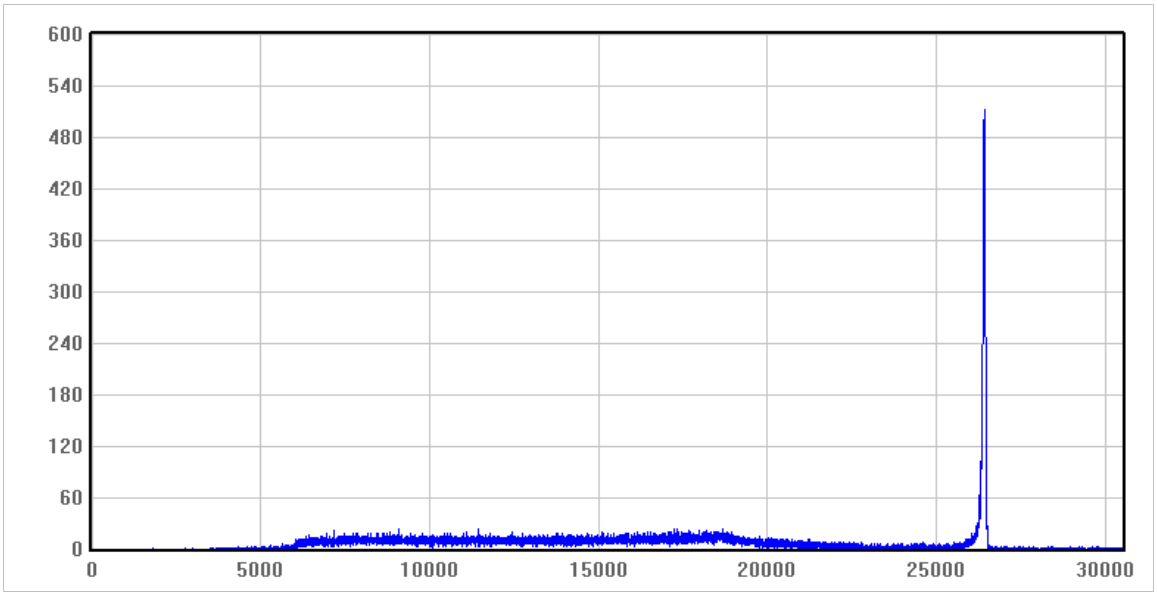

Figure 5.3: ^{137}Cs spectrum from the HPGe detector showing 0.30% FWHM at 662 keV.

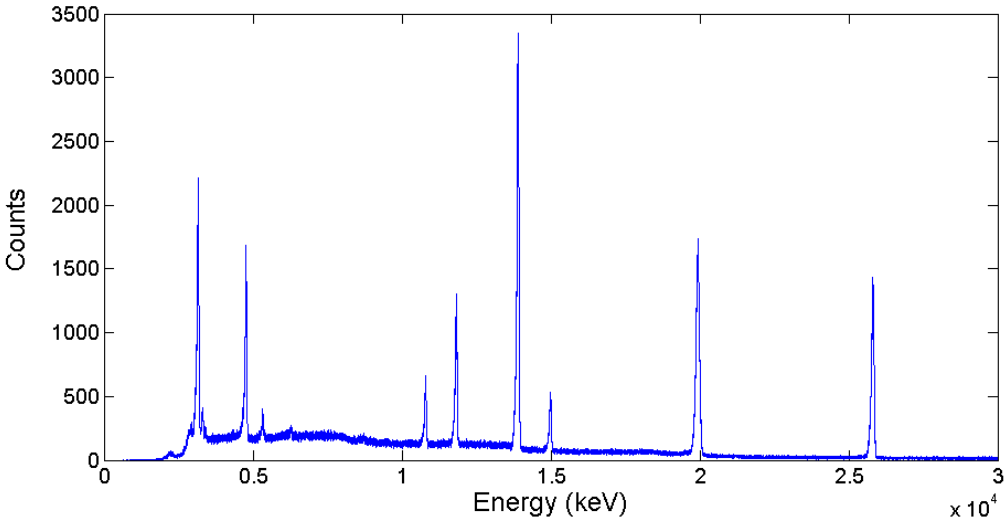

Figure 5.4: Spectrum using ^{133}Ba, ^{57}Co, ^{137}Cs, and ^{22}Na sources for the energy calibration of the HPGe detector.

only events with a coincident trigger from the HPGe detector and CdZnTe detector are saved for post-processing. For each HPGe event, both the energy and CdZnTe event number are recorded. The lining up of the coincident events in the two systems is completed in software during post-processing by matching events with identical

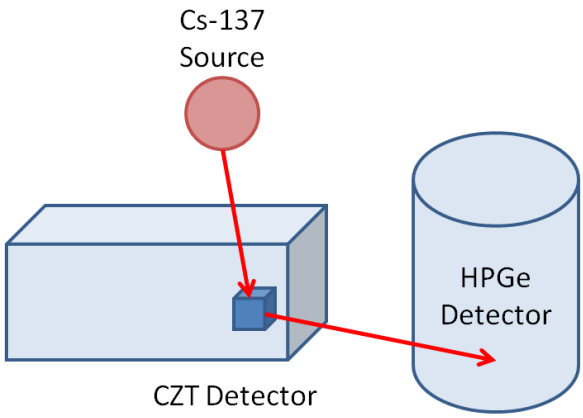

Figure 5.5: Diagram of the setup of the ^{137}Cs source and the two detectors.

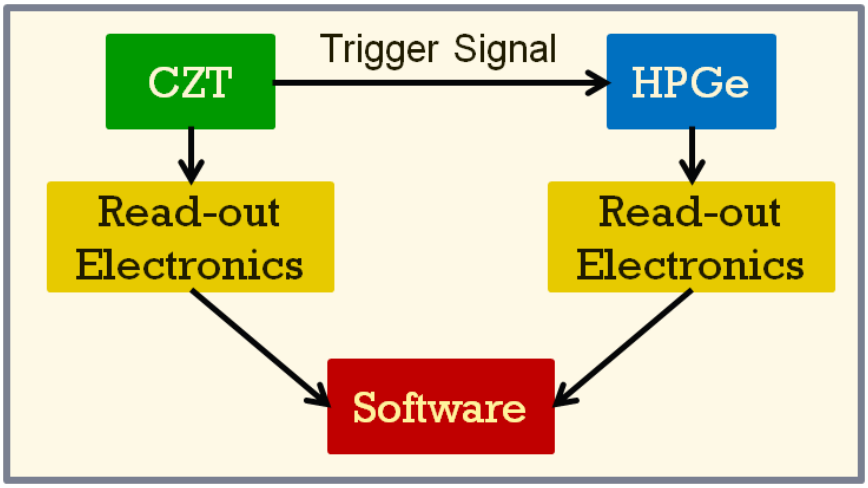

Figure 5.6: Block diagram of the setup of the coincidence between the CdZnTe and HPGe detector systems.

event numbers.

To reduce the background of counts that are not caused by the ^{137}Cs gamma rays scattering between the two detectors, the HPGe detector was surrounded by lead blocks. A picture of the setup of the two systems is shown in Fig. 5.7. The background count rate in the HPGe deteector was reduced to approximately 6 counts per second. With a 30 μCi ^{137}Cs source placed near the CdZnTe detector in a geometry such that the source was shielded from the HPGe detector, a count rate of 15-20 counts per second was achievable, indicating that a coincidence count rate of approx-

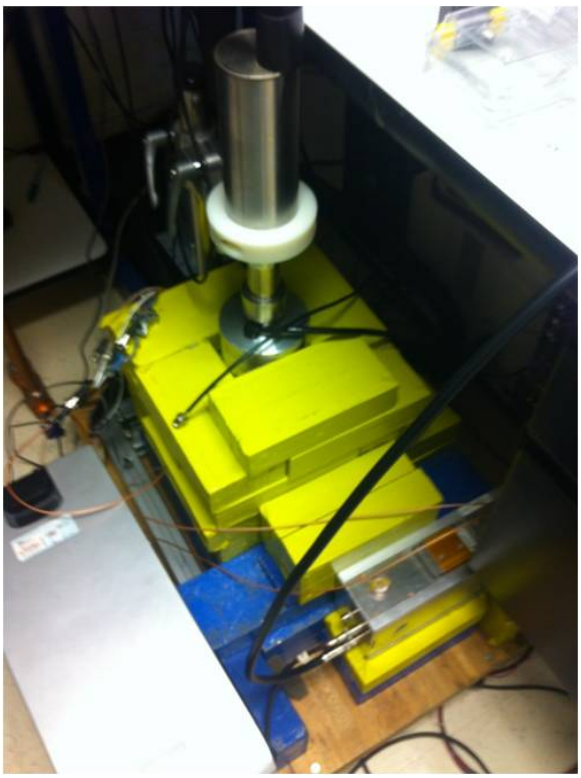

Figure 5.7: Picture of the setup of the coincidence experiments between the CdZnTe and HPGe detector systems.

imately 10 counts per second was accomplished. With this count rate, enough data to characterize the energy resolution and energy linearity of the CdZnTe detector could be acquired in 1-2 months.

To study the efficiency of the CdZnTe detector as a function of position and energy, the same number of events required for the energy resolution and linearity analysis of the entire detector would need to be collected in each of the 4,840 voxels. This would require increase the data collection time by a factor of over 1000. Even with a higher activity source that allowed for the coincidence system to operate at the maximum allowed count rate for the GaGe card, the data acquisition time is too long to pursue without the guarantee of the experiment producing any meaningful results for the efficiency of CdZnTe detectors as a function of energy and position in the device. The efficiency of the CdZnTe detectors were therefore studied using different

techniques that will be described in Chapter VI.

5.2 Coincidence Confirmation

The first step in completing the coincidence experiments is to confirm the operation of the setup. A ^{22}Na source that emits two coincident 511 keV annihilation gamma rays in opposite directions was placed directly between the two detectors. After post-processing of the results, the coincidence energy spectrum shown in Fig. 5.8 was generated. The spectrum from each detector has a photopeak at 511 keV and a Compton continuum at lower energies. The combined spectrum has a peak at 1022 keV for the events depositing their full energies in each detector. A continuum is also present due to incomplete charge deposition in either system. The energy correlation plot in Fig. 5.9 shows that most of the events lie along the photopeak portion of either the CdZnTe detector or HPGe detector, with the hottest spot corresponding to a photopeak 511 keV event in each detector.

Next, coincidence was confirmed for a ^{137}Cs source located close to the CdZnTe detector but shielded from the HPGe detector. The setup for this measurement is shown in Fig. 5.10. A diagram, in Fig. 5.11, for the source positioning relative to the CdZnTe crystal shows that the source is irradiating the detector mostly from the anode surface. The anode surface of the CdZnTe detector is facing the HPGe detector. Therefore, it would be expected that most of the events for this geometric setup would consist of backscattered gamma rays with energy depositions approaching the backscatter energy of 486 keV in CdZnTe detector. The coincidence energy spectrum in Fig. 5.12 for only events in the range near 662 keV deposited between the two systems shows the expected relationship between the energy in each system. The energy correlation plot shown in Fig. 5.13 also shows that the energy deposited in the CdZnTe detector is typically close to the backscatter energy. To help confirm that the correct geometry is applied in the data processing, the number of coincidence

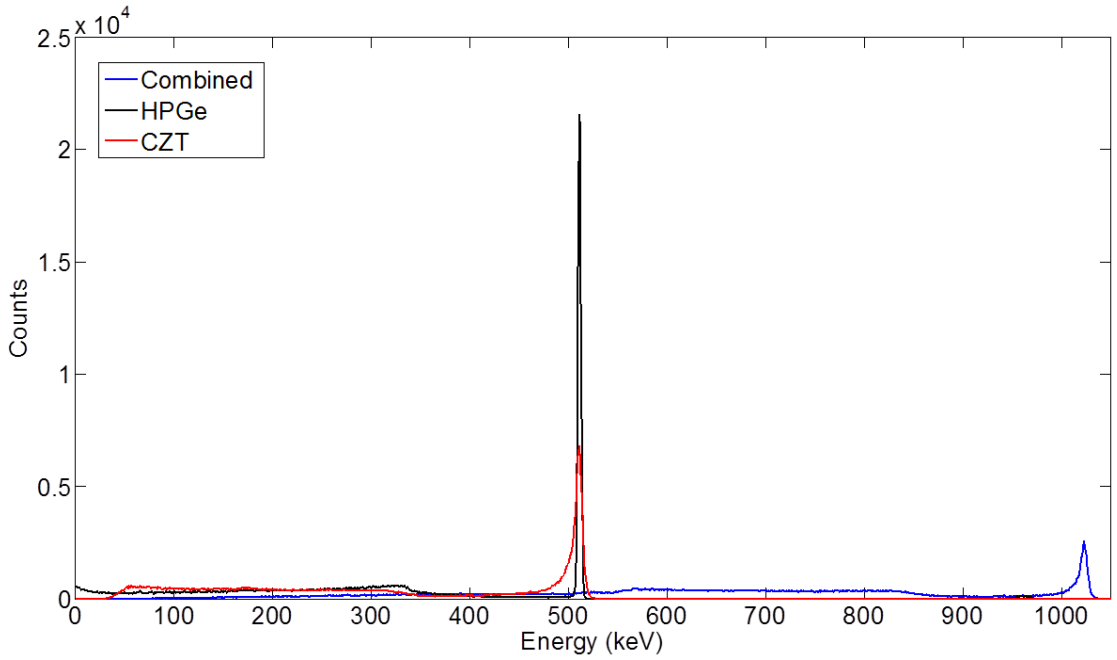

Figure 5.8: Coincidence spectrum obtained using a ^{22}Na source located on the axis between the CdZnTe and HPGe detectors.

events recorded in each pixel as a function of depth of interaction is plotted in Fig. 5.14. Since the source is located on the anode side of the detector, it was expected that the depths nearest the anode have a larger number of recorded counts. It was also expected that there would be more counts along the left side of the detector and towards the bottom, as the source was also slightly below and to the left of the detector as shown in the diagram in Fig. 5.11.

With coincidence confirmed between the CdZnTe and HPGe detector systems, the measurements to study the energy resolution and energy linearity in the CdZnTe detector could be performed.

5.3 Results

A single measurements, such as that used to confirm the coincidence between the CdZnTe and HPGe detectors using ^{137}Cs, cannot investigate the full range of

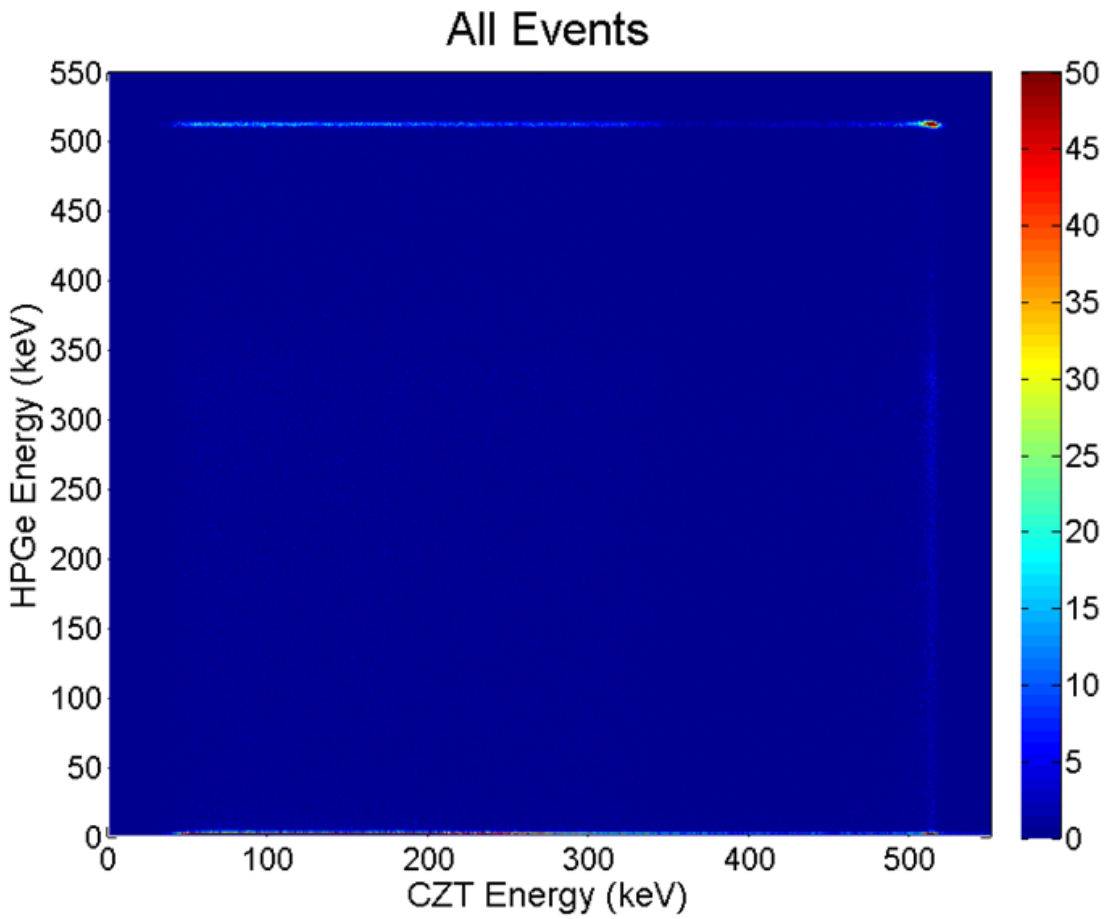

Figure 5.9: Energy correlation plot for coincidence measurements of a ^{22}Na source.

possible energies. Multiple measurements need to be used to cover all possible energy depositions by varying the source location and therefore varying the scattering angles. The diagram in Fig. 5.15 shows that the ^{137}Cs was placed along an arc either above or in front of the CdZnTe system. The arc above the system allowed for closer placement of the source to the detector, however provided less shielding between the source and HPGe detector. Therefore, the positions along both arcs were used to optimize the source to background ratio. A total of 11 measurements were used to sample the entire energy range.

The coincidence energy spectrum for photopeak events for all measurements combined is shown in Fig. 5.16. Enough counts were collected to study the energy resolution and linearity as a function of energy from the backscatter energy of 486

Figure 5.10: Picture of the setup used for measurements of ^{137}Cs gamma rays that are backscattered in the CdZnTe detector and absorbed in the HPGe detector.

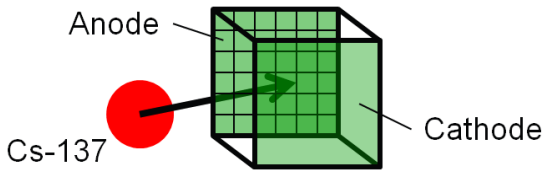

Figure 5.11: Diagram of the position of the ^{137}Cs source relative to the CdZnTe detector for the backscatter measurement used to confirm coincidence between the CdZnTe and HPGe detectors.

keV down to the lower level threshold of the CdZnTe detector. The energy correlation plot between the two detectors is shown for singple-pixel CdZnTe events, two-pixel CdZnTe events and all events in Fig. 5.17, 5.18, and 5.19, respectively.

From the energy correlation plots, there are two apparent peaks. One peak falls along the line that represents a full energy deposition between the two detectors combined. The other peak represents a full energy deposition in the CdZnTe detector along with a background event in the HPGe. It can also be seen that there are full energy depositions in the HPGe detector as well, indicating that the shielding

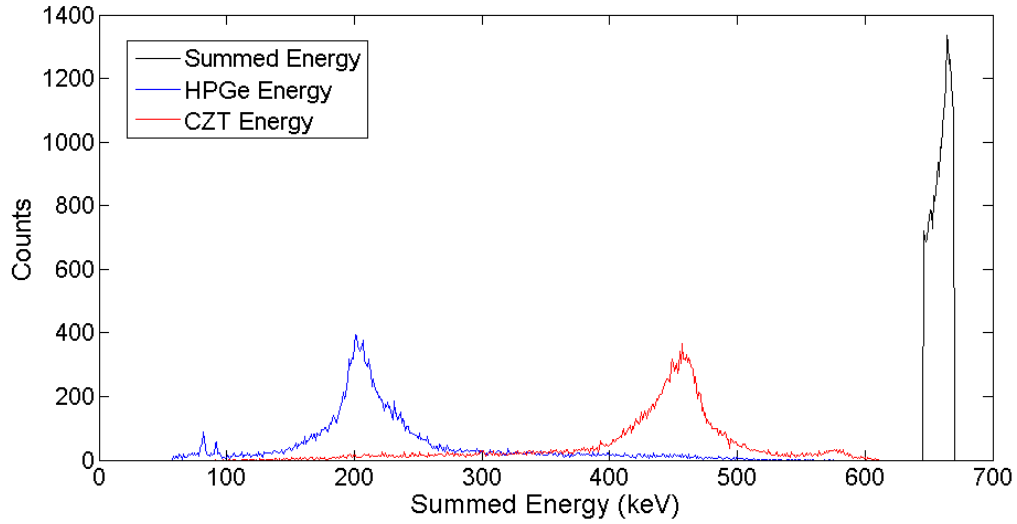

Figure 5.12: Coincidence spectrum for full-energy events obtained using a ^{137}Cs source to create backscattered gamma rays in the CdZnTe detector.

was insufficient to block all of the ^{137}Cs gamma rays. However these events that do not correspond to a scattered coincidence measurement between the two systems are removed and their impact on the overall analysis is minimal.

An energy correlation plot was also generated for each pixel in the detector to show the uniformity of the coincidence measurements. Shown in Fig. 5.20, the results indicate the low statistics achievable on a pixel-by-pixel basis for these coincidence measurements.

The energy resolution and energy linearity are first characterized for single-pixel interactions in the CdZnTe as a function of energy. These results are then compared to the two-pixel coincidence results to better understand the multiple pixel performance.

5.3.1 Energy Resolution vs. Energy

To calculate the energy resolution in the CdZnTe detector as a function of the deposited energy, the data is first split into energy slices corresponding to events with the same deposited energy. This is completed by creating a spectrum of all events with the same energy recorded in the HPGe detector from the data shown in

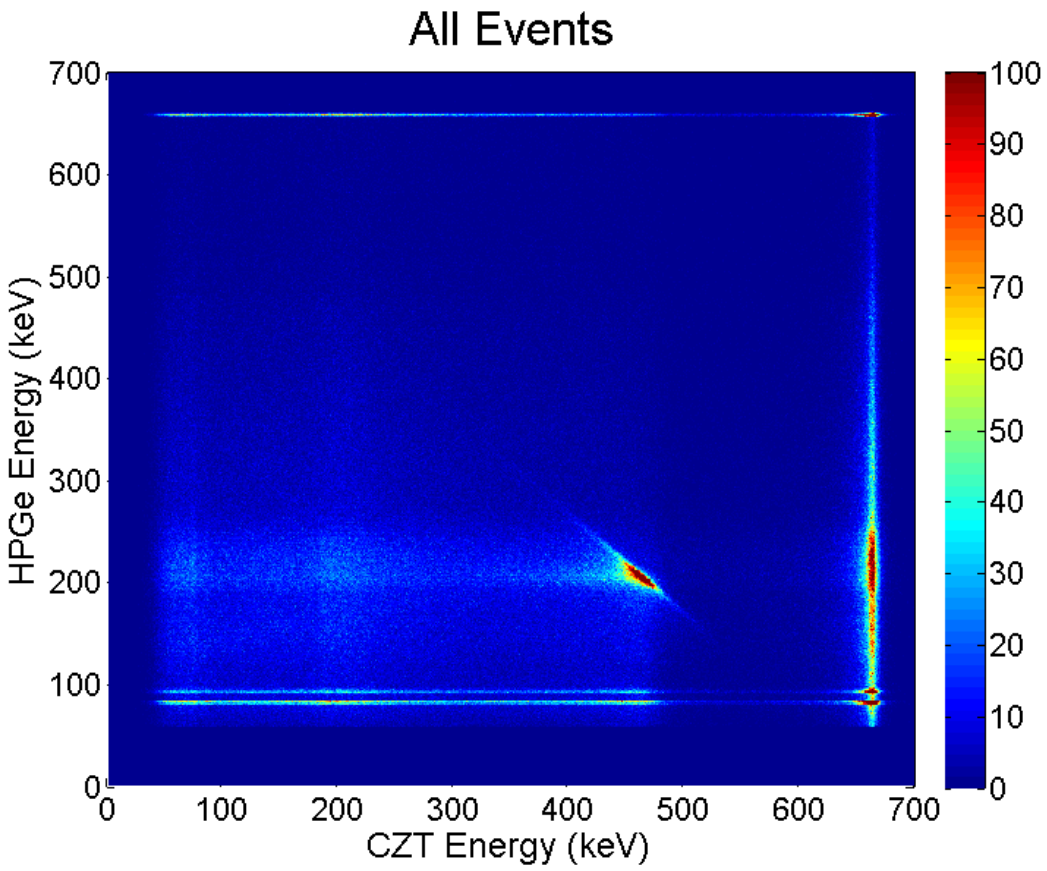

Figure 5.13: Energy correlation plot for backscattered coincidence measurements of a ^{137}Cs source.

Fig. 5.17. An example of an energy slice for events with 300 keV deposited in the HPGe detector is shown in Fig. 5.21. The full energy deposition is determined from Equation 5.2, and the FWHM for that energy can be described by Equation 5.3.

$$E_{HPGe+CZT} = E_{HPGe} + E_{CZT} \tag{5.2}$$

$$FWHM^2_{HPGe+CZT}(E_{HPGe+CZT}) = FWHM^2_{HPGe}(E_{HPGe}) + FWHM^2_{CZT}(E_{HPGe+CZT} - E_{HPGe}) \tag{5.3}$$

The energy resolution calculated for the example slice in Fig. 5.21 determines

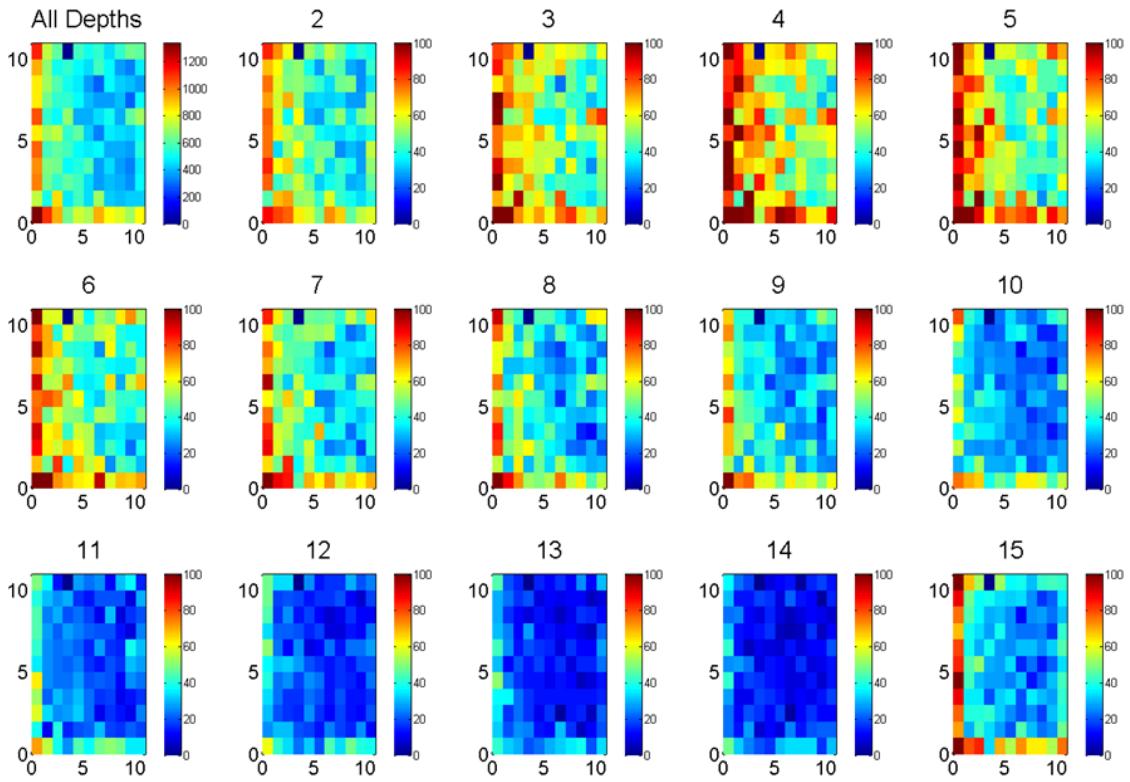

Figure 5.14: Plot of the number of coincidence events in each pixel of the CdZnTe detector as a function of depth of interaction. Only single-pixel events in the CdZnTe detector were used. The plot in the upper left corner is for all depths combined, each other plot is for a 1-mm slice as labeled above each plot.

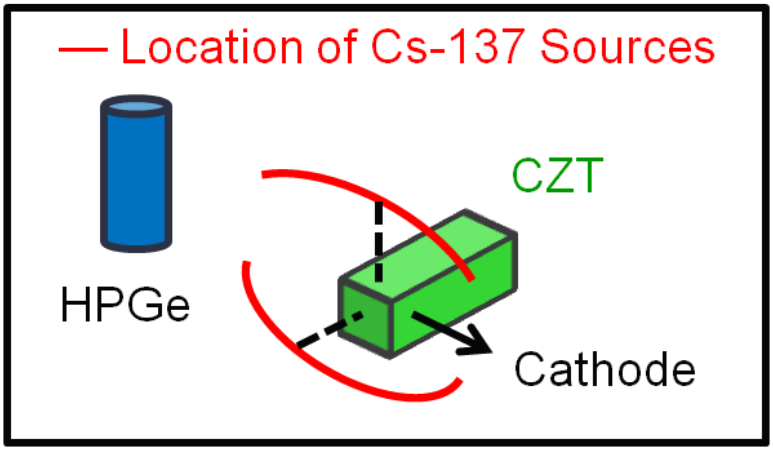

Figure 5.15: Diagram showing the placement locations of the ^{137}Cs sources for the coincidence measurements.

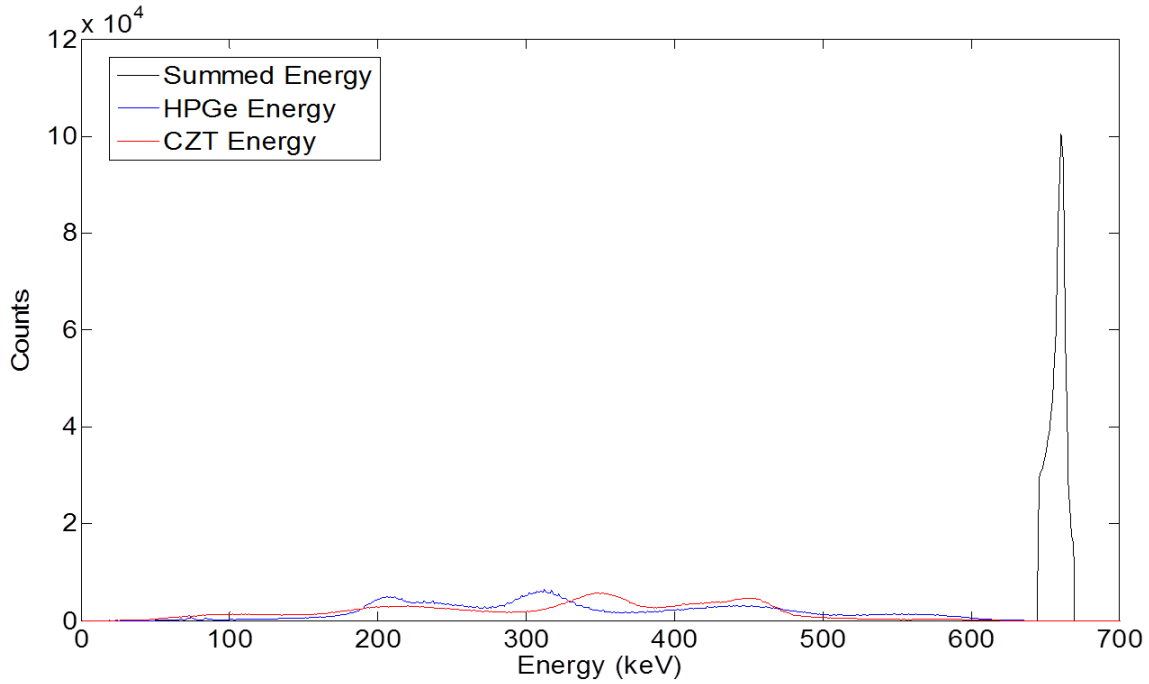

Figure 5.16: Coincidence energy spectrum for photopeak events between the CdZnTe and HPGe detector systems for all coincidence measurements.

$FWHM_{HPGe+CZT}$. $FWHM^2_{HPGe}$ is found from a fit of the energy resolution of each of the photopeaks from the HPGe energy calibration in Fig. 5.4. Equation 5.4 for the energy resolution of the HPGe detector as a function of the energy deposited has a 0.98 correlation coefficienct based on the data from the HPGe energy calibration. Therefore, $FWHM_{CZT}$ can be calculated as a function of the energy deposited in the CdZnTe.

$$R_{HPGe} = \frac{1.5876}{E_{HPGe}} \tag{5.4}$$

Since each slice lays on top of a background, a background subtraction is performed for each slice prior to calculating $FWHM_{HPGe+CZT}$. The background above the full-energy peak is caused by photopeak events in the CdZnTe detector coincident with background events in the HPGe detector, and should be relatively constant in this region. The background below the full-energy peak is caused by Compton scatter

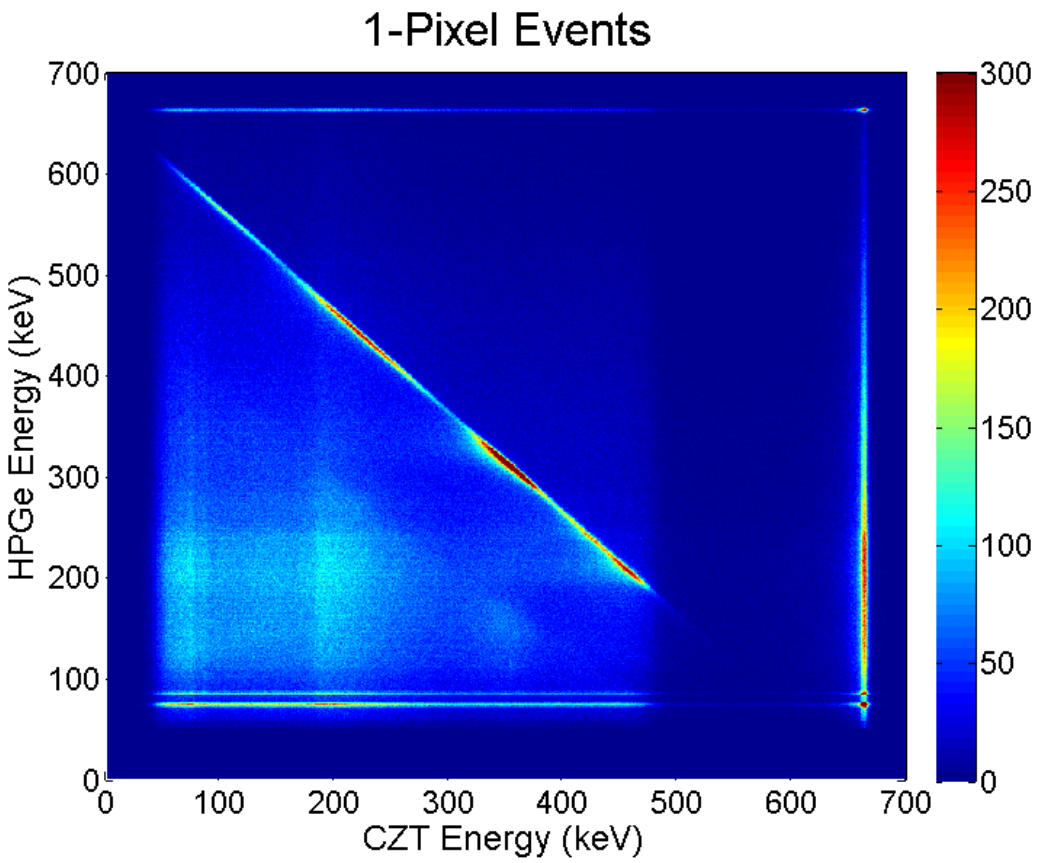

Figure 5.17: Energy correlation plot for single-pixel events in the CdZnTe detector.

events in the HPGe detector—events that would fall in a higher energy bin for the HPGe energy if photoelectric absorption occurred, but instead is mis-classified due to the partial energy collection in the HPGe detector. This background region is also relatively constant. Therefore a step background model, as shown in Fig. 5.22, can be used for the background subtraction. This subtraction eliminates extra noise in the calculation of the energy resolution of the CdZnTe detector.

The calculated energy resolution of the CdZnTe detector as a function of energy deposited is shown in Fig. 5.23. The coincidence data corresponds well to values for the energy resolution in the CdZnTe detector for discrete energies from the sources used during the energy calibration. The total FWHM in the detector can be described as the quadrature summation of the FWHM due to charge generation and other factors, as displayed in Equation 5.5. The most dominant of the other factors described

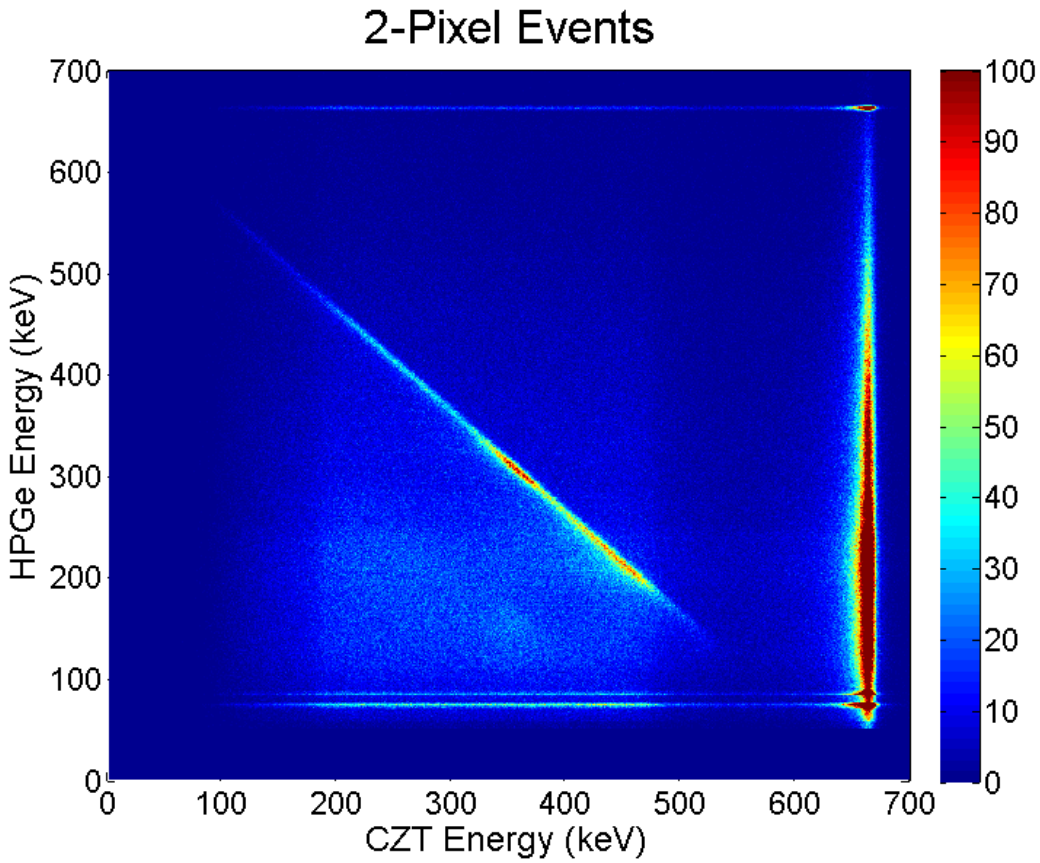

Figure 5.18: Energy correlation plot for two-pixel events in the CdZnTe detector.

in Equation 5.6 is the electronic noise, but there are other minor factors including the energy misalignment between pixels. The major trend between these other factors are that they are energy independent, which allows them to be combined into a single term. Solving for the energy resolution as a function of energy gives Equation 5.7, which was used to fit the coincidence data for the energy resolution as a function of deposited energy. Nearly all of the data falls within the $\pm\sigma$ error bars. This fit provides values for $FWHM_{Other}$ and F.

$$FWHM^2_{Total}(E) = FWHM^2_{ChargeGeneration}(E) + FWHM^2_{Other} \tag{5.5}$$

$$FWHM^2_{Other} = FWHM^2_{Noise} + FWHM^2_{EnergyMisalignment} + \ldots \tag{5.6}$$

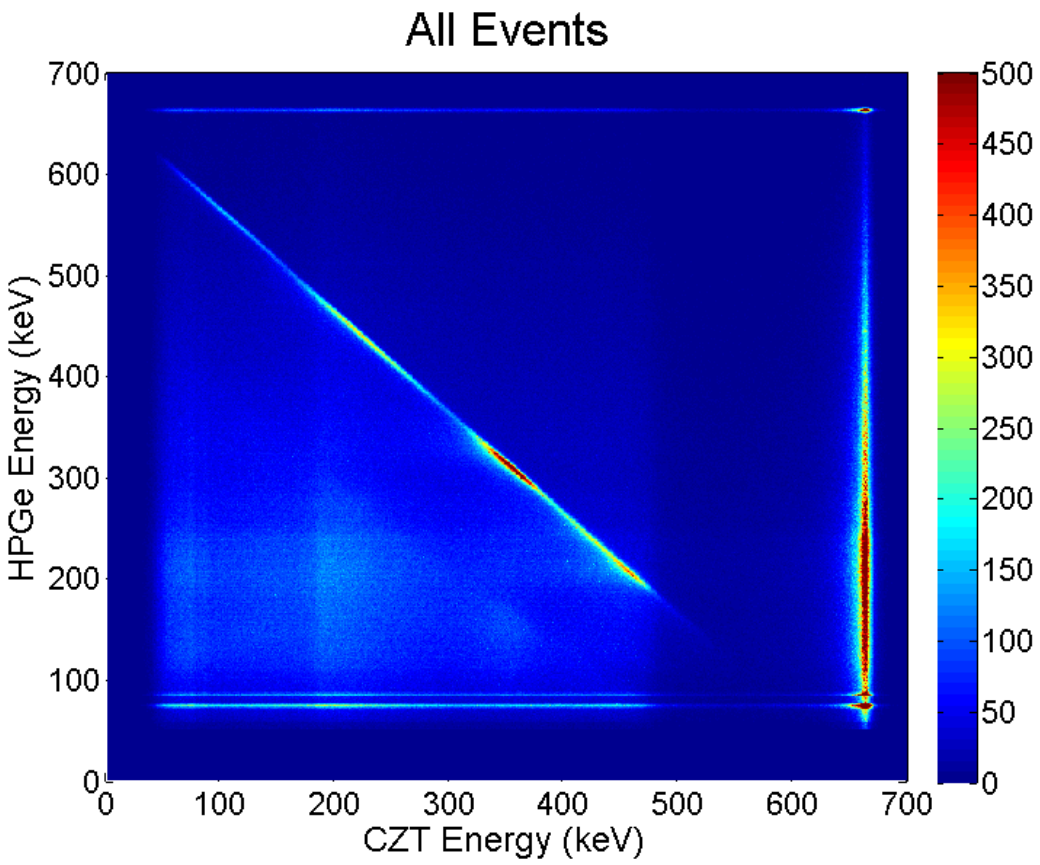

Figure 5.19: Energy correlation plot for all events in the CdZnTe detector.

$$R_{CZT}(E) = \sqrt{\frac{FWHM_{Other}^2}{E^2} + \frac{2.35^2 \epsilon F}{E}} \tag{5.7}$$

where the fano factor F is found to be 0.058 ± 0.027 and $FWHM_{Other}$ is 5.63 keV. To validate these results, the values are compared to previously calculated values. The fano factor for CdZnTe was calculated in 1997 by Redus et al. to be 0.089 ± 0.005 [60]. Since $FWHM_{Other}$ is dominated by the electronic noise, this gives an upper bound of the electronic noise to be 5.63 keV. The electronic noise of the ASIC was previously measured to be 5.2 keV [47]. The upper bound from the energy resolution fit corresponds well with expectation since it falls above the expected value for $FWHM_{Noise}$ with the difference contributed to misalignment of the energy misalignment between pixels and other minor factors.

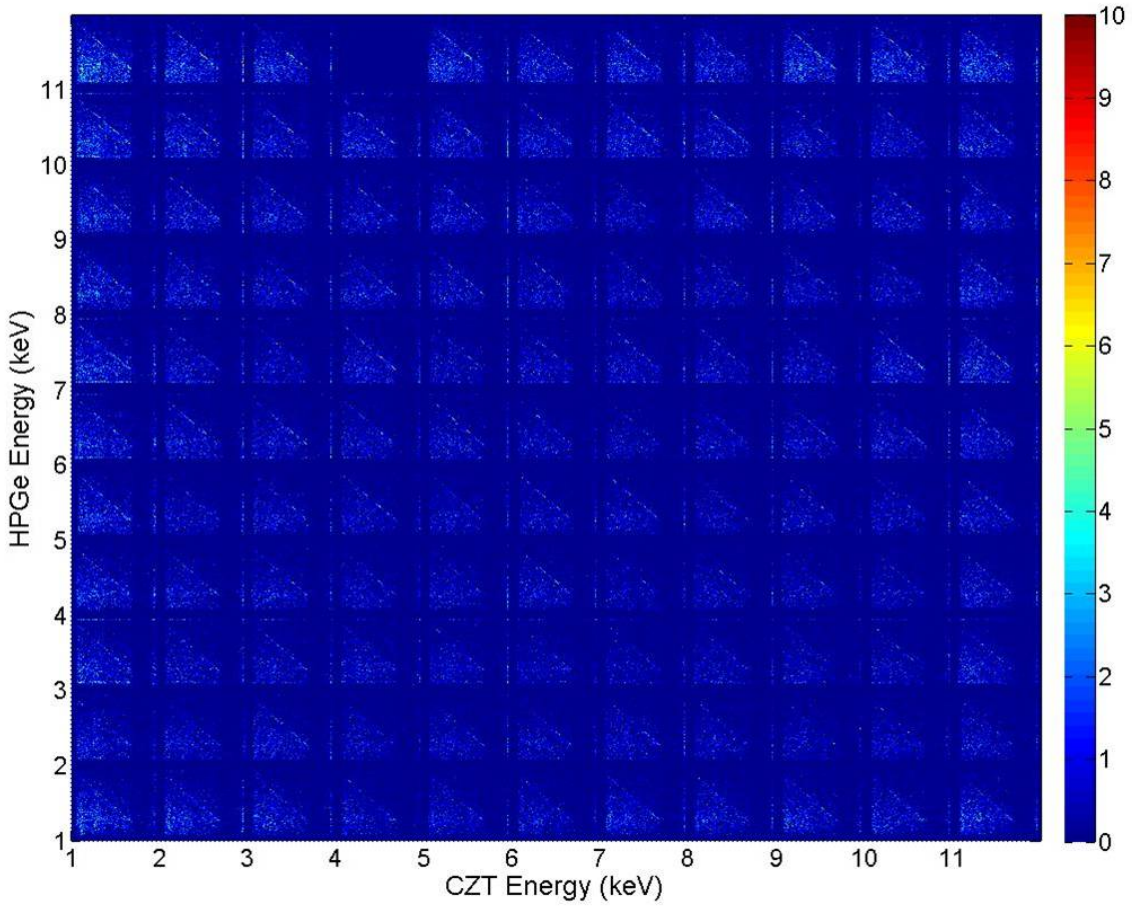

Figure 5.20: Energy correlation plot for each pixel in the CdZnTe detector.

The fit to the energy resolution as a function of energy shown in Equation 5.7 provides a means to predict an energy resolution for a source at any energy for single-pixel events. This equation should not be used for multiple pixel events as other factors would need to be considered.

5.3.2 Energy Linearity

The energy linearity is determined through the same method used to calculate the energy resolution. E_{CZT} is calculated from Equation 5.2 since $E_{HPGe+CZT}$ is 662 keV and E_{HPGe} is measured. The energy offset is the expected energy deposited in the CdZnTe detector based on the energy recorded in the HPGe detector minus the calculated energy deposited, shown in Equation 5.8.

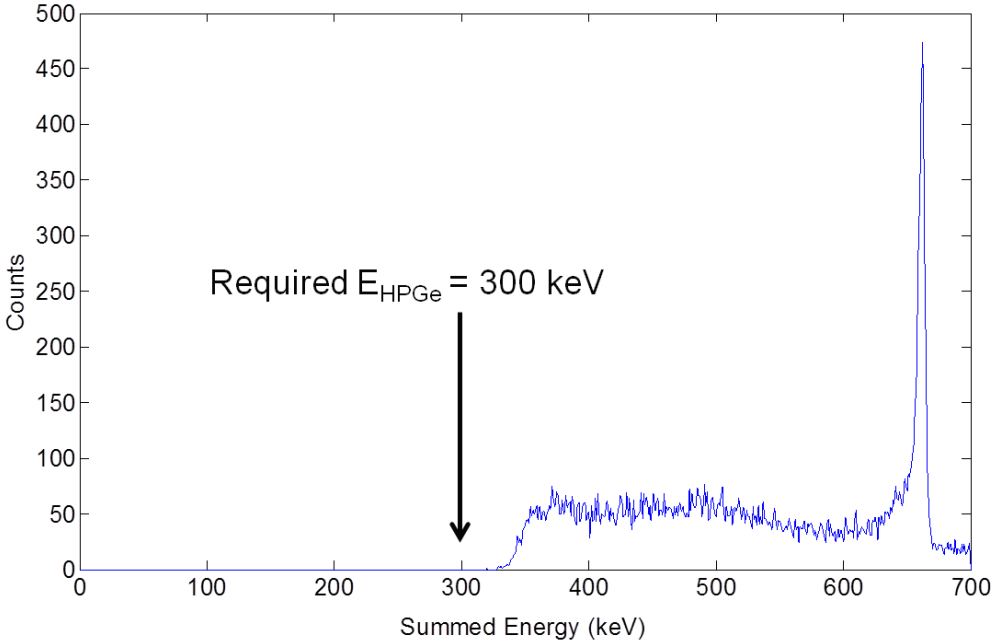

Figure 5.21: Energy spectrum for the combined events from the CdZnTe and HPGe detectors for events having 300 keV deposited in the HPGe detector.

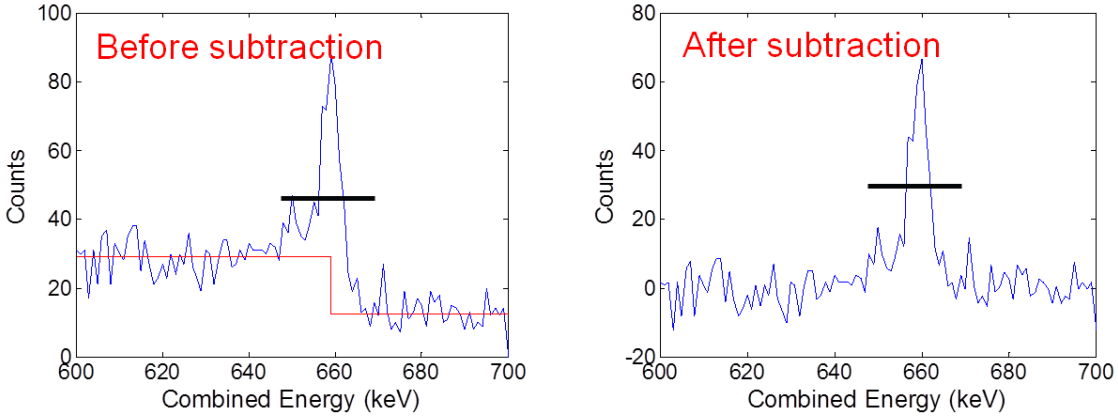

Figure 5.22: Example spectra showing the background subtraction completed prior to calculation of the energy resolution in the CdZnTe detector.

$$Offset = E_{Expected} - E_{Calculated} \tag{5.8}$$

The calculated energy linearity is shown in Fig. 5.24. Results are shown for when the energy non-linearity calibration is applied and not applied. Both situations com-

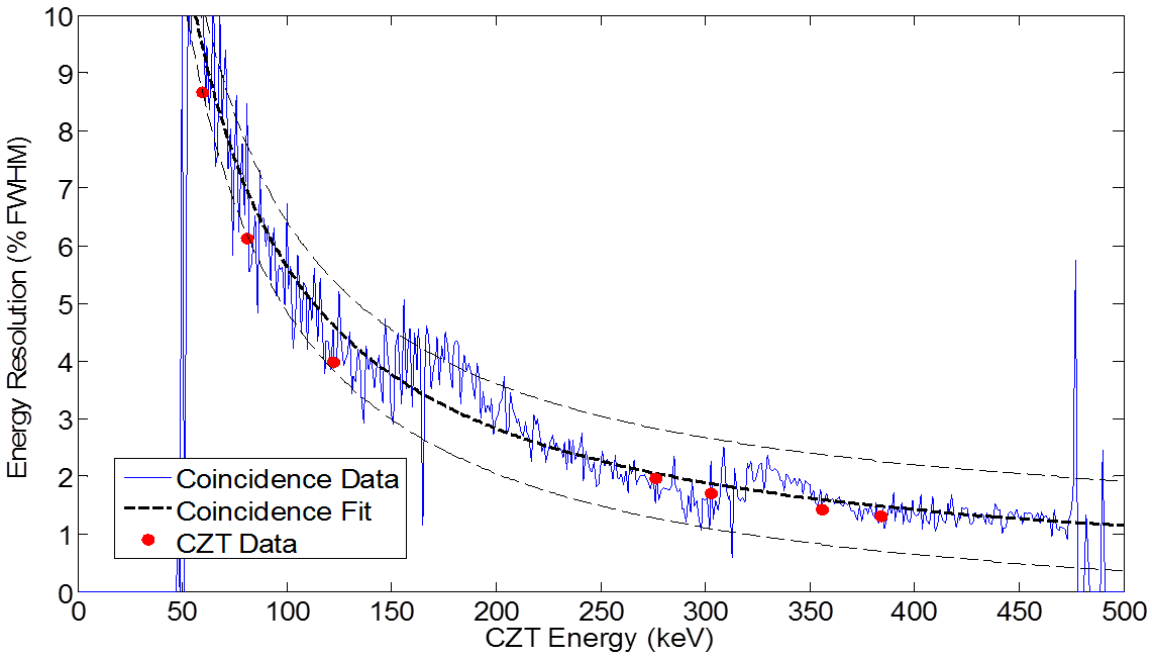

Figure 5.23: Graph of the energy resolution as a function of energy for CdZnTe based on the coincidence measurements. The results are compared against values from discrete energies from standard gamma ray sources. A fit to the data along with $\pm\sigma$ error bars is also plotted.

pare favorably with offset values from discrete energies for standard sources—^{241}Am, ^{133}Ba, and ^{57}Co. For the case using the non-linearity calibration, the calculated energy offset at low energies is at most 2 keV, showing good energy linearity for the CdZnTe. One noticeable relationship seen in Fig. 5.24 is that the shape of the energy offset is not affected by the energy non-linearity calibration. Therefore, the energy non-linearity calibration is not optimal, since it cannot account for the exhibited shape of the energy offset.

To determine the causes for the observed shape of the energy linearity shown in Fig. 5.24, the linearity of the ASIC channels was studied. Fig. 5.25 shows the linearity of two of the anode ASIC channels. The general shape of the curves follow the same trends shown in the coincidence data above 150 keV. The energy offset reaches a minimum between 300 and 450 keV, and then begins to increase with increasing energy. The non-linearity observed above 150 keV is dominated by the gain non-

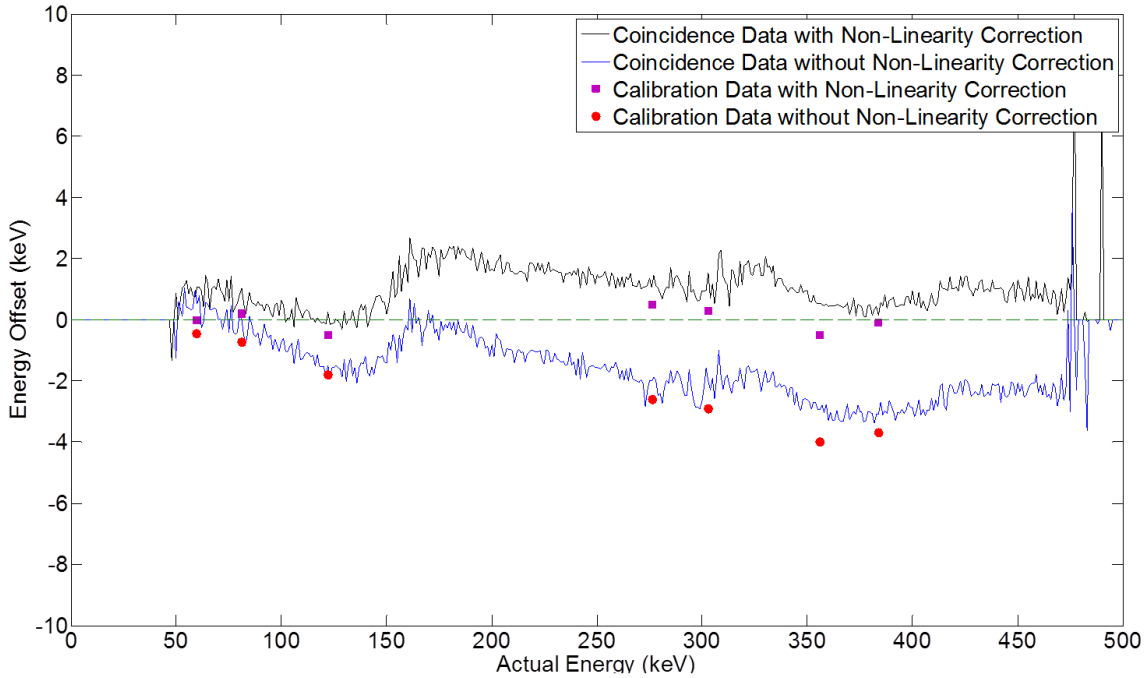

Figure 5.24: Graph of the energy non-linearity as a function of energy for CdZnTe with and without the non-linearity correction applied. The results are compared against values from discrete energies from standard gamma ray sources.

linearity of the anode ASIC channels. Below 125 keV, the observed non-linearity becomes dominated by the peak-hold drop correction. The peak-hold drop has its largest effect on low energy events because the drop becomes a significant portion of the measured energy and and the peak-hold drop calibration is correcting for the large observed offset in the ASIC non-linearity. In the middle is the transition region, where the dominant factor is slowly changing from the peak-hold drop to the ASIC non-linearity.

The current non-linearity calibration creates one fit for all of the calibration data points. However, the analysis of the causes of the non-linearity leads to the notion that a piece-wise non-linearity calibration, such as that shown in Fig. 5.26, would improve the energy calibration. The piece-wise non-lineiarty would separately fit the higher energy calibration data and the lower energy calibration data, and use a

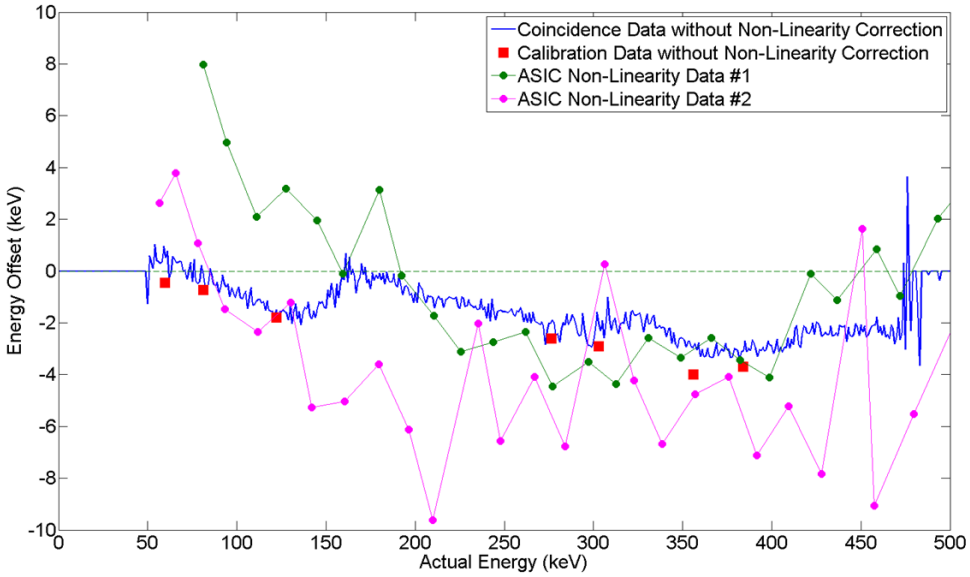

Figure 5.25: Graph of the energy non-linearity as a function of energy for CdZnTe without the non-linearity correction applied compared against the non-linearity of two of the anode ASIC channels.

weighted average for the transition region.

If the piece-wise non-linearity correction were to improve system performance, it would be expected to be observed in the energy resolution and linearity for multiple pixel events. This is because one of the factors leading to degraded energy resolution for multiple pixel events is the mis-reconstruction of the energy linearity in each pixel. Results comparing the standard non-linearity correction to the piece-wise non-linearity correction for energy resolution and energy linearity for multiple pixel events are shown in Fig. 5.27 and 5.28. The results show that the piece-wise non-linearity mostly breaks even with the standard calibration, but in some instances does worse.

One key instance of worse performance is for two-pixel events at 356 keV. These will have a higher portion of events at low energies and in the transition region. The lack of improvement using the piece-wise non-linearity for these events indicates that the transition region is non-uniform for all pixels, which is a required assumption since the non-linearity from the coincidence measurements cannot be determined on

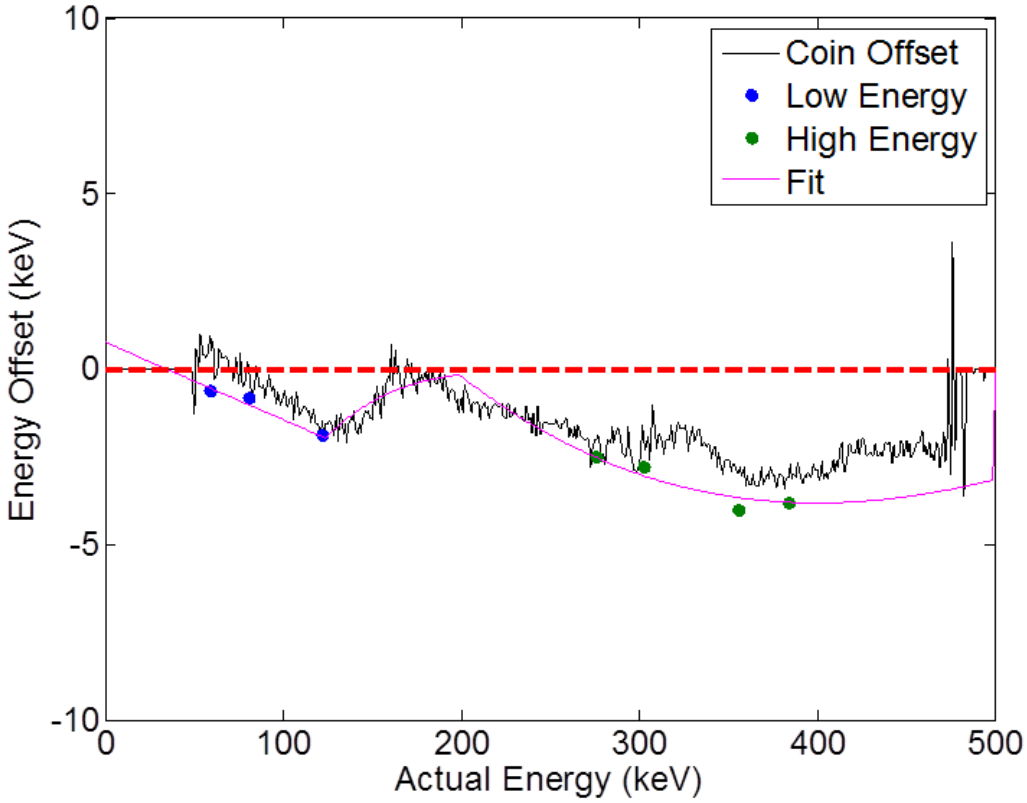

Figure 5.26: Proposed piece-wise non-linearity calibration fit to account for the observed energy non-linearity.

a pixel-by-pixel basis. Further analysis of the energy offset at energies approaching the lower level threshold of the ASIC were explored by lowering the threshold to be able to measure the 32 keV x rays from ^{137}Cs. Fig. 5.29 shows that the non-linearity caused the peak-hold drop decreases at low energies. This also changes on a pixel-by-pixel basis, and cannot be appropriately accounted for through a piece-wise non-linearity fit.

Therefore, the best achievable fit is the standard fit that creates a single fit from all of the calibration data points. This results in a slight energy non-linearity as a function of energy due to the different ASIC non-linearity factors—peak-hold drop and the gain non-linearity of each anode channel. Overall, the CdZnTe detector has a maximum energy offset of 2 keV for events below 500 keV, which is small compared

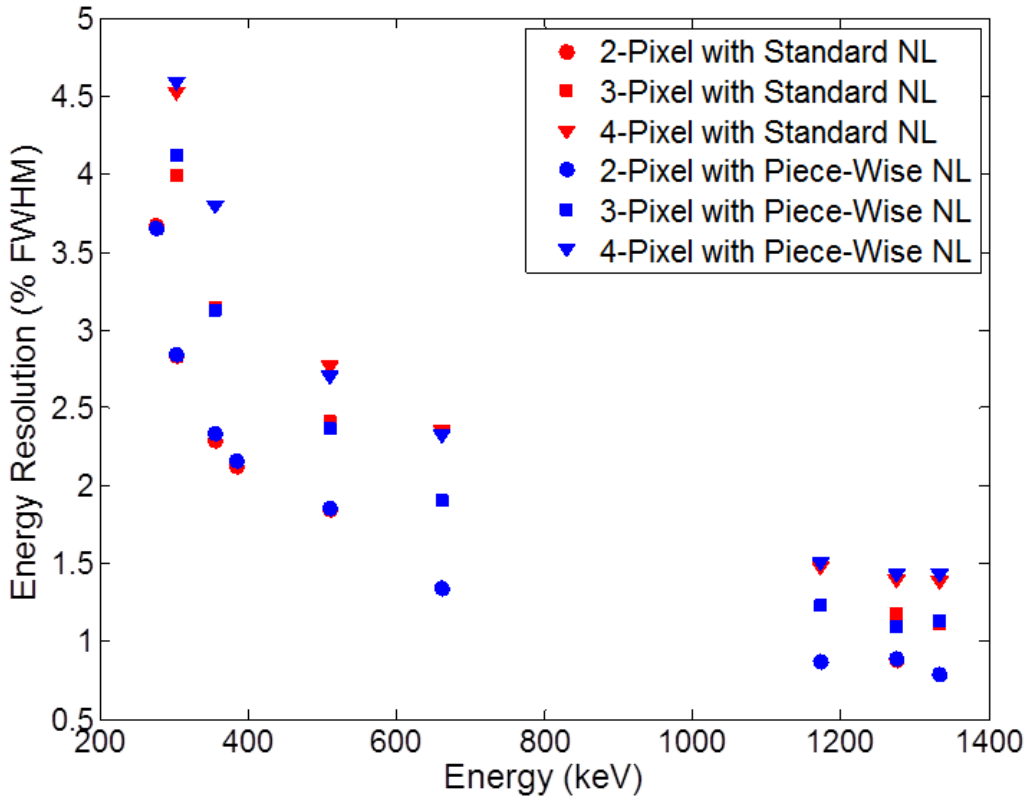

Figure 5.27: Energy resolution results comparing the standard non-linearity calibration and the piece-wise non-linearity calibration.

to the ~6 keV FWHM energy resolution at these energies.

5.3.3 Two-Pixel Results

Performing the same energy resolution and linearity analysis on the two-pixel events shown in Fig. 5.18, gives insight into the multiple pixel performance of CdZnTe detectors.

The two-pixel energy resolution as a function of deposited energy relationship is plotted in Fig. 5.30. As expected, the energy resolutions are worse than their single-pixel counterparts, but match well with data acquired from ^{133}Ba. The best statistics occur near the 356 keV photopeak from ^{133}Ba, which will be used for further analysis.

The two-pixel coincidence data at 356 keV were first analyzed to determine the

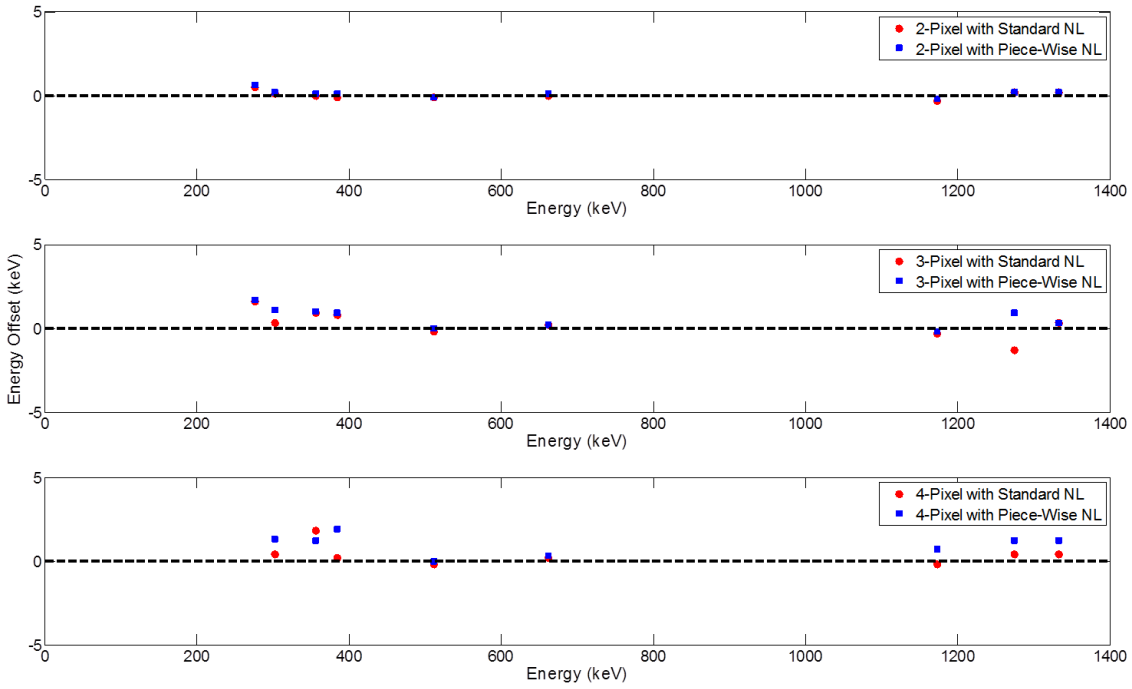

Figure 5.28: Energy linearity results comparing the standard non-linearity calibration and the piece-wise non-linearity calibration.

distribution of the energies. As shown in Fig. 5.31, the individual energies recorded in each pixel have a uniform distribution. Therefore, an expected energy resolution for two-pixel events at 356 keV can be determined assuming the uncertainty in the combination of the energies from the two-pixels was simply the quadrature summation of the uncertainty in each individual energy—this will be an overestimate of the energy resolution as the two individual energies are actually correlated. The individual energy uncertainties would be determined from the energy resolution calculated for that energy from the single-pixel coincidence analysis. The combination of all possible energies that sum to 356 keV sampled with a uniform distibution generates the expected energy resolution for two-pixel events at 356 keV in Fig. 5.32. The average of this distribution would generate an expected energy resolution of 2.28% FWHM at 356 keV, which is smaller than the measured 2.35% FWHM at 356 keV from measurements of a ^{133}Ba source. This matches previous results that have shown that the

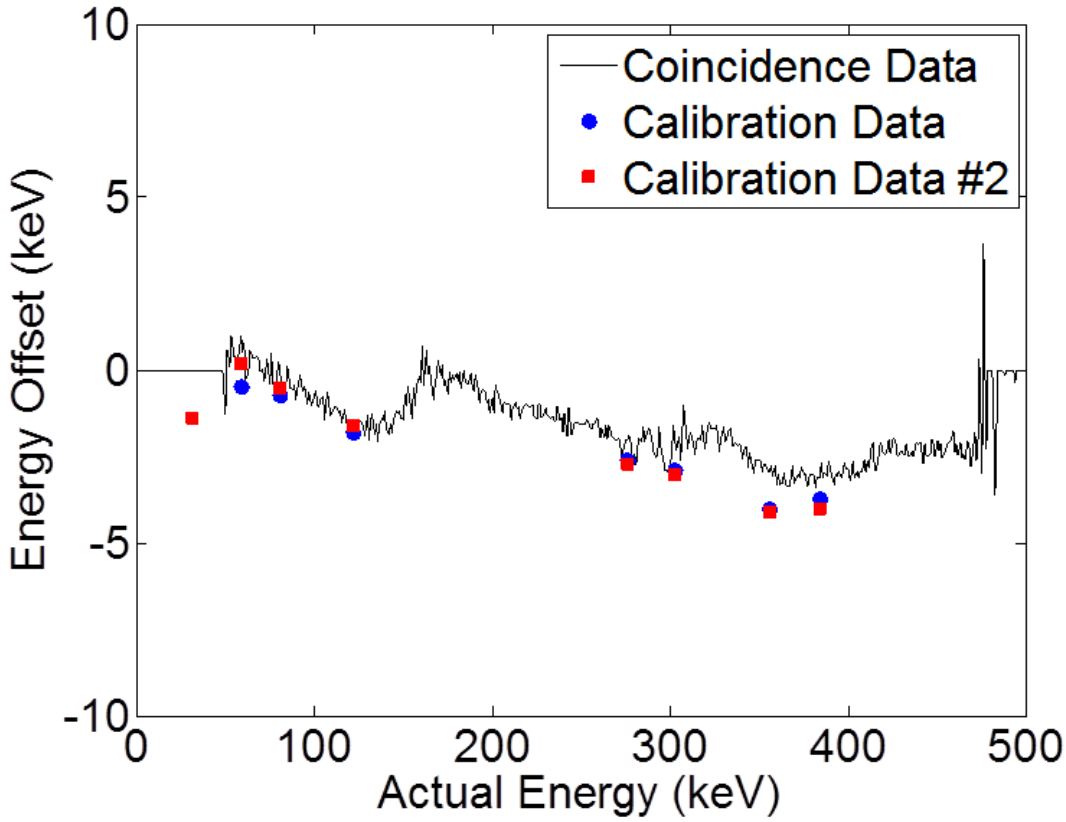

Figure 5.29: Energy linearity results comparing the coincidence data to two sets of discrete data from standard gamma-ray sources. Data set #2 is with a lower threshold set compared to the original data.

multiple pixel energy resolution degrades more than estimated from the quadrature summation of the single-pixel energy resolution.

One potential explanation of this worse degradation is the misalignment of the energies in each pixel. This can be studied through comparisons of the energy offset for the two-pixel events. The energy offset for two-pixel events is shown in Fig. 5.33. Completing the same analysis for creating the two-pixel events based on a uniform distribution of interaction energies results in the expected energy offset distribution displayed in Fig. 5.34. The calculated two-pixel offset matches well the predicted average from the summation of the single-pixel coincidence data.

Fig. 5.34 shows that there is a several keV wide range in the calculated energy

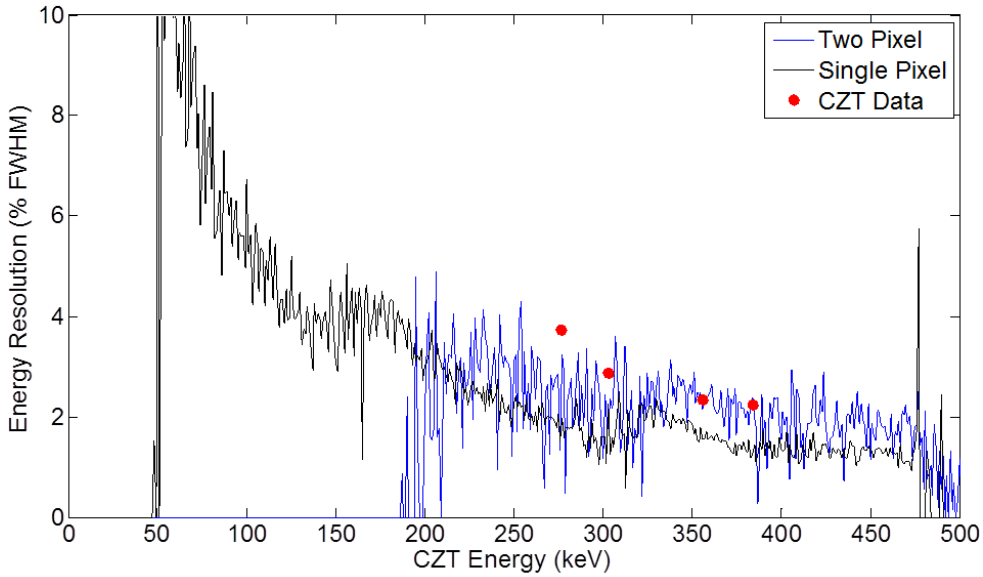

Figure 5.30: Plot of the energy resolution as a function of deposited energy for two-pixel events in the CdZnTe detector. The distribution is compared against values for single-pixel events as well as from gamma rays from a ^{133}Ba source.

distribution for two-pixel events due to the cominbation of misaligned lower energies. Accounting for this extra spread would degrade the expected energy resolution of two-pixel events from 2.28% FWHM to 2.31% FWHM at 356 keV. Therefore, degraded performance of the energy resolution for multiple pixel events can be partially attributed to the energy misalignment of single-pixel events at lower energies.

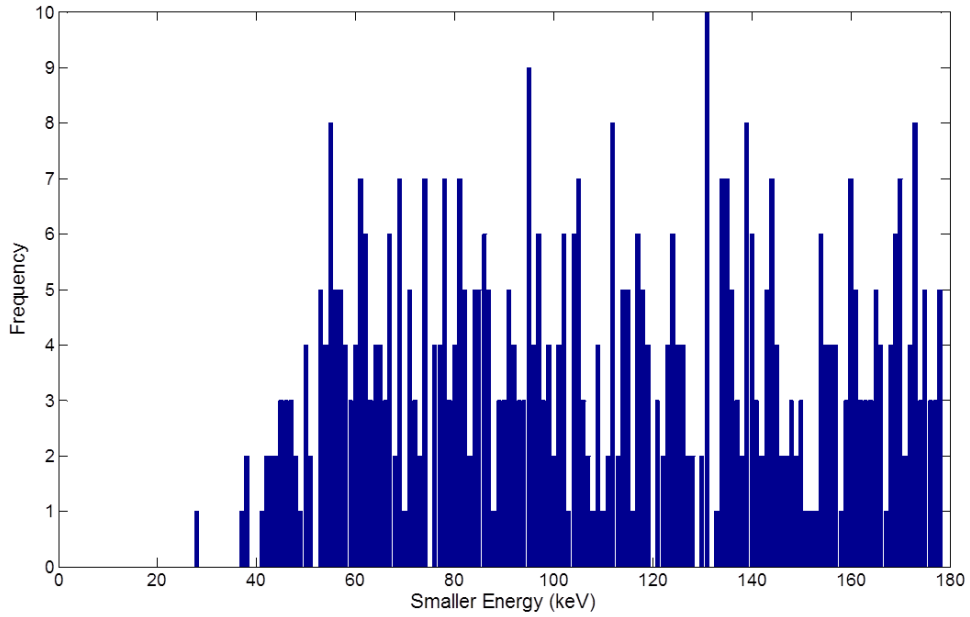

Figure 5.31: Plot showing the uniformity of the energies recorded in events depositing 356 keV over two pixels in the CdZnTe detector. Only the smaller energy is plotted as the distribution will be symmetric over the 178 keV line.

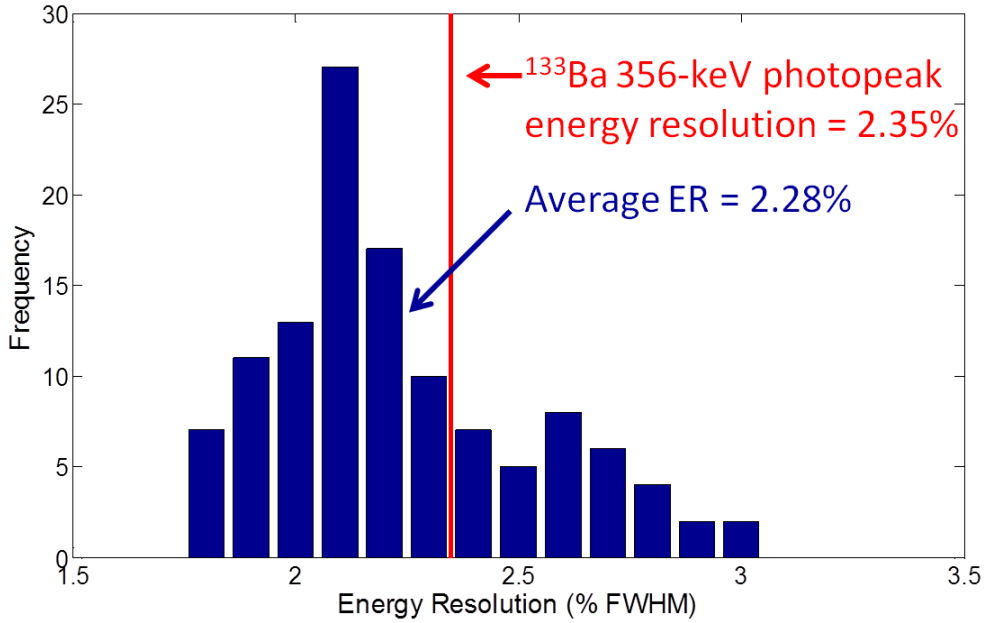

Figure 5.32: Histrogram of the expected energy resolution for two-pixel events based on the quadrature summation of the energy uncertainy in the individual energies.

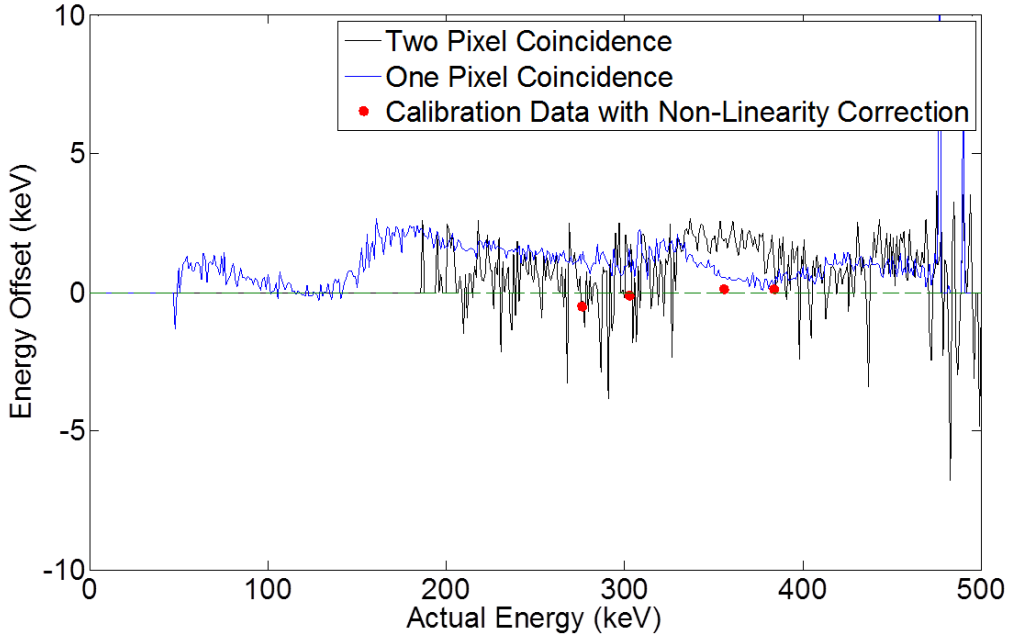

Figure 5.33: Plot of the energy linearity as a function of deposited energy for two-pixel events in the CdZnTe detector.

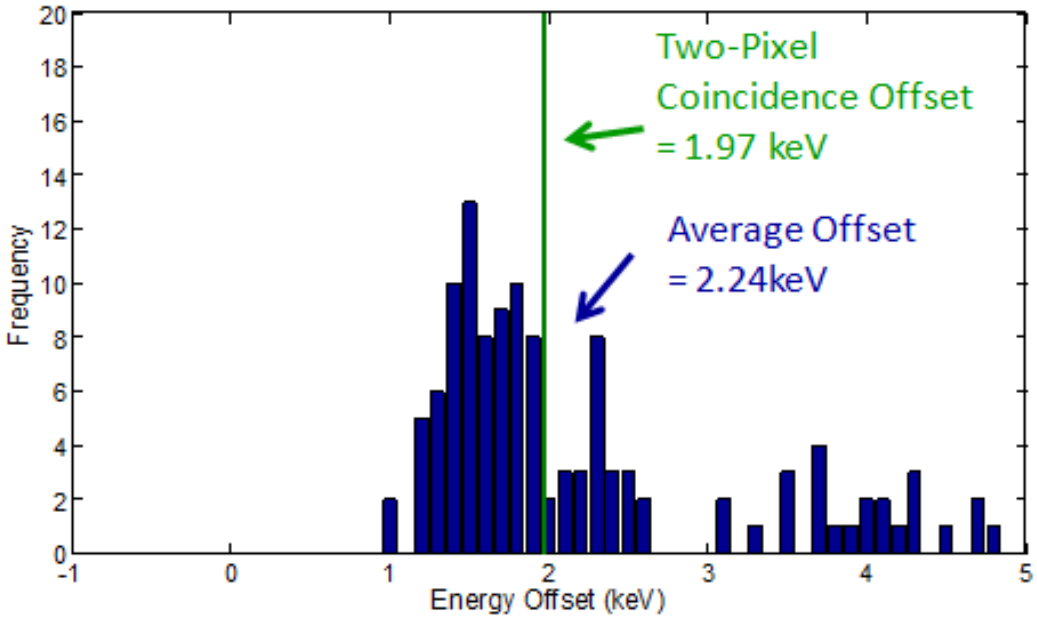

Figure 5.34: Histrogram of the expected energy linearity for two-pixel events based on the summation of the energy offset in the individual energies.

CHAPTER VI

CdZnTe Detector Efficiency

The efficiency of a detector is important for many applications. Certain situations may only allow for a short measurement, and low efficiency detectors may not find a radioactive source of interest. For imaging, a larger number of counts will produce better statistics and a higher image quality. There are not many applications when a low efficiency detector is more advantageous.

The efficiency can be defined in several different ways. Absolute efficiency is the percentage of pulses recorded out of all of the radiation quanta emitted by the source, whereas intrinsic efficiency is the percentage of pulses recorded out of all of the radiation quanta incident on the detector [2]. Typically, absolute efficiency is used to compare different detector types to one another since each detector has a different size, subtending a different solid angle of the gamma-ray source. In the studies in the following sections, the intrinsic efficiency will mainly be studied to better understand the performance of the 18-detector CdZnTe array system.

6.1 Factors Affecting CdZnTe Efficiency

There are several different factors that can effect the efficiency of a device. Each factor can be broken down into one of two categories. Either it will cause an event to be entirely not collected or it will cause an event to have a lower energy recorded.

In both cases, a full-energy event will not be recorded, reducing the efficiency of the device. Compton scattering events that have partial energy escaping the system altogether contribute to the degraded efficiency; however, these events have the proper recorded energy and do not degrade the efficiency below expectation based on the detector's effective atomic number.

One of the factors leading to degraded instrinsic efficiency is electron trapping. Electron trapping can be broken down into four different cases [36]. Case I is the standard, uniform electron trapping along the entire depth of the pixel. Case II is when a trapping defect at a particular depth decreases the number of electrons passing through it by an additional percentage for all events over that pixel. Case III is when a trapping defect at a particular depth over a pixel stop all electrons from passing. Finally, Case IV is when a small trapping defect is present over the pixel, similary to Case II, but the defect does not effect all events over the pixel. Cases II-IV all have a negative impact on the intrinsic efficiency of the device.

Case III's negative impact on efficiency is the most clear, since many counts will not be recorded over the top of any pixels with a complete trapping defect. Case II's effect is less clear. Since all events the interact above the defect are effected by the additional trapping, the 3-D depth calibration will account for the additional trapping. However, the cathode signal for these events will be larger than expected since the drift prior to the trapping defect will induce a larger than expected signal based on the recorded signal on the anode electrode. This will lead to cathode-side events being discarded since they have a depth reconstucted beyond the extent of the crystal. Case IV has a similar effect as Case II for events near the cathode side. But the efficiency will be additionally degraded for events that are affected by the trapping defect. The calibration parameters for the pixel will be based on the events not affected by the trapping defect, meaning that events affected by the trapping defect will result in a smaller recorded signal compared to the deposited

energy. These events will either fall outside of the full-energy range if the trapping defect traps a significant percentage of the electrons, or they will fall near the full-energy range, creating a degraded FWHM for events in that region of the pixel if the trapping defect only traps a small percentage of the charge.

The intrinsic efficiency can also be degraded by losing events that interact in the dead regions near either the cathode or anode surface. This is the case if the drift of the event is too short, preventing a large enough weighting potential change to induce a charge on the anode or cathode electrodes. The dead regions have been measured to be about 0.1 mm and 0.5 mm for the cathode and anode surfaces, respectively [48].

Efficiency losses due to the non-collection of generated electrons is also possible. If the electric field lines do not end on the anode electrode, but instead draw the charges to the grid or the side surface of the detector, then entire events may be lost. Losses to the grid were more probable for early detectors from Redlen Technologies, Inc.; more recent detectors have shown improved grid fabrication, which should indicate better steering of the electrons to the anode electrodes. Electron losses to the side surface will only effect the edge pixels, and can be studied by comparing results from edge pixels to the inner pixels.

Finally, interactions that deposit less energy than the energy threshold will contribute to the efficiency losses. For measurements of gamma-rays at energies near 1 MeV, a significant portion of the full-energy events are due to multiple interaction events. Forward scattering interactions will deposit energies near or below the threshold. The loss of these events will create a low-energy tail on the full-energy peak, and significant enough losses will degrade the efficiency by pulling events below the full-energy peak region.

The efficiency results for the 18-detector CdZnTe array system will be studied, with special considerations for the above factors. First, the calibration of the detectors will be studied to discern the extent of the potential trapping defects. A comparison

to simulated data from a Co-60 source and analysis of data from interplane events also allow for conclusions as to the extent of the degradation of the intrinsic efficiency of the system due to the above factors.

6.2 Calibration Results Analysis for Defects

The electron trapping in each detector in the 18-detector CdZnTe array system can be studied using the ^{137} calibration data. The trapping in each detector can be tracked via the relationship between the photopeak centroid and the depth of interaction in each pixel. A clear change in slope of the relationship is evidence of a Case II trapping defect. A Case III trapping defect will be evident since all depths beyond the defect will not have a photopeak centroid as no electrons were collected from interactions beyond that depth. Case IV trapping defects will not necessarily be evident from the photopeak centroid versus depth relation.

The photopeak counts versus depth relation will also show the effects of trapping defects. Case III defects will show no counts for depths beyond the trapping defect. Due to the distortion in the cathode-to-anode ratio caused by a Case II defect, there should be a slight drop in the photopeak counts at the depth corresponding to the defect [36].

In the FWHM versus depth relation for each pixel, again there will be no results for depths beyond the defect for Case III trapping defects. Since all events with greater depths than the defect depth are affected in Case II trapping defects, the FWHM versus depth should be constant. For Case IV trapping, there may or may not be a degradation in the FWHM for depths beyond the trapping defect. If the trapping defect is small relative to the average trapping throughout the pixel, then the FWHM should be degraded since the events affected by the defect will widen the photopeak; however if the trapping is large, then the events affected by the defect will fall below the defect photopeak range and will not cause a degraded FWHM.

The photopeak centroid versus depth relation for each pixel is shown in Fig. 6.1 and 6.2. The majority of pixels show a constant slope and there is only one pixel that shows a complete trapping layer. These results indicate that the array system is not degraded by Case III defects.

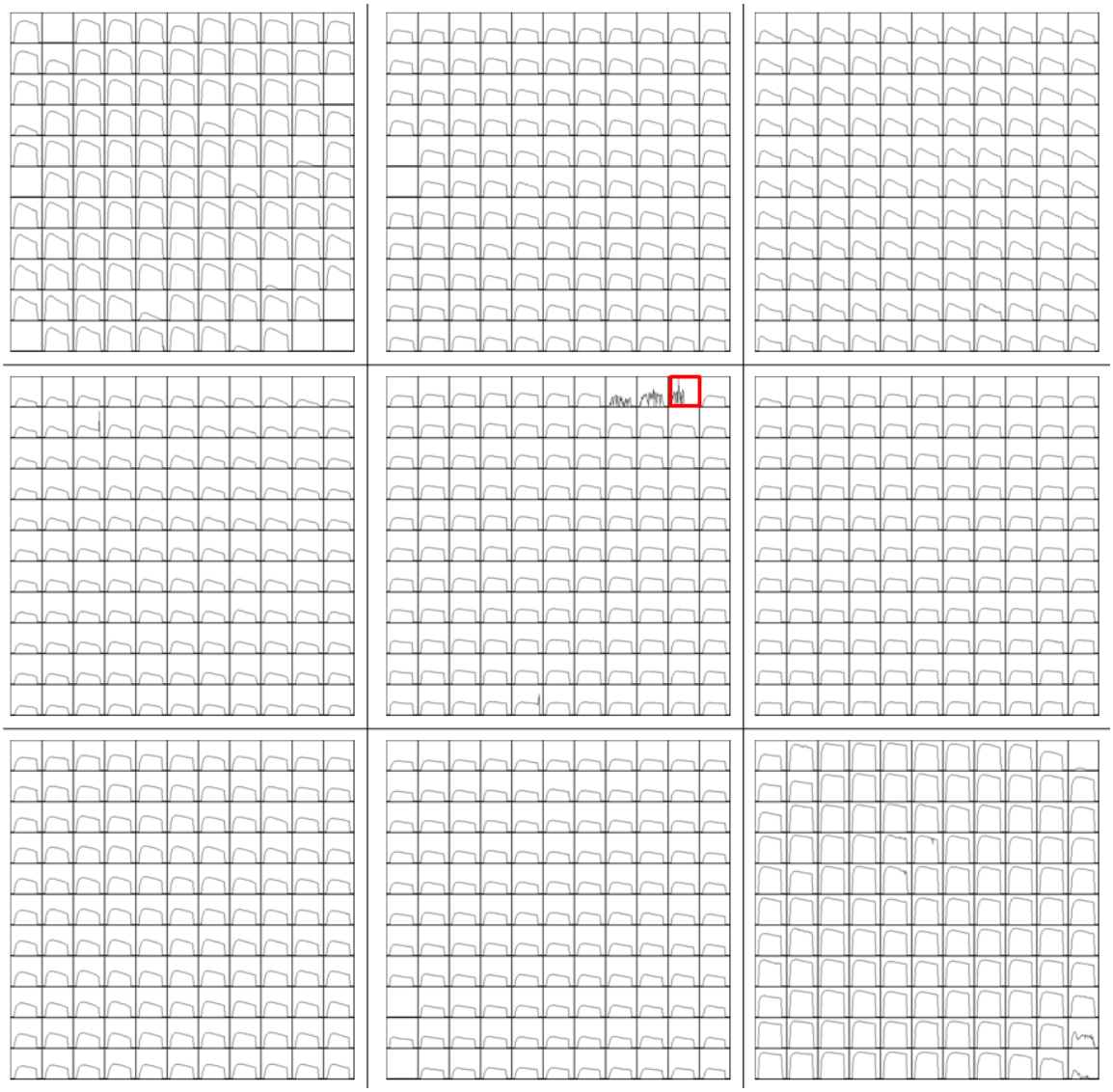

Figure 6.1: Plots of the photopeak centroid versus depth for single-pixel events in each of the 9 detectors in the first plane of the second CdZnTe array system. For each pixel, the x-axis covers the depth of interaction from 0 mm (anode) to 15 mm (cathode) and the y-axis is the photopeak centroid in ADC units with a range of 1300-1500 ADC units. A boxed pixel represents a pixel with a Case III defect.

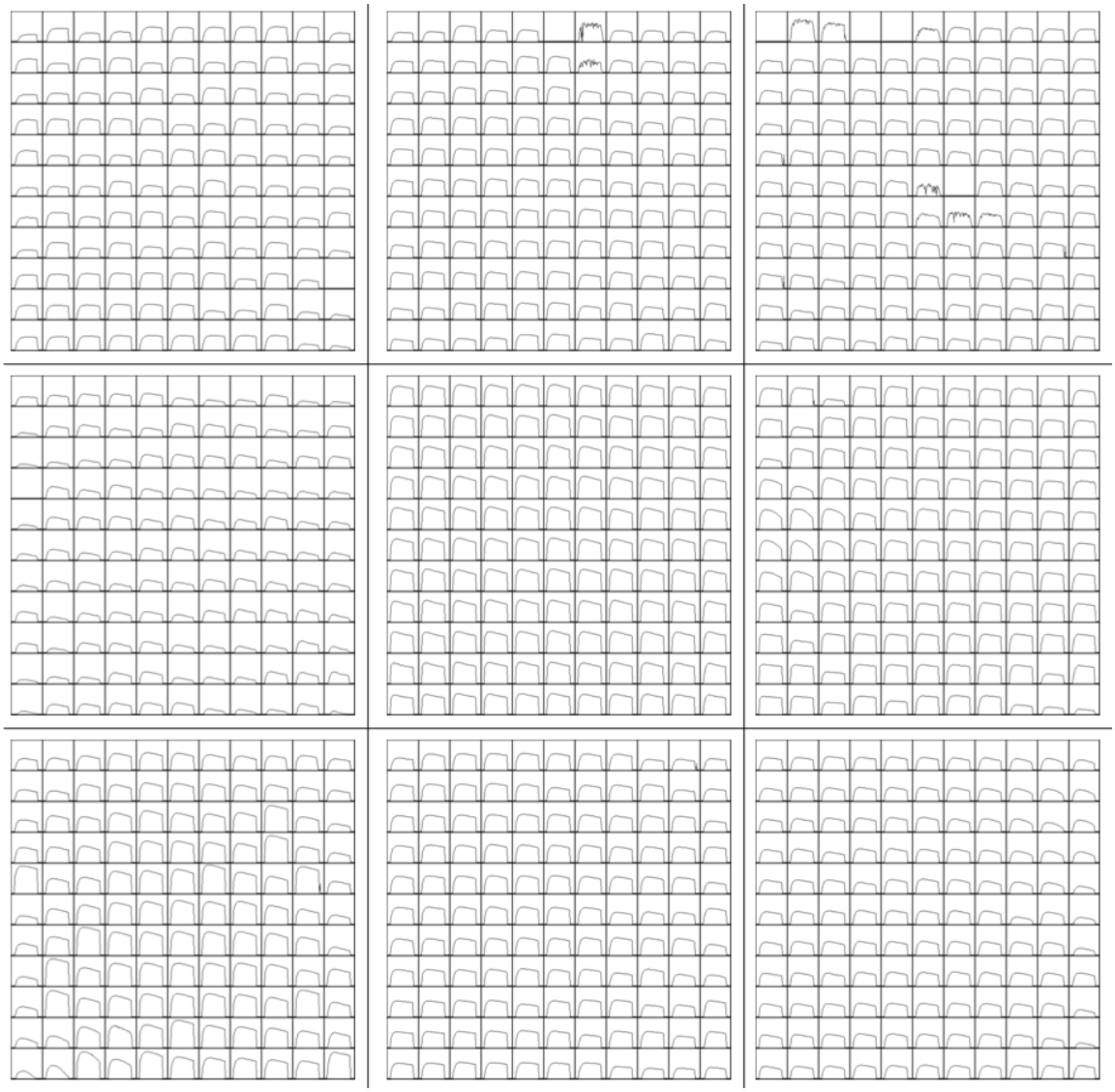

Figure 6.2: Plots of the photopeak centroid versus depth for single-pixel events in each of the 9 detectors in the second plane of the second CdZnTe array system. For each pixel, the x-axis covers the depth of interaction from 0 mm (anode) to 15 mm (cathode) and the y-axis is the photopeak centroid in ADC units with a range of 1300-1500 ADC units. A boxed pixel represents a pixel with a Case III defect.

From the results in Fig. 6.1 and 6.2, it appears that there are several pixels that received no counts. These pixels are actually degraded by the effects of gain deficit. From the photopeak counts versus depth relation shown in Fig. 6.3 and 6.4, all but 1 pixel shows photopeak events. Most pixels show a constant relation between the

photopeak counts and the depth of interaction, indicative of pixels exhibiting no Case II or III trapping defects. Several pixels, particular in the center-right region of the detector in the third column of the first row or the same region of the detector in the first column of the fifth row, show a decrease in counts indicative of Case II trapping.

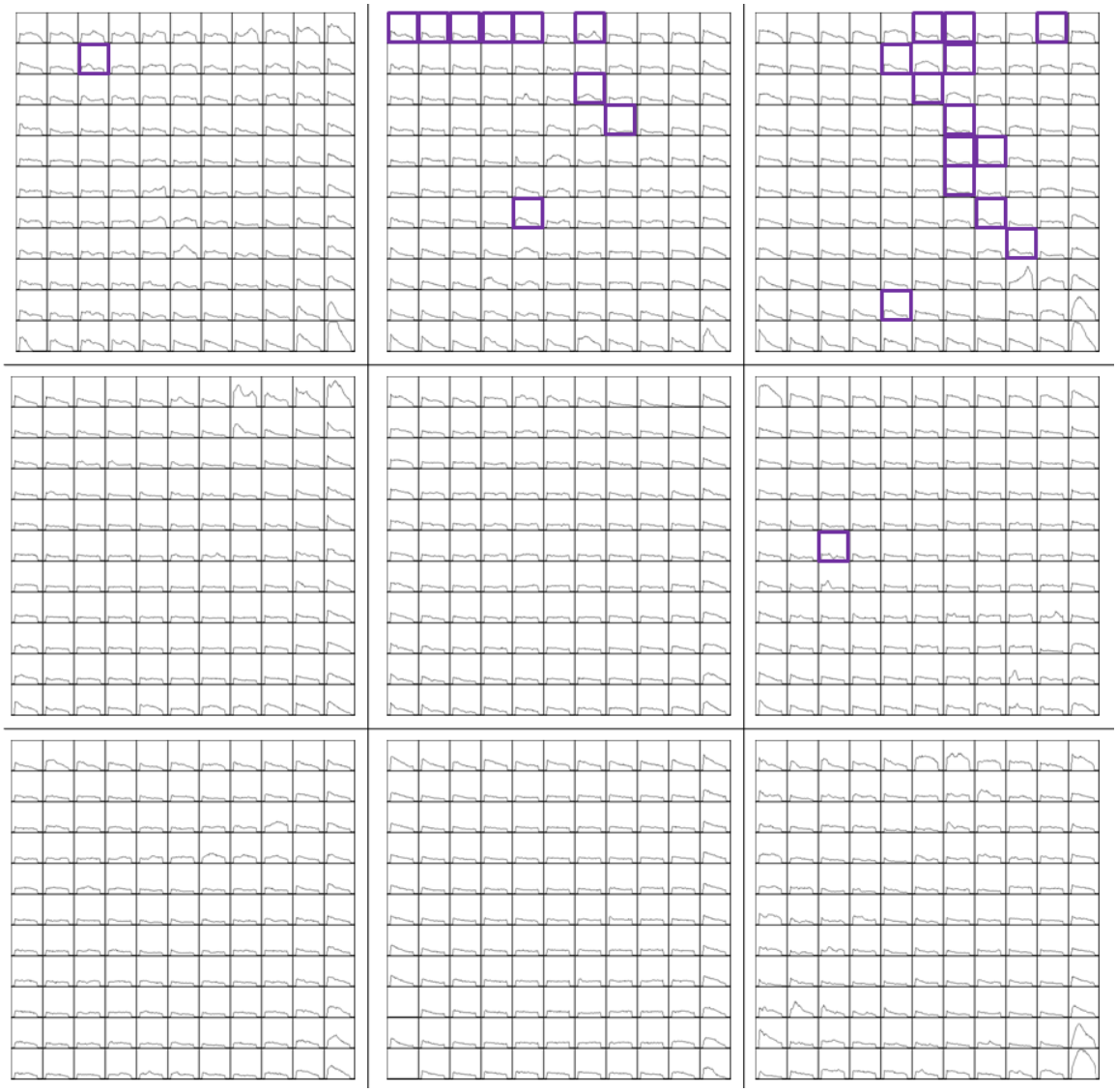

Figure 6.3: Plots of the photopeak counts versus depth for single-pixel events in each of the 9 detectors in the first plane of the second CdZnTe array system. For each pixel, the x-axis covers the depth of interaction from 0 mm (anode) to 15 mm (cathode) and the y-axis is the photopeak counts with a range of 0-1500 counts. A boxed pixel represents a pixel with a Case II trapping defect.

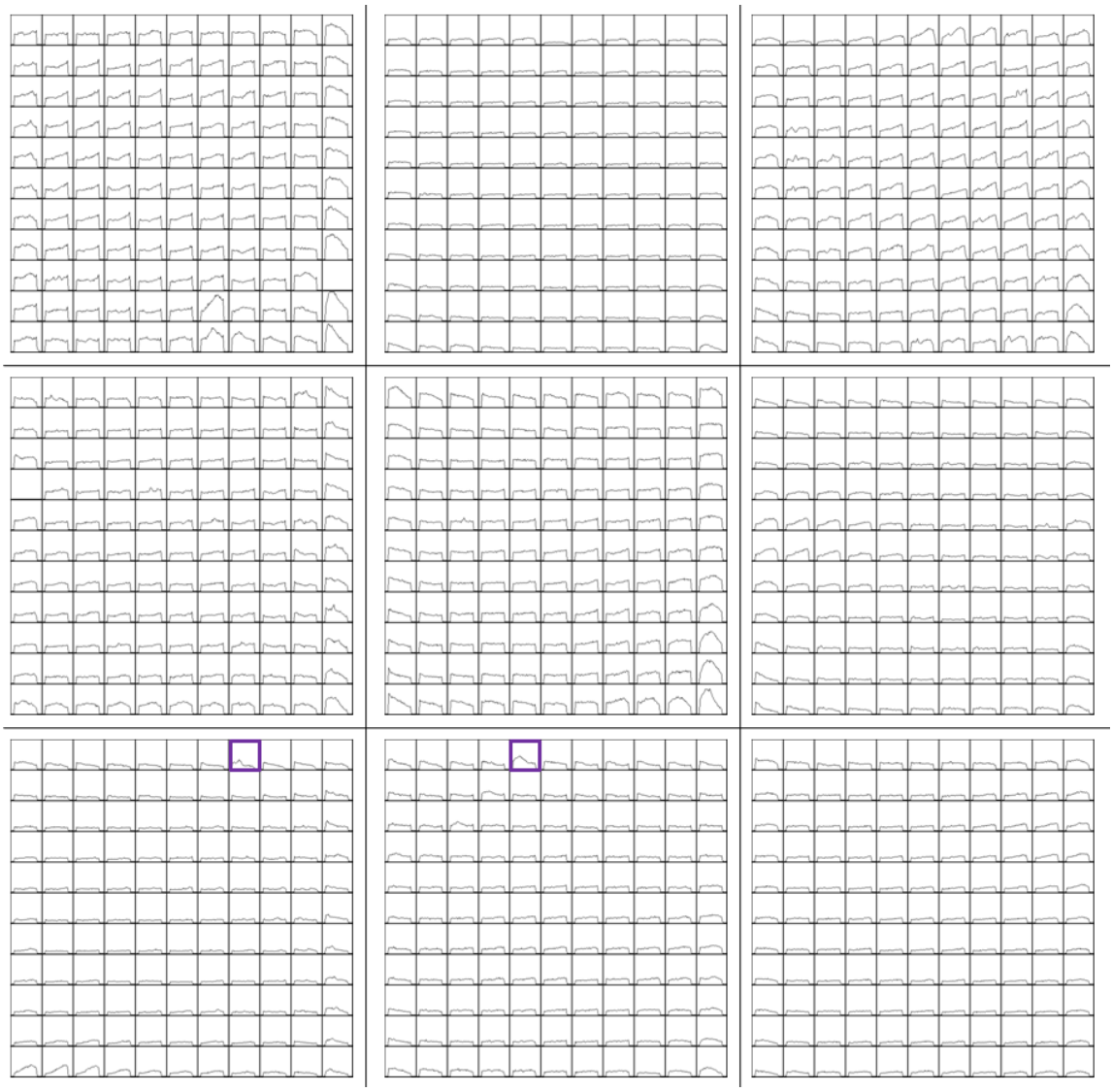

Figure 6.4: Plots of the photopeak counts versus depth for single-pixel events in each of the 9 detectors in the second plane of the second CdZnTe array system. For each pixel, the x-axis covers the depth of interaction from 0 mm (anode) to 15 mm (cathode) and the y-axis is the photopeak counts with a range of 0-1500 counts. A boxed pixel represents a pixel with a Case II trapping defect.

Only a few detectors in the entire array system show evidence of a Case IV trapping defect based on the FWHM versus depth relation displayed in Fig. 6.5 and 6.6. Most of these pixels are in the detector in the third column of the third row. This does not indicate that there are not more than a few pixels exhibitting Case IV trapping

defects, but only a few that trap a fraction of electrons comparable to the overall trapping in that pixel. Further analysis of the effects of trapping defects will be studied along with the effects of missing events through analysis of the measurement and simulation of a ^{60}Co source.

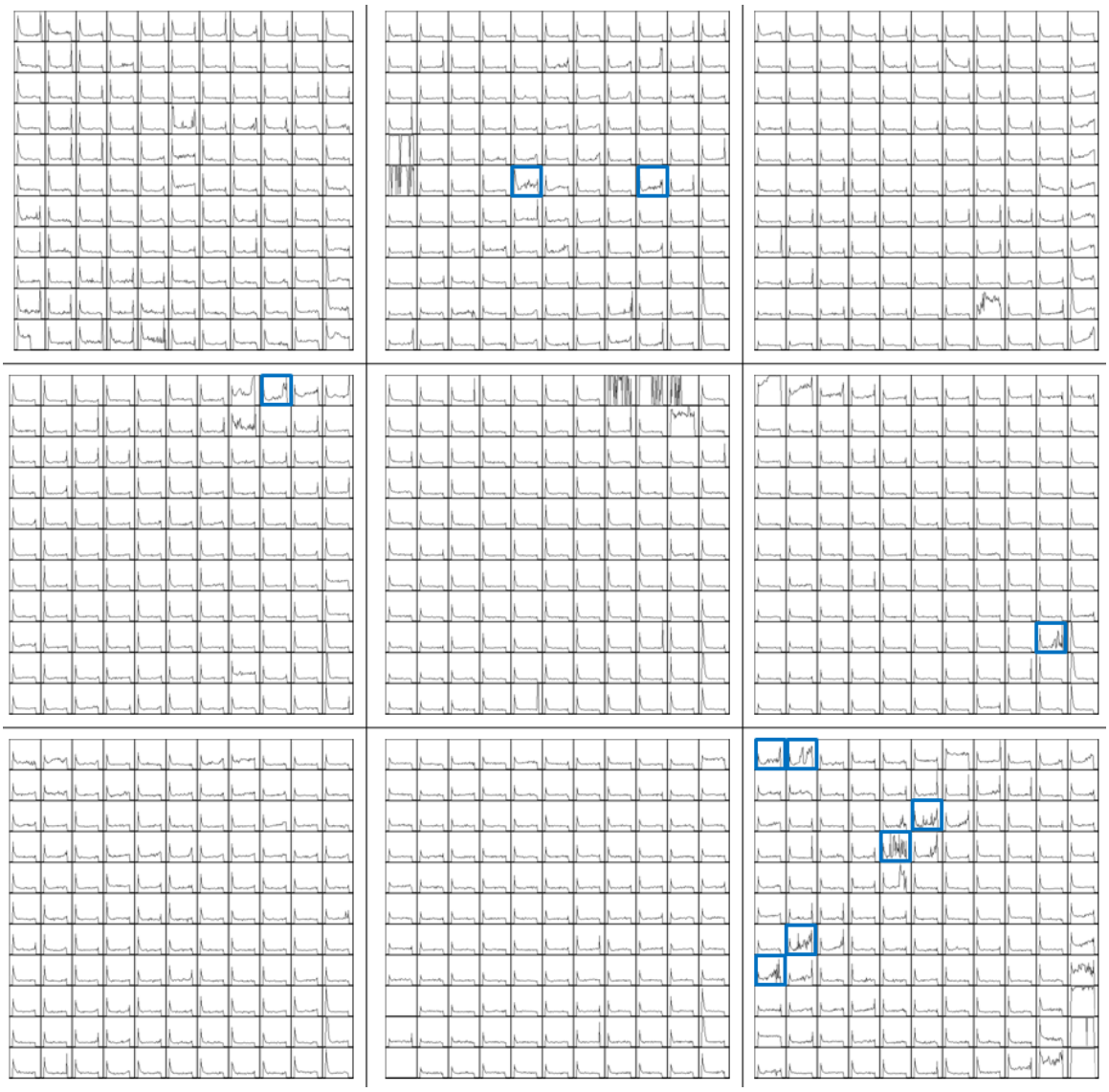

Figure 6.5: Plots of the FWHM versus depth for single-pixel events in each of the 9 detectors in the first plane of the second CdZnTe array system. For each pixel, the x-axis covers the depth of interaction from 0 mm (anode) to 15 mm (cathode) and the y-axis is the % FWHM at 662 keV with a range of 0-5%. A boxed pixel represents a pixel with a Case IV trapping defect.

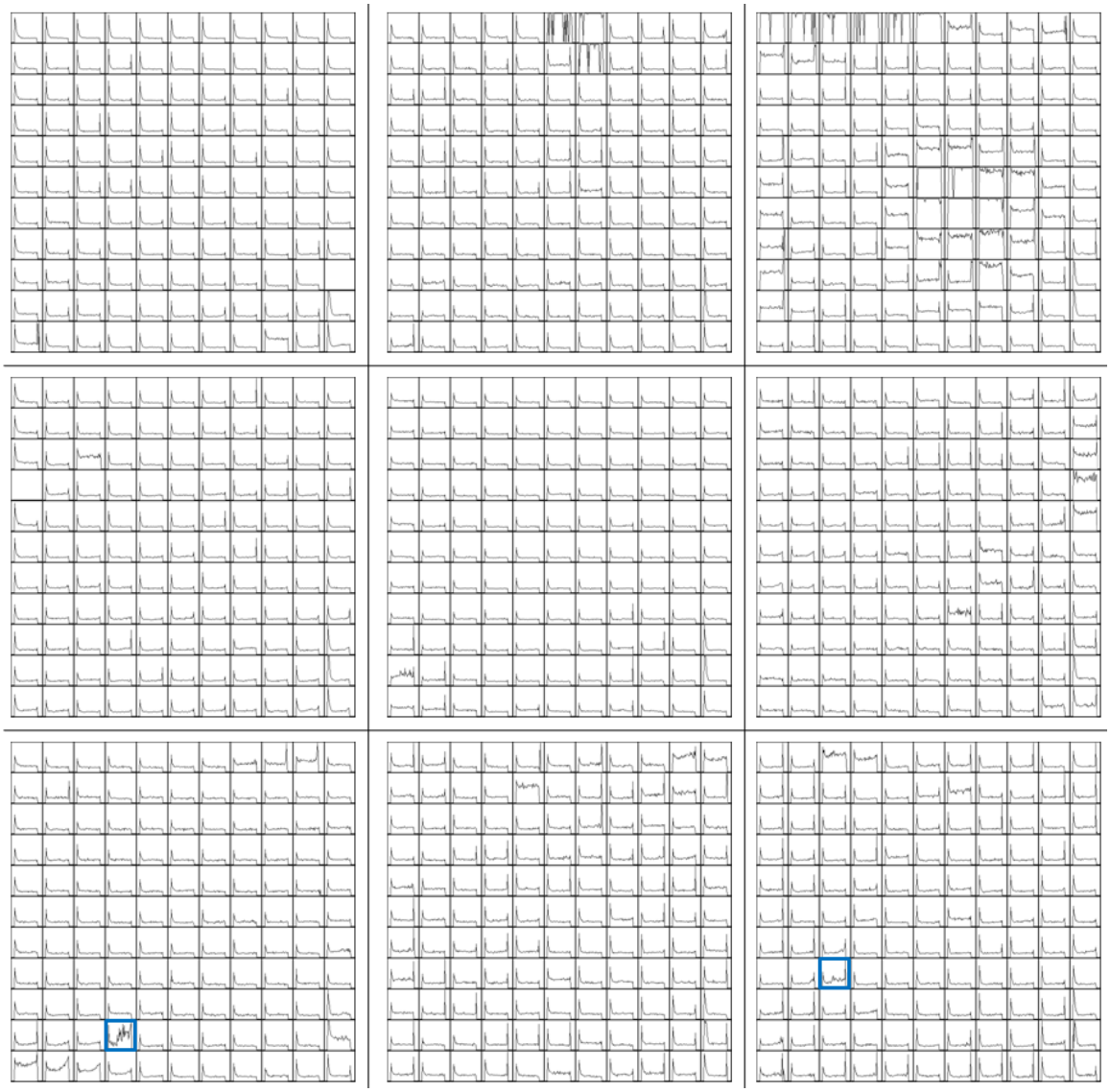

Figure 6.6: Plots of the FWHM versus depth for single-pixel events in each of the 9 detectors in the second plane of the second CdZnTe array system. For each pixel, the x-axis covers the depth of interaction from 0 mm (anode) to 15 mm (cathode) and the y-axis is the % FWHM at 662 keV with a range of 0-5%. A boxed pixel represents a pixel with a Case IV trapping defect.

6.3 Measurement and Simulation Comparison

A simulation of the system's response to a gamma rays will generate the ideal spectrum for the detector's best achievable intrinsic efficiency. There will be systematic efficiency losses due to Compton scattered gamma rays that do not deposit their

full energy in the detector, but no other losses due to imperfect detectors will be encountered. Comparisons between the measurement and simulation will then allow for better assumptions to be asserted for the simulation and for the determination of what factors are causing a degradation in the measurement.

6.3.1 Measurement and Simulation Description

A ^{60}Co source was placed 25 cm from the center of the cathode surface of one of the planes. The results in Fig. 6.7 show the expected photopeaks at 1173 and 1333 keV. A low activity source was used to limit the dead time effects on the measurement.

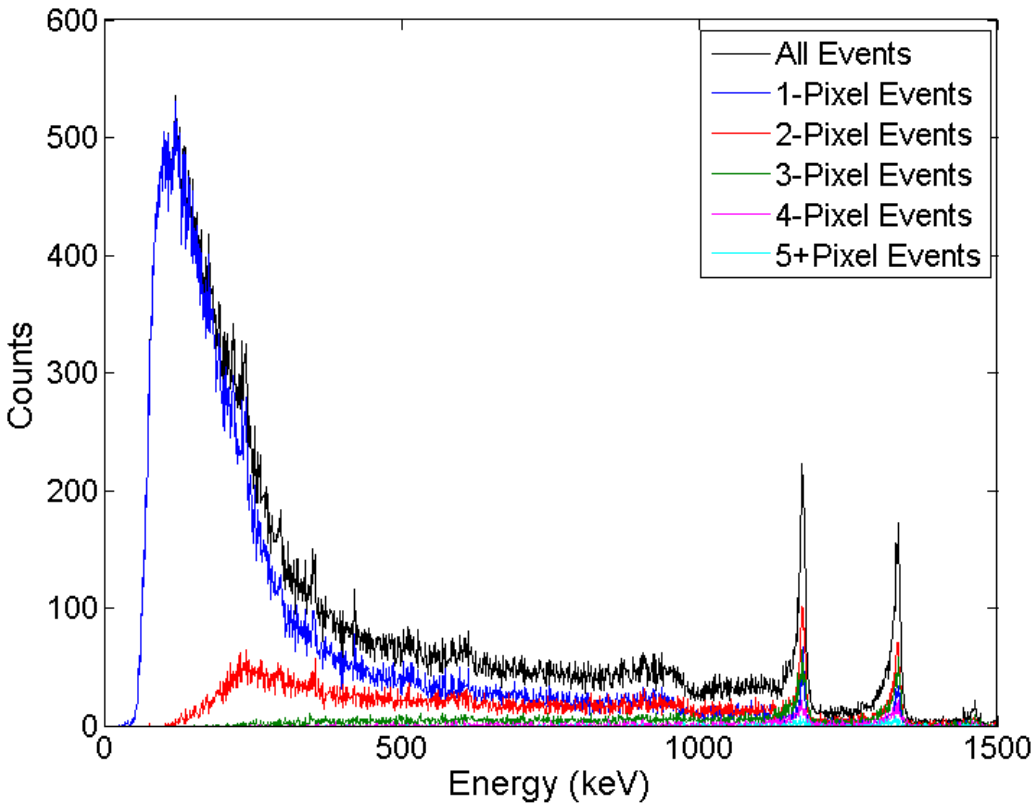

Figure 6.7: Measured spectrum using the second CdZnTe array system and a ^{60}Co source located 25 cm from the center of the cathode surface of one of the planes.

With a low activity source, background becomes a valid concern, as the 18-detector

CdZnTe system typically records 150-200 counts per second of background. Most of these counts are at low energies. Therefore, a background spectrum was collected and subtracted from the measurment's spectrum. The results are shown in Fig. 6.8.

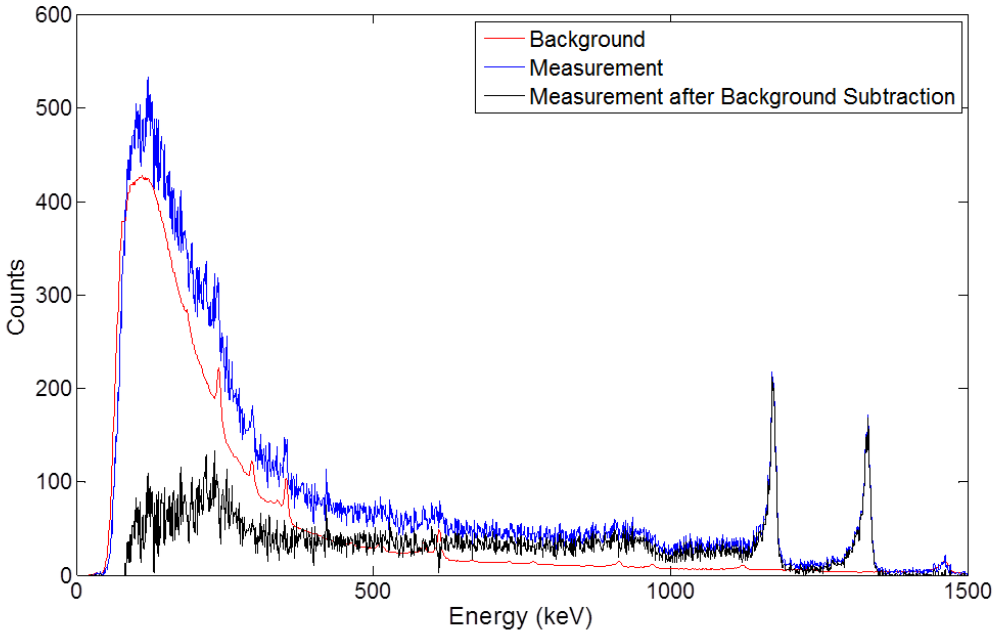

Figure 6.8: Spectrum for a ^{60}Co following the subtraction of the background spectrum.

The GEANT4 simulation of a Co-60 source located 25 cm from the center of the cathode surface of one of the plances was provided by Dr. Yuefeng Zhu. The simulated spectrum is contained in Fig. 6.9. The simulation assumes no surrounding material, so slight differences to the measurement can be attributed to scatter into the detector from the non-detector materials present in the device. However, as will be shown in the next section, the results show a significant efficiency degradation beyond any effects related to the exclusion of the surrounding materials from the simulation. The simulation does consider certain measurement effects such as charge-sharing between neighboring pixels.

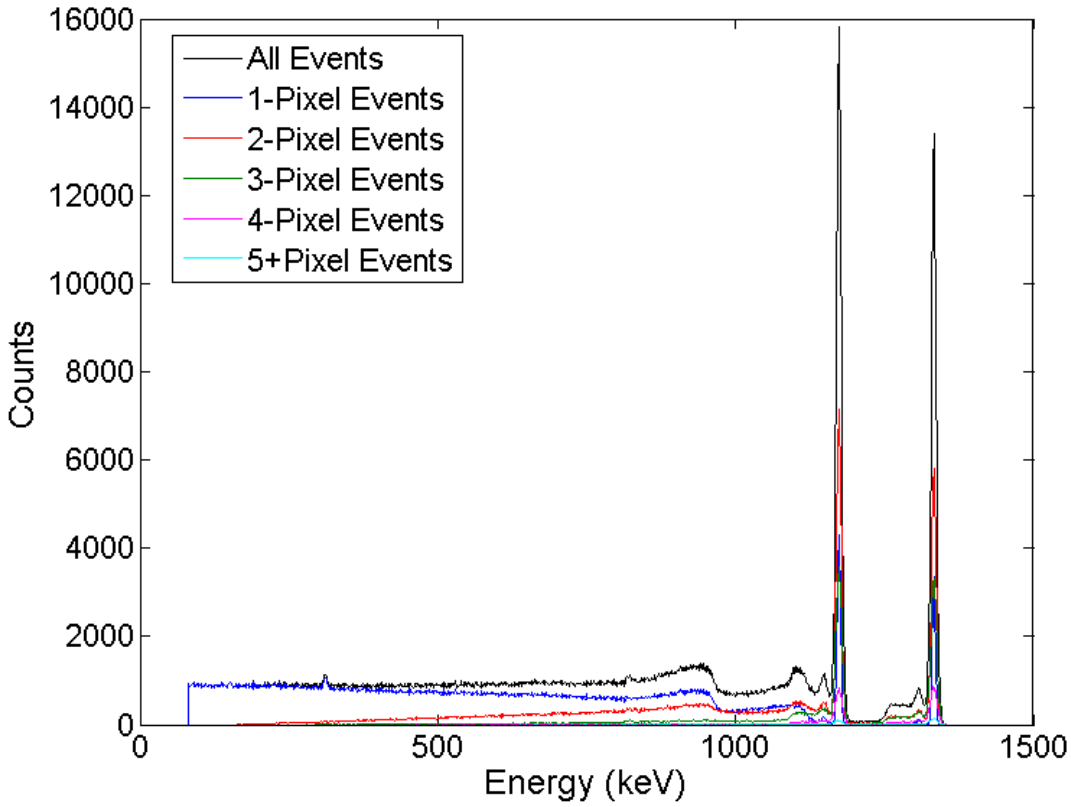

Figure 6.9: Simulated spectrum for the second CdZnTe array system and a ^{60}Co source located 25 cm from the center of the cathode surface of one of the planes.

6.3.2 Measurement and Simulation Comparison

The measurement and simulation are normalized to account for the activity of the source relative to the number of simulated particles. The 1333 keV photopeak for the measurement is compared to the ideal simulation in Fig. 6.10; both spectra contain all events regarless of number of triggered pixels. The measured spectrum contains 54.28% of the counts contained in the simulated spectrum. The shapes of the two spectra are clearly different, with the simulated spectrum having a much more Gaussian shape. The extended low energy tail is due to the incomplete collection of energy during the measurement.

For a more realistic comparison, several known factors are included in the simu-

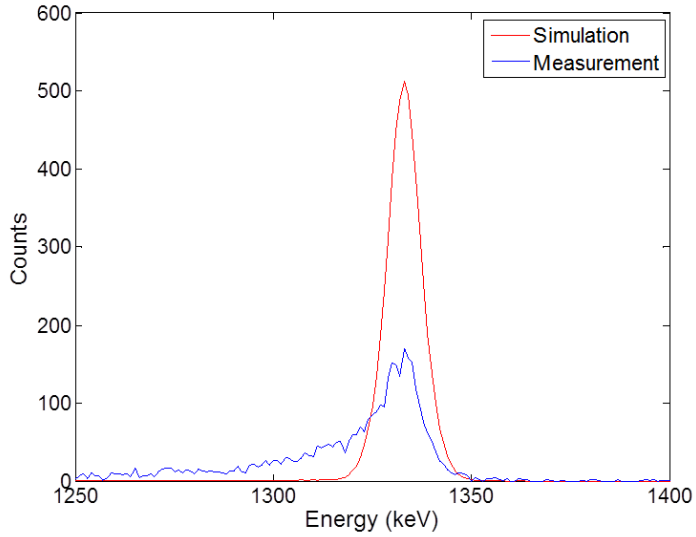

Figure 6.10: Comparison between the ^{60}Co measurement and simulation for the case of the ideal simulation.

lation results. A low energy threshold is set at 80 keV—80 keV corresponds to the lowest energy recorded in the ^{60}Co measurement after background subtraction. A 0.5 mm dead layer is added to the anode side events, and the dead time is accounted for. The measurement comparison to the simulation with these added factors is shown in Fig. 6.11. The ratio between measurement and simulation improves to 67.05% with these changes.

Peak-to-total ratios are calculated for the 1333 keV peak for each case. The measured peak contains 6.01% of the total measured counts whereas the simulated peak contains 11.15% of the total simulated counts. This shows that much of the degraded efficiency shown by the measurement is not due to entire events missing from the spectrum, but are due to events being reconstructed at a lower energy than expected.

The two most likely factors for this degradation are Case IV trapping defects and missing events from multiple gamma ray interactions. Case IV defects would prevent the full collection of generated electons, decreasing the reconstructed energy. Missing

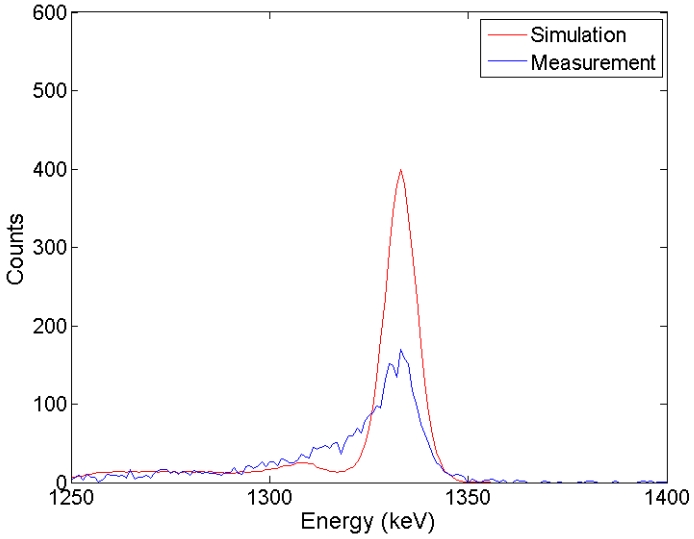

Figure 6.11: Comparison between the ^{60}Co measurement and simulation when the simulation also accounts for the energy threshold, dead time and anode dead layer.

one or more of the events from a gamma ray which interacted multiple times in the system would also produce a lower than expected energy in the system. An event may be missing if it was collected by the side surface of the crystal or grid instead of the anode electrode. Alternatively, the interaction could occur within the anode dead layer or be too small of an energy to trigger the system. These two factors will be further studied through analysis of the single-pixel efficiency as a function of depth of interaction, analysis of multiple pixel events and analysis of events in the edge pixels.

Events that are negatively affected by electron trapping defects are expected to be worse for depths nearer to the cathode since it is more likely they will encounter a randomly distributed defect than an event occurring nearer to the anode surface. Therefore, a decrease in the peak-to-total ratio for cathode side events would indicate efficiency loss due trapping defects. It would not be expected for any correlation to exist between depth of interaction and missing events in the system. Fig. 6.12 shows a decrease in the peak-to-total ratio for the measured 1333 keV photopeak from the ^{60}Co source. The simulated photopeak has a more flat peak-to-total ratio.

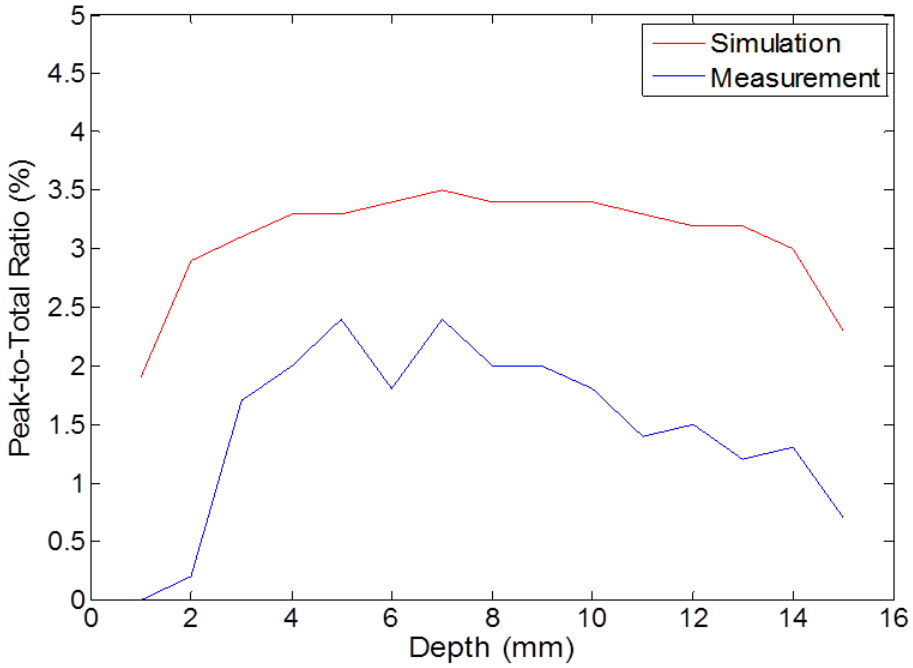

Figure 6.12: Comparison between the single-pixel peak-to-total ratios for the ^{60}Co measurement and simulation as a function of the depth of interaction.

In addition to the noted efficiency degradation due to trapping defects, the results show that the measurement reconstructs no counts in the 1-mm depth bin, and very few counts in the 2-mm depth bin. This indicates that a larger "dead" region exists near the anode surface. This region is not actually dead, but the events occurring in the first 1.5 mm are not properly reconstructed into the photopeak, but instead are reconstructed with lower energy. As an extreme example, if it were assumed that all of these events were lost from the simulation, the simulated efficiency will decrease, improving the comparability between the measurement and simulation. Fig. 6.13 shows the resulting comparison, which produces a 74.62% ratio between measurement and simulation. Therefore, as much as a 7% efficiency degradation is due to the improper reconstruction of anode side events.

Also noticeable from Fig. 6.12 is the lower peak-to-total ratio for depths near the anode surface. If the only factor contributing to the efficiency loss was the trapping

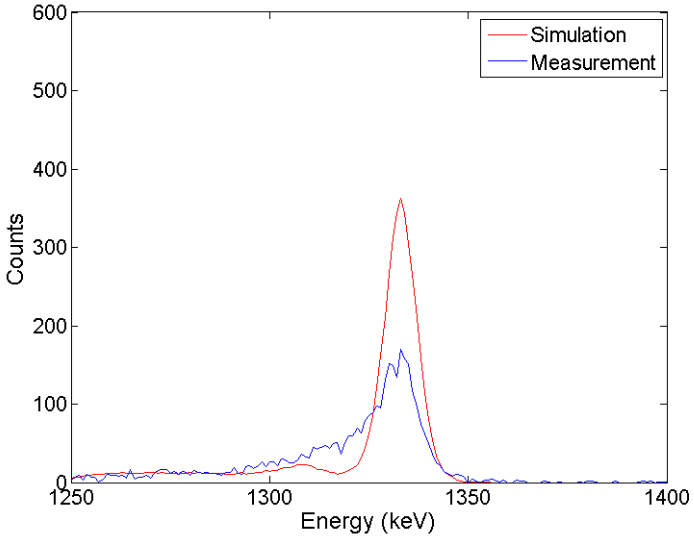

Figure 6.13: Comparison between the ^{60}Co measurement and simulation with a 1.5 mm anode dead layer.

defects, then it would not be expected to have a drop in the peak-to-total ratio at the anode side. This indicates that the issues are also related to interactions not being collected properly. If a gamma ray interacts twice with the system, but only one interaction is collected, then the event will contribute to the total number of single-pixel events, but will not be a photopeak event. Meanwhile, in the simulation, this event will register as a two-pixel photopeak event. Thererfore, the peak-to-total ratio for one-pixel events in the measurement will be worse than for the simulation, and the overall efficiency for all events will also decrease.

Comparing the ratios of number of counts for each number of triggered pixels to the total number of counts will show to what extent the number of triggered pixels is shifted to lower values. The results shown in Fig. 6.14 display that the number of triggered pixels is shifted slightly to lower values. Since above 50% of the total events are single-pixel events, an increase of 3% percent is significant when considering that thousands of events are recorded. Along with the measurement's higher percentage of single-pixel events are a lower percentage of two and three-pixel events. The

percentage of three-pixel events has a worse degradation than for two-pixel events, which is expected since three-interaction events would most likely only miss a single interaction and become a two-pixel event.

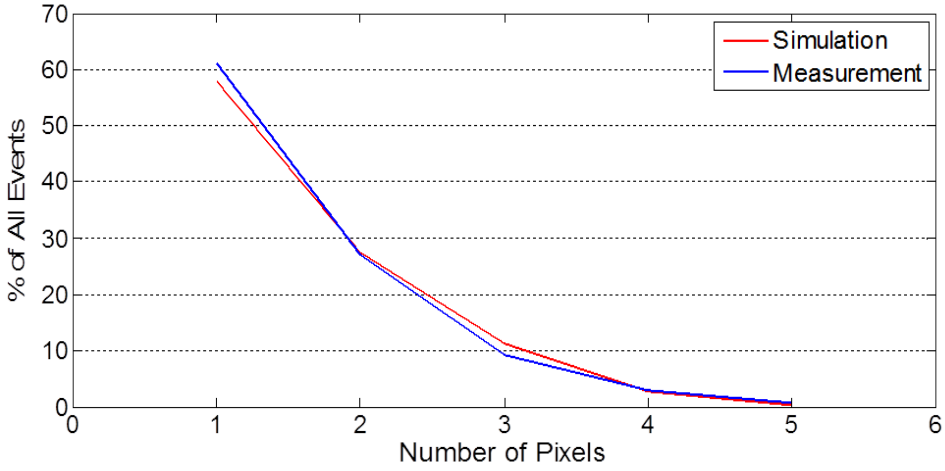

Figure 6.14: Comparison between the fraction of total counts for the ^{60}Co measurement and simulation as a function of the number of triggered pixels.

To show that missing events are indeed causing a degradation in the measured efficiency, the peak-to-total ratios as a function of number of pixels is plotted in Fig. 6.15. The peak-to-total ratio increases with the number of interactions since it is more likely that with more interactions that the full-energy of the gamma ray is deposited in the system. It appears that the simulation's peak-to-total ratio is increasing more rapidly than the measurement's peak-to-total ratio. However, this is misleading since the measurement has a peak-to-total ratio half that of the simulation for single-pixel events. The peak-to-total ratios for the simulation and measurement are compared in Fig. 6.16. This shows that the ratio between the peak-to-total ratios for measurement and simulation is worse for one and two-pixel events than for three or more pixel events. Therefore the efficiency loss is greater for fewer number of triggered pixels, which is due to an increase in the total number of events with fewer number of pixels that are not full-energy events due to missing one or more of the

actual interactions.

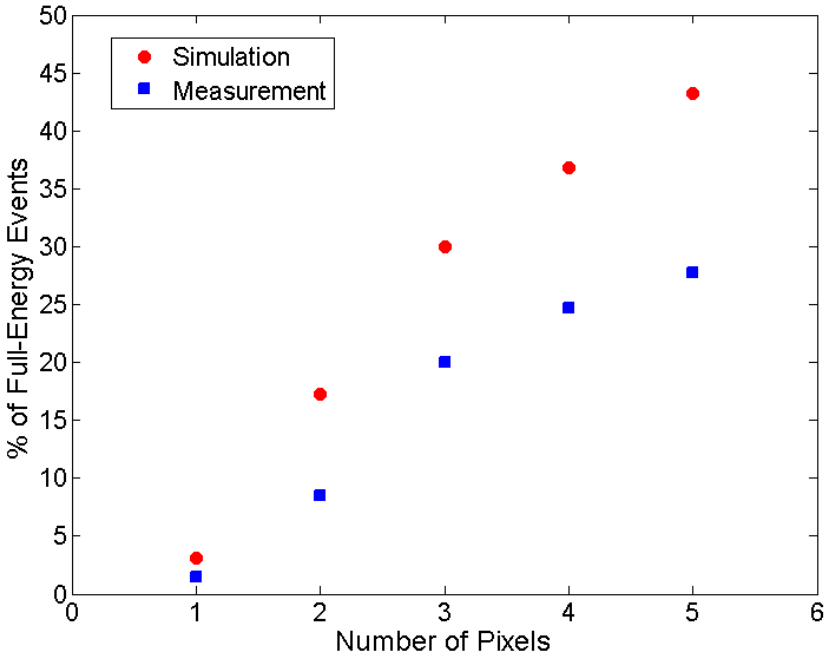

Figure 6.15: Comparison between the peak-to-total ratios for the ^{60}Co measurement and simulation as a function of the number of triggered pixels.

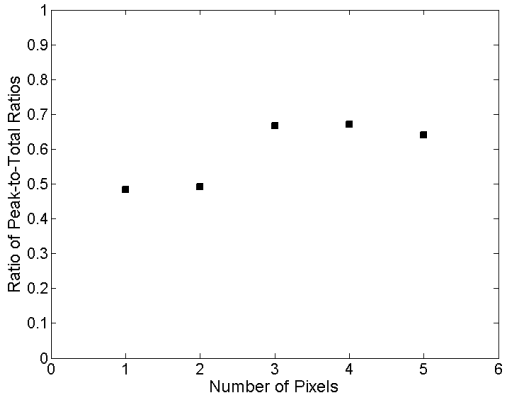

Figure 6.16: Ratio of the peak-to-total ratios for the ^{60}Co measurement and simulation as a function of the number of triggered pixels.

Further evidence that events are missing from the system can be obtained from studying the edge pixels. If events were collected on the side surface instead of the

anode electrode of the edge pixels, then the fraction of events on the edge pixels should be smaller for the measurement than for the simulation. Alternatively, the fraction of events that contain only events in the inner 9×9 should increase. This fraction is plotted as a function of number of pixels in Fig. 6.17. The measurement shows a higher fraction of events that do not have an edge pixel involved. This fraction increases for larger number of pixel interactions, consistent with the loss of events to the side surface.

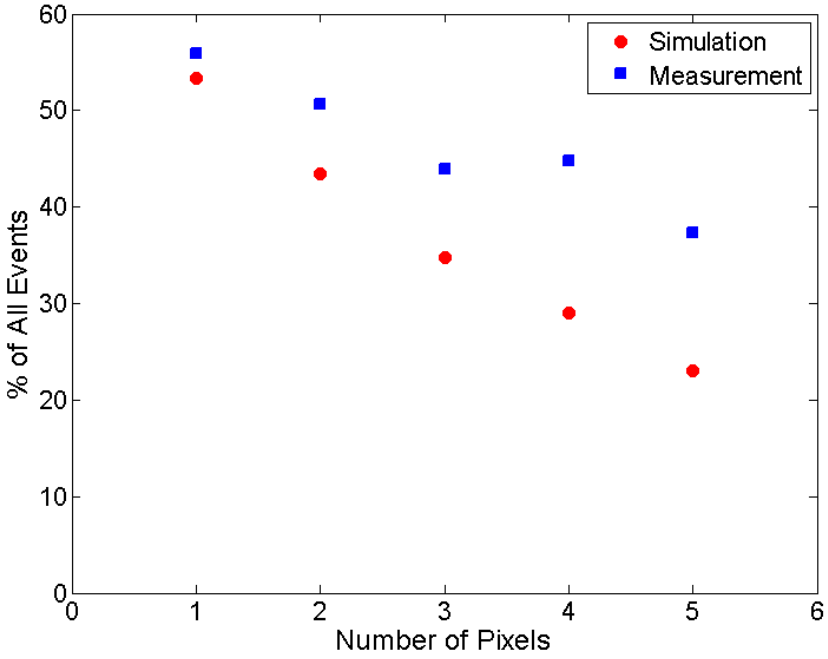

Figure 6.17: Comparison between the fraction of events only interacting with the inner 9×9 pixels for the ^{60}Co measurement and simulation as a function of the number of triggered pixels.

6.3.3 Measurement and Simulation Comparison Conclusions

The measurement of a ^{60}Co source is shown to record only 67% of the full-energy events as expected from the simulation. The efficiency loss can be tracked to correspond with losses due to trapping defects as well as missing events to collection by

the side surface or grid, interaction in the anode dead layer or deposition of energy below the system's threshold. An increase of an additional 1 mm to the anode dead layer can have as much as a 7% decrease in the efficiency.

6.4 Interplane Scattering Experiment and Analysis

Evidence of the efficiency loss due to trapping defects can be further exemplified through the study of interplane scattering events in the system. Due to the 3-D position sensitivity of the CdZnTe array system, the known position of the interactions in each plane can be used to determine the expected energy of the first interaction. Comparisons between this expected energy and the measured energy can be used to gain insight into the system's efficiency.

6.4.1 Measurement Description

A diagram of the setup used for the interplane scattering experiment is shown in Fig. 6.18. The ^{137}Cs source was placed 174 mm from the center of the face of the first 3×3 array of CdZnTe detectors. Since only 1% of all events are interplane events, a long measurements was acquired with 210 μCi of ^{137}Cs to achieve good statistics. A background measurement was also taken to allow for a background subtraction. Only two-pixel interplane events are used to eliminate any effects from implementing the wrong sequence reconstruction. The recorded spectra for the measurement and the background are shown in Fig. 6.19.

Under the assumption that the first interaction occurs in the plane nearest the ^{137}Cs source, the vector of the incident gamma ray is determined using the source position and the measured position in the first plane. The vector for the scattered gamma ray is then determined from the measured positions of each of the two interactions. The dot product of these two vectors determines the scattering angle. This assumes that forward scattering is the primary means for interplane events to occur,

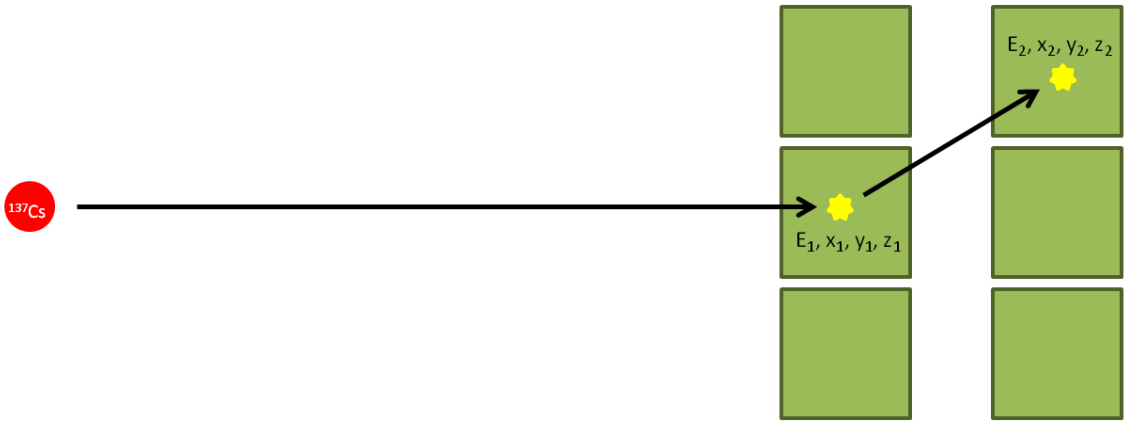

Figure 6.18: Diagram of the interplane efficiency experimental setup. The diagram is not to scale. The source-to-detector distance was 174mm. The distance between the two planes is 41 mm.

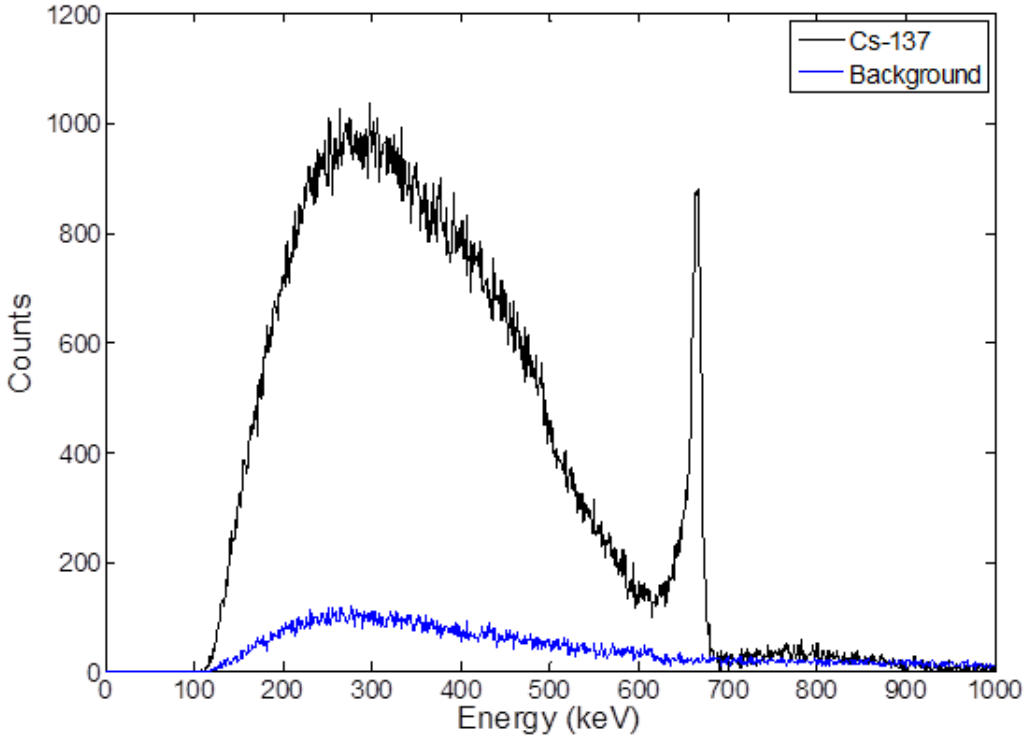

Figure 6.19: Spectra for two-pixel interplane events for measurements of background and a ^{137}Cs source.

which is a valid assumption for 662 keV gamma rays. It is unlikely for the gamma ray to pass unattenuated through the first plane of CdZnTe detectors, backscatter in

the second plane producing a low energy gamma ray which escapes the second plane and reaches the first plane again to generate a second interction in the CdZnTe array system. These backscatter events can also be determined and removed if there is a large percentage of them—this will be discussed further in Section 6.4.2.

The energy deposited in the first interaction is then determined from Equation 6.1, which is based on the Compton scattering formula.

$$E_d = E - \frac{E}{1 + \frac{E}{mc^2}(1 - cos\theta)} \tag{6.1}$$

where E_d is the deposited energy, E is the energy of the incidenct gamma ray, and $cos\theta$ is determined from the dot product of the incoming and scattered gamma ray vectors. The calculated deposited energy can then be compared to measured energy to study the system's efficiency. No assumptions can be made about the energy of the interaction in the second plane since it cannot be assumed that the second interction was not another Compton scattering interaction and the scattered photon escaped the system. Since the energy in the second plane does not affect the calculated energy for the first interaction, events that are not in the photopeak due to the second interation being a Compton scatter can still be used for the analysis.

To compare the measured and expected energy, the uncertainty in each needs to be calculated. The uncertainty in the measured energy can be determined from the energy resolution fit calculated for CdZnTe detectors from the coincidence experiment shown in Equation 5.7. The uncertainty in the expected energy calculated using Equation 6.1 is based on the uncertainty in the source position, the position of each interaction, and the doppler broadening. The uncertainty in the source position was conservatively estimated from the extent of the sources to be approximately 5 mm in each the x, y and z directions. The uncertainty in the x and y positions of each interaction were conservatively estimated to be the size of the pixel, 1.72 mm, since sub-pixel position information is not known. The uncertainty in the depth of

interaction is 0.5 mm [48]. The uncertainty due to doppler broadening was derived in Ref. [61].

6.4.2 Experimental Results

The background measurement shown in Fig. 6.19 is also analyzed with the assumption of the first interaction occurred in the first plane and the expected energy is calculated from Equation 6.1. The resulting correlation plot is shown in Fig. 6.20 and indicates that the background is uniform and will have a negligible impact on the results. The low number of counts for two-pixel interplane events in the background spectrum compared against the two-pixel interplane events with the source present also shows that background should not have an impact on the comparison results.

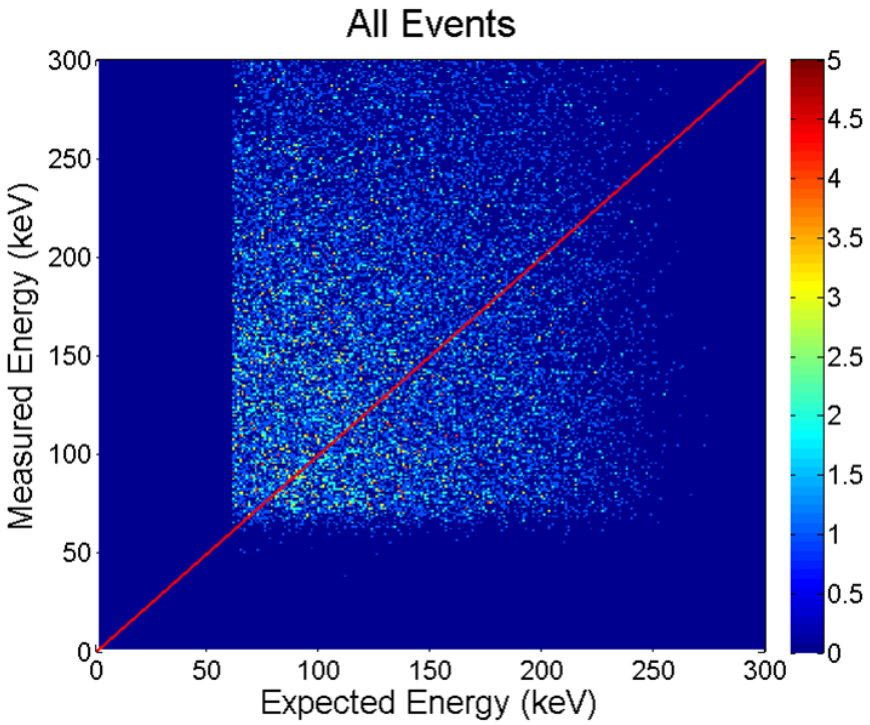

Figure 6.20: Correlation plot for the measured and expected energy for two-pixel interplane background events.

It is possible that the incident gamma ray travelled through the first plane, and the interaction measured in the second plane was actually the first interaction. In this

case, the interaction in the front plane was actually the second interaction. Equation 6.1 is used with the opposite interaction sequence to determine the possibility of that sequence. If the measured energy falls within the energy uncertainty for those events, the event is removed from the results as it is probable that the incorrect sequence was used. The removed events due to backscatter from the second plane to the first plane can be seen from the correlation plot for the full-energy events from the measurement of the ^{137}Cs source, shown in Fig. 6.21. Most events in the range of measured energies near 186 keV have been removed due to their potential to be back-scatter events instead of the assumed forward scatter events. The correlation plot shows that most of the full-energy events in the system fall along the expected line denoting a comparable energy between measurement and calculation. More events tend to fall below this line, which is expected due to the low energy tail on the measured photopeaks.

The measured versus expected energy correlation for all events in the spectrum shown in Fig. 6.19 is plotted in Fig. 6.22. Those events that have measured and calculated energies that fall within uncertainty of each other can be classified as good events and are shown in Fig. 6.23. Those events with energies that fall outside of one another's uncertainty are classified as bad events, and are shown in Fig. 6.24. The uncertainty noticeably widens with increasing energy, which is expected due to doppler broadening [61]. The good events account for 39.4% of all events.

The percentage of good events is slightly lower than expected based on the simulated efficiency results from Section 6.3. However, there are a large number of bad events that fall just above or below the classification range based on the energy uncertainty for events with lower expected energies. These events are likely misclassified as bad events due to poor estimation of the energy uncertainty. The energy uncertainty calculated from Equation 5.7 is averaged from all depths. However, it is shown in Fig. 6.25 that the energy resolution for anode side events is much degraded than

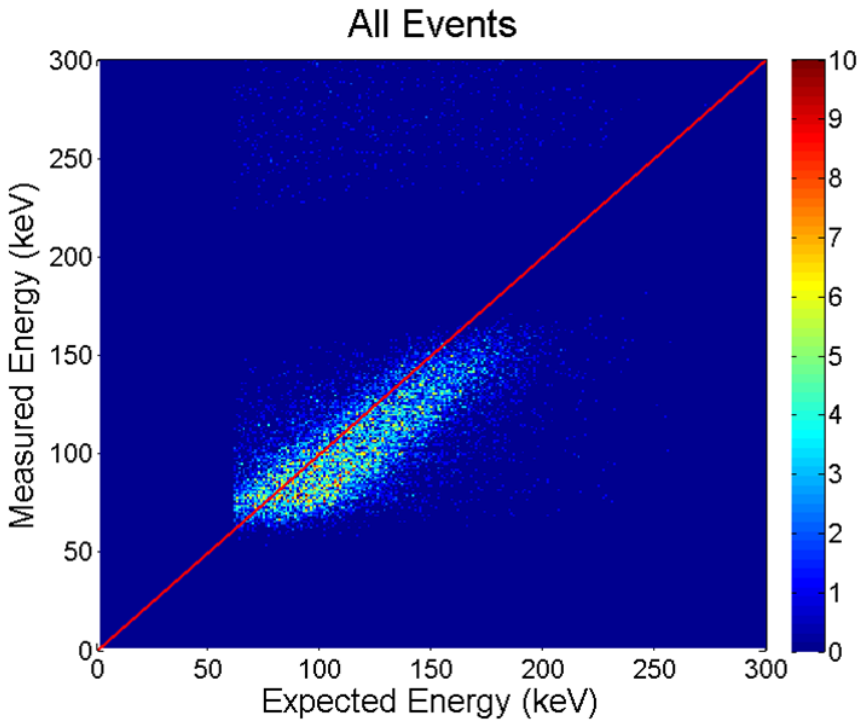

Figure 6.21: Correlation plot for the measured and expected energy for two-pixel interplane ^{137}Cs photopeak events. The gap centered around 186 keV without counts is due to the background subtraction.

for cathode side events. The depth distribution for the two-pixel interplane events is skewed towards the anode side since it is less likely for an interaction to occur near the cathode surface and not interact a second time in the first plane again before reaching the second plane. The depth of interaction distribution for two-pixel interplane events from the ^{60}Co simulation is shown in Fig. 6.26. The lower energy of the ^{137}Cs source should skew the depth distribution even more towards the anode surface. The events that have a larger than expected energy uncertainty can account for bad events falling just below the classification range for good events.

If there were issues related to trapping defects, then it would be expected to see a larger fraction of events nearer to the cathode to be classified as bad events, but to see no correlation between the lateral position of the interaction. The percentage of events classified as bad events as a function of x or y position and depth of in-

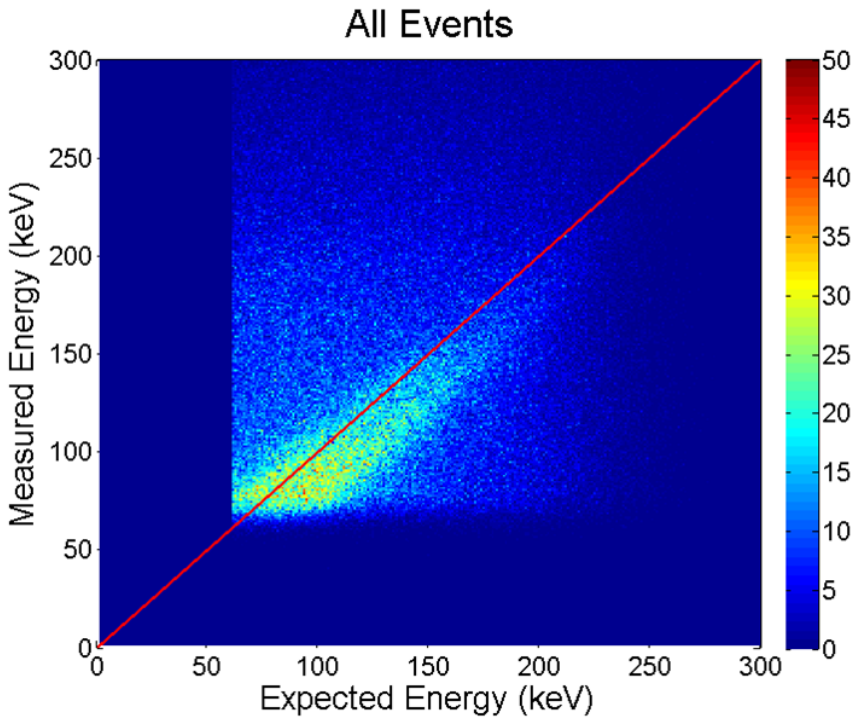

Figure 6.22: Correlation plot for the measured and expected energy for all two-pixel interplane ^{137}Cs events.

tercation are shown in Fig. 6.27. There is not apparent correlation between events classified as bad and lateral position of the events in the CdZnTe detector. There is a correlation between the bad events and the depth of interaction. This means that more events that occur on the cathode side of the detector have a measured energy that is not within uncertainty of the expected energy. These events therefore have a energy reconstruction problem, and would not likely fall within the photopeak range if the incident gamma ray had been completely absorbed in the system. This is further evidence of trapping defects causing an efficiency degradation in the 18-detector CdZnTe array system.

The effects of missing events are also apparent in the interplane scattering experiment. If events were missing because they were absorbed by the side surface or grid instead of the anode electrodes, or occurred in the anode dead layer, or deposited energy below the threshold, there should be no correlation with the x, y or z position

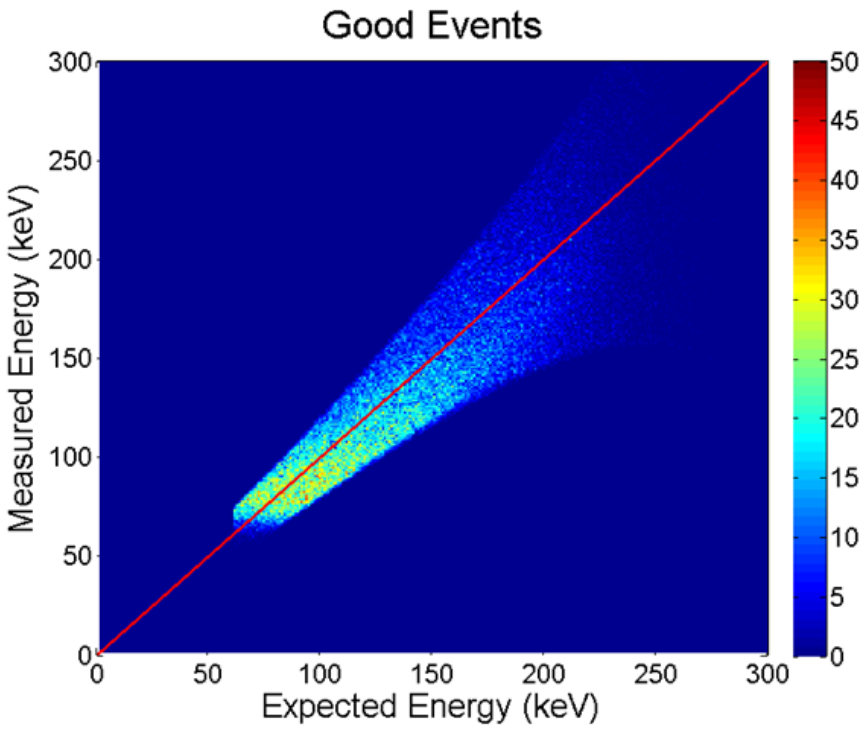

Figure 6.23: Correlation plot for the measured and expected energy for all two-pixel interplane ^{137}Cs events classified as good.

of the interaction since the measured event's position should be uncorrelated with the missing events position. However, if the first or second interaction were missing, it would drastically affect the calculation of the expected energy. The scattering angles would be incorrect, and depending on where the missing event occurred, a larger or smaller expected energy could be calculated than what should have been calculated. These events account for the large number of bad events that appear uniformly distributed throughout the correlation plot, but at a level significantly stronger than the background correlation shown in Fig. 6.20. These events should have been classified as three or more pixel interplane events, but were instead classified as two-pixel interplane events due to the missing interaction.

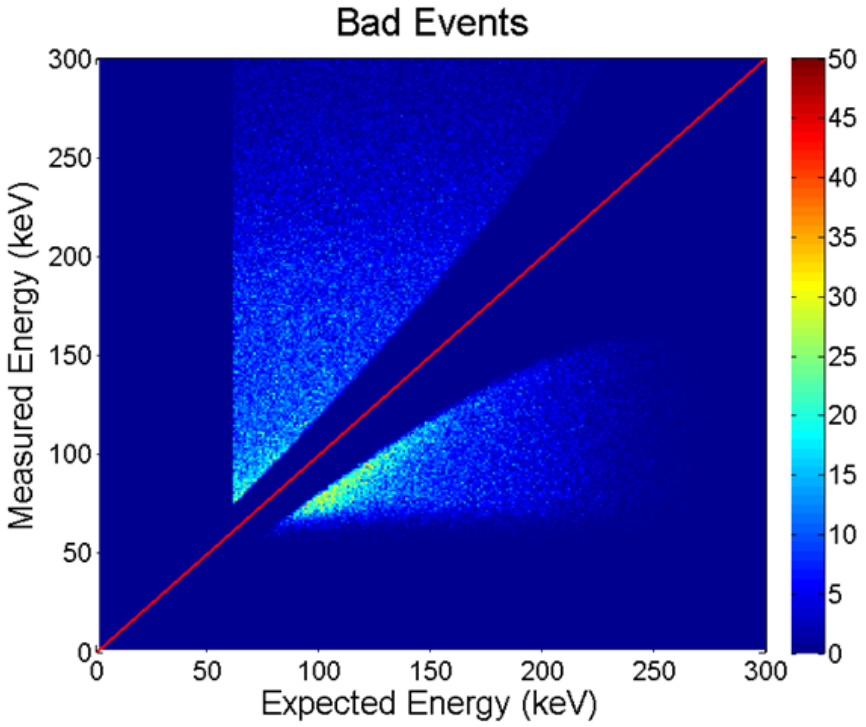

Figure 6.24: Correlation plot for the measured and expected energy for all two-pixel interplane ^{137}Cs events classified as bad.

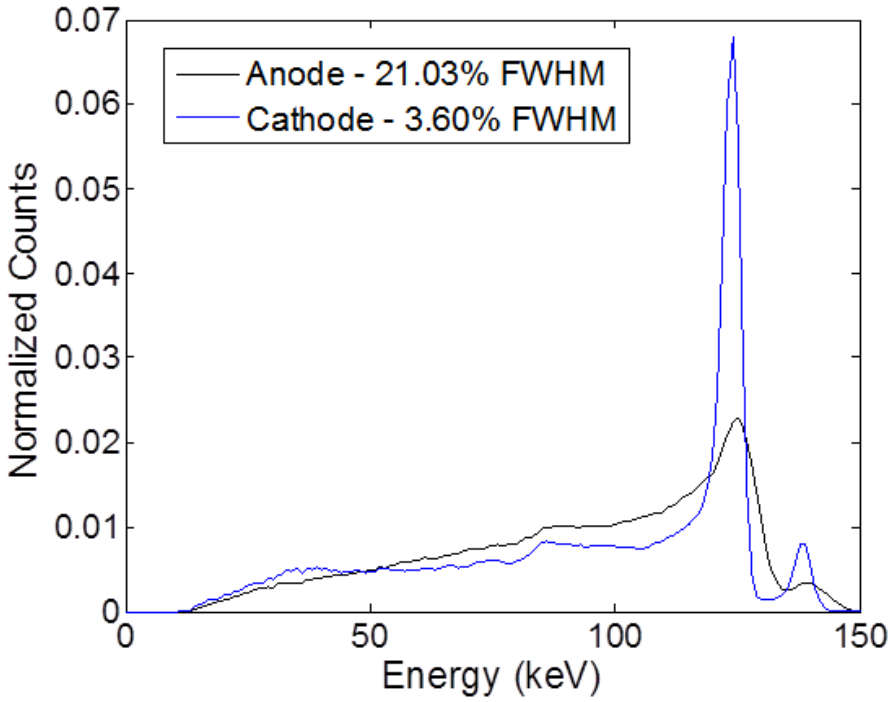

Figure 6.25: Energy spectra for a CdZnTe detector with a ^{57}Co source placed either on the anode or cathode surface. The short penetration distance of the 122 keV gamma rays means the events only occur near the surface of the side of the detector the source is placed on. Therefore the degraded energy resolution for the anode side events indicate that there is a depth dependence to the energy resolution that has not been accounted for in the interplane efficiency experimental analysis.

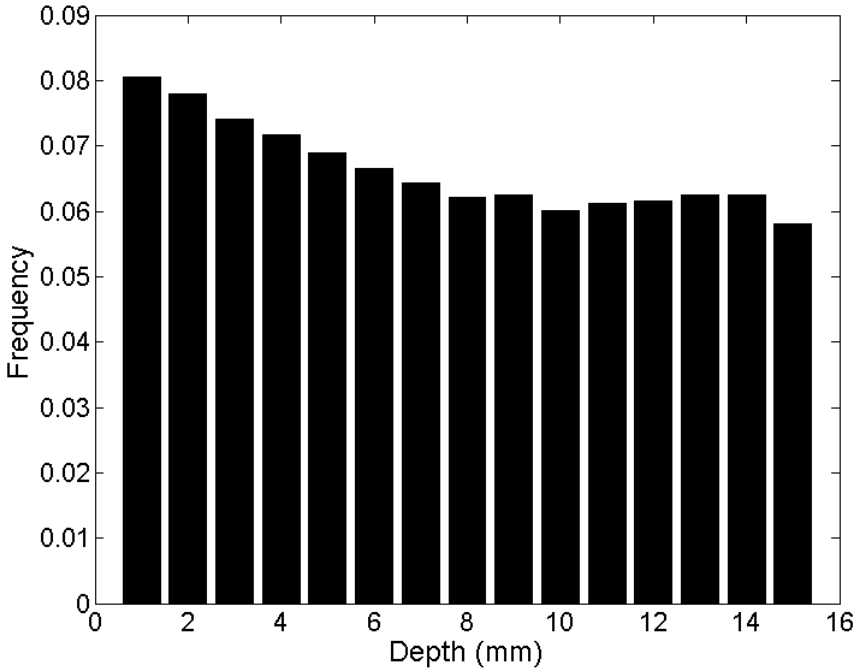

Figure 6.26: Depth distribtion for two-pixel interplane ^{60}Co events from simulation. It is expected that for lower energy incident gamma rays, the depth distribution will become more skewed toward anode side events.

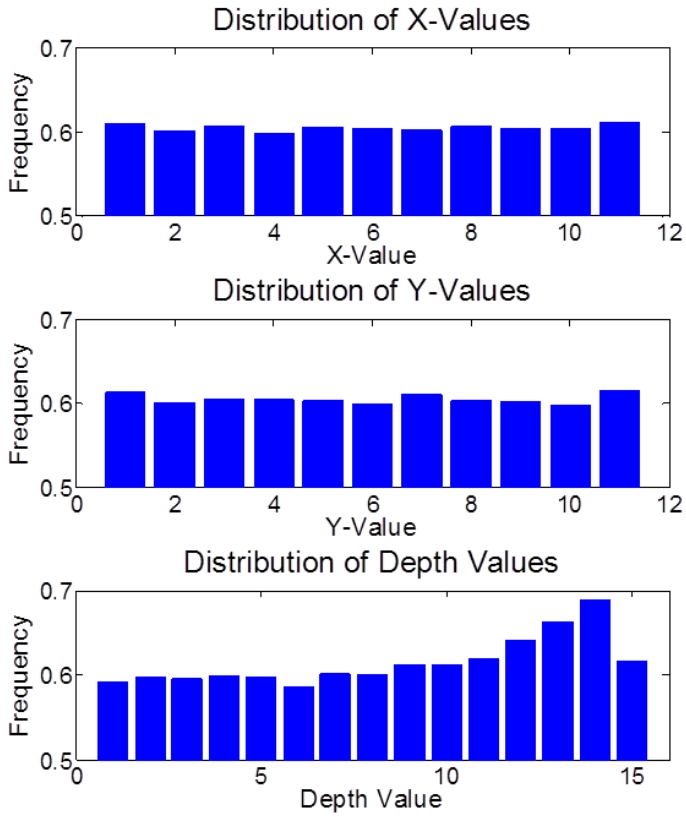

Figure 6.27: Relation between the probability for bad events to occur as a function of the x, y and z position of the first interaction. The depth distribution has units of mm from the anode surface.

CHAPTER VII

Conclusions

7.1 Brief Summary of Results

Cadmium Zinc Telluride (CdZnTe) is a promising material for gamma-ray measurement applications. It is operable at room-temperatures and offers better energy resolution than other room-temperature options, such as NaI. For many applications, slightly worse energy resolution than HPGe systems is acceptable, especially when the advantages of not requiring cryogenic cooling are considered. Due to the ability to use pixellated anode read-out, the small pixel effect and the theory behind weighting potential can be used to determine the 3-D position of each interaction in the device. If an incident gamma ray interacts via Compton scattering, the physics of the interaction can be used to predict the incident direction of the gamma ray, allowing for gamma-ray imaging to also be performed using CdZnTe detectors. The combination of gamma ray imaging and high-quality spectroscopic performance makes CdZnTe one of the most promising materials for gamma-ray measurement applications.

Two 18-detector CdZnTe array systems have been built and operated over the past several years. Each system operates at room temperature and is capable of high-quality spectroscopy and gamma-ray imaging. The first system achieved 1.44% FWHM at 662 keV for all events. The second system used higher-quality CdZnTe detectors and achieved 1.21% FWHM at 662 keV. The second system also showed better

long-term stability, which can be attributed to the better manufacturing performed by Redlen Technologies, Inc.

A large number of 20×20×15 mm^3 CdZnTe detectors were studied to determine the factors that are correlated to better spectroscopic performance. The electron transport properties of the detectors were found to be correlated to the uncalibrated spectroscopic performance, but uncorrelated to the calibrated spectroscopic performance. It was determined that the consistency of the electron trapping was the most dominant factor in determing whether or not a detector was going to achieve excellent spectroscopic performance.

Further analysis of the performance of CdZnTe detectors were performed through coincidence interactions with a HPGe detector. From the measurement of coincident full-energy interactions from a ^{137}Cs source, the energy resolution and energy non-linearity were studied as a function of deposited energy in the CdZnTe detector. A fit to the energy resolution versus energy relationship was found and used to determine a new value for the Fano factor for CdZnTe; the Fano factor was measured to be 0.058 $\pm$ 0.027. Analysis of the energy non-linearity showed that most of the measured offset in energy at low energies is related to the ASIC's non-linearity.

Finally, the efficiency of CdZnTe detectors were studied through various means. Studying the calibration data for the second 18-detector array system showed that there are not any complete trapping defects, which would cause a degraded efficiency. Yet, comparisons between simulation and measurement of a ^{60}Co source showed that the intrinsic efficiency of the CdZnTe system is lower than expected due to energy losses to small trapping defects and unreconstructed events. These events may be unreconstructed due to the electrons being collected by the side surface or grid instead of the anode electrodes, the deposition of energy in the anode dead layer, or the deposition of energy below the low-energy threshold. These factors also were shown to degrade the efficiency for two-pixel interplane events.

7.2 Future Work and Considerations

There are several improvements that can be made to improve the future performance of CdZnTe array systems. Higher quality detectors will greatly improve the spectroscopic performance. Active control of the temperature of the system and better containment of the detector head to prevent humidity or dust build-up around the detectors will help with system's spectroscopic stability. Yet one of the biggest areas for improvement for performance is an improvement to the ASIC.

Ideally, an ASIC would have at least half the electronic noise as the GMI VAS_UM2.3/TAT4 ASIC. The detector would also read out the waveform of each pixel instead of only recording the signal and time amplitudes. Having the entire waveform would allow for additional reconstructions which would improve the system's spectroscopic and imaging performance. Event classificaiton becomes achievable and neighboring waveforms can be used to monitor for transient signals to reject. Many of the issues discussed for using the current system at high-energy applications are completely solved by having access to the waveform for each pixel.

The ideal ASIC would have an adjustable dynamic range which could be set based on the application. For low energy measurements, a lower dynamic range improves the signal-to-noise ratio, which improves the energy resolution. Raising the dynamic range would allow for higher efficiency for high-energy applications. The ASIC would also be extremely energy linear. The limitations found from the coincidence measurements between a CdZnTe detector and a HPGe detector showed that the energy nonlinearity was dominated by the ASIC nonlinearity. The CdZnTe detector itself was shown to be linear to the best of the experiments ability.

If a future ASIC can be developed to be able to construct a similar 18-detector CdZnTe array system, many of the experiments presented in this work should be repeated to further characterize and understand the performance of CdZnTe systems. The efficiency could be better studied since event classification will allow for a better

comparison to simulation. A more linear ASIC would remove the ASIC's nonlinearity from coincidence experiments, and the true linearity of CdZnTe detectors can be studied. Experiments at high energies should be conducted and a more realistic breakdown of events can be determined.

Cadmium zinc telluride has a bright future in the field of gamma-ray measurements, and it will only become brighter with improvements to the read-out electronics.

BIBLIOGRAPHY

BIBLIOGRAPHY

[1] Wikipedia, "Gamma ray — wikipedia, the free encyclopedia," 2012. [Online; accessed 2-January-2013].

[2] G. F. Knoll, *Radiation Detection and Measurement*. New York: John Wiley & Sons, Inc., third ed., 2000.

[3] J. Butler, C. Lingren, and F. Doty, "Cd1-xznxte gamma ray detectors," *Nuclear Science, IEEE Transactions on*, vol. 39, pp. 605 –609, aug 1992.

[4] P. Luke, "Unipolar charge sensing with coplanar electrodes-application to semiconductor detectors," *Nuclear Science, IEEE Transactions on*, vol. 42, pp. 207 –213, Aug 1995.

[5] F. Zhang, C. Herman, Z. He, G. De Geronimo, E. Vernon, and J. Fried, "Characterization of the H3D asic readout system and 6.0 cm ^{3} 3-D position sensitive CdZnTe detectors," *Nuclear Science, IEEE Transactions on*, vol. 59, pp. 236 –242, feb. 2012.

[6] G. A. Carini, A. E. Bolotnikov, G. S. Camarda, G. W. Wright, R. B. James, and L. Li, "Effect of te precipitates on the performance of CdZnTe detectors," *Applied Physics Letters*, vol. 88, pp. 143515 –143515–3, Apr. 2006.

[7] A. Bolotnikov, G. Camarda, G. Carini, Y. Cui, K. Kohman, L. Li, M. Salomon, and R. James, "Performance-limiting defects in CdZnTe detectors," *Nuclear Science, IEEE Transactions on*, vol. 54, no. 4, pp. 821 –827, 2007.

[8] A. Bolotnikov, S. Babalola, G. Camarda, Y. Cui, S. Egarievwe, R. Hawrami, A. Hossain, G. Yang, and R. James, "Te inclusions in czt detectors: New method for correcting their adverse effects," *Nuclear Science, IEEE Transactions on*, vol. 57, no. 2, pp. 910 –919, 2010.

[9] A. Hossain, A. Bolotnikov, G. Camarda, Y. Cui, G. Yang, K.-H. Kim, R. Gul, L. Xu, and R. James, "Extended defects in CdZnTe crystals: Effects on device performance," *Journal of Crystal Growth*, vol. 312, no. 11, pp. 1795 – 1799, 2010.

[10] H. Chen, S. A. Awadalla, K. Iniewski, P. H. Lu, F. Harris, J. Mackenzie, T. Hasanen, W. Chen, R. Redden, G. Bindley, I. Kuvvetli, C. Budtz-J andrgensen, P. Luke, M. Amman, J. S. Lee, A. E. Bolotnikov, G. S. Camarda, Y. Cui,

A. Hossain, and R. B. James, "Characterization of large cadmium zinc telluride crystals grown by traveling heater method," *Journal of Applied Physics*, vol. 103, pp. 014903 –014903–5, Jan. 2008.

[11] H. Chen, S. Awadalla, J. Mackenzie, R. Redden, G. Bindley, A. Bolotnikov, G. Camarda, G. Carini, and R. James, "Characterization of traveling heater method (thm) grown cd0.9zn0.1te crystals," *Nuclear Science, IEEE Transactions on*, vol. 54, no. 4, pp. 811 –816, 2007.

[12] S. Awadalla, J. Mackenzie, H. Chen, B. Redden, G. Bindley, M. Duff, A. Burger, M. Groza, V. Buliga, J. Bradley, Z. Dai, N. Teslich, and D. Black, "Characterization of detector-grade CdZnTe crystals grown by traveling heater method (thm)," *Journal of Crystal Growth*, vol. 312, no. 4, pp. 507 – 513, 2010.

[13] Z. He, G. F. Knoll, and D. K. Wehe, "Direct measurement of product of the electron mobility and mean free drift time of CdZnTe semiconductors using position sensitive single polarity charge sensing detectors," *Journal of Applied Physics*, vol. 84, no. 10, pp. 5566–5569, 1998.

[14] Y. A. Boucher, F. Zhang, W. Kaye, and Z. He, "New measurement technique for the product of the electron mobility and mean free drift time for pixelated semiconductor detectors," *Nuclear Instruments and Methods in Physics Research Section A: Accelerators, Spectrometers, Detectors and Associated Equipment*, vol. 671, no. 0, pp. 1 – 5, 2012.

[15] W. Willig, "Mercury iodide as a gamma spectrometer," *Nuclear Instruments and Methods*, vol. 96, no. 4, pp. 615–616, 1971.

[16] H. Malm, "A mercuric iodide gamma-ray spectrometer," *Nuclear Science, IEEE Transactions on*, vol. 19, no. 3, pp. 263–265, 1972.

[17] K. Hull, A. Beyerle, B. Lopez, J. Markakis, C. Ortale, W. Schnepple, and L. Van den Berg, "Recent developments in thick mercuric iodide spectrometers," *Nuclear Science, IEEE Transactions on*, vol. 30, no. 1, pp. 402–404, 1983.

[18] P. Olmos, G. Garcia-Belmonte, J. Perez, and J. Diaz, "Use of thick hgi¡ sub¿ 2¡/sub¿ detectors as intelligent spectrometers," *Nuclear Instruments and Methods in Physics Research Section A: Accelerators, Spectrometers, Detectors and Associated Equipment*, vol. 299, no. 1, pp. 45–50, 1990.

[19] T. Mohammed-Brahim, A. Friant, and J. Mellet, "Structure mis effects on polarization of hgi 2 crystals used for γ-ray detection," *Nuclear Science, IEEE Transactions on*, vol. 32, no. 1, pp. 581–584, 1985.

[20] Z. He and R. Vigil, "Investigation of pixellated hgi2γ-ray spectrometers," *Nuclear Instruments and Methods in Physics Research Section A: Accelerators, Spectrometers, Detectors and Associated Equipment*, vol. 492, no. 3, pp. 387–401, 2002.

[21] J. Baciak and Z. He, "Spectroscopy on thick hgi¡ sub¿ 2¡/sub¿ detectors: a comparison between planar and pixelated electrodes," *Nuclear Science, IEEE Transactions on*, vol. 50, no. 4, pp. 1220–1224, 2003.

[22] Y. Zhu, W. Kaye, Z. He, and F. Zhang, "Stability and characteristics of 3d hgi2 detectors at different cathode bias," in *Nuclear Science Symposium Conference Record, 2007. NSS'07. IEEE*, vol. 2, pp. 1537–1540, IEEE, 2007.

[23] M. Saleno, L. Van den Berg, R. Vigil, J. Baker, W. Kaye, Y. Zhu, F. Zhang, and Z. He, "Use of pixelated detectors for the identification of defects and charge collection effects in mercuric iodide (hgi¡ sub¿ 2¡/sub¿) single crystal material," *Nuclear Instruments and Methods in Physics Research Section A: Accelerators, Spectrometers, Detectors and Associated Equipment*, vol. 652, no. 1, pp. 197–200, 2011.

[24] C. Thrall, W. Kaye, Z. He, H. Kim, L. Cirignano, and K. Shah, "Transient behavior in TlBr gamma-ray detectors and its analysis using 3-D position sensing," *Nuclear Science, IEEE Transactions on*, vol. 99, 2012.

[25] H. Kim, A. Churilov, G. Ciampi, L. Cirignano, W. Higgins, S. Kim, P. O'Dougherty, F. Olschner, and K. Shah, "Continued development of thallium bromide and related compounds for gamma-ray spectrometers," *Nuclear Instruments and Methods in Physics Research Section A: Accelerators, Spectrometers, Detectors and Associated Equipment*, 2010.

[26] K. Hitomi, Y. Kikuchi, T. Shoji, and K. Ishii, "Polarization phenomena in tlbr detectors," *Nuclear Science, IEEE Transactions on*, vol. 56, no. 4, pp. 1859–1862, 2009.

[27] B. Donmez, C. Thrall, Z. He, L. Cirignano, H. Kim, and K. Shah, "Investigation of polarization effect with tlbr detectors at different operating temperatures," in *Nuclear Science Symposium Conference Record (NSS/MIC), 2010 IEEE*, pp. 3773–3775, IEEE, 2010.

[28] Z. He, "Review of the shockley–ramo theorem and its application in semiconductor gamma-ray detectors," *Nuclear Instruments and Methods in Physics Research Section A: Accelerators, Spectrometers, Detectors and Associated Equipment*, vol. 463, no. 1, pp. 250–267, 2001.

[29] P. Luke and E. Eissler, "Performance of cdznte coplanar-grid gamma-ray detectors," *Nuclear Science, IEEE Transactions on*, vol. 43, no. 3, pp. 1481–1486, 1996.

[30] M. Amman, J. Lee, P. Luke, H. Chen, S. Awadalla, R. Redden, and G. Bindley, "Evaluation of thm-grown CdZnTe material for large-volume gamma-ray detector applications," *Nuclear Science, IEEE Transactions on*, vol. 56, no. 3, pp. 795 –799, 2009.

[31] F. Doty, H. Barber, F. Augustine, J. Butler, B. Apotovsky, E. Young, and W. Hamilton, "Pixellated cdznte detector arrays," *Nuclear Instruments and Methods in Physics Research Section A: Accelerators, Spectrometers, Detectors and Associated Equipment*, vol. 353, no. 1, pp. 356–360, 1994.

[32] H. Barrett, J. Eskin, and H. Barber, "Charge transport in arrays of semiconductor gamma-ray detectors," *Physical review letters*, vol. 75, no. 1, pp. 156–159, 1995.

[33] Z. He, G. Knoll, D. Wehe, R. Rojeski, C. Mastrangelo, M. Hammig, C. Barrett, and A. Uritani, "1-D position sensitive single carrier semiconductor detectors," *Nuclear Instruments and Methods in Physics Research Section A: Accelerators, Spectrometers, Detectors and Associated Equipment*, vol. 380, no. 1, pp. 228–231, 1996.

[34] Z. He, W. Li, G. F. Knoll, D. K. Wehe, J. E. Berry, and C. M. Stahle, "3-D position sensitive CdZnTe gamma-ray spectrometers," *Nucl. Instr. and Meth. A*, vol. 422, pp. 173–178, 1999.

[35] W. Li, Z. He, G. Knoll, D. Wehe, and C. Stahle, "Spatial variation of energy resolution in 3-D position sensitive CZT gamma-ray spectrometers," in *Nuclear Science Symposium, 1998. Conference Record. 1998 IEEE*, vol. 1, pp. 628–633, IEEE, 1998.

[36] F. Zhang, Z. He, and D. Xu, "Analysis of detector response using 3-d position-sensitive CZT gamma-ray spectrometers," *Nuclear Science, IEEE Transactions on*, vol. 51, no. 6, pp. 3098–3104, 2004.

[37] F. Zhang, Z. He, D. Xu, G. Knoll, D. Wehe, and J. Berry, "Improved resolution for 3-D position sensitive CdZnTe spectrometers," *Nuclear Science, IEEE Transactions on*, vol. 51, no. 5, pp. 2427–2431, 2004.

[38] Y. Du, Z. He, G. Knoll, D. Wehe, and W. Li, "Evaluation of a compton scattering camera using 3-D position sensitive CdZnTe detectors," *Nuclear Instruments and Methods in Physics Research Section A: Accelerators, Spectrometers, Detectors and Associated Equipment*, vol. 457, no. 1, pp. 203–211, 2001.

[39] C. Lehner, Z. He, and F. Zhang, "4 pi; compton imaging using a 3-d position-sensitive CdZnTe detector via weighted list-mode maximum likelihood," *Nuclear Science, IEEE Transactions on*, vol. 51, pp. 1618 – 1624, aug. 2004.

[40] D. Xu, Z. He, C. Lehner, and F. Zhang, "4π compton imaging with single 3D position sensitive CdZnTe detector," in *Proc. of SPIE Vol*, vol. 5540, p. 145, 2004.

[41] D. Xu and Z. He, "Gamma-ray energy-imaging integrated deconvolution," in *Nuclear Science Symposium Conference Record, 2005 IEEE*, vol. 2, pp. 882–886, IEEE, 2005.

[42] W. Wang, C. Wahl, J. Jaworski, and Z. He, "Maximum-likelihood deconvolution in the spatial and spatial-energy domain for events with any number of interactions," *Nuclear Science, IEEE Transactions on*, vol. 59, no. 2, pp. 469–478, 2012.

[43] J. Jaworski, C. Wahl, W. Wang, J. Fessler, and Z. He, "Model-based reconstruction of spectral and spatial source distribution from objects with known motion," in *Nuclear Science Symposium Conference Record (NSS/MIC), 2010 IEEE*, pp. 1518 –1524, 30 2010-nov. 6 2010.

[44] J. Jaworski and Z. He, "3D compton image reconstruction using a moving 3d-position-sensitive room-temperature CdZnTe detector array," in *Nuclear Science Symposium and Medical Imaging Conference (NSS/MIC), 2011 IEEE*, pp. 976 –981, oct. 2011.

[45] S. Kaye, W. Kaye, and Z. He, "Experimental demonstration of coded aperture imaging using thick 3D-position-sensitive CdZnTe detectors," in *Nuclear Science Symposium Conference Record (NSS/MIC), 2009 IEEE*, pp. 1902–1906, IEEE, 2009.

[46] F. Zhang, Z. He, and C. Seifert, "A prototype three-dimensional position sensitive CdZnTe detector array," *Nuclear Science, IEEE Transactions on*, vol. 54, no. 4, pp. 843–848, 2007.

[47] F. Zhang and Z. He, "New readout electronics for 3-D position sensitive CdZnTe/HgI_2 detector arrays," *Nuclear Science, IEEE Transactions on*, vol. 53, pp. 3021–3027, Oct. 2006.

[48] W. Kaye, *Energy and Position Reconstruction in Pixelated CdZnTe Detectors*. PhD thesis, University of Michigan, 2012.

[49] E. M. Becker, C. E. Seifert, M. J. Myjak, L. E. Erikson, S. J. Morris, D. T. Balvage, and R. P. Lundy, "Performance characteristics of pixelated CZT crystals used on the gammatracker project," vol. 8142, p. 81420F, SPIE, 2011.

[50] T. Schlesinger and R. James, *Semiconductors for room temperature nuclear detector applications*. Semiconductors and semimetals, Academic Press, 1995.

[51] B. C. Reed, "Linear least-squares fits with errors in both coordinates. ii: Comments on parameter variances," *American Journal of Physics*, vol. 60, no. 1, pp. 59–62, 1992.

[52] J. D. Valentine and A. E. Rana, "Centroid and full-width at half maximum uncertainties of histogrammed data with and underlying gaussian distribution —the moments method," *Nuclear Science, IEEE Transactions on*, vol. 43, no. 5, pp. 2501–2508, 1996.

[53] H. Y. Cho, J. H. Lee, Y. K. Kwon, J. Y. Moon, and C. S. Lee, "Measurement of the drift mobilities and the mobility-lifetime products of charge carriers in a CdZnTe crystal by using a transient pulse technique," *Journal of Instrumentation*, vol. 6, no. 01, p. C01025, 2011.

[54] W. Wang, *Techniques and Applications of Compton Imaging for Position-Sensitive Gamma-Ray Detectors*. PhD thesis, University of Michigan, 2011.

[55] V. Reglero, F. Ballesteros, P. Blay, E. Porras, F. Snchez, and J. Suso, "Legri operations. detectors and detector stability," *Astrophysics and Space Science*, vol. 276, pp. 239–254, 2001. 10.1023/A:1011694215328.

[56] Y. Z. Hao Yang and Z. He, "Identification and reconstruction of side-neighbor charge leak events on 3-D semiconductor detectors using digital asic," in *Nuclear Science Symposium Conference Record (NSS/MIC), 2012 IEEE*, Nov. 2012.

[57] B. Rooney and J. Valentine, "Benchmarking the compton coincidence technique for measuring electron response nonproportionality in inorganic scintillators," *Nuclear Science, IEEE Transactions on*, vol. 43, pp. 1271 –1276, jun 1996.

[58] P. Ugorowski, A. Kargar, and D. Mcgregor, "Pulse height linearity of cdznte," in *Nuclear Science Symposium Conference Record (NSS/MIC), 2009 IEEE*, pp. 2023 –2031, 24 2009-nov. 1 2009.

[59] M. Szawlowski, M. Kapusta, L. Swiderski, R. Marcinkowski, M. Moszynski, T. Szczesniak, M. Grodzicka, D. Wolski, and A. Celler, "Linearity and energy resolution of compton electrons in czt measured using the wide angle compton coincidence technique," in *Nuclear Science Symposium Conference Record (NSS/MIC), 2010 IEEE*, pp. 3877 –3879, 30 2010-nov. 6 2010.

[60] R. Redus, J. Pantazis, A. Huber, V. Jordanov, J. Butler, and B. Apotovsky, "Fano factor determination for czt," in *MRS Proceedings*, vol. 487, Cambridge Univ Press, 1997.

[61] D. Xu, *Gamma-ray imaging and polarization using 3-D position-sensitive CdZnTe detectors*. PhD thesis, University of Michigan, 2006.